DURBAN UNIVERSITY OF TECHNOLOGY
INYUVESI YASETHEKWINI YEZOBUCHWEPHESHE

ENVISION2030

transparency • honesty • integrity • respect • accountability
fairness • professionalism • commitment • compassion • excellence

DEVELOPMENT OF ELECTROCHEMICAL BIOSENSORS FOR SWEETENERS USING ENGINEERED NANOMATERIALS SUPPORTED BY COMPUTATIONAL MODELLING

By:

PHATHISANANI HLOMA

(Reg. No: 21215083)

Submitted in fulfilment of the requirements of the degree of Doctor of Philosophy in Chemistry in the Faculty of Applied Sciences at the Durban University of Technology

December 2023

DECLARATION

I, **Phathisanani Hloma,** declare that the thesis submitted for the degree Doctor of Philosophy in Chemistry at the Durban University of Technology is the result of my investigation and has not already been accepted in substance for any degree and is not being concurrently submitted for any other degree. All the work was done by the author.

Student name : Phathisanani Hloma

Student signature: Date: 28/11/2023

Supervisor name : Professor K. Bisetty

Supervisor signature : Date: 28/11/2023

Co-Supervisor name : Dr. MI Sabela

Co-Supervisor signature : Date: 28/11/2023

Co-Supervisor name : Dr G Uwaya

Co-Supervisor signature : Date: 28/11/2023

DEDICATION

The author dedicates this thesis to his extended family for their firmly undivided support that they have shown throughout his studies. The extended family includes grandparents, parents, siblings and cousins, and the great-grandchildren of the “**Xhate** clan, **Xesibe**, **Mganu**, **Malandelwa**, malandelwa yintombi ithi mayizekwe”.

The author acknowledges and appreciates the sacrifices made by his family so that he can pursue his dreams, and he would like to place on record that, all that he is doing is for improving his and their lives.

The author himself deserves dedication for never giving up on himself despite the challenges he has faced since the start of his career 11 years ago.

ACKNOWLEDGMENTS

I acknowledge the assistance and guidance from different spheres of life for the realization of this dream, and all praise is directed to GOD for providing wisdom, strength, and courage to pursue this route.

I would like to wholeheartedly extend my sincere gratitude to my supervisor, Professor K. Bisetty, for his constant involvement, support, and direction-giving pieces of advice throughout the project. I am grateful to have had the opportunity to be supervised by such a profound researcher of his kind. I am gratefully acknowledging my co-supervisors, Dr G. Uwaya and Dr M.I. Sabela, for always being available to assist and guide me throughout the project. Their shared experience and support is highly appreciated. I would also like to acknowledge Mrs Mavis Xhakaza, Mrs Mpume Cele, Miss Avy Naicker and Ayanda Shabangu, for providing a healthy working environment in the laboratory and assistance while performing experiments.

My acknowledgements extend to all Computational Modelling and BioAnalytical Chemistry (CMBAC) research group colleagues and friends (Lyndon Naidoo, Matshidiso Lephalala, Khethiwe Mthiyane, and Calvin Harilal), who have motivated and assisted me countless times throughout my project. It would not be fair not to acknowledge the DUT Steve Biko library staff for their writing assistance and training workshops.

I am forever grateful to my mother, **Nonyameko Prelly Hloma,** my father, **Bulelani Emanuel Zimase** and the rest of my family, who have never left my corner with every decision I have taken in my life.

Lastly, the Council of Scientific and Industrial Research (CSIR) and the Durban University of Technology provided financial support for the research, and the Centre for High Performance Computing, an initiative supported by the Department of Science and Technology of South Africa, provided valuable support and is gratefully acknowledged by the author.

ABSTRACT

Electrochemical immunosensors are a powerful tool in analytical applications. The current methods for the isolation and detection of artificial and natural sweeteners suffer from challenges in sample preparation and a lack of specificity. However, electrochemical immunosensors offer a sensitive, economical, and selective analytical solution to analyse these commonly used sweeteners, such as aspartame.

The author of this work developed electrochemical immunosensors for the food and beverage industries to use in the detection and measurement of aspartame, a non-nutritive sweetener, and rebaudioside A, a natural sweetener. Most artificial sweeteners are low-calorie options that are suggested for ailments linked to health. These sweeteners' ability to remain stable at even high temperatures has greatly expanded the range of meals that can use them. Aspartame and rebaudioside A have not been linked to any health risks, although regulation is still necessary because of their extensive use in the food industry. The developed immunosensors for the detection of aspartame and rebaudioside A were achieved and presented as three case studies in this study.

In the first case study, the immunosensor was achieved by fabricating green synthesized PVP-capped silver nanoparticles (PVP-AgNPs) with functionalized multi-walled carbon nanotubes (fMWCNTs) and immobilizing the human sweet tase receptor T1R2 in a glassy carbon electrode (GCE), resulting in GCE/PVP-AgNPs/fMWCNTs/T1R2. The electrochemical assessment of aspartame was achieved using cyclic voltammetry (CV), electrochemical impedance spectroscopy (EIS), and differential pulse voltammetry (DPV), respectively, under optimum pH 8 in a 0.1 M phosphate buffer with reference to the Ag/AgCl reference electrode. The electro-oxidation of ASP was noticed by a well-defined oxidation peak potential at 1.4 V. The immunosensor sensor showed a linear dynamic range of 2.89 to 27.61 μM (R^2 = 0.9170) based on differential pulse voltammetry, with limits of detection (LOD) and quantification (LOQ) (S/N = 3) of 0.40 μM and 1.34 μM, respectively.

The second case study focused on the indirect electrochemical detection of rebaudioside A in the presence of ferro/ferricyanide as a redox probe. The immunosensor was developed by fabricating GCE with zeolitic imidazolate framework-67 (ZIF-67) in combination with fMWCNTs and the immobilization of the T1R2 receptor. The qualitative and quantitative

analysis of rebaudioside A was done using CV, EIS, and DPV utilizing a 5 mM $[Fe (CN)_6]^{3-/-4}$ redox probe. The stable electrode had an exponential dynamic range of 0.9901 µM to 8.2569 µM (R^2 = 0.9996). The LOD and LOQ were computed to be 1.10 µM and 3.33 µM, respectively. This case study also used Patch Dock and PyRx to better understand the interactions between Reb A and T1R2.

The final case study employed a platinum electrode (PtE) as the working electrode (WE) for the electrochemical immunosensing of aspartame. The modification of PtE involved the utilization of a nanocomposite consisting of PVP-AgNPs and reduced graphene oxide (rGO), with T1R2 immobilized. The electrochemical detection of aspartame was achieved under optimized conditions at pH 8 in a 0.1 M phosphate buffer, utilizing CV, EIS, and DPV as electrochemical tools. The PVP-AgNPs/rGO/T1R2 was used to fabricate Pt and the electrode performed well with a linear increase in oxidation peak currents as aspartame concentrations were increased from 2.38 µM to 25.78 µM (0.9529). The LOD and LOQ were calculated to be 5.85 µM and 17.73 µM, respectively.

The synthesized nanoparticles and nanocomposites (PVP-AgNPs/fMWCNTs, ZIF-67/fMWCNTs, and PVP-AgNPs/rGO) were characterized using conventional techniques such as UV-Vis spectroscopy, thermogravimetric analysis (TGA), Fourier transform infrared spectroscopy (FTIR), field flow fractionation (FFF), single particle inductively coupled plasma mass spectrometry (sp-ICPMS), energy-dispersive X-ray spectroscopy (EDS), and scanning electron microscopy (SEM).

In addition to the experimental results, computational chemistry methods were undertaken. These included adsorption assessments, density functional theory (DFT), and molecular docking techniques. These techniques were all aimed at achieving a deeper molecular-level understanding of the interactions among the analytes (Aspartame and Reb A), T1R2, and the nanocomposites employed in the modification of the working electrodes (GCE and Pt-E).

A schematic representation of the three case studies is shown in **Scheme 0-1** below.

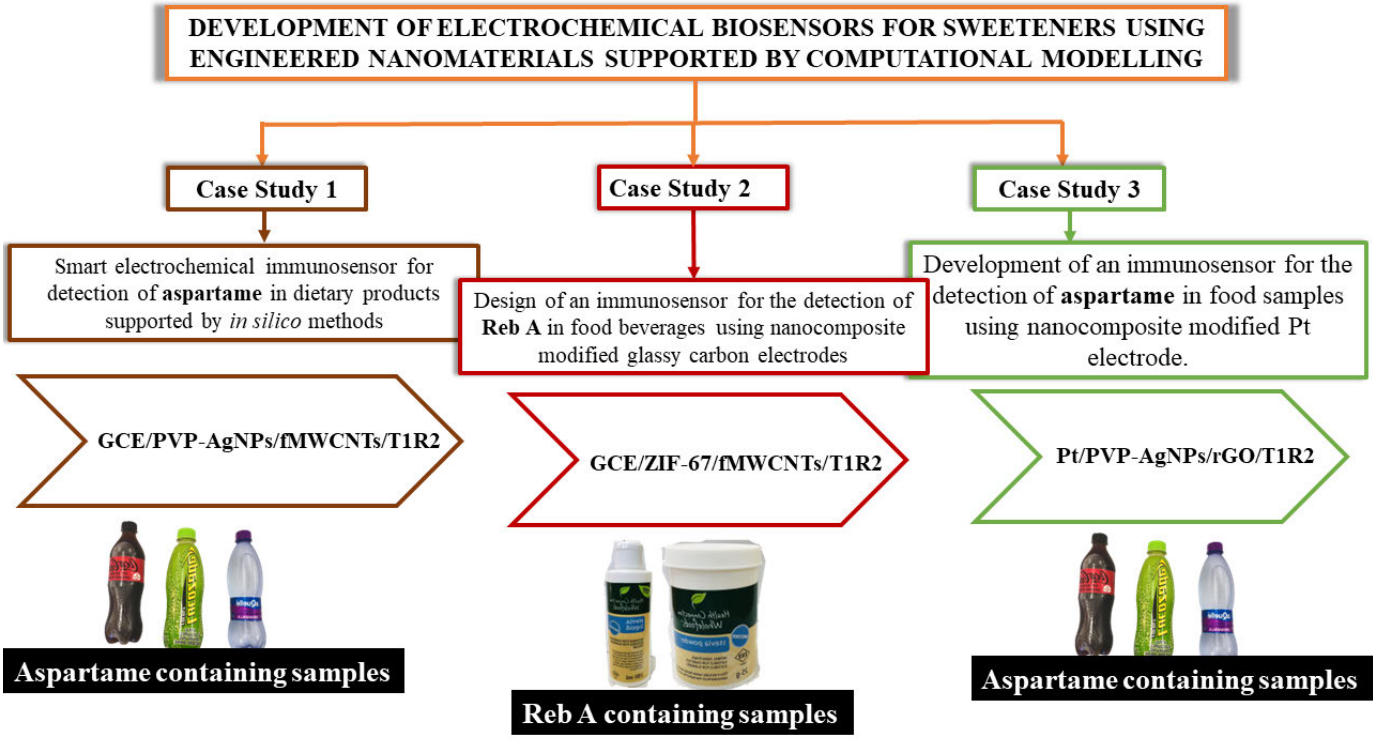

Scheme 0-1 Graphical abstract and structural representation of the thesis.

TABLE OF CONTENTS

LIST OF TABLES

LIST OF FIGURES

LIST OF ACRONYMS AND SYMBOLS

1D: One-dimensional

3D: 3D nanostructures

ADI: advised daily intake

AF4: asymmetric field flow fractionation

AgNPs: silver nanoparticles

AgNPs: Silver nanoparticles

AL: Adsorption locator

ASP: Aspartame

ATD: amino-terminal domain

BDD: Boron-doped diamond

BPA: bisphenol A

CE: Capillary Electrophoresis

CeO_2 NPs: cerium oxide nanoparticles

CF4: centrifugal field flow fractionation

CNTs: Carbon nanotubes

CRD: cysteine-rich domain

CuO NPs: copper oxide nanoparticles

CV: cyclic voltammetry

DAD: diode array detector

DFT: Density Functional Theory

DLS: dynamic light scattering

DPV: differential pulse voltammetry

DSC: differential scanning calorimeter

DWCNTs: double-walled carbon nanotubes

EDS: Energy dispersive spectrometer

EFSA: European Food Safety Authority

EIS: electrochemical impedance spectroscopy

E_{pa} : anodic peak potential

E_{pc} : cathodic peak potential

FDA: Food and Drug Administration

Fe_2O_3 NPs: iron oxide nanoparticles

FFF: Field flow fractionation

FTIR: Fourier transform infrared

GCE: glassy carbon electrode

GO: graphene oxide

GRAS: Generally Recognized as Safe

HOMO: highest occupied molecular orbital

ICP-MS: inductively coupled plasma mass spectrometry

I_{pa} : anodic peak current

I_{pc} : cathodic peak current

ISO: International Organization for Standardization

KCCs: key characteristics of carcinogens

LSPR: localized surface plasmon resonance

LUMO: lowest unoccupied molecular orbital

MC: Monte Carlo

MD simulations: Molecular dynamic simulations

MD: molecular dynamic

MIR: mid-infrared

MM: molecular modeling

MnO_2 NPs: manganese oxide nanoparticles

MOFs: metal organic frame works

MONPs: metal oxide nanoparticles

MS: mass spectrometric

MWCNTs: Multi walled carbon nanotubes

NiO NPs: nickel oxide nanoparticles

NIR: near-infrared

NMR: nuclear magnetic resonance

NMs: nanomaterials

PKU: phenylketonuria

PVP: polyvinylpyrrolidone

Q: constant-phase element

R_{ct} : charge transfer resistance

rGO: reduced graphene oxide

R_{s} : resistance

SEM: Scanning electron microscope

SGs: steviol glycosides

sp-ICPMS: single particle-Inductively coupled plasma mass spectrometry analysis

SWCNTs: single-walled carbon nanotubes

TEM: transmission electron microscopy

TGA: Thermogravimetric analysis

TiO_2 NPs: titanium oxide nanoparticles

UFF: universal force field

UV: Ultraviolet

W: Warburg impedance

XRD: X-ray diffraction

Z: impedance

$Z_{\mathrm{imaginary}}$: imaginary impedance

ZnO NPs: zinc oxide nanoparticles

Z_{real} : real impedance

ΔE_{p} : peak to peak separation

LIST OF PUBLICATION AND CONFERENCE

Publication:

i. **Hloma, P.**, Uwaya, G. E. and Bisetty, K. 2022. Smart electrochemical immunosensor for detection of aspartame in dietary products supported by in silico methods. *Biosensors and Bioelectronics: X,* 11: 100203.
DOI: https://doi.org/10.1016/j.biosx.2022.100203

Oral Conferences attended:

i. **Phathisanani Hloma**, "Smart electrochemical immunosensor for detection of aspartame in dietary products supported by in silico methods ", 44th SACI National Convention under the theme of Chemistry for sustainable development in Africa, held on the 8th – 13th of January 2023 at Stellenbosch University, Stellenbosch, Western Cape, South Africa.
ii. **Phathisanani Hloma**, "Electrochemical immunosensing of sensing of Aspartame supported by AF4 and computational chemistry", Applications of field flow fractionation (FFF) hybrid seminar hosted by DUT, at the Institute for Waste and Water Technology seminar room, on the 23rd of November 2022.
iii. **Phathisanani Hloma**, "Smart electrochemical immunosensor for detection of aspartame in dietary products supported by *in silico* methods", SACI National Young Chemist's Symposium held virtually on the 3rd-4th of October 2022.
iv. **Phathisanani Hloma**, "Electrochemical detection of Aspartame on green PVP-AgNPs based sensor, supported by computational modelling", 73rd Annual Meeting of the International Society of Electrochemistry held virtually, from 12th-16th September 2022.

CHAPTER 1: INTRODUCTION

In this chapter, an overview of sweetener classification is undertaken, with a particular emphasis on non-nutritive sweeteners, considering their widespread use in the food and beverage industry. Additionally, this chapter serves as a guide, outlining the study's aims and objectives and providing an outline of the entire thesis structure.

1.1 Sweeteners

Materials that show sweetness are classified as nutritive sweeteners, non-nutritive sweeteners, or artificial sweeteners. A sugar substitute is an ingredient in food that has a sweetness like that of sugar but with much fewer calories than sugar-based sweeteners, making it a low-calorie (non-nutritive) intake, or low-calorie sweetener. Artificial sweeteners can be extracted through processing chemical synthesis or by synthesizing from plant extracts (Chen *et al.* 2023). Commercially accessible sugar substitutes come in a variety of shapes and sizes, including capsules, powders and packs, with examples of sweeteners being honey, coconut sugar, molasses, agave nectar, sucralose, aspartame, acesulfame K, rebaudioside A, xylitol, saccharin, and many others. Contrary to nutritive sweeteners, which contain carbohydrates and calories, non-nutritive sweeteners are low-calorie chemicals that are used to substitute sugar and other caloric ones (Praveena, Cheema and Guo 2019). There have been quite a number of toxicities associated with artificial sweeteners. Acesulfame K and saccharin’s toxicity effects on young adult rats were studied by (Murali *et al.* 2022). Overall, the data show that the artificial sweeteners only slightly alter the diversity of the intestinal microbiota.

Although sweeteners are a necessary part of daily life and those used in food are safe, some researchers are still doubtful about the potential long-term health risks associated with their consumption. Additionally, some businesses' excessive addition of sweeteners also poses a threat to consumer health (Chen *et al.* 2023).

To guarantee consistency in the quality of the final product, it is crucial to determine the presence of these sweeteners in foods. Due to their low or non-existent calorie content, these non-nutritive sweeteners aid in maintaining healthy body weight and insulin levels. The ingestion of non-nutritive substances like acesulfame K, aspartame, and xylitol, on the other hand, has been linked by numerous authors to the development of gastrointestinal disorders in patients (Bueno-Hernández *et al.* 2019).

It is acknowledged that the food business has relied heavily on chromatographic methods like high-performance liquid chromatography to identify non-nutritive sweeteners (Woelwer-Rieck *et al.* 2010a; Liu *et al.* 2021). Mass spectrometry and capillary electrophoresis have secondarily been employed for simultaneous detection of artificial sweeteners (Stojkovic, Mai and Hauser 2013; Li *et al.* 2021b). The existing methods are acceptable and sensitive for detecting sweeteners; however, they require highly skilled personnel for operation and are costly. Recently, researchers have shifted their attention to developing cheap, robust, selective, and yet stable ways of detection through molecularly imprinted polymer-based sensors and electrochemical immunosensors (Uwaya, Sagrado and Bisetty 2022; Singh and Singh 2023).

As the need for sensitive, quick, and selective analyte identification rises, electrochemical sensors offer an essential analytical tool. Electrochemical sensors, as opposed to spectroscopic and chromatographic equipment, are affordable and simple to modify for the detection of a variety of analytes (Kimmel *et al.* 2012). The performances of electrochemical sensors are improved by the modification of carbon-based nanomaterials, metal/metal oxide nanoparticles, and metal organic frameworks (MOFs) with zeolitic imidazolate frameworks due to catalytic and electric properties, chemical inertness, increased surface area, high electron transfer efficiency, and porosity (Uwaya, Sagrado and Bisetty 2022). For example, metal nanoparticles such as Au (Dang *et al.* 2020), Ag (Verma *et al.* 2021), Pd (Chen *et al.* 2015), Ni (Fall *et al.* 2023), Co/Cu (Zhou *et al.* 2022; Uwaya and Bisetty 2023), Fe_3O_4 (Yu *et al.* 2011) and Cu_2O (Xia *et al.* 2022), to mention but a few, have proven to improve sensor performance by lowering the overpotential of the oxidizing or reducing agent. AgNPs, on the other hand, are intriguing metal nanoparticles for sensing because of their special characteristics. Sensing applications include biocompatibility, chemical stability, high surface area, and electrical conductivity (Cheng *et al.* 2018). AgNPs are one of the most studied metal nanoparticles in sensing applications due to their unique characteristics such as biocompatibility, chemical stability, high surface area, and electrical conductivity (Cheng et al. 2018; (Bindhu *et al.* 2020). The authors argue that a considerable number of metal organic frameworks, such as ZIF-67, have insulating properties, restrict charge transfer of electrons, and are soluble in aqueous medium, therefore limiting their applications in sensors (Kajal *et al.* 2022). However, their applications in sensors mainly depend on ZIF-67 possessing a high surface area, having porosity, selectivity properties due to vacant sites within the MOF structure, and their crystallinity (Ling *et al.* 2018; Kajal *et al.* 2022). In addition, the electrical conductivity of ZIF-67 can be enhanced by the integration of carbon-based materials such as carbon nanotubes (CNTs) and graphene oxide (Sun *et al.* 2022; Xie *et al.* 2023). CNTs are differentiated into single-walled carbon nanotubes (SWCNTs), double-walled carbon nanotubes (DWCNTs), and multi-walled carbon nanotubes (MWCNTs), and by definition, carbon nanotubes are graphite sheets that are folded into a tube, with multi-walled carbon nanotubes being defined as multiple concentric tubes of SWCNTs (Van der Bruggen, Mänttäri and Nyström 2008; Brandão *et al.* 2022). Pristine CNTs exhibit poor solubility and dispersibility and are susceptible to self-aggregation. By altering its surface composition through acid functionalization, it can be made more dispersible and soluble, thereby improving its quality for electrochemical sensing applications (Jun *et al.* 2018; Jun *et al.* 2019). Literature reports indicate that MWCNTs decorated with metal nanoparticles as well as MOFs enhance electron transport in designed sensors (Hoyos-Palacio *et al.* 2019). This study is aimed at designing immunosensors for the detection of commonly used sweeteners (Aspartame and Rebaudioside A) based on AgNPs/fMWCNTs composite and ZIF-67/fMWCNTs nanocomposite immobilized with TIR2 with real-time analysis, respectively.

In addition, the chemical or structural relationship between the sweeteners and the sweet taste T1R2 receptor subunit (T1R2) molecule was investigated using molecular docking experiments (Schneidman-Duhovny *et al.* 2005). The layer-by-layer adsorption studies mimicking the construction of the electrode surface were also carried out using Material Studio (Akkermans, Spenley and Robertson 2013). In this study, the optimal adsorption sites between the nanomaterials utilized for electrode modification were determined using the Adsorption Locator (AL) module built into MS software (Akkermans, Spenley and Robertson 2013) in conjunction with the Forcite module. Monte Carlo searches of the configurational space of the substrate-adsorbate system with a mild temperature ramp were used to determine potential adsorption configurations (Naidoo *et al.* 2020).

Density Functional Theory (DFT) calculations were utilized on the 3D structures of the analytes (sweeteners) to acquire electronic properties and therefore deduce the energy difference between the highest occupied molecular orbital (HOMO) and the lowest unoccupied molecular orbital (LUMO) (Hloma, Uwaya and Bisetty 2022). Molecular dynamic simulations

(MD simulations) were used to deduce the interactions in terms of binding affinity between the respective analytes and the nanostructured materials for electrode modifications (Uwaya, Sagrado and Bisetty 2022).

1.2 Background and Problem Statement

Most artificial sweeteners are low-calorie sweeteners recommended for health-related illnesses. The stability of these sweeteners at even high temperatures and their intense sweetening ability over sugar have increased their applications in foodstuffs widely. Although sweeteners are a necessary part of daily life when substituting sucrose and those used in food are approved by the Food and Drug Administration, some researchers are still doubtful about the potential long-term health risks associated with their consumption. Additionally, some businesses' excessive addition of sweeteners also poses a long-term threat to consumer health.

Over the years, techniques like liquid chromatographic techniques and capillary electrophoresis have been employed in qualitative and quantitative detection of sweeteners, coupled to different types of detectors such as diode array detectors (DAD), ultraviolet (UV) detectors, and mass spectrometry detectors. Despite the possible simultaneous detection of sweeteners with these methods, there are some drawbacks, such as high solvent consumption, lack of selectivity, operation by experienced personnel, and time consumption.

In spite of the long-term use of artificial sweeteners, some studies have suggested that ASP may be harmful to human health. Since the beginning of the 1970s, there has been debate about whether aspartame can cause genotoxicity or cancer in humans (Yılmaz and Uçar 2014). Particularly for patients with phenylketonuria (PKU), a condition in which the amino acid phenylalanine cannot be broken down, high levels of phenylalanine can be harmful. Therefore, it is recommended that patients with PKU refrain from using ASP (Marinovich *et al.* 2013). There is therefore a need to detect and determine ASP levels in beverages, medications, and food, and many studies have been conducted in the design and optimization of ASP monitoring systems.

Therefore, due to the widespread use of artificial sweeteners such as aspartame in foodstuffs, this study proposes electrochemical sensing as an alternative technique. The proposed method, therefore, addresses the need for a fast detection method that is cost-effective, selective, environmentally friendly, and capable of on-site monitoring.

1.3 Aim and Objectives

1.3.1 Aim and hypothesis of the study

Aim: To develop AgNPs/fMWCNTs-TIR2 and ZIF-67/fMWCNTs based immunosensors for the detection of aspartame and rebaudioside A in food products.

Hypothesis: The synthesized nanomaterials (AgNPs and ZIF-67) and nanocomposites will improve the electrocatalytic properties of bare working electrodes, for the application of detecting sweeteners.

1.3.2 Objectives of the Study

- To synthesise silver nanoparticles (AgNPs) using aqueous *Eucalyptus Globulus* leaf extracts and polyvinylpyrrolidone (PVP), to synthesize ZIF-67 and to acid functionalize MWCNTs for the preparation of PVP-Ag NPs and fMWCNTs and ZIF-67/fMWCNTs composites, and lastly, to develop a PVP-AgNPs/rGO nanocomposite for sensing.
- To characterize prepared nanoparticles and nanocomposite using a scanning electron microscope (SEM), X-ray diffraction (XRD), thermogravimetric analysis (TGA), UV-Visible, Fourier transform infrared (FTIR), asymmetric field flow fractionation (AF4) coupled to dynamic light scattering (DLS), inductively coupled plasma mass spectrometry (ICP-MS), cyclic voltammetry (CV), and electrochemical impedance spectroscopy (EIS).
- To develop electrochemical immunosensors for aspartame and rebaudioside A by immobilizing TIR2 antibody onto the surface of nanocomposite-modified glassy carbon electrodes (GCE) and platinum electrodes (PtE).
- To optimise the immunosensor parameters (sensitivity) and measure the performance of the bare and modified electrodes towards the detection of sweeteners using CV, EIS, and differential pulse voltammetry (DPV).

- To validate the performance of the designed immunosensors (PVP-AgNPs/fMWCNTs/TIR2, ZIF-67/fMWCNTs/TIR2, and PVP-AgNPs/rGO/T1R2) for real sensing of sweeteners in dietary drinks (Coca-Cola, Lucozade Energy, aQuelle sparkling flavored drinks, and Steviol Glycoside flavored supplements).

- To investigate the molecular interaction of the analytes (sweeteners) with the receptors using molecular docking, identify the reactive sites of analytes with electron density maps by HOMO-LUMO computed using density functional theory (DFT) and assess the intermolecular interactions of the fabricated electrode surfaces with analytes using Monte Carlo and molecular dynamics simulations.

1.4 Structure of the Thesis

Chapter 1: This chapter presented the introduction, background, problem statement, objectives of the study, and thesis outline.

Chapter 2: This chapter elucidates the characteristics of various sweeteners, providing detailed insights into the key components of the specific analytes under investigation, namely, aspartame and rebaudioside A. The analytical techniques used for the detection of these sweeteners are outlined. The chapter also discusses biosensing methods used for the detection of the above-mentioned sweeteners. Lastly, different methods employed for the synthesis of silver nanoparticles are explained.

Chapter 3: This chapter details the theoretical principles of experimental and computational chemistry techniques employed in this study. This chapter explains how experimental work and computational chemistry are interdependent.

Chapter 4: The materials and research methodology employed in this study are the main topics of this chapter. This chapter describes the synthesis and characterization of several nanomaterials as well as the fabrication of electrochemical immunosensors for the detection of respective sweeteners.

Chapter 5: This chapter explores three case studies focused on developing electrochemical immunosensors for detecting specific compounds in dietary products. The first case study deals with an immunosensor for aspartame, utilizing *in silico* methods to support experimental findings. It includes characterizing synthesized silver nanoparticles and electrochemical analysis. Computational aspects involve molecular docking, Monte Carlo studies, and DFT calculations, highlighting the integration of computational and experimental approaches.

The second case study details the design of electrochemical immunosensors by modifying glassy carbon electrodes with ZIF-67/fMWCNTs/T1R2 for detecting rebaudioside A in dietary samples. Similar to the first case study, it presents both experimental and computational results, covering ZIF-67 synthesis, immunosensor fabrication, electrochemical characterization, and interference studies. Computational analyses include Monte Carlo and molecular docking studies, showcasing the interdisciplinary nature of the research.

The last part of this chapter details the third case study, discussing the results of the designed aspartame sensor from platinum electrodes using PVP-AgNPs/rGO nanocomposite with the T1R2 antibody under optimized conditions. The developed immunosensor consolidates the practical implications of this research through its application in qualitative and quantitative assessments.

Chapter 6: This chapter emphasizes key findings from both experiments and computations, highlighting trends and connections between these results. Concluding observations are provided, and the chapter suggests avenues for future work, particularly in the electrochemical determination of aspartame and Reb A, focusing on applying the developed electrochemical immunosensors.

CHAPTER 2: LITERATURE REVIEW

This chapter provides an overview of the literature review, including discussions on artificial and natural sweeteners, their toxicity, and detection methods. It also explores immunosensors, recognition elements, and various methods for synthesizing silver nanoparticles applied in the detection of sweeteners in food samples.

2.1 Aspartame

Aspartame (ASP, E951) is a 'first generation' artificial sweetener introduced in the 1950s along with saccharin (SAC, E954) and cyclamate (CYC, E952), followed by the 'new generation' high-intensity artificial sweeteners acesulfame (ACE, E950), sucralose (SUC, E955), alitame (ALI, E956), and neotame (NEO, E961). Based on current literature, ASP (L-alpha-aspartyl-L-phenylalanine methyl ester) is a commonly used synthetic dipeptide sweetener in a range of beverages because it is about 15-20 times sweeter than sucrose. ASP is broken down in the body into 40 percent aspartic acid as amino acids, 50 percent phenylalanine as the methyl ester, and 10% methanol throughout metabolism (Chen *et al.* 2021). Figure 2.1 below displays the 2D chemical structure of ASP.

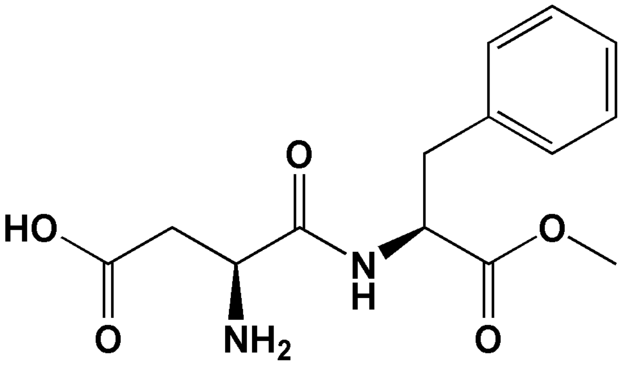

Figure 2-1: showing 2D chemical structure of the artificial sweetener, Aspartame.

To reduce sugar and caloric intake, the food manufacturers introduced a combination of selected 'first and new generation' sweeteners into the food and beverages (Okasha 2016; Le, Su and Cheng 2019). Despite the long-term use of artificial sweeteners, some studies have suggested that ASP may be harmful to human health. Since the beginning of the 1970s, there has been debate about whether aspartame can cause genotoxicity or cancer in humans (Yılmaz and Uçar 2014). Particularly for patients with phenylketonuria (PKU), a condition in which the amino acid phenylalanine cannot be broken down, high levels of phenylalanine can be harmful. Therefore, it is recommended that patients with PKU refrain from using ASP (Marinovich *et al.* 2013). There is therefore a need to detect and determine ASP levels in beverages, medications, and food, and many studies have been conducted on the design and optimization of ASP monitoring systems.

Several analytical approaches, including capillary electrophoresis (An *et al.* 2018; Medrano *et al.* 2019), liquid chromatography (Tighrine *et al.* 2019; Üstün Özgür and Kasapoğlu 2019), gas chromatography coupled to mass spectroscopy (Celiński *et al.* 2020), quartz microbalance (Yang and Park 2018), and electrochemical methods (Chen *et al.* 2021), have been employed in the determination of artificial sweeteners and their metabolite components. Despite chromatographic techniques offering acceptable selectivity and detection limits, they have the disadvantage of expensive instrumentation compared to electrochemical techniques, which have the advantages of rapid response time, high sensitivity, and ease of operation. Nanomaterials, however, have been gaining popularity for electrode modifications, and their unique properties are improving the quality of electrochemical assays. **Table 2-1**. highlights and briefly describes the documented methods for determining Reb A and other significant steviol glycosides.

Researchers have long used multiwalled carbon nanotubes (MWCNTs) as electrode catalysts for chemical and biosensors because they have a large specific surface area, are biocompatible, have an electrocatalytic effect, and are chemically inert. These properties make electrochemical sensors much more effective (Oliveira and Morais 2018). Pristine MWCNTs have low solubility and dispersibility and are prone to self-aggregation. By altering its surface composition through acid functionalization, it can be made more dispersible and soluble, thereby improving its quality for electrochemical sensing applications (Jun *et al.* 2018; Jun *et al.* 2019). In contrast, AgNPs, due to their unique properties, are promising metal nanoparticles for sensing. These properties include electrical conductivity, high surface area, chemical stability, and biocompatibility (Liao, Li and Tjong 2019; Luo *et al.* 2022). Metal nanoparticles, such as silver, gold, and platinum nanoparticles, improve sensor performance by lowering the overpotential of the oxidizing or reducing agent. Several literature reports indicate that

MWCNTs decorated with metal nanoparticles enhance the transfer of electrons in designed sensors (Hoyos-Palacio *et al.* 2019).

The purpose of the present study was to develop an electrochemical immunosensor for fast and accurate detection of ASP. For the first time, the electrocatalytic properties of fMWCNTs and the biocompatibility of AgNPs made from green *Eucalyptus* were used to detect ASP. In addition, DFT equations were used to investigate the chemical reactivity of ASP. MC simulations were used to determine the electrostatic interactions between the working electrode surface (GCE/PVP-AgNPs/fMWCNTs/TIR2) and ASP. The binding affinity of ASP for T1R2 was determined using molecular docking.

2.1.1 Properties of Aspartame

Aspartame is a white crystalline powder or colourless needle with a melting point between 246-250 ^{o}C and a water solubility of 10 g/L (Leung and Grant 1997). The sweetness of aspartame is around 200 times greater than that of sucrose. Its stability and solubility in aqueous systems are highly influenced by pH. As it is most stable at pH 4.3, sweetening carbonated beverages with it is a great idea. It can be used in "no-heat" recipes but is unstable at regular cooking and baking temperatures. Compared to other artificial sweeteners, aspartame is thought to more closely resemble the characteristics of sucrose (such as flavour taste duration, and low aftertaste) (Stegink 2020).

2.1.2 Occurrence of Aspartame in dietary drinks

Nowadays, aspartame is widely used in over 9000 different types of beverages, foods, medicines, and other items and has received approval for usage in over 130 countries and territories. The products sweetened by this artificial sweetener are not only limited to sugar-free soft drinks, but other foodstuffs such as sugar-free candy and gum, instant coffee, yoghurt, milk, cereals, frozen desserts, and many more use the sweetener instead of sugar. However, this wide application of aspartame in food beverages calls for fast and robust determination methods (Chen *et al.* 2023).

2.1.3 Regulations of Aspartame

Authorities from around the world, including the European Food Safety Authority (EFSA) and the U.S. Food and Drug Administration (FDA), have approved the use of aspartame in a variety of foods and beverages (Roberts 2016). According to the FDA, aspartame has undergone the most extensive research of any food additive, with more than 100 studies demonstrating its safety (Wikoff *et al.* 2020).

Aspartame is around 200 times sweeter than sugar. In order to obtain a delicate taste, only a very small amount needs to be added to the dish or drink. The following is the advised daily intake (ADI) by the FDA and EFSA: FDA: 50 mg/kg body weight, and EFSA: 40 mg/kg body weight. To surpass the daily recommendations of the FDA and EFSA, a person weighing 68 kg (150 lb) should consume more than 15 cans of diet Coke (each of which contains roughly 185 mg of aspartame).

2.1.4 Toxicity of Aspartame

Currently, aspartame is one of the most commonly used artificial sweeteners in food beverages, such as soft drinks, sugar-free desserts, chewing gum, and children's medicine. As a result, many researchers have developed an interest in studying its metabolic long-term effects upon consumption (Abhilash *et al.* 2011). Long-term high doses of aspartame intake were investigated on the serum enzyme and antioxidant system in the liver, and it was found that aspartame may cause some liver damage due to the increased activity of the enzyme (Abhilash *et al.* 2011).

Using key characteristics of carcinogens (KCCs), the test that was done to see if aspartame could cause cancer proved to be negative (Wikoff *et al.* 2020). In another study, the human pancreatic cancer cell line was used to examine the effects of long-term glucose and aspartame exposure on CSC population and cancer aggressiveness, and the findings showed that long-term aspartame exposure increased CSC population and tumour cell aggressiveness but did not affect tumorigenicity (Gezginci-Oktayoglu *et al.* 2021).

2.1.5 Detection methods for Aspartame

Table 2-1: Analytical procedures for the determination of Aspartame in different food products

Analyte	Sample	Technique	Mobile phase/Electrolyte	Column/Capillary/ Electrode/Detector/Nanocomposite	LOD/LOQ	Ref.
Aspartame	Diet Cola and a Pharmaceutical product	HPLC-Electrochemical detection	0.1% perchloric Acid-Methanol (85: 15, v/v)	C_6 Column (150 by 4.6 mm I.D), coupled to Colonche Model 5100A electrochemical detector.	LOD = 0.5 mg/L (signal-to-noise ratio 3:1)	(Galletti and Bocchini 1996a)
Aspartame	Soft drinks (Diet Pepsi, Diet Coke, and Diet Sprite)	High-performance liquid chromatography	methanol–acetonitrile–phosphate buffer (2:17:81) at pH 4.3	Microcomb RP18 column with spectrofluorimetric and spectrophotometric detectors	LOD = 0.06 mg/L	(Wróbel and Wróbel 1997)
Aspartame	Tabletop powdered table, Fruit	Ion Chromatography coupled with	27.5 mmol/ l NaOH isocratic elution	Dione Ion Pac AS4A-SC separation column	LOD = 0.031 µg/mL (signal to	(Qu *et al.* 1999)

	juice, and Carbonated drinks	electrochemical amperometric detection			noise ratio of 3:1)	
Aspartame	Coca-Cola Zero	two-dimensional high-performance liquid chromatography	2mM copper (II) sulphate–methanol (80:20, v/v)	C8 reversed-phase chromatographic column with UV detection at λ = 254 nm	LOD = 1.3 µg/mL and LOQ = 4.3 µg/mL	(Cheng and Wu 2011)
Aspartame	Not specified	Molecular imprinted polymer and colloidal sphere lithography	ASP was extracted from MIP film matrix through washing with methanol	MIP deposited into PS-templated Au-coated QCM crystal by cyclic voltammetry	LOD = 31 µM	(Tiu *et al.* 2016)
Aspartame	Pharmaceutical formulation	capillary zone electrophoresis (CZE)	borate buffer 50 mmol L^{-1} at pH 9.4 (BGE)	fused-silica capillary column (55 cm total length × 75 µm ID) coupled to a diode array detector at 235 nm	LOD = 0.3 µg/mL	(Corrêa de Carvalho, Pereira Netto

						and Marques 2014)
Aspartame	Not specified	quartz crystal microbalance	Not specified	monomers 3-thiopheneacetic acid (3-TAA) and 3,4ethylenedioxythiophene (EDOT) MIP for ASP	LOD = 1.26 µM	(Yang and Park 2018)
Aspartame	Diet Coca Cola and Pepsi light	Electrochemical bioenzyme biosensors	An oxygen saturated phosphate buffer (50 mM, pH 7)	graphite epoxy composite electrode (GECE)	LOD not specified	(Kirgöz *et al.* 2006)
Aspartame	Coke Zero, Huletts and Sprite zero	Electrochemical biosensor	Phosphate buffer at pH 2.0	Glassy carbon electrode, modified with ZnONPs/MWCNTs nanocomposite	LOD = 3.68 µM LoQ = 12.25 µM	(Balgobind *et al.* 2016b)

Aspartame	Dietary products (Not specified)	Electrochemical biosensor	0.5 molL^{-1} sulfuric acid solution	Boron-doped diamond (BDD) working electrode	LOD = 3.0×10^{-4} molL^{-1}	(Medeiros *et al.* 2008a)
Aspartame	Coca-Cola, Lucozade energy, and aQuelle sparkling flavoured drinks	Electrochemical immunosensor	0.1 M phosphate buffer at pH 8	Glassy carbon electrode, modified with PVP-AgNPs/fMWCNTs/T1R2 nanocomposite	LOD = 0.4 µM and LOQ = 1.34 µM	(Hloma, Uwaya and Bisetty 2022), Current Study

2.2 Rebaudioside A

Stevia is the collective name for components in food that come from the herb *Stevia rebaudiana* (Bertoni). A more accurate name for a collection of overly sweet substances that were taken from *S. rebaudiana* and refined is steviol glycoside. The two main steviol glycosides present in S. rebaudiana are stevioside and rebaudioside A (Carakostas *et al.* 2008). Figure 2.2 below shows the chemical structure of Reb A.

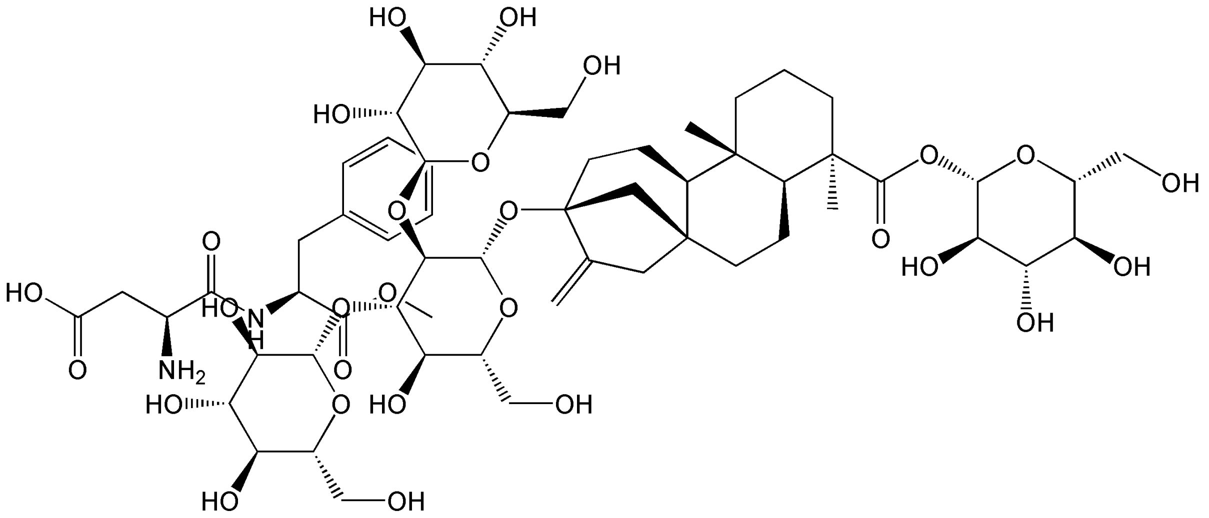

Figure 2-2: 2D chemical structure of Rebaudioside A

Stevia rebaudiana leaves are composed of steviol glycosides (SGs), with Rebaudioside A being one of the main components of the SGs.

Sweet leaf stevia Bertoni is a perennial plant commonly found in Brazil and Paraguay that is a member of the Compositae family. In many nations, stevia sweetener is utilized commercially and is made by extracting the juices from the plant leaves. powdering these leaves and extracting the juice. Due to the sweetener being more than 500 times sucrose sweeter than, having medicinal qualities as a leaf, and non-nutritive sweetener rank Reb A, also known as the sweet leaf, it has attracted a lot of scientific and economic attention (Bathinapatla *et al.* 2016).

The quality assurance departments are concerned about the presence of steviol glycosides in food and beverages since more people are drinking them and because the amount of steviol glycosides ingested needs to be controlled. A review of the literature finds that chromatography and capillary electrophoresis are frequently employed in food technology to identify fake sweeteners (Mauri *et al.* 1996; Kakigi *et al.* 2013).

Due to the similarities in their functional groups and chemical behaviour, steviol glycosides are a category of chemical species. Chromatographic separations of these species can provide qualitative information about the species of interest, and more recently, the separated species can be quantified. Chromatography is one of the reliable techniques utilized to separate such species (Samah, Hisham and Rahim 2013). The primary method for separating steviol glycosides is column chromatography. Column chromatography and planar chromatography are the two primary categories of chromatography. In column chromatography, the stationary phase is stored and kept in a very thin tube, and the analyte-caring mobile phase is driven down the tube by exerting pressure and utilizing gravity to separate distinct substances of interest (Yrjönen 2004).

The most popular method for separating and measuring steviol glycosides (Reb A) is found to be HPLC (Pundir and Malik 2019), where the instrument is connected to a number of detectors, including a UV-Vis detector (Samah, Hisham and Rahim 2013), a diode array detector (DAD), and mass spectrometric (MS) detectors (Gardana *et al.* 2003).

Steviol glycosides are claimed to be separated and quantitated using capillary electrophoresis in conjunction with a variety of detectors, including diode array detectors (Ayyappa *et al.* 2015a). The various mobilities and rates of migration that the charged species have in an applied DC electric field are the basis for the macro-size separation technique known as electrophoresis. The power of electrophoresis, with its exceptional capacity to separate charged macromolecules under examination, is relied upon by scientists. When capillary electrophoresis was developed, it allowed for automation, improved resolution, and reduced analysis time by performing these macromolecule separations in tiny amounts of the material inside a fused silica capillary cube. The selectivity of high-performance liquid chromatographic techniques is diminished despite their high sensitivity (Yang and Chen 2009), resulting in high solvent consumption, requiring experienced personnel for operation, and thus therefore inspiring studies using electrochemical methods.

The aforementioned approaches are indeed sensitive, but they also consume a lot of solvent and have low selectivity, which has led to studies employing electrochemical techniques. There have been recent advancements in the electrochemical detection of Reb A. The advantages of the fundamental approaches can be offset by electrochemical techniques since it is possible to create a sensor that is more responsive, inexpensive, sensitive, and selective to the desired substance (Bathinapatla *et al.* 2016).

This study aims to make an electrochemical immunosensor with electrocatalytic activity and conductivity for detecting Rebaudioside A in food samples by attaching a nanocomposite (AgNPs/fMWCNTs/T1R2) onto a bare carbon screen-printed electrode. As shown in Table 2-2, the documented ways to find Reb A and other significant steviol glycosides are highlighted and briefly explained.

2.2.1 Regulations of Rebaudioside A

Since being introduced to the U.S. market, steviol glycosides' status in terms of regulation for use in food has changed. Several factors affected the regulatory environment for steviol glycosides. One of these was more information becoming available about the safety of pure elements made from the leaves of *S. rebaudiana* leaves.

The Food and Drug Administration (FDA) continues to evaluate GRAS (Generally Recognized as Safe) notices for the use of steviol glycosides in food. An important point is that GRAS notices are not product-specific licenses or registrations for a manufacturer. The use of a purified steviol glycoside is covered by an existing GRAS notice if it has the same identity, method of manufacture, specifications, intended use, and dietary exposure. While a “no questions” response letter from the FDA may be used as documentation to allow for the importation of steviol glycosides (Perrier, Mihalov and Carlson 2018).

2.2.2 Toxicity effect of Rebaudioside A

Several studies have been undertaken to study the toxicological profiles of steviol glycosides (Reb A) (Brusick 2008; Roberts and Renwick 2008; Chappell *et al.* 2021). In general, the toxicity studies undertaken here prove that there are no health effects related to the consumption of steviol glycosides, stating the lack of carcinogenetic causes arising from long term consumption of steviol glycosides (Chappell *et al.* 2021).

This study (Maki *et al.* 2008) evaluated the hemodynamic effects of consuming Reb A among healthy adult individuals. The current study showed that giving 1000 mg/day of rebaudioside A for 4 weeks was well tolerated and did not have a big effect on most of the blood pressure values that were measured, including resting and seated SBP, which was the main outcome variable. It was also able to detect small changes in blood pressure (>90% power to detect a 4.5 mmHg difference in SBP). Finally, the study concluded that steviol glycosides are not genotoxic or carcinogenic (Brusick 2008).

2.2.3 Detection methods of Rebaudioside A

Table 2-2: Analytical procedures for the determination of Reb A in samples of different food products

Analyte	**Sample**	**Technique**	**Mobile Phase/Electrolyte**	**Column/Capillary/ Electrode/Detector/Nanocomposite**	**LOD/LOQ**	**Ref.**
Rebaudioside A	Stevia (Powder), Green Canderel (Tablet), Tantalize (Liquid)	Electrochemical biosensor y	pH 11.0 in a 0.1 M borate buffer	Cytochrome c/AuNPsGO/MWCNTs nanocomposite	LOD/LOQ not specified.	(Bathinapatla *et al.* 2016)
Rebaudioside A and Stevioside	Real stevia samples	Capillary Electrophoresis (CE)	1 M and 0.1 M Sodium Hydroxide, phosphate buffer and deionized water	30-mM heptakis-(2,3,6-tri-o-methyl beta-cyclodextrin) as a separating agent, fused silica capillary with 50 mm inner diameter and 363 mm outer diameter, and a diode array detector (DAD) at	$LOD_{Reb\ A}$= 2.017×10^{-5} M LOD_{Stv}= 7.386×10^{-5} M	(Ayyappa *et al.* 2015b)
Rebaudioside A and Steviolbioside	*Stevia rebaudiana* leaves	Capillary electrophoresis (CE), High-performance	20 mM sodium tetraborate buffer, pH 8.3, and 30 mM	The fused-silica capillary was 56 cm (50 cm to the detector) X 50 pm ID, equipped with a 3D extended light	LOD/LOQ not specified.	(Mauri *et al.* 1996)

		liquid chromatography, Mass spectrometry.	sodium dodecyl sulphate.	path (bubble cell) from Hewlett-Packard, equipped with diode array detector (DAD)		
Stevioside	*Rebaudiana* Plant	Reversed phase HPLC	Methanol and 0.1% orthophosphoric acid (v/v) (70:30)	Model G1316A thermostat column and UV array detector	LOD=0.02µg/mL LOQ=0.05µg/mL	(Jadhao, Katekhaye and Thorat 2011)
Stevioside and Rebaudioside A	*Stevia Rebaudiana* leaves	Soxhlet extraction method via HPLC.	Acetonitrile: water (80 :20, v/v)	Waters XBridge C18 column ((150 mm x 4.6 mm I.D., 5µm), UV detector range, 205-215 nm.	LOD/LOQ not specified.	(Samah, Hisham and Rahim 2013)
Rebaudioside A	*Stevia rebaudiana* leaves	Isocratic HPLC	Water/Acetonitrile (65: 35, v/v)	PurospherÒ STAR RP-18 endcapped 3 lm HibarÒ RT 250-4.6 column at 50 °C, UV spectrophotometer detector at 210 nm.	LOD =0.0004 mg /mL LOQ =0.0038 mg/mL.	(Bergs *et al.* 2012)
Stevioside and rebaudioside A	Dried leaves of *Stevia rebaudiana*	Solvent extraction followed by HPLC	Acetonitrile/water (80:20, v/v)	NH_2 column (250 × 4.6 mm), UV detection in 210 nm	LOD and LOQ not specified	(Kolb *et al.* 2001)
Stevioside and rebaudioside A	*Stevia* plants	Water extraction, solid phase extraction reversed phase HPLC	[Acetonitrile/ water (85:15 v/v)]	[Luna HILIC (250 9 4.6 mm) column]	LOD/LOQ not specified.	(Woelwer-Rieck *et al.* 2010a)

			[Acetonitrile/water (75:25 v/v)]	[Luna NH2 100 A column (250 9 4.6 mm)]		
Stevioside and rebaudioside A	*Stevia rebaudiana* leaves	Super critical fluid extraction HPLC	Water/Acetonitrile (20: 80)	Cosmosil® 5NH2-MS column (4.6mm×150mm), UV detector	LOD$_{\mathrm{Stv}}$= 1.19 μg/mL LOQ$_{\mathrm{Stv}}$= 3.98 μg/mL LOD$_{\mathrm{Reb\ A}}$= 1.98 μg/mL LOQ$_{\mathrm{Reb\ A}}$= 3.98 μg/mL	(Erkucuk, Akgun and Yesil-Celiktas 2009)
Stevioside	Food beverages	Liquid chromatography/tandem mass chromatography (LC-MS/MS)	Gradient elution of 10 mM ammonium acetate in water and 10 mM ammonium acetate in methanol	Phenomenex Luna PhenylHexyl (5 mm, 4.6 mm × 150 mm) column, AB SCIEX QTRAP 4000 triple quadrupole tandem mass spectrometer.	LOQ$_{\mathrm{Stv}}$= 0.1 μg/kg	(Chang and Yeh 2014)
Rebaudioside A	Soft drinks	LC and time-of-flight MS (LC-TOF-MS)	Gradient elution of formic acid in the water and solvent B was acetonitrile.	Asahipak NH2P-50 2D column (150 × 2.1 mm inner diameter), Triple TOF 5600 system (AB Sciex, Framingham, MA, USA)	LOD/LOQ not specified.	(Kakigi *et al.* 2013)
Stevioside and Rebaudioside A	*Stevia* leaves	Ultrahigh performance liquid chromatography–tandem mass spectrometry (UHPLC-MS)	Isocratic elution of 50 % 10 mM aqueous ammonium acetate	QTRAP 3200 mass spectrometer (AB/Sciex) equipped with SIL-HTc column oven	LOD$_{\mathrm{Stv}}$= 5.7 ng/mL LOQ$_{\mathrm{Stv}}$= 19.1 ng/mL LOD$_{\mathrm{Reb\ A}}$= 5.0 ng/mL	(Shafii *et al.* 2012)

			and 50 % Acetonitrile		$LOQ_{Reb\ A}$= 16.8 ng/mL	
Oligosaccharides, nucleic acid bases, and nucleosides	N/A	Hydrophilic interaction liquid chromatography (HILIC) mode, and FTIR	Mobile phase H2O/ACN at 50/50 (v/v).	Rebaudioside A immobilized on silica surface through "thiol-ene" click chemistry (Click TE-Reb A) Column, Waters 2998 diode array detector (DAD)	LOD/LOQ not specified.	(Liang *et al.* 2015)
Rebaudioside A and Stevioside	*Stevia* leaves and commercial sweetener.	Ultra-high-performance liquid chromatography coupled with electrospray ionization mass spectrometry (UHPLC-MS)	isocratic with 5 mmol/L ammonium acetate pH 6: CH_3CN (45:55, v/v)	A 1.8 µm HSS C18 column (100mm×2.1mm, Waters),	$LOD_{Reb\ A}$= 0.1-10 µg/mL LOD_{Stv}= 0.05-10 µg/mL	(Gardana, Scaglianti and Simonetti 2010)
Stevioside, rebaudioside A and rebaudioside C	*S. rebaudiana* leaves	Near-infrared reflectance spectroscopy (NIRS), using HPLC as a reference method	Isocratic elution using acetonitrile/water (80/20, v/v)	Zorbax NH2 column (5 mm, 250 mm ×4.6 mm), multiple UV wavelength detectors	LOD/LOQ not specified.	(Hearn and Subedi 2009)
Stevioside, Steviolbioside and Rebaudioside A	S. *rebaudiana* leaves	[HPLC] and [LC-MS-ESI]	[Isocratic elution using of acetonitrile: water (3:2)]	[C_{18} column of size 25x4.6 mm] [C18 Column (SGE, 25X1.6mm), Waters 2696 photodiode array detector (DAD)]	LOD/LOQ not specified.	(Rajasekaran *et al.* 2008)

Stevioside and Rebaudioside A	*Stevia rebaudiana* Bertoni leaves	HPLC	Isocratic elution in Acetonitrile and Water (8: 2) and Gradient elution with many ramps.	Develosil ODSHG 140 Å (250 mm × 4.6 mm × i.d., 5 lm) and Luna HILIC (150 mm × 4.6 mm i.d., 5 lm) columns, DAD detector, was set at 210, 256, 330, 360 and 450 nm.	LOD_{Stv}= 1.07 mg/L LOQ_{Stv}= 3.55 mg/L $LOD_{Reb\ A}$= 1.07 mg/L $LOQ_{Reb\ A}$= 3.56 mg/L	(Lorenzo *et al.* 2014)
Rebaudioside A and stevioside	Food products	Electrospray ionization liquid chromatography-mass spectrometry	Gradient elution with mobile phase A consisted of 10mM NH4OAc in water/ACN (50/50 v/v), and mobile phase B consisted of 10mM NH4OAc in water/ACN (5/95 v/v)	Restek (Bellefonte, PA, USA) Pinnacle II Amino column with guard (100mm×2.1mm×3 mm, 110A˚), MS detector	The method had LOD of 0.01–0.34 µg/g.	(Shah, De Jager and Begley 2012)
Major Steviol Glycosides (Stevioside and Rebaudioside A)	Plants of *Stevia rebaudiana* (Bertoni)	High-performance thin-layer chromatography (HPTLC) analysis	Ethyl acetate-ethanol-water (80:20:12, v/v/v)	Precoated silica gel HPTLC 60 F254 (20×10 cm) plate of 0.20 mm layer thickness.	LOD/LOQ not specified.	(Jaitak, Bandna and Kaul 2009; Kumar *et al.* 2012)

Stevioside	Food samples	High-performance liquid chromatography (HPLC) coupled with electrospray ionization mass spectrometric detection (ESI-MS)	A buffer solution was prepared by dissolving 0.8 mL of formic acid and 1.5 mL of triethylamine in1Lof water. The HPLC mobile phase A was prepared by mixing methanol with buffer solution and acetone (69:24:7, v/v/v), whereas the HPLC mobile phase B was prepared by mixing methanol with buffer solution and acetone (11:82:7, v/v/v).	The spherical analytical column was packed with 5 µm C_{18} silica (250 mm × 4.5 mm i.d.)	LOD≤ 0.10 µg/mL LOQ≤ 0.30 µg/mL	(Yang and Chen 2009)

Stevioside	*Stevia rebaudiana* Bertoni	Thin-layer chromatography, high-performance liquid chromatography, and proton NMR	Gradient elution was performed using the mobile phase was a mixture of deionized water, pH 5.5 (A) and acetonitrile (B).	Luna NH2 column (250×4.6 mm, 5 mm), the UV detector was tuned to 210 nm.	The LOD was 0.1 g/l	(Kedik *et al.* 2003)
Rebaudioside A	*Stevia Rebaudiana* Bertoni crude extracts.	Macro-porous adsorption resin (MAR) and high-performance liquid chromatography (HPLC)	Acetonitrile (A)-70% and potassium dihydrogen phosphate (10 mM) (B)-30% was used as the mobile phase.	MAR mixed bed of HPD750–LSA40–LSA30–DS40. NH2 column (AT LICHROM, 150 × 4.6 mm, 5 lm), with 210 nm DAD detector wavelength.	LOD/LOQ not specified.	(Li, Chen and Di 2012)
Diterpene glycosides	*Stevia* leaves	Desorption electrospray ionization mass spectrometry.	The solvent used in this study was MeOH: H2O (1: 1).	A 3 mL sample (stevia) of the commercial sample (1 mg/mL made up in MeOH: H2O (1: 1); 3 mg absolute amount) was spotted onto a porous Teflon substrate.	The LOD and LOQ is not specified.	(Jackson *et al.* 2009)

2.3 Biosensors

A biosensor is a simple device defined by transforming a biological response into an electrical signal. It must be extremely precise, unaffected by physical factors like pH and temperature, and reusable. The IUPAC introduced the definition of the term "biosensor," which was first used by Cammann (Mehrotra 2016).

Together, the biosensor's components complementarity, transmit, and convert chemical or biological data into a signal that can be understood, as shown in Figure 2.3. A transducer, a sensitive biological component (bio-element), and a signal processing unit make up a conventional immunosensor. When the sensitive molecule binds to the target analyte, stable complexes of enzyme-substrate, antibody-antigen, and other types are made. These stable complexes must be recognized and measured by the transducers.

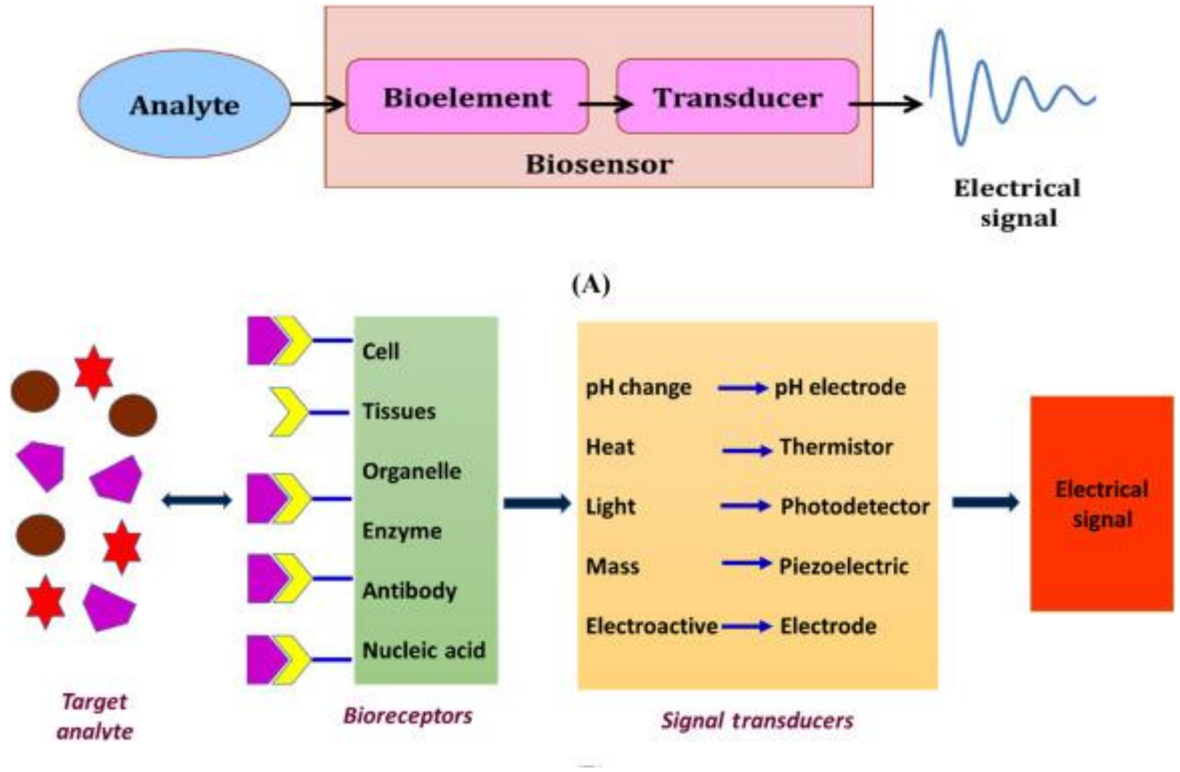

Figure 2-3: Components of a biosensor working in complementary with each other shown schematically and adopted from (Karunakaran and Keskin 2022)

2.3.1 Types of biosensors

There are different types of biosensors, namely, enzyme-based, tissue-based, immunosensors, DNA biosensors, thermal, and piezoelectric biosensors, which are used for different applications.

An enzyme identifies the target analyte and then reacts with it to produce a chemical signal in an enzyme-based biosensor. A transducer then converts that chemical signal into a physical signal and an amplified electrical signal under subsequent conditions. There are evident engagements of enzyme-based biosensors in clinical, environmental, and pharmaceutical industries (Bollella 2022).

Immunosensors were developed based on the notion that antibodies have a high affinity for their specific antigens, which means that they attach to pathogens, toxins, or other immune system components in a specific way (Mehrotra 2016). Sensing components in nucleic acid-based biosensors are oligonucleotides with a defined base sequence or a DNA or RNA fragment. Nucleic acid biosensors either function as extremely specific receptors for biochemical species or are based on the very specific hybridization of complementary strands of DNA and RNA molecules (Kavita 2017). Recently, DNA-based biosensors have been applied in the environmental industry for the detection of toxic heavy metals (Yang, Li and Liu 2021).

By sensing changes in magnetic characteristics or magnetically induced effects such as changes in coil inductance, resistance, or magneto-optical properties, magnetic biosensors use paramagnetic or super-paramagnetic particles, or crystals, as a technique for detecting biological interactions (Nabaei, Chandrawati and Heidari 2018). By incorporating the above stated biosensor materials into a physical transducer, thermal biosensors or calorimetric biosensors can be created (Mehrotra 2016). Biosensors based on magnetic nanomaterials are of great interest in the agro-food and environmental industries for detecting toxins such as mycotoxins and aquatic toxins (Reverté, Prieto-Simón and Campàs 2016).

The surface acoustic wave device and the quartz crystal microbalance are two different forms of piezoelectric biosensors. They are based on the detection of variations in a piezoelectric crystal's resonance frequency as a result of changes in the crystal's mass (Skládal 2016). Lastly, in recent years, optical biosensors have become an extremely hot topic. It is a type of sensor that relies on light transmission and signal collection (Lei and Guo 2022). Piezoelectric and optical sensors have played an important role in disease control, specifically in the rapid and sensitive detection of protozoan pathogens (Feyziazar *et al.* 2022).

2.3.2 Immunosensors

Enzymes, nucleic acids, plant or animal tissues, and antibodies are used as sensitive biological elements in biosensors. These elements are immobilized on the surfaces of transducers. When antibodies or antibody fragments are used as the sensitive biological component for a particular analyte (antigen) to generate the stable antibody-antigen complexes that are recognized by transducers, the small devices previously described are referred to as immunosensors. Immunosensors are also divided into different types, namely, electrochemical, optical, microgravimetric, and thermometric immunosensors. These categories of immunosensors can all be used as direct (non-labelled) or indirect (labelled) immunosensors (Cecilia *et al.* 2015).

Electrochemical immunosensors have been used more frequently than the other two types of immunosensors covered in this study because of their distinctive qualities, including low cost, robustness, quick time of reaction, small sample amounts needed, ease of use, and sensitivity (Felix, Baccaro and Angnes 2018). Immunosensors are best suited for the detection and monitoring of trace compounds in clinical, food, and environmental industries due to their great selectivity and sensitivity (Cecilia *et al.* 2015).

Therefore, this study aimed to develop nanomaterial-based electrochemical immunosensors for the detection of artificial and natural sweeteners in food beverages.

2.4 Computational modelling on artificial sweeteners

Sugar substitutes are widely used in our daily lives due to many health-related reasons, as more than average daily intakes of sugar may lead to degenerate diseases. Therefore, a computational perspective is needed to understand the molecular-level interaction of these artificial sweeteners with other materials. In another study, *ab initio* density functional theory (DFT) calculations and an experimental infrared spectrum were used to study the vibrational and structural characteristics of sucralose (Brizuela *et al.* 2013). In a different study, DFT calculations were employed to study the stability of the lactim/lactam tautomerization of an artificial acesulfame K, due to cyclic amides consisting of proton bridging leading to tautomerization (Popova, Velcheva and Stamboliyska 2012).

These modelling calculations are useful in understanding properties such as charge transfer, stability, highest occupied molecular orbital (HOMO), lowest unoccupied molecular orbital (LUMO) energy values, and geometrical properties via DFT calculations (Brizuela *et al.* 2013; Altunayar-Unsalan and Unsalan 2021).

2.5 Nanomaterials

The International Organization for Standardization (ISO) defines the term "nano" as a size between 1 and 100 nm (ISO 2008). In comparison to small clusters of atoms or even a single atom, nanomaterials (NMs) are far larger. When discussing dimensional tolerances for semiconductor operations while machining and finishing in 1974, Norio Taniguchi used the term "nanotechnology" for the first time (El-Kady *et al.* 2023).

Nanomaterials (NMs) are very useful for making electroanalytical biosensors because of their small size, quantum size effect, and surface and interface effects (Zhang and Wei 2016). In addition, the use of NMs as electrode modifiers has the following benefits: increased electroactive area; improved surface kinetics; improved selectivity of the electrode because NMs provide stable support for functionalization with specific groups; and improved analyte adsorption on the electrode surfaces, which increases sensitivity (Sharma *et al.* 2018).

There are many advanced microscopic methods that can be used to find the shape, size distribution, average diameter, and morphology of the nanomaterial surfaces. These include X-ray diffraction (XRD), scanning electron microscopy (SEM), and transmission electron microscopy (TEM) (Ojha 2020).

2.5.1 Classification of Nanomaterials

Nanomaterials serve as illustrations for a variety of classes because of their distinctive properties. Dimensions, occurrence or origin, natural and synthetic chemical compositions, toxicity, and a host of other factors are used to classify objects. NMs can be divided into several classes according to various factors. NMs can typically be divided into groups based on their size, shape, condition, and chemical make-up (El-Kady *et al.* 2023). Nonetheless, several publications have categorized nanomaterials using the following five criteria: geometry, morphology, composition, homogeneity, and aggregation of nanoparticles (Uwaya 2021; El-Kady *et al.* 2023).

One-dimensional (1D) nanomaterials include thin films and surface coatings. Some are 3D (3D) nanostructures, and some are two-dimensional (2D) nanostructure films that are used in various fields, such as the separation and filtration of small particles when bonded to a substance. Nanomaterials may consist of a single material or several materials with changing modulations of dimension, such as zero, one, two, and three with atomic clusters, filaments, and cluster assemblies; multilayers; or buried or ultrafine-grained layers (Ojha 2020; Uwaya 2021), as illustrated in Figure 2.4 below.

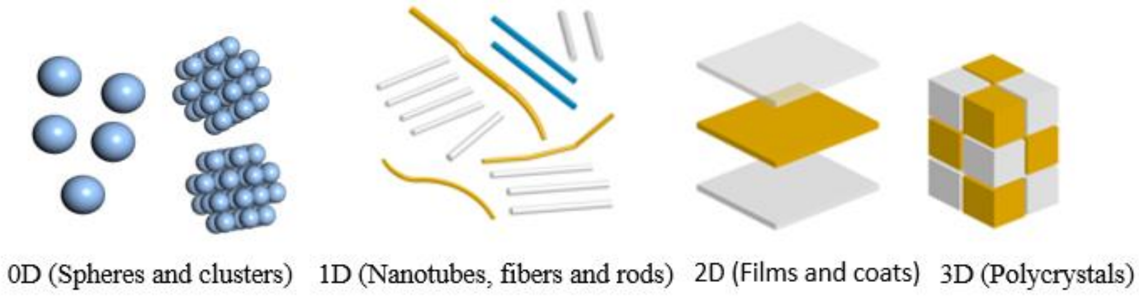

Figure 2-4: Classes of nanomaterials from 0D: spheres and clusters, 1D: nanofibers, nanowires and nanorods, 2D: nanofilms, nanoplates, and networks, and 3D: polycrystals.

2.5.2 Types of nanomaterials

Nanomaterials are grouped into different types, namely naturally occurring nanomaterials, metals and their oxide-based nanomaterials, carbon-based nanomaterials, and newly structured and engineered nanomaterials.

2.5.2.1 Naturally occurring nanomaterials

Naturally occurring nanomaterial examples include cellulose, chitins, and peptides. Biological nanoparticles are widely used in different industrial fields due to their various unique characteristics. As a result of its easy functionalization, robustness, and great mechanical strength, this nanomaterial is employed in the manufacture of nanomembranes (Ojha 2020).

2.5.2.2 Metals and their oxide-based nanomaterials

This category of nanomaterial is mostly made up of nanoparticles created through the synthesis of metals, their oxides, or sulfides. Metals from the transition series make up most of the nanoparticles in this group. When utilized at the nanoscale, noble metals like Ag, Au, Pd, and Pt demonstrate a wide range of applications. They are an excellent photocatalytic system because of their strong optoelectronic activity caused by localized surface plasmon resonance (LSPR) (Ojha 2020) (Zhang and Wei 2016).

Due to their various components and morphologies, noble metal NPs, alloy NPs, and metallic oxide NPs all apply differently to electroanalytical biosensors. The precursors used to create metal oxide nanoparticles (MONPs) are all metal. Several disciplines, including physics, chemistry, and the study of materials, depend heavily on these nanoparticles. Examples of metal oxide nanoparticles include iron oxide nanoparticles (Fe_2O_3 NPs) (Jabbar, Barzinjy and Hamad 2022), copper oxide nanoparticles (CuO NPs) (Alavi and Moradi 2022), nickel oxide nanoparticles (NiO NPs) (Imran Din and Rani 2016), zinc oxide nanoparticles (ZnO NPs) (Jiang, Pi and Cai 2018), manganese oxide nanoparticles (MnO_2 NPs) (Ding *et al.* 2020), cerium oxide nanoparticles (CeO_2 NPs) (Rajeshkumar and Naik 2018), titanium oxide nanoparticles (TiO_2 NPs) (Haider, Jameel and Al-Hussaini 2019), etc.

2.5.2.3 Carbon-based nanomaterials

The carbon that makes up the basis of these nanomaterials can be found in a wide range of configurations, including sheets (graphene, graphene oxide (GO), or reduced graphene oxide (rGO)), spheres, and hollow tubes (carbon nanotubes, or CNTs) (such as fullerenes). They are superior to other macromolecules in terms of surface area to volume ratio, making them a good material for the treatment of water. These nanoparticles can be created using a variety of techniques, including chemical vapor deposition, discharge tubes, and laser applications (Ojha 2020).

Nanotubes are regarded as having a high length-to-diameter ratio, making them almost one-dimensional structures. Single-walled nanotubes (SWNTs) and multi-walled nanotubes (MWNTs) are the most significant structures of carbon-based nanomaterials (Belin and Epron

2005), as shown in Figure 2.5 below. The imperfections on the walls (surface) and at the terminals of the nanotubes affect their characteristics. The hydroxyl (-OH) and carboxylic acid (-COOH) from the oxidizing agents such as sulphuric acid and nitric acid can be used to functionalize or deactivate carbon-based nanomaterials (Belin and Epron 2005; Jun *et al.* 2018; Ojha 2020). In comparison to unfunctionalized carbon-based nanomaterials, the functional groups are connected via covalent or noncovalent interactions, and they tend to increase the dispersion in water as well as their adsorption capabilities, resulting in more applications in fields such as sensors and wastewater treatment plants.

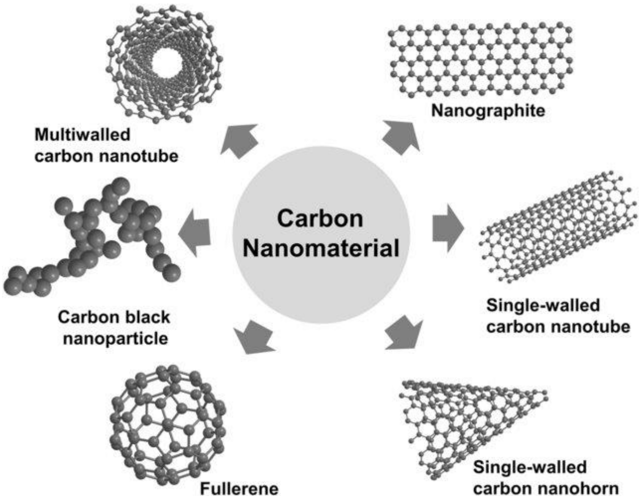

Figure 2-5: Different pristine carbon-based nanomaterials represented in balls and sticks, adopted from (Yuan *et al.* 2019).

Graphene oxide is a two-dimensional carbon compound with a single atomic layer and polydisperse sheets of different sizes. It is usually used as a starting material to make graphene oxide that is reduced or functionalized. Since there are more oxygen-containing functional groups on the graphene oxide sheet layer than there are on graphene, the structure of graphene oxide is more complex and affects its properties (Yu *et al.* 2020). The synthesis of graphene oxide is detailed in the modified Hummers method, with the functionalization of this compound improving its mechanical, electrical, and thermal properties, leading to many sensors developed using reduced graphene oxide (rGO) (Shamkhalichenar and Choi 2020). Figure 2.6 shows the production of reduced graphene oxide from pristine graphite.

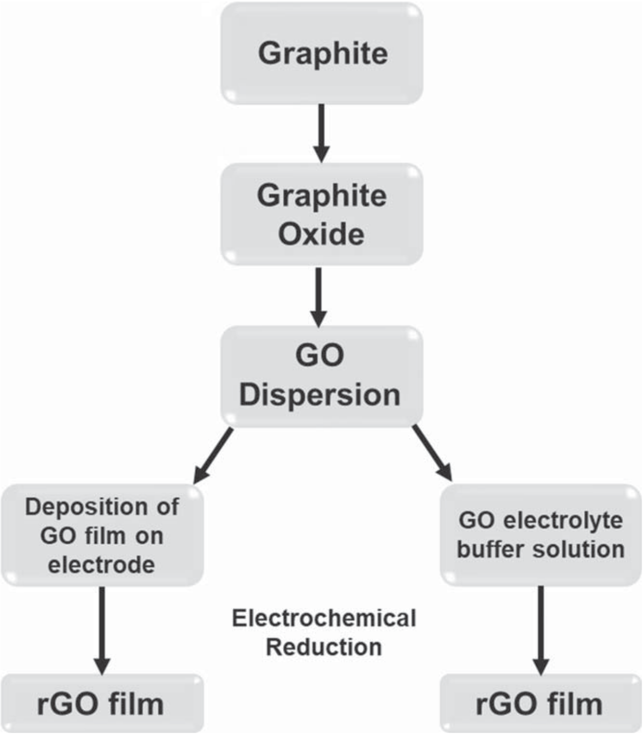

Figure 2-6: The production of reduced graphene oxide from graphite, adopted from (Yu *et al.* 2020).

2.5.2.4 Newly structured and engineered nanomaterials

This category of nanoparticles comprises those whose properties can be adjusted in accordance with their intended applications and are made up of two or more nanomaterials. The main constituents of such designed materials are multidimensional nanoparticles or nanocomposite materials, with at least one component falling within the nanoscale (Ojha 2020).

2.5.3 Nanoparticles

An expanding discipline of research known as nanotechnology involves the creation and synthesis of different nanomaterials. Nanoparticles are defined as small objects, 100 nm or smaller, that may differ from the main substance. Currently, copper, zinc, titanium, magnesium, gold, alginate, and silver are used to make various metallic nanostructures (Hasan 2015). The synthesis of nanoparticles can be either a chemical or a biological synthesis.

2.5.4 Methods of synthesis for nanoparticles

The preparation or synthesis of nanoparticles is mainly divided into two categories; the chemical method involving top-down and bottom-up strategies (Jamkhande *et al.* 2019) and the green route (Gour and Jain 2019), with the generation of NPs from this method producing

NPs that can be scaled up, are fiscally smart, and have less toxicity due to the use of fewer chemicals during synthesis. The primary distinction between the two approaches is the raw material used to prepare the nanoparticles. Whereas atoms or molecules are the starting material in bottom-up approaches, top-down methods start with bulk material and use various physical, chemical, and mechanical processes to reduce particle size to nanoparticles, as illustrated in Figure 2.7 below.

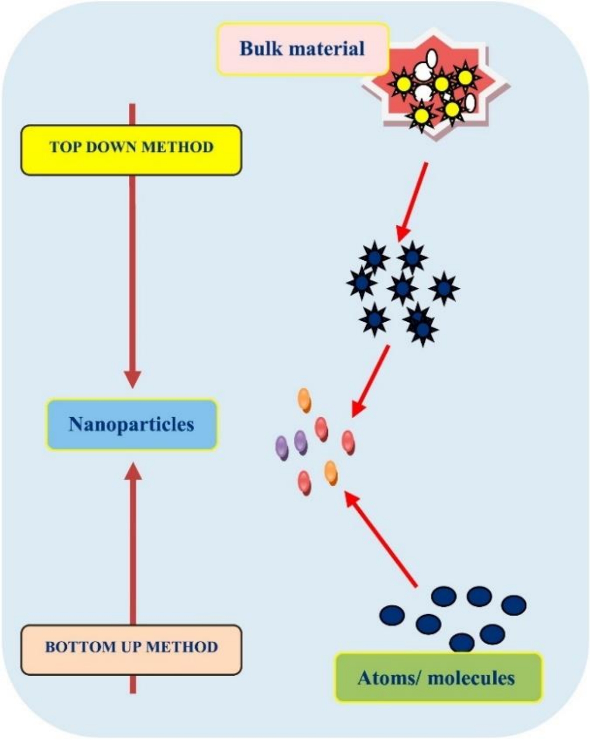

Figure 2-7: A schematic representation of the top-down and bottom-up methods for synthesis of nanoparticles, adopted from (Jamkhande *et al.* 2019).

2.5.4.1 Bottom-up chemical method of synthesis

a) Hydrothermal synthesis

The term "hydrothermal synthesis" refers to the chemical synthesis of materials in a sealed, heated solution above ambient pressure and temperature, mostly in an autoclave. Important solids such as microporous crystals, superionic conductors, chemical sensing oxides, electronically conducting solids, complex oxide ceramics and fluorides, magnetic materials, and luminescence phosphors have all been successfully prepared by hydrothermal synthesis. It also provides a path to novel condensed materials, such as nanometer-sized particles (Zhang *et al.* 2019), gels, thin films, distinctive helical and chiral structures, and in particular stackingsequence materials (Rane *et al.* 2018). The use of this method of synthesis has advantages such as the synthesis of high-purity large crystals and the synthesis of substances that tend to be unstable near their melting points (Modan and PLĂIAȘU 2020). The control of size, crystallinity, shape distribution, and morphology is easily achieved with this method due to the easy adjustment of parameters such as reaction type and reaction temperature (Rane *et al.* 2018).

However, the main drawback of this method is the use of expensive equipment, the safety issues during the reaction, and the fact that one is not able to observe changes in the reaction vessel during the course of the “black box” (Rane *et al.* 2018; Modan and PLĂIAȘU 2020).

b) Microwave assisted synthesis.

Popular applications of microwave-aided synthesis include nanotechnology and biological processes. Chemical reactions frequently occur more quickly than conventional convection heating techniques, with the advantages of higher yields and fewer by-products formed during the reaction. In addition to withstanding high temperatures and pressures, this method shows repeatability from reaction to reaction, and microwave reactors offer exceptional control over reaction mixing (Rane *et al.* 2018).

The two categories of microwave instruments are mono-mode (or single-mode) reactors and multimode reactors. Only one reactor vessel can be irradiated at a time in mono-mode reactors; multiple vessels can be irradiated simultaneously in multi-mode reactors; however, this is optional, as shown in the figure below (Dąbrowska *et al.* 2018).

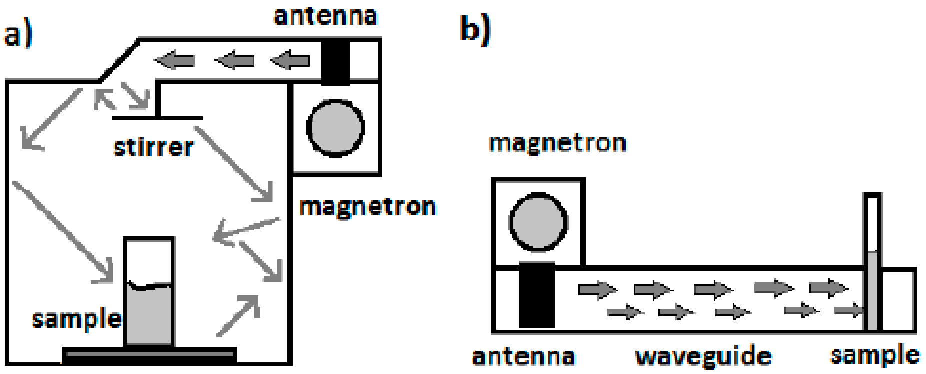

Figure 2-8: Microwave reactors recently used for the synthesis of nanomaterials (a) Multimode reactor, and (b) mono-mode reactor, adopted from (Dąbrowska *et al.* 2018).

c) Sol-gel method

There are two types of components used in the sol-gel processing method: "sol," which is a colloidal suspension of solid particles in a liquid, and "gel," which are polymers that contain liquid. As a result, this process also involves the production of "sols" in the liquid, which join to form a network of discrete particles or network polymers (Dhand *et al.* 2015).

In the sol-gel process, the two main steps are hydrolysis and condensation. Hydrolysis uses water to break up the bonds of the precursor, which is also the initial step in the production of the gel phase. Condensation occurs next, which results in the creation of nanomaterials. Excess water is subsequently removed to reveal the material's ultimate structure. In the recent study by (Arya *et al.* 2021), the effect on morphology and optical properties of operating parameters such as the pH of the sol, annealing temperature, calcination effect, and effects of capping agents used were investigated during the sol-gel synthesis of ZnO nanoparticles.

The advantages of this technique are that high-purity homogeneous products are obtained from materials at the molecular level, and it is relatively easy to obtain the desired sizes of nanomaterials. However, the drawback of this method is the non-eco-friendliness of the organic solvents used and longer reaction times (Rane *et al.* 2018).

d) Ultra-sound method

Another eco-friendly, easy, fast, and green method of producing metal nanoparticles is the ultrasound method. Sonochemistry and ultrasonic spray pyrolysis are the two main techniques used in ultrasound-assisted synthesis (Jamkhande *et al.* 2019).

Ultrasonic cavitation is based on the radiation of a liquid with ultrasonic irradiation. This ultrasonic cavitation produces several physical and chemical effects, including high temperature, pressure, and cooling rate, which provides a unique setting for chemical reactions under difficult circumstances.

The advantages of this type of synthesis of nanoparticles are that the reaction times are short and simple, with the desired nanoparticles synthesized at ambient temperatures, whereas with this method's acoustic cavitation, heat-sensitive materials can be employed (Rane *et al.* 2018).

e) Spray pyrolysis method

By spraying a solution over a heated surface, a thin film is formed, and the contents react to generate a chemical compound. This process is known as spray pyrolysis. The chemical reactants are chosen so that, at the deposition temperature, the products other than the intended molecule are volatile (Dhand *et al.* 2015; Rane *et al.* 2018).

2.5.4.2 Top-down method of synthesis

It's also called the physical approach to NP synthesis. To make a nanoparticle, physical processes such as ultrasonication, electrochemical, and microwave irradiation are applied to a bulk metal precursor (Gour and Jain 2019).

2.5.4.3 Synthesis of MOFs

Metal organic frameworks (MOFs) are classified as porous hybrid organic-inorganic compounds, which consist of an inorganic metal centre, organic linker or ligand, and the topology of the framework, with bivalent and trivalent carboxylic acids commonly used to form frameworks with metals such as aluminium, zinc, cobalt, copper, chromium, and many other metals (Lee, Kim and Ahn 2013; Kumar *et al.* 2015). MOFs are synthesized by employing relatively different methods owing to their different functionality and porosity. The methods of synthesis are, but are not limited to, mechanochemical (Chen *et al.* 2019), slow diffusion (Li *et al.* 2009), microwave-assisted (Zhao *et al.* 2022), and hydrothermal (solvothermal) (Choi *et al.* 2004).

In this study, the method employed for synthesizing ZIF-67 is the modified solvothermal method (Zhang *et al.* 2020).

2.5.5 Silver nanoparticles

Silver nanoparticles (AgNPs) have been extensively studied and used in many fields because they have excellent physical, chemical, and biological qualities, as well as their size, shape, content, crystallinity, and structure (Sharma and Tripathi 2022).

Furthermore, surface plasmon resonance, electrical resistance, and toxicity are all recognized to be special attributes of AgNPs. On the basis of these, extensive research has been done to examine their characteristics and possible uses for a variety of things, including antimicrobial agents in wound dressings, anticancer agents, electrical gadgets, and water purification (Syafiuddin *et al.* 2017).

2.5.6 Methods of synthesizing silver nanoparticles (AgNPs)

Silver nanoparticles (AgNPs) can typically be synthesized in three different ways: physically, chemically, and biologically. There are three physical ways to synthesize silver nanoparticles: the condensation method, which is also called the evaporation method; the laser ablation method; and the thermal decomposition method (Syafiuddin *et al.* 2017).

The top-down and bottom-up are synthetic methods for metallic nanoparticles. In the top-down method, an appropriate bulk substance is reduced in size using several methods to produce small particles. The phenomenon of self-assembly of atoms into new nuclei that grow into nanoscale particles can be used to create nanoparticles in the bottom-up strategy using chemical and biological approaches, as depicted by the figure below (Nie, Zhao and Xu 2023).

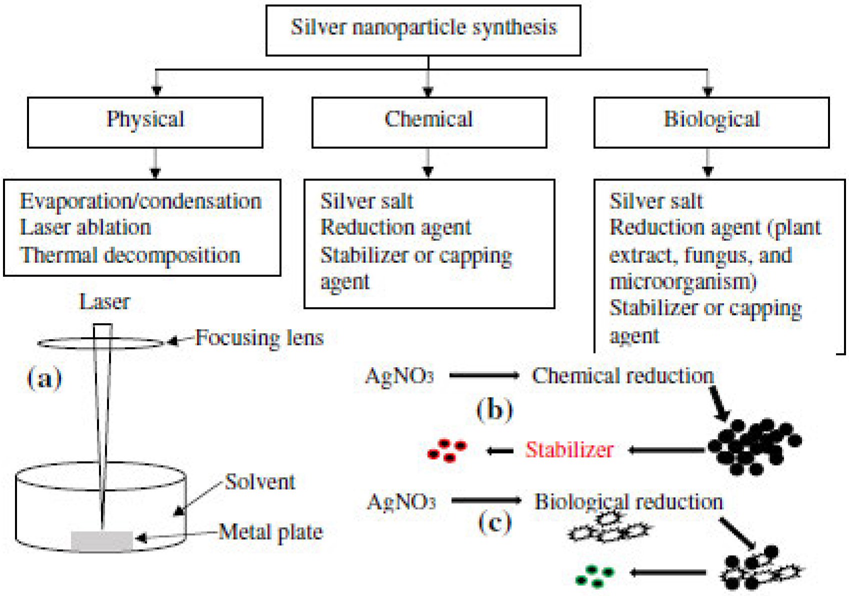

Figure 2-9: Different routes of synthesis for of silver nanoparticles, adopted from (Syafiuddin *et al.* 2017)

2.5.6.1 Chemical synthesis of AgNPs

In general, there are three primary components used in the chemical synthesis of AgNPs in solution: metal precursors, reducing agents such as sodium borohydride or citrate, and stabilizing or capping agents such as polyvinyl pyrrolidone. Silver salt reduction results in colloidal solutions that go through two stages of nucleation and growth. Additionally, it has been discovered that these steps have a significant impact on the size and shape of the AgNPs (Natsuki, Natsuki and Hashimoto 2015). Although this method is widely used, it is not environmentally friendly as there are often toxic residues produced from organic solvents and reducing agents.

2.5.6.2 Physical synthesis of AgNPs

The physical synthesis of AgNPs is divided into three different types: the evaporation-condensation method, the laser ablation method, and the thermal decomposition method:

(i) Evaporation-condensation method

Typically, the evaporation-condensation method is utilized in the physical process of creating AgNPs. It is frequently carried out in a tube furnace operating at atmospheric pressure, which effectively synthesizes a range of sizes. Biological synthesis of AgNPs (Natsuki, Natsuki and Hashimoto 2015).

The evaporation/condensation process can create highly pure particles from readily available and reasonably priced pure metals (Förster, Wolfrum and Peukert 2012).

(ii) Laser ablation method

This method uses a top-down method to create nanoparticles by concentrating a high-energy laser beam on the surface of a solid object immersed in a solution. When a laser pulse is applied to the surface of a solid target, the electrons in the target substance absorb the energy from the pulse and transmit it to the lattice. The material from the target surface is then released in the form of a plasma plume, which is constrained by the strong pressure of the liquid surrounding it (Balachandran *et al.* 2022). The temperature differential between the liquid and the plume is also significant. When energy from the plasma decay is transferred to the liquid surrounding it, a cavitation bubble is produced. A layer of vapour with the same volume as the plasma emerges as a result of this action. The cavitation bubble eventually collapses after a cycle of expansion and contraction, releasing nanoparticles into the fluid around it. Recently, there has been a demonstration of producing bimetallic gold-silver nanoparticles from thin film nanocomposites in water to produce pure bimetallic nanoparticles (Petrikaitė, Skapas and Stankevičius 2023).

However, the generation of AgNPs using a tube furnace has several drawbacks, because a tube furnace occupies a large space, consumes a great deal of energy while raising the environmental temperature around the source material, and requires a lot of time to achieve thermal stability (Natsuki, Natsuki and Hashimoto 2015).

(iii) Thermal decomposition method

Heat-induced chemical decomposition is known as thermolysis or thermal decomposition, the temperature at which a substance decomposes chemically is known as the decomposition temperature of the substance. Since heat is necessary to break the chemical bonds in the substance that is undergoing breakdown, the process is typically endothermic.

> The reaction geometry and the physical and chemical processes occurring at the reaction interface, such as heat transfer, diffusional removal of the gaseous product, nucleation and crystal growth of the solid product, and destruction of the reactant's crystal lattice, control a large portion of the thermal decomposition of solids (Nakano, Fujiwara and Koga 2016).

2.5.6.3 Biological synthesis of AgNPs

The third method for AgNPs is biological synthesis; similarly, to the aforementioned method, the precursor salt is a prerequisite; the only difference is in the type of reducing agent employed. Biological synthesis of AgNPs uses reducing agents such as plant extracts, fungus, and microorganisms, followed by stabilizing or caping agents to prevent agglomeration and control particle size (Natsuki, Natsuki and Hashimoto 2015; Gandhi and Khan 2016).

The non-environmentally friendly, expensive, and toxic conventional synthesis of AgNPs has pushed researchers to use green routes; therefore, in this study, AgNPs were synthesized from *eucalyptus* plant extract. Comparable to the other methods, the green synthesis of AgNPs is environmentally friendly as reducing agents are naturally occurring (Rafique *et al.* 2017). Table 2-3 shows the different properties of AgNPs synthesized from different plant extracts.

Table 2-3: Different plant bases extracts for the synthesis of $AgNO_3$

Plant extract	**Precursor salt**	**Reducing/capping agent**	**Size of NPs**	**Shape of NPs**	**Reference**
Alfalfa sprouts plant	$AgNO_3$	Root extract	2-4 nm	Icosahedral	(Gardea-Torresdey *et al.* 2003)
Persimmon leaf	$AgNO_3$	*Persimmon* leaf extract	32 nm	Spherical	(Song and Kim 2009)
Magnolia Kobus plant	$AgNO_3$	*Magnolia Kobus* leaf extract	38-61 nm	Triangles and hexagons	(Lee, Salunke and Kim 2014)
Eucalyptus globulus plant	$AgNO_3$	*Eucalyptus globulus* Leaf Extract	1.9-4.3 nm	Spherical and oval	(Ali *et al.* 2015)

Due to their strong antibacterial efficiency against bacteria, viruses, and other eukaryotic micro-organisms, silver nanoparticles have proven to be the most effective. They are unquestionably the most commonly utilized nanomaterials, being utilized as antibacterial agents in the textile industry, for the treatment of water, and in sunscreen lotions (Hasan 2015).

2.6 Capping of Nanomaterials with polymers

Polyvinylpyrrolidone (PVP) a surfactant, is crucial in the production of AgNPs because it covers the surface of nanoparticles to produce a stable colloid that can be used for manufacturing or any other AgNPs application. It can preserve nanoparticles during AgNP creation and prevent agglomeration (Natsuki, Natsuki and Hashimoto 2015). The size of AgNPs is influenced by the amount of PVP used as a dispersant.

PVP, which has C=O, C-N, and CH_2 functional groups, is a large, non-toxic, non-ionic, and popular polymer utilized in the synthesis of NPs. The pyrrolidone moiety, which makes up a significant portion of the PVP molecule, is extremely hydrophilic. Water and many non-aqueous liquids that aren't water are great at getting rid of PVP because the pyrrolidone ring has a very polar amide group inside it, as well as polar methylene and methine groups inside the ring and along its backbone (Koczkur *et al.* 2015).

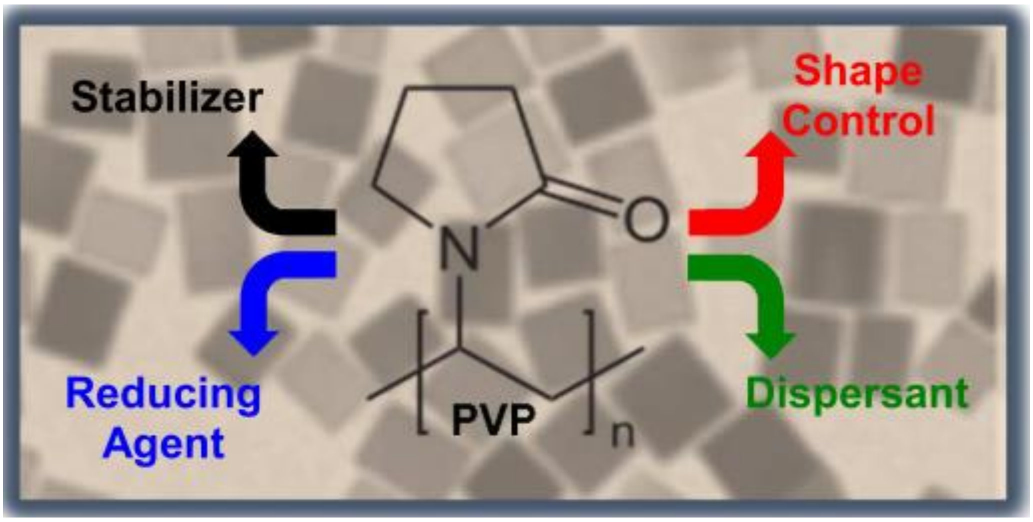

Figure 2-10: The role played by PVP during nanoparticle synthesis due to the multi-functional nature, adopted from (Koczkur *et al.* 2015)

2.7 Functionalization of multiwalled carbon nanotubes

Carbon nanotubes have had huge scientific interest and applications in fields such as sensors due to their profound properties such as chemical inertness and electrical conductivity (Ahmed, Haider and Mohammad 2013).

A challenge in maximizing the properties of MWCNTs is the improvement of dispersion to combat self-aggregation. Chemical modification of multi-walled carbon nanotubes (MWCNTs) is recognized as an effective method for functionalization. Chemical modification that promotes dispersion and surface activation at the same time, or using surfactants, is recognized as an effective method to improve their wettability and adhesion to host matrix materials (Sajid *et al.* 2022). Reagents with oxidizing abilities, such as oxidative nitric acid and sulfuric acid, are used to introduce carboxylic functional groups onto the surfaces of bare MWCNTs, as shown in the figure below. The fMWCNTs possess advantages over pristine MWCNTs, such as less self-aggregation, improved electrical conductivity, and more reactivity with other nanomaterials used for electrode modification (Ahmed, Haider and Mohammad 2013).

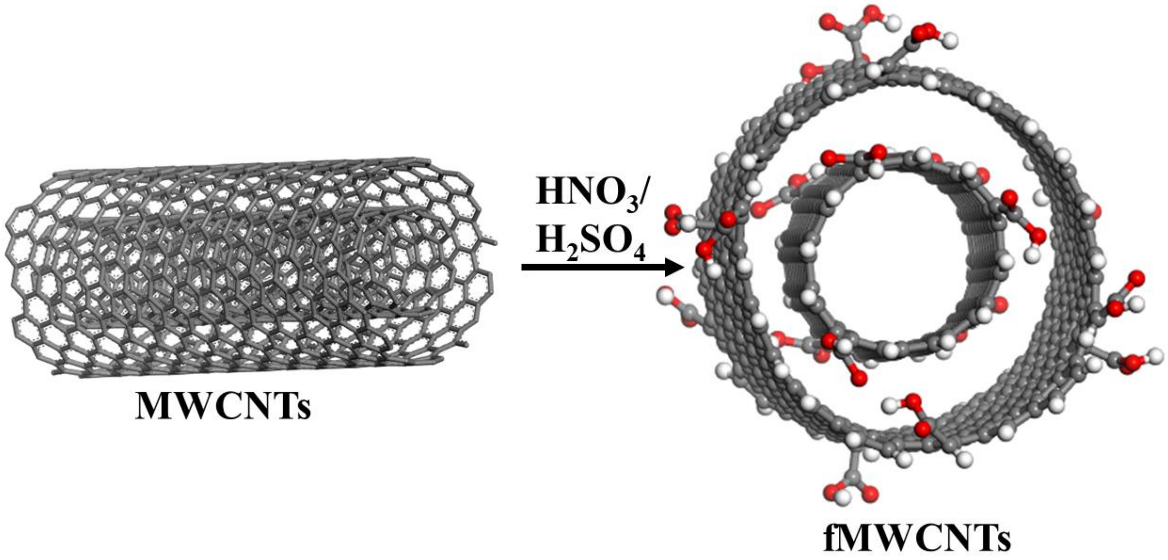

Figure 2-11: Surface modification of MWCNTs using oxidative Nitric/Sulfuric acid combination, resulting in carboxylic acid functional groups attached to the walls of bare MWCNTs.

2.7.1 Application of fMWCNTs in combination of AgNPs in sensing

fMWCNTs have attracted interest in many research fields as their desirable catalytic properties are of importance. Hybrid nanocomposites have proven to be applicable in many research fields, such as biosensors, bio-imaging devices, and solar cells (Jaballah, Messaoud and Dridi 2022). Individually, AgNPs are known to be conductive and have antimicrobial properties; the same can be said for individual fMWCNTs, which are also electrically conductive. Combining the two nanomaterials produces not only an electrically conductive nanocomposite but instead an electrically conductive and antimicrobial hybrid nanocomposite (Natsuki and Natsuki 2023). This hybrid nanocomposite has been applied in this study for electrochemical sensing of aspartame in food beverages (Hloma, Uwaya and Bisetty 2022). In another biosensor application, a novel green synthesis of AgNPs from *s* extract was presented and later integrated with fMWCNTs for the sensitive electrochemical detection of bisphenol A (BPA) (Jaballah, Messaoud and Dridi 2022).

2.7.2 ZIF-67 and fMWCNTs in Sensors

The building blocks of metal organic frameworks (MOFs) are metal ions or clusters connected to organic ligands. The benefits of huge surface areas, various metal centres, and customizable structures have made MOF materials the research highlight of the previous decade. They have been extensively used in sensors, electrocatalysis, and hydrogen production (Sun *et al.* 2022). In the same study, the conductivity of the cobalt-based nanomaterial was improved in cooperation with MWCNTs, resulting in further increased surface area to anchor hydrogen in electrochemical storage of hydrogen (Sun *et al.* 2022).

2.7.3 AgNPs and rGO in Sensors

The functionalization of graphene oxide has diminished its limitations across fields such as sensors, but in most cases, it is used in conjunction with or decorated with metal oxide nanoparticles. In environmental monitoring, the AgNPs/rGO nanocomposite was recently used for developing a reliable sensor for the detection of NO_2 (Li *et al.* 2020). The same AgNPs/rGO nanocomposite was used with TiO_2 NPs in a different experiment to design a label-free electrochemical immunosensor for the detection of the cancer biomarker CA 15-3 (Shawky and El-Tohamy 2021).

A further look into the AgNPs/graphene nanocomposite in terms of its synthesis and applications is well presented in this work by (He *et al.* 2018).

2.8 T1R2 sweet receptor and its sensing application

Proteins make up receptors, which are bearers of chemical messages. The classification of receptors in biological systems is based on their location as well as whether they relay, integrate, or amplify the chemical signal. Transmembrane receptors include ion-channel-associated receptors and hormone receptors that are G-protein-linked.

The human sweet taste receptor is a member of the C-GPCR family, which consists of the heterodimeric subunits T1R2 and T1R3 (STR). All classes of C-GPCR share the extracellular cysteine-rich domain (CRD). T1R2, one of the most prominent subunits of STR, uses this domain to connect its big amino-terminal domain (ATD) to a seven-transmembrane helical domain (Jaitak 2015).

T1R2 has a broad amino-terminal domain that contains between 500 and 600 residues, as well as binding sites with various functions for ligands. With dipeptidyl sweeteners covalently binding specifically to the binding sites of the T1R2 subunit of STR by hydrogen bonding, the food and pharmaceutical industries are making steviol glycoside relevant for their application as sweeteners (Ayyappa *et al.* 2015a).

There are no reports found in the literature wherein the T1R2 receptor was employed in electrochemical sensors, to be specific. However, other techniques, such as NMR, have exploited the interaction between sweet taste receptor T1R2 and sweeteners in a study where the authors concluded that the receptor is useful in the sensation of more than 50 diverse sweeteners (Assadi-Porter *et al.* 2010).

Using data from (Jaitak 2015), the antibody is then used in this study to create an electrochemical immunosensor for the detection of Rebaudioside A in food samples.

CHAPTER 3: THEORETICAL PRINCIPLES

The theoretical foundations of the experimental and computational techniques used in this study, focus on a wide spectrum of characterization techniques used in electrochemistry. Here, the supporting role of computational chemistry in constructing electrochemical immunosensors is underscored, emphasizing techniques such as molecular docking, density functional theory (DFT), Monte Carlo (MC) simulations, and molecular dynamic (MD) simulations.

3.1 Experimental Techniques

The experimental techniques of this study range from conventional characterization techniques for nanoparticle size and morphology to electrochemical characterization through voltammetric methods.

3.1.1 Voltametric Techniques

Voltammetric procedures are electroanalytical methods that primarily rely on determining the system current as the applied potential. The analyte's rate of oxidation or reduction is limited by how fast its mass moves the analyte from the solution (the supporting electrolyte) to the working electrode’s surface.

Several well-known rules govern voltammetry and define how the applied potential affects the redox current's behaviour. The concentrations of the redox species at the electrode surface and the rate of the reaction are both governed by the applied voltage (Kounaves 1997). A potentiostat, a computer, and an electrochemical cell make up the core elements of a contemporary electroanalytical system for voltammetry. In this work, cyclic and differential pulse voltammetry, which are qualitative and quantitative techniques, respectively, are discussed.

3.1.1.1 Cyclic Voltammetry

One of the most widely used electroanalytical methods is cyclic voltammetry, which is rarely used in quantitative analysis but is extensively used in qualitative studies like oxidation and reduction reactions, the detection of reaction intermediates, and examining the properties of the products produced at electrodes (Skoog, Holler and Crouch 2017).

In a typical cyclic voltammetry experiment, the current is measured while the potential is first ramped in one direction, and then the potential is ramped in the opposite direction. The characteristics of the analyte and the makeup of the sample determine the direction of the potential scan; a forward scan is obtained when the current ramps to more positive potentials, whereas a reverse scan is obtained in the opposite direction. This results in a cyclic voltammogram with key parameters for qualitative differentiation, such as cathodic and anodic peak potentials and cathodic and anodic peak currents, as shown in the figure below for a perfectly reversible reaction (Elgrishi *et al.* 2018).

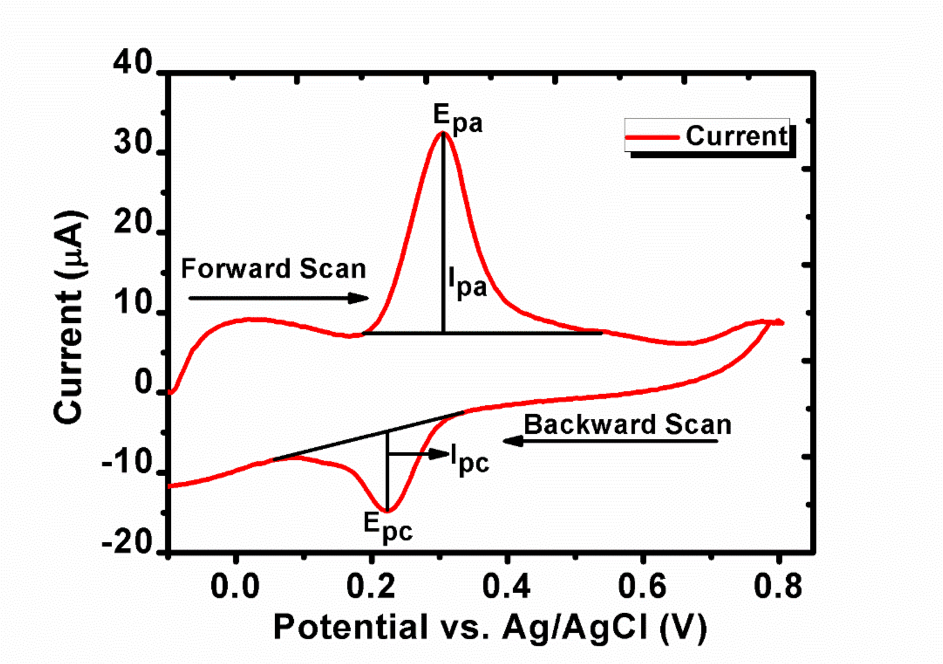

Figure 3-1: A typical cyclic voltammogram is a three-electrode system with a working electrode, counter electrode, and reference electrode that plots the change in current as the system's potential is ramped in both the forward and backward scans. The parameters are used in their typical contexts, where E_{pa} and E_{pc} are anodic and cathodic peak potentials, Ipa and Ipc are anodic and cathodic currents, respectively.

The cyclic voltammogram, shown above at Figure 3-1, shows the voltammogram in a three-electrode system. It shows the anodic peak current (I_{pa}), cathodic peak current (I_{pc}), anodic peak potential (E_{pa}), and cathodic peak potential (E_{pc}). The parameters are very useful in determining the properties of the electroactive species under investigation; thus, a formal reduction potential ($E^o/E_{1/2}$) can be calculated using the following equations:

$$E^o \ or \ E_{1/2} = \frac{E_{pa} + EpcE_{pc}}{2}$$ Equation 3-1

$$\Delta E_p = E_{pa} - E_{pc}$$ Equation 3-2

$$\Delta E_p = /E_{pa} \ - E_{pc}/= \frac{0.0591}{n} \cong \frac{2.303RT}{nF}$$ Equation 3-3

$$I_{\mathrm{p}} = (2.69 \ \times 10^5)n^{3/2}AD^{1/2}Cv^{1/2}$$ Equation 3-4

Where I_p is the peak current, n is the number of electrons transferred, A is the area of the electrode in cm^2, D is the diffusion coefficient in (cm^2/s), C is the concentration in (mol/cm^3), and v is the scan rate in (V/s).

The kinetics of electron transport between the electrode and the analyte are referred to as electrochemical reversibility. When the barrier to electron transport is minimal (there is electrochemical reversibility), the Nernstian equilibrium is reached right away when the applied voltage changes. While electron transfer reactions are slow and more negative (positive) potentials are needed to witness reduction (oxidation) reactions when there is a high barrier to electron transfer (electrochemical irreversibility), this results in a bigger ΔE_p as shown in the Figure below (Elgrishi *et al.* 2018).

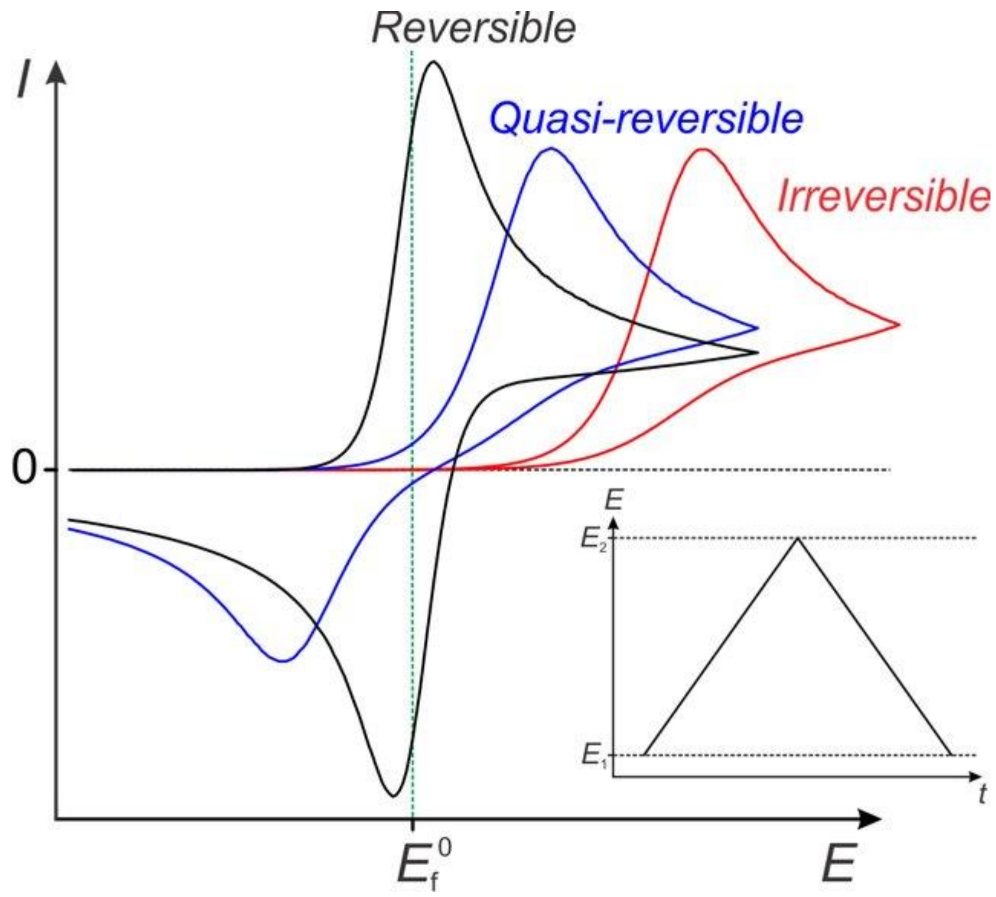

Figure 3-2: A comparison of the cyclic voltammetric wave patterns for the same formal potential's reversible, quasi-reversible, and irreversible electron transfer processes, adopted from (Lee 2014).

3.1.1.2 Differential Pulse voltammetry (DPV)

Voltammetric techniques are divided into qualitative and quantitative methods. DPV is a quantitative technique that has been employed in many fields due to the sensitivity of the method for determining the concentrations of a wide range of samples. With a sequence of voltage pulses superimposed on the potential linear sweep, DPV is used as a quantitative chemical analysis to explore the processes, kinetics, and thermodynamics of chemical reactions (Karimi *et al.* 2022).

The concentration of the analyte, as well as the desired accuracy and precision, frequently determine which approach should be used. Normal pulse polarography detection limits typically range from 10^{-6} M to 10^{-7} M, whereas those for differential pulse, staircase, and square wave polarography are in the range of 10^{-7} M to 10^{-9} M (Harvey 2000).

3.1.1.3 Electrochemical impedance spectroscopy (EIS)

One of the most significant electrochemical techniques is electrochemical impedance spectroscopy (EIS), in which the impedance of a circuit is measured in ohms (as a resistance unit). The EIS differs from the DC circuit resistance, which follows Ohms law, and thus, in an electrochemical cell, the EIS is employed to study the inherent properties of the system such as charge-transfer, diffusion, and mass transfer (Magar, Hassan and Mulchandani 2021).

The impedance (Z) is represented as real impedance (Z_{real}) and imaginary impedance ($Z_{imaginary}$) and is obtained by applying a potential wave at a certain frequency while measuring the produced current wave. Nyquist plots, also known as Argand diagrams, express the solution resistance (R_s), charge transfer resistance (R_{ct}), and Warburg impedance (W) by plotting Z_{real} on the X-axis against $Z_{imaginary}$ on the Y-axis, as displayed in the figure below.

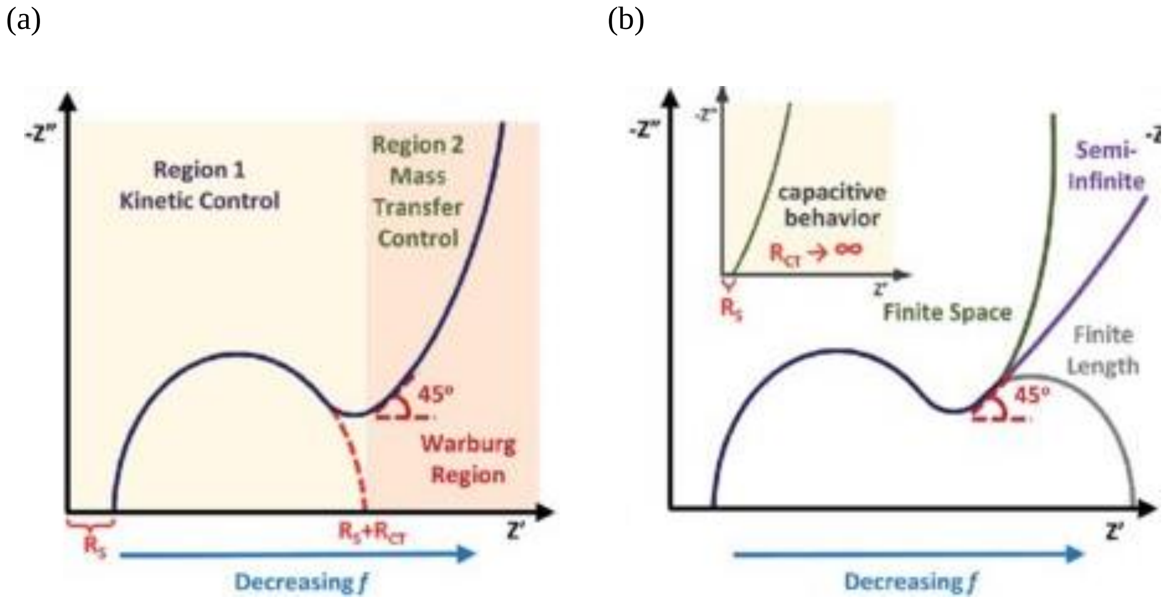

Figure 3-3: Nyquist plot in (a) with highlighted sections. (b) An expansion of Nyquist plot region 2 showing typical Warburg impedances for various electrode materials. The inset in (b) depicts the Nyquist plot as it would look when exhibiting capacitive behaviour. Adopted and modified from (Laschuk, Easton and Zenkina 2021).

In a typical electrochemical cell, in addition to the resistance of the electrolyte, interactions between matter (redox species) and the electrode also involve the concentration of electroactive species, charge transfer, and mass transfer from the bulk solution to the electrode surface. An electrical circuit that consists of resistances, capacitors, or constant-phase elements connected in parallel or in series to create an equivalent circuit characterizes each of these characteristics (Choi *et al.* 2020).

For many conductive surfaces, the "Randles equivalent circuit model" is a typical application for fitting data. The magnitude of the previously mentioned circuit components, R_s, R_{CT}, and C_{dl}, can be deduced from the Randles circuit. The Warburg impedance (W), which is also known as the impedance of diffusion or the mass-transfer term, is another characteristic whose magnitude changes significantly in the presence of a diffusion-controlled electron transfer mechanism. In the Randles circuit, the constant-phase element (Q), also known as CPE, is occasionally used in place of C_{dl} to account for non-ideal capacitor behaviour that results from the non-homogeneity of the surface at the double-layer interface (Laschuk, Easton and Zenkina 2021).

An EIS experiment is carried out in a three-electrode system by setting up a fixed applied voltage. The generated Warburg impedance (*W*), charge transfer resistance (R_{ct}), and solution resistance (R_s) are fitted in the diagram below to follow Randles circuit requirements and plotted in the Nyquist plots.

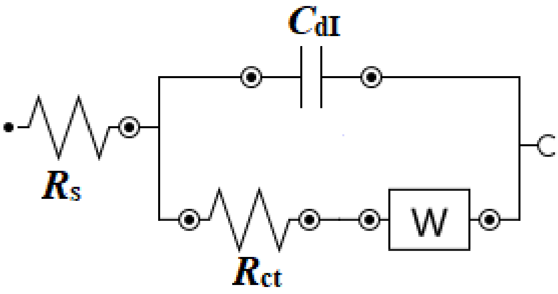

Figure 3-4: Randles circuit simplified version, fitted to meet Randles requirements in the Nyquist plot.

3.1.2 Characterization techniques

This section of the thesis consists of the theoretical principles of structural and morphological characterization techniques. UV-visible spectroscopy, Fourier transform infrared spectroscopy, thermogravimetric techniques, energy dispersive spectrometer analysis, single-particle inductively coupled plasma, and asymmetric flow field flow fractionation (AF4) are some of the structural characterizations, while high-resolution and scanning transmission spectroscopy are employed for the morphological characterization of nanomaterials in this study.

3.1.2.1 Ultraviolet visible (UV–vis) spectroscopic analysis

Ultraviolet (UV) spectroscopy is a physical method of optical spectroscopy that uses light in the visible, ultraviolet, and near-infrared ranges. It is based on Beer-Lambert's law, which states that the absorbance of a solution is proportional to the concentration of the absorbing species in the solution and the path length. As a result, it can be used to calculate the concentration of the absorber in a solution for a particular path length (Verma and Mishra 2018).

Overall, UV-Vis spectroscopy’s mechanism of operation uses electromagnetic light with a wavelength range of 190 to 800 nm. Lambert-Beer Law, which uses the following equation to relate the concentration of the measured material to its absorbance:

$$A\lambda = \varepsilon \mathrm{bc} \qquad \text{Equation 3-5}$$

Where A is absorbance, ε is the molar absorption coefficient, L/(mol cm), b is the measurement's path length in cm, and c is the concentration, mol/L, are all present. The Lambert-Beer law is only applicable to monochromatic radiation, according to the index (Mäntele and Deniz 2017).

The essential working principle of a UV spectrophotometer is that light with a specific wavelength range passes through a solvent-filled cell and strikes a photoelectric cell, which converts the radiant energy into electrical energy that can be measured by a galvanometer.

Many inorganic, chemical, and biological species can be identified quantitatively using ultraviolet and visible spectroscopy, and these substances can also be qualitatively described using information about the wavelengths at which they absorb the most monochromatic light (Verma and Mishra 2018).

3.1.2.2 Fourier-transform infrared (FTIR) spectroscopy

Infrared spectroscopy has four main applications: compound identification, structural clarification, quantitative study of one or more known species, and assessment of a molecule's basic properties. In this study, Fourier-transform infrared spectroscopy is used in the characterization and assessment of nanomaterials employed in the fabrication of the working electrode.

Electromagnetic radiation with a wavelength between 0.78 mm (780 nm) and 1000 mm is known as infrared radiation. It has a shorter wavelength than microwaves and a longer wavelength than the visible spectrum. The near-infrared (NIR), mid-infrared (MIR), and far-infrared (FIR) ranges are the most practicable subdivisions for the evaluation of materials by absorption spectroscopy, even though the IR spectral region can be divided into as many as five subregions (Berthomieu and Hienerwadel 2009).

3.1.2.3 Thermogravimetric characterization technique

The device created for detecting the energy that goes into or out of the sample is a differential scanning calorimeter (DSC). As the temperature is scaled up to observe material transitions like melting or recrystallization, the heat flows into or out of the sample material are measured with the DSC technique, and heat flow curves are recorded (Schick 2009).

Thermogravimetric analysis (TGA) is a quantitative analytical method that measures the mass of a sample as it ramps up in temperature in a furnace to as high as 1600 ^{o}C while being subjected to either a constant or fluctuating gas flow (Saadatkhah *et al.* 2020). A graph of the sample mass change vs. temperature or time is called a TG thermal curve or thermogram. Every compound's thermogram is different and conveys information on the material's thermal stability, oxidative stability, multi-component composition, product lifetime, decomposition kinetics, and moisture and volatile content.

Consequently, TGA in this study is qualitatively used for qualitatively study the thermal properties of the nanomaterials employed in biosensor development.

3.1.2.4 Energy dispersive spectrometer analysis

Energy dispersive spectrometer (EDS), also referred to as EDX or XEDS, is an analytical method that allows for the chemical characterization and elemental analysis of materials. A material that has been activated by an energy source (such as the electron beam of an electron microscope) releases a core-shell electron that helps to release part of the energy that has been absorbed. The difference in energy is subsequently released as an X-ray with a distinctive spectrum depending on its parent atom as a higher-energy outer-shell electron moves in to take its place. As a result, it is possible to analyze the composition of a sample volume that has been excited by an energy source. The location of the peaks in the spectrum identifies the element, while the signal's strength reflects the element's concentration.

In this study, the successfulness of the AgNPs synthesis and capping has been confirmed with EDS, together with the characterization of the AgNPs/fMWCNTs nanocomposite.

3.1.2.5 Single particle-Inductively coupled plasma mass spectrometry analysis.

A crucial piece of equipment that can measure practically every element in the periodic table down to the lowest detection limits is inductively coupled plasma mass spectrometry. Although it has been shown to be more effective than single-particle characterization, it is one of the top techniques for bulk compositional characterization. Aqueous dispersed metal nanoparticles can be quickly analysed using single-particle inductively coupled plasma mass spectrometry, providing the researcher with data on size, size distribution, and particle concentration (Laborda, Bolea and Jimenez-Lamana 2014). In this study, single particle-inductively coupled plasma mass spectrometry analysis (*sp*-ICPMS) has been used to study the effect of capping the *eucalyptus* extract-synthesized AgNPs with polyvinylpyrrolidone.

3.1.2.6 Asymmetric Field flow fractionation analysis

Field flow fractionation (FFF), which can be divided into asymmetric flow field flow fractionation (AF4) and centrifugal field flow fractionation (CF3), is a high-resolution separation technique for a variety of substances, including nanomaterials and polymers. FFF's two potent components can separate colloids as small as one micron and nanoparticles as small as 1 nm and 100 nm (Sogne *et al.* 2017).

As opposed to field flow fractionation, where the separation is caused by physical forces, chromatography attributes the separation to the partitioning of the separated species, which leads to chemical interactions between them and the stationary phase. The application of a cross-flow in a ribbon-like channel separates species in AF4, whereas the application of a circular cross-flow in CF3 separates species (Caputo, Industry and Sieg).

The fractionation procedure does not require a stationary phase, and the ideal separation range can be adjusted to the measurement parameters. This renders FFF versatile and complicated pharmaceutical items, including vaccines, monoclonal antibodies, and nanomedicines, which can be measured accurately. For this study, AF4 MALs were employed for the size separation of *eucalyptus* synthesized AgNPs. This method may acquire physio-chemical parameters such as the molar mass of macromolecules and particle size for target nanoparticles thanks to the FFF multi-detector (UV and light scattering detectors) linkage (Dubascoux *et al.* 2010).

3.1.2.7 Scanning electron microscope analysis

The scanning electron microscope (SEM), often known as SEM analysis or SEM technique, is a tool that has been employed across a wide range of fields. On a nanoscale to a micrometre scale, it can be regarded as an efficient approach for the analysis of organic and inorganic materials. With a high magnification that can reach 300,000x and even 1000000x (in some recent models), SEM creates extremely exact images of a variety of materials (Mohammed and Abdullah 2018).

SEM is a tool that allows for the observation of the microscopic and nanoscale worlds and can show details and intricacy that are hidden from view by light microscopy. The performance of the nanomaterials on the surface of the working electrodes in sensor development is linked to their morphologies; hence, the attachment of AgNPs onto fMWCNTs is observed using SEM in this study.

The basic components of SEM responsible for the imaging consist of a gun (which is basically the source of high-energy electrons), electromagnetic lenses to direct the high-energy electrons, a deflection and an electron detector system, and finally a viewing screen for the observation of the scanned images of either organic or inorganic materials.

3.2 Computational Methods

Numerous tools can be used in computational chemistry, also known as molecular modelling, to solve chemical problems outside of wet laboratories. These methods include ab initio, semiempirical and density functional theory, and molecular dynamics and mechanics. Molecular modelling can be used, depending on the application, to comprehend a system's chemical reactivity, the energy of molecules and their transition states, the physical properties of substances, molecular geometry, and the interaction of a substrate with a protein or enzyme of interest. Understanding the ligand-protein interaction through molecular docking studies was the main goal of this study's application of molecular modelling.

3.2.1 Molecular Docking Studies

Molecular docking is a commonly used tool in computer-assisted drug design and structural molecular biology. While molecular modelling has been employed as a tool for drug development, standard characterization techniques like X-ray crystallography and nuclear magnetic resonance (NMR) are used experimentally to anticipate and determine unknown protein structures. The behaviour of tiny ligands in a target protein's binding site is investigated using molecular docking methods (Schneidman-Duhovny *et al.* 2005).

The goal of molecular docking is to identify the dominant 3-dimensional molecular binding modes. In order to anticipate the binding modes of a ligand to the 3-dimensional protein structure, ligand-protein docking methods are used as a search algorithm. These docking scores are preferred as lower energy scores. The search process continuously assesses the ligand's structure until convergence to minimal energy is attained (Liu *et al.* 2020).

In this study, we use molecular docking tools to investigate different ways that the sweeteners (ligands) interact with the recognition element, T1R2 (antibody). The lower the docking score, the greater the affinity of the ligand to bind with the antibody or protein of interest.

3.2.2 Density Functional Theory

In physics, chemistry, and materials science, density-functional theory (DFT) is used as a computational quantum mechanical modelling technique to investigate the electronic structure (or nuclear structure) of many-body systems, specifically atoms, molecules, and condensed phases. Predicted attributes of fair to excellent quality can now be produced because of advancements in techniques and implementation. DFT calculations can thus supplement experimental research or even confidently enter into areas that have not yet been examined experimentally (Orio, Pantazis and Neese 2009).

The selection of functionals utilized affects the accuracy of DFT calculations significantly. Even though a precise energy functional has not yet been established, approximations of many materials' behaviour are accurately predicted by existing models, which are the Born-Oppenheimer approximation, the Hartree-Fock approximation, the Hohenberg-Kohn theorems, and the Kohn-Sham equation.

To simulate chemical reactions and forecast the properties of atoms, molecules, clusters, surfaces, and other materials in all three phases of matter, DMol3 is a computer modelling application. Geometry optimization, transition-state search, and optimization, which allow geometry stabilization by bringing the structure's energy to a stationary point, and molecular dynamics, which allow the simulation of atom motion as a function of time while taking temperature effects into account, are some of DMol3's capabilities. Numerous other calculations are also performed by DMol3, including those for reaction kinetics, which are estimated from the transition state; total and single-point energy, which is typically negative and corresponding to a bound state; elastic constants, which provide mechanical properties of a substance by an elastic constant’s tensor calculated from energies corresponding to an applying finite displacement distortion; and many others.

3.2.3 Monte Carlo Simulations

In essence, Monte Carlo simulation involves using a computer to generate random objects or processes. These items might 'naturally' appear during the modeling of a real-world system, such as a complicated road system, neutron transfer, or stock market development (Kroese *et al.* 2014).

There are several ways to use Monte Carlo methodologies, from conventional configuration sampling to structural inference from experimental diffraction data to simulated annealing. The Adsorption Locator acts like a substrate being loaded with an adsorbate or a mixture of adsorbates with a defined composition. Adsorption Locator is designed for the study of individual systems to locate low-energy adsorption sites on both periodic and non-periodic substrates or to explore the preferential adsorption of mixtures of adsorbate components, for example. A substrate structure, such as a metal surface, and the structure of one or more adsorbate molecules make up the input to the Adsorption Locator (Akkermans, Spenley and Robertson 2013).

The Adsorption Locator changes the temperature externally to mimic the system's annealing process. This is to enable the system to stabilize at a condition of minimal energy. The temperature is first abruptly elevated to a high value, then gradually dropped to the ultimate value. The procedure can be repeated several times to let the system investigate states with even lower energy. Adsorption Locator produces a research table containing all of the lowest energy configurations discovered throughout the adsorbate/substrate interactions. They can go through additional processing, such as serving as the input for a quantum mechanical optimization. As part of an adsorption calculation, the energy distribution can be determined (Akkermans, Spenley and Robertson 2013; Kroese *et al.* 2014).

3.2.4 Molecular Dynamic Simulations

The molecular modeling environment in the Materials Studio application is incorporated. In addition to offering users a number of tools with which to develop and show atomistic models, Materials Studio includes a number of modules that execute simulations on a variety of lengths and timelines (Akkermans, Spenley and Robertson 2013).

By drawing forth a wealth of data from dynamic systems, molecular dynamic (MD) simulation is a potent time-dependent tool for predicting the structural and functional features of molecules. Biological macromolecules like proteins and nucleic acids, as well as their interactions with tiny molecules, undergo structural changes that can be evaluated using this technique to determine the inhibitory effects of ligands (Mollazadeh *et al.* 2021).

3.2.4.1 Force fields!

For the past few decades, molecular force fields have been helpful to materials scientists in biomolecular simulations. Recent advancements in all-atom, nucleic acid, and small-molecule forcefield techniques parameterize and represent nonbonded interactions (He *et al.* 2022).

Force fields like AMBER ff94, CHARM22, and OPLS-AA have been used to successfully model many proteins and relatively short peptides. While experiments have shown that it is challenging to simulate intrinsically disordered molecules, small single-domain proteins with about 100 amino acids are feasible to simulate in these force fields. In molecular modeling (MM), a force field is created and used to calculate the potential energy of atomic systems or large particles. This is done by using derivatization forms from mathematical models and setting parameters. Discussed below are some of the few examples of different force fields.

- **COMPASS**

The Condensed-phase Optimized Molecular Potentials for Atomistic Simulation Studies (COMPASS) force field was developed with applications in material science in mind, while other well-known force fields like AMBER, CHARMM, and MM3 were also created with recent applications in mind to study biological molecules of interest. The COMPASS force field is used to predict attributes of molecules, including molecular vibrations, structures, and conformations, because it has been shown to be comparatively faster than other ab initio techniques. The main notable drawback of this force field is that it cannot be used to investigate reactions; as a result, a reactive force field must be created in order to study reactions (Sun, Ren and Fried 1998b).

Calculations in molecular mechanics and dynamics are used to validate the COMPASS force field parametrization (Savin and Mazo 2020).

- **Universal force field**

With unstrained and uncongested organic molecules, the universal force field (UFF) is frequently used to forecast the structures of the molecules and to calculate bond lengths and angles. For validation and comparison without altering the molecules of interest, other force field types, such as MM2 and MM3, were used. While determining fundamental parameters, Universal Force Field applies universal force field laws depending on the element being studied, its hybridization, and its connectedness (Rappe, Colwell and Casewit 1993; Alazwari *et al.* 2021).

.

CHAPTER 4: MATERIALS AND METHODS

This chapter deals with the materials and research methodology employed in this study. It describes the synthesis and characterization of several nanomaterials and outlines the fabrication process of electrochemical immunosensors for the detection of specific sweeteners.

4.1 Experimental Methods

In this section, the results are discussed, starting with the characterization techniques used to study the composition and properties of the nanocomposite (PVP-AgNPs/fMWCNTs) that was used for modifying the glassy carbon working electrode for the electrochemical detection of ASP in drinks.

4.1.1 Reagents and Materials

Silver nitrate ($AgNO_3$), cobalt nitrate hexahydrate ($Co(NO_3)_2$ $6H_2O$), 2-methylimidazole ($CH_3C_3H_2N_2H$), reduced graphene oxide (rGO), multiwalled carbon nanotubes (MWCNTs), methanol (CH_3OH), dimethylformamide ($(CH_3)_2NC(O)H$), sodium hydrogen phosphate (Na_2HPO_4), sodium dihydrogen orthophosphate (NaH_2PO_4), potassium ferrocyanide trihydrate ($C_6FeK_4N_6.3H_2O$), potassium ferricyanide ($C_6FeK_3N_6$), sulfuric acid (H_2SO_4), aspartame ($C_{14}H_{18}N_2O_5$), acesulfame K ($C_4H_4KNO_4S$), ascorbic acid ($C_6H_8O_6$), Rebaudioside A ($C_{44}H_{70}O_{23}$), saccharin ($C_7H_5NO_3S$) and nitric acid (HNO_3) were procured from Merck in South Africa. Sodium hydroxide (NaOH), hydrochloric (HCl) acid, and anti-TAS1R2 (Extracellular Domain) antibodies produced in rabbits were obtained from Capital Lab Supplies in Durban, South Africa, while alumina powder ≤ 3.0 μm was acquired from Metrohm of South Africa. The sugar-free Coca Cola sample was purchased from the local supermarket. All solutions and samples were prepared with deionized water from Aqua MAXTM-Basic 360 Series water purification equipment. Phosphate buffer solution (PBS) was prepared using an appropriate amount of sodium hydrogen phosphate (Na_2HPO_4) and sodium dihydrogen orthophosphate (NaH_2PO_4), supplied by Merck in South Africa, and all reagents used were of analytical grade.

4.1.2 Instrumentation

The electrochemical measurements were performed using Metrohm AUTOLAB, PGSTAT 302 with 663A Computrace, with a three-electrode system consisting of a GCE, GCE/PVP-AgNPs, GCE/fMWCNTs, and GCE/PVP-AgNPs/fMWCNTs as the working electrode, Ag/AgCl (3.0 M KCl) as a reference electrode, and platinum wire as the counter electrode, controlled by NOVA 2.1.4 software. The UV-vis spectrophotometer was used to confirm the formation of the green synthesized AgNPs and the nanocomposite using the Cary 300 UV–vis spectrometer. Morphological studies were conducted using scanning electron microscopy (SEM), and their elemental compositions were obtained using an energy dispersive X-ray (EDX) employing the ThermoFisher Nova NanoSEM with an Oxford X-max 20 mm^2 detector and INCA software. Single-Particle Inductively Coupled Plasma Mass Spectrometry (*sp*ICP-MS) equipped with the Syngistix nano module software was employed to deduce the size distribution of PVP-AgNPs. The hydrodynamic diameter of the biosynthesized AgNPs was determined using the Asymmetric Flow (AF4) AF2000 Multiflow supplied by Postnova Analytics, equipped with the AF2000 software coupled with a dynamic light scattering detector (DLS).

Morphological studies were conducted using SEM, and their elemental compositions were obtained using an energy dispersive X-ray (EDX) employing the ThermoFisher Nova NanoSEM with an Oxford X-max 20 mm^2 detector and INCA software. The functional groups in the synthesized ZIF-67 MOFs, fMWCNTs, PVP-AgNPs, rGO, PVP-AgNPs/rGO, and ZIF-67/fMWCNTs were determined with FTIR. The thermal stabilities of ZIF-67 and ZIF-67/fMWCNTs were studied via TGA.

4.1.3 Preparation of working solutions

All the working solutions were prepared using deionized water, unless mentioned otherwise.

4.1.3.1 Preparation of phosphate buffer

The calculated amounts of dipotassium hydrogen phosphate (K_2HPO_4) and potassium dihydrogen phosphate (KH_2PO_4) were dissolved in Millipore water in separate volumetric flasks to later prepare a 0.1 M phosphate buffer solution (PBS). The prepared PBS solutions had a pH range of 4-9 and were kept refrigerated at 4 °C until use without exceeding 2 weeks.

4.1.3.2 Preparation of 5 mM $[Fe(CN)_6]^{3-/4-}$

The calculated amounts of ferricyanide $[Fe(CN)_6]^{3-}$ and ferrocyanide $[Fe(CN)_6]^{4-}$ were dissolved in a volumetric flask containing a 0.1 M PBS solution to make the 5 mM $[Fe(CN)_6]^{3-/4-}$ in a 0.1 M PBS solution.

4.1.3.3 Preparation of ASP and Reb A stock solutions

The phosphate buffer (0.1 M, pH 8) was used to prepare the stock solution of ASP and Reb A, which were then kept refrigerated at 20 °C. The stock solutions were then used to prepare various concentrations of ASP and Reb A in a PBS by utilizing the conventional dilution technique.

4.1.4 Synthesis of electrode sensing materials

In this section, methods for the synthesis of different nanostructures are discussed.

4.1.4.1 Preparation of *Eucalyptus* leaf extract and Synthesis of PVP-AgNPs

The *Eucalyptus* leaves were collected from Flagstaff, located in Eastern Cape Province, South Africa. The leaves were washed several times with tap water to remove dust particles adsorbed on the surfaces of the leaves, rinsed with deionized water, dried at 60 °C for 12 h and ground to powder using a blender upon cooling.

About 4 g of the dried ground leaf was weighed into a beaker containing 140 mL deionized water and heated at 80 °C for 20 minutes under stirring conditions. Upon cooling, the mixture was centrifuged, and the supernatant solution was collected and used in the synthesis of PVP-AgNPs. The PVP-AgNPs were synthesized by adding 40 mL of *Eucalyptus* leaf extract with a pH of 4.97 to 40 mL of 0.2 M $AgNO_3$ (1:1 volume ratio) in the presence of 1 mL 1% polyvinylpyrrolidone (PVP) as a reducing agent. The reaction vessel was covered with aluminium foil, and the content was heated at 85 °C under an 800 rpm stirring condition for 90 minutes. The formation of colour-change in the mixture from greenish to reddish brown precipitates was noticed, suggesting the formation of PVP-AgNPs. The resulting precipitates were washed several times with deionized water and separated from the supernatant solution with centrifugation at 4000 rpm. The washed precipitate was dried at 50 ^{o}C for 24 h.

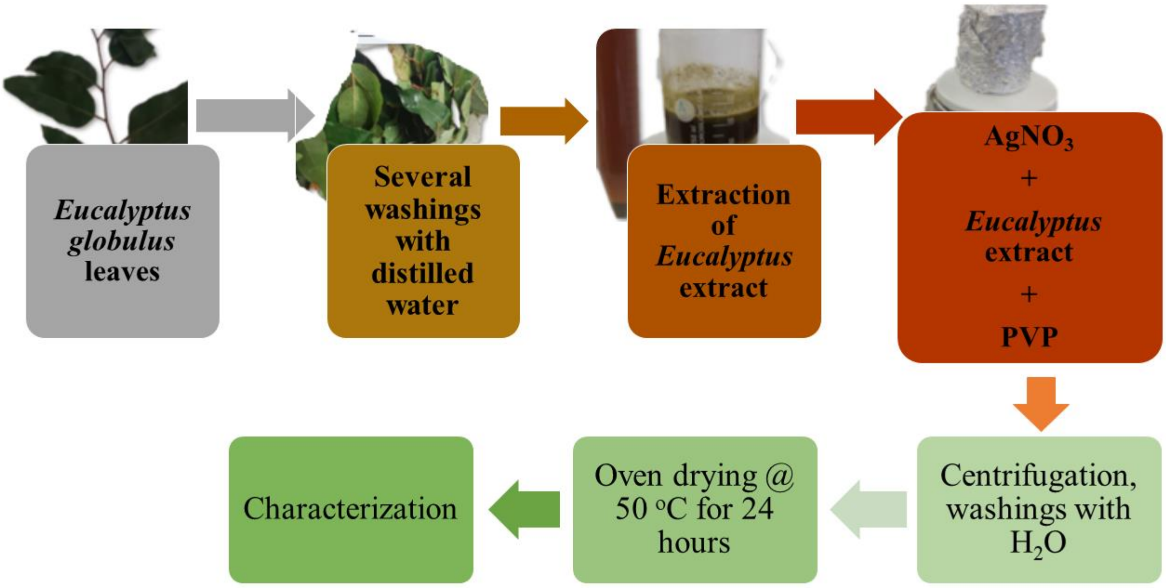

Figure 4-1: Schematic representation of green (*eucalyptus* extract reduced) of PVP capped silver nanoparticles (Koczkur *et al.* 2015; Alghoraibi *et al.* 2020).

4.1.4.2 Synthesis of ZIF-67

In this synthesis of zeolitic imidazole framework derived from cobalt (ZIF-67), 0.328 g of 2-methylimidazole was dissolved in 20 mL methanol: 10 mL water (2:1) solution to form a colourless solution, and 0.29105 g of cobalt nitrate hexahydrate salt was dissolved in 20 mL ethanol: 10 mL water (2:1) solution to form an orange solution. The organic linker (2-imidazole solution) solution was mixed with a cobalt nitrate hexahydrate solution while being stirred at temperature to form a purple solution. The resulting purple solution was then heated at 100 ^{o}C for 30 minutes while being stirred. The precipitated purple solution was then allowed to cool to room temperature without being stirred, followed by several washings of the precipitate with ethanol and deionized water. The resulting precipitate was then dried at 80 ^{o}C overnight, followed by calcination at 300 ^{o}C for 3 h.

4.1.5 Functionalization of MWCNTs and preparation of nanocomposite (PVP-AgNPs/fMWCNTs)

Pristine MWCNT was functionalized using a mixture of acids in a ratio of 3:1 (H_2SO_4, 75 mL: HNO_3, 25 mL). About 0.5 g of MWCNTs were dissolved in the solution and stirred under heat (50 ^{o}C) for 30 minutes. The contents of the reaction vessel were then allowed to be at room temperature, washed with deionized water until a neutral pH was obtained, and oven dried at 100 ^{o}C for 24 h (Uwaya and Fayemi 2021a).

PVP-AgNPs/fMWCNTs were prepared by thorough homogenization of 0.0075 g of fMWCNTs and PVP-AgNPs (0.0025 g) in 3-5 drops of dimethylformamide (DMF) under stirring conditions at room temperature until a homogenous paste was formed. The potion of the formed nanocomposite paste was dried in an oven at 50 ^{o}C for 5 h for characterization purposes, while the remaining undried portion was used for electrode modification.

4.1.6 Functionalization of graphene oxide

The carboxylated reduced graphene oxide (rGO) used in this study was commercially obtained.

4.1.7 Preparation of immunosensor (PVP-AgNPs/fMWCNTs/T1R2)

50 µg of T1R2 antibody was dissolved in 2 mL of pH 7 with a 0.1 M phosphate buffer. The immunosensor was achieved by dropping 1.2 µL of the prepared T1R2 in pH 8 phosphate buffer electrolyte, and the analysis of ASP was carried out using GCE/PVP-AgNPs/fMWCNTs. The complete immunosensor for this analysis is represented as GCE/PVP-AgNPs/fMWCNTs/T1R2 for the analysis of aspartame.

4.1.8 Preparation of nanocomposite (f-MWCNTs/ZIF-67)

By thoroughly homogenizing 0.0054 g of fMWCNTs and 0.0058 g of ZIF-67 in 1 mL of DMF and stirring for 1 h until a homogeneous paste was formed, f-MWCNTs/ZIF-67 were prepared. The remaining undried component of the produced nanocomposite paste was used for electrode modification, while a tiny quantity was dried in an oven at 50 ^{o}C for 5 h for characterization reasons.

4.1.9 Preparation of nanocomposite (PVP-AgNPs/rGO)

PVP-AgNPs/rGO was made by extensively homogenizing an equal amount of PVP-AgNPs and rGO in 3 mL of DMF and stirring for an hour until a homogenous paste was formed. A portion of the generated nanocomposite paste was dried in an oven at 50 ^{o}C for 5 h for characterization purposes, and the remaining undried component was used for electrode modification for the sensing of aspartame using Pt/PVP-AgNPs/rGO/T1R2 in food beverages.

4.1.10 Characterization of synthesized nanostructures and nanocomposites

Ultraviolet visible spectra were obtained with the Cary Series UV-vis spectrophotometer (UV-vis), 300 UV-vis model. Morphological studies were conducted using SEM, and their elemental compositions were obtained using an energy dispersive X-ray (EDX) employing the Thermo Fisher Nova NanoSEM with an Oxford X-max 20 mm^2 detector and INCA software. Single-Particle Inductively Coupled Plasma Mass Spectrometry (*sp*ICP-MS) was employed to deduce the size distribution of PVP-AgNPs, while AF4-MALS-DLS was used to obtain the radius of gyration of the uncapped and PVP capped AgNPs.

The structural properties of prepared nanomaterials were studied using Fourier transform infrared (FTIR) spectroscopy, a product of Opus Alpha-P, Brucker Corporation, Billerica, MA, USA.

4.1.11 Electrode treatment and Modification

The bare GCE was thoroughly cleaned prior to modification by gently polishing the electrode surface with alumina nano powder paste placed on a micro cloth pad. The alumina particles were washed off the electrode surface using deionized water. The electrode was then kept in 50% methanol for a few minutes, rinsed with deionized water, and dried at 50 ^{o}C for 3 minutes to obtain a clean, mirror-like surface. The electrodes for analysis were prepared using a drop-cast method. An aliquot of the prepared nanocomposite pastes (ZIF-67/fMWCNTs) was dropped onto the cleaned GCE and oven dried at 50 ^{o}C for 2 minutes to give GCE/f-MWCNTs/ZIF-67. The other electrodes, GCE/ZIF-67 and GCE/fMWCNTs, were prepared following the same procedure.

Prior to modification, the bare PtE was completely cleaned by gently polishing the electrode surface with an alumina nano powder paste that was mixed with a micro pad. In order to get a clean, mirror-like surface, the alumina particles were first removed from the electrode surface using deionized water. The electrode was then placed in 50% methanol for a short period of time, rinsed with deionized water, and dried at 50 ^oC for three minutes. The analytical electrodes were made utilizing the drop-cast technique. The other electrodes, Pt/PVP-AgNPs and Pt/rGO, were created using the same technique by dropping an aliquot of the prepared nanocomposites paste (PVP-AgNPs/rGO) onto the cleaned Pt electrode and oven-drying it at 50 ^oC for 2 minutes.

4.1.12 Real sample preparation

(i) Case Study 1 and 3

Using Whatman filter papers, 10 mL each of sugar-free Coca-Cola, Lucozade energy drink, and aQuelle sparkling-flavoured drink samples containing ASP were filtered into separate 50 mL volumetric flasks and made up with deionized water. About 500 µL of the prepared samples were transferred separately into an electrolytic cell containing 10 mL of PBS buffer; thereafter, they were spiked with known concentrations of ASP standard using the standard addition method and analysed using DPV.

(ii) Case Study 2

0.0216 g of health connection wholefoods sample containing Reb A was dissolved in 2 mL methanol and topped up to 10 mL with 5 mM $[Fe(CN)_6]^{-3/-4}$ solution. 6 drops of health connection whole foods containing Reb A were topped up with 5 mM $[Fe(CN)_6]^{-3/-4}$ solution. The prepared sample solutions were properly mixed and sonicated prior to indirect determination of Reb A at the surface of the GCE/fMWCNTs/ZIF-67/T1R2 electrode and analysed by differential pulse voltammetry in triplicate (n = 3) after, respectively, spiking samples with known concentrations of Reb A standard solution.

4.2 Computational Methods

4.2.1 Nanomaterials modelling

Materials Studio (MS) BIOVIA was used to construct each nanocluster and nanostructure except T1R2 (Ulicny and Kozar 2018). The MS software's implementation of the Forcite module (Sun, Ren and Fried 1998a) was utilized to optimize the geometry of the nanomaterials. A tool for classical molecular mechanics, Forcite in the MS program is intended to carry out various tasks such as quick energy calculations and geometry optimizations for both single molecules and periodic systems. A thorough understanding of surface interactions is essential for the design of numerous materials and sensor developments. Creating a model of molecules adsorbed onto a surface with optimum geometry, that is, one that minimizes energy, is a crucial initial step in this kind of research.

4.2.2 Template Selection

Since the human taste receptor 1 (T1R2) does not have a crystal structure, homology modelling was used to model the sequence from Uniprot (ID: Q8TE23). Chimera was used as an interface between the Modeller Software version 9.1 and Chimera.

4.2.3 Molecular Docking

Molecular docking was performed to investigate the active binding sites of ASP and Reb A on the T1R2 receptor separately. The PatchDock server was used in this study for blind molecular docking between ASP and T1R2 and between Reb A and T1R2.

4.2.4 Adsorption and Molecular Dynamic (MD) studies

Here, the Adsorption Locator (AL) module as it is implemented in the MS program can be used as a screening and preparation tool in conjunction with the forcefield approach to determine the preferred adsorption sites by ranking the energies for each created configuration (Biovia 2016). For the Monte Carlo (MC) and molecular dynamics (MD) simulations, the substrate-adsorbate interactions of the three case studies were investigated by replicating the experimental electrodes using a layer-by-layer technique to analyze the interactions. The adsorption energies were calculated using the equation below:

$$E_{ads} = E_{adsorbate} + E_{surface} - E_{adsorbate/surface}$$ Equation 4-1

In this instance, if Eads < 0, the chemical process is exothermic, and the adsorption energy suggests stability; a larger negative value indicates a stronger adsorption energy.

.

CHAPTER 5: RESULTS AND DISCUSSION

This chapter focuses on the results and discussion in the form of three case studies:

5.1 Case Study 1

Smart electrochemical immunosensor for the detection of aspartame (ASP) in dietary products supported by in silico methods.

In this section, the results for ASP using biosynthesized polyvinylpyrrolidone-capped silver nanoparticles (PVP-AgNPs) with functionalized multiwalled carbon nanotubes (fMWCNTs) and TIR2 antibodies doped onto glassy carbon electrodes (GCEs) are presented (**Scheme 5-1)**. A variety of complementary analytical measurement techniques were employed for the separation and characterization of AgNPs capped with PVP. In addition, coupled molecular docking and Monte Carlo (MC) simulations revealed a high binding affinity between ASP and the developed GCE/PVP-AgNPs/fMWCNTs/T1R2 electrode. Molecular dynamics (MD) simulations were used to examine the conformational profile of the docked structure.

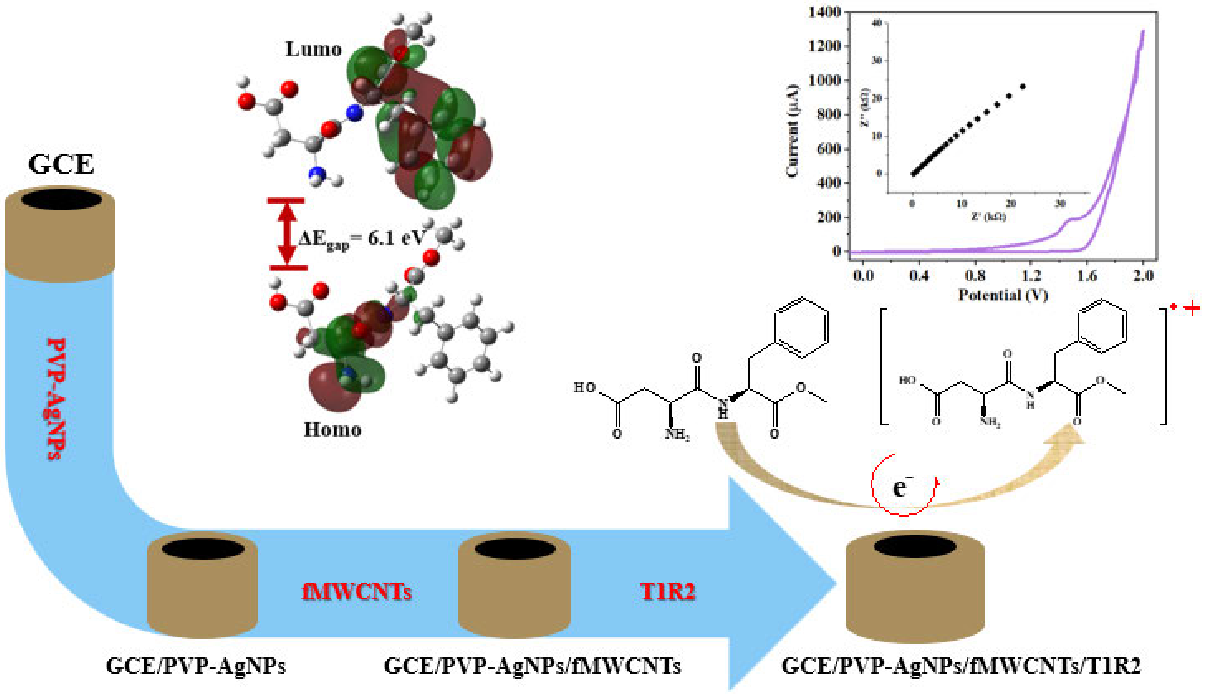

Scheme 5-2. Schematic diagram for the oxidation reaction mechanism of 240 µM ASP on GCE/PVP-AgNPs/fMWCNTs/T1R2 electrode.

5.1.1 Experimental

5.1.1.1 Characterization results

(i) Ultraviolet visible (UV–vis) spectroscopic analysis

The UV–vis spectra, Figure 5-1, confirmed the formation of the green synthesized AgNPs and the nanocomposite (PVP-AgNPs/fMWCNTs) from 200 to 800 nm. The formation of AgNPs was confirmed by the appearance of the dark brown solution in the presence of *eucalyptus* extract as the reducing agent and polyvinylpyrrolidone (PVP) employed as both the stabilizing and capping agent (Tsuji *et al.* 2008). A strong absorption band at 460 nm confirms the presence of AgNPs, which correlates with the literature (Khalil, Hassan and Ward 2017), whereas the absorption at 350 nm is attributed to the presence of phenolic compounds in the *eucalyptus* extract (Sadiq *et al.* 2023). Figure 5-1 displays the overlays of UV–vis spectra for *eucalyptus*-reduced synthesized AgNPs in the presence of a PVP capping agent, together with functionalized multiwalled carbon nanotubes (fMWCNTs) and the nanocomposite (fMWCNTs: PVP-AgNPs 3:1).

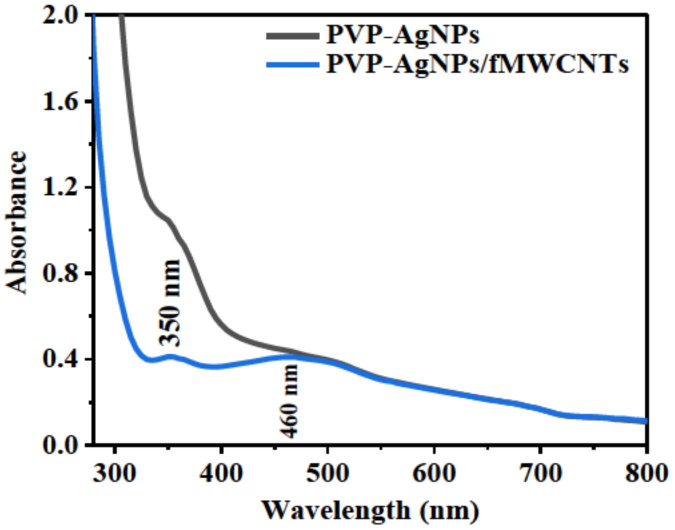

Figure 5-1: UV spectra of PVP-AgNPs and PVP-AgNPs/fMWCNTs

(ii) Energy-dispersive X-ray spectroscopy (EDS) analysis

EDS analysis was conducted to determine the elemental compositions of PVP-AgNPs, fMWCNTs and PVP-AgNPs/fMWCNTs nanocomposite. Figures 5-2a, b, and c revealed the presence of silver (Ag), oxygen (O) chlorine (Cl), and carbon (C), with a 56% abundance of

Ag introduced in the synthesis of PVP-AgNPs. The emission of aluminium (Al) might have resulted from the sample holder and part of the composition of the aqueous sample, as suggested in the literature (Hernández-Morales *et al.* 2019). The presence of sulphur is observed only on fMWCNTs and PVP-AgNPs/fMWCNTs nanocomposite; this is due to the carboxylic functionalization of MWCNTs in a mixture of H_2SO_4 and HNO_3.

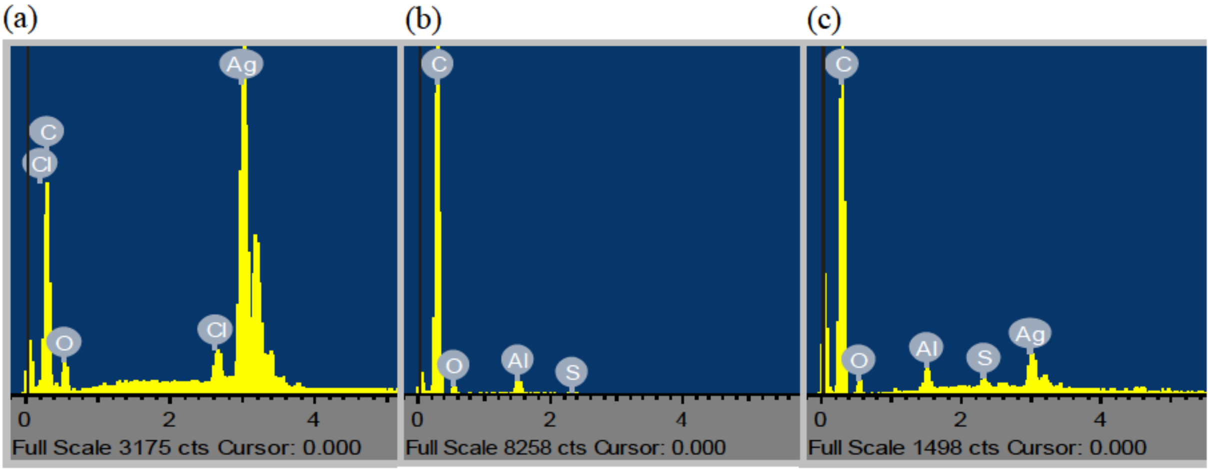

Figure 5-2: EDS of (a) PVP AgNPs, (b) fMWCNTs, and (c) PVP-AgNPs/fMWCNTs.

(iii) Scanning Electron Microscope (SEM)

Figures 5-3a-c show the surface morphology of PVP-AgNPs, fMWCNTs, and PVP-AgNPs/fMWCNTs, respectively. The SEM image of PVP-AgNPs presented in Figure 5-3a demonstrates the agglomeration of spherically shaped particles (Liao, Li and Tjong 2019), while that of fMWCNTs displayed as agglomerated cylindrical intertwined tube (Figure 5-3b). On the other hand, Figure 5-3 c shows the attachment of PVP-AgNPs to fMWCNTs (see the circle on the image), confirming the existence of interaction between PVP-AgNPs and fMWCNTs and their successful synthesis.

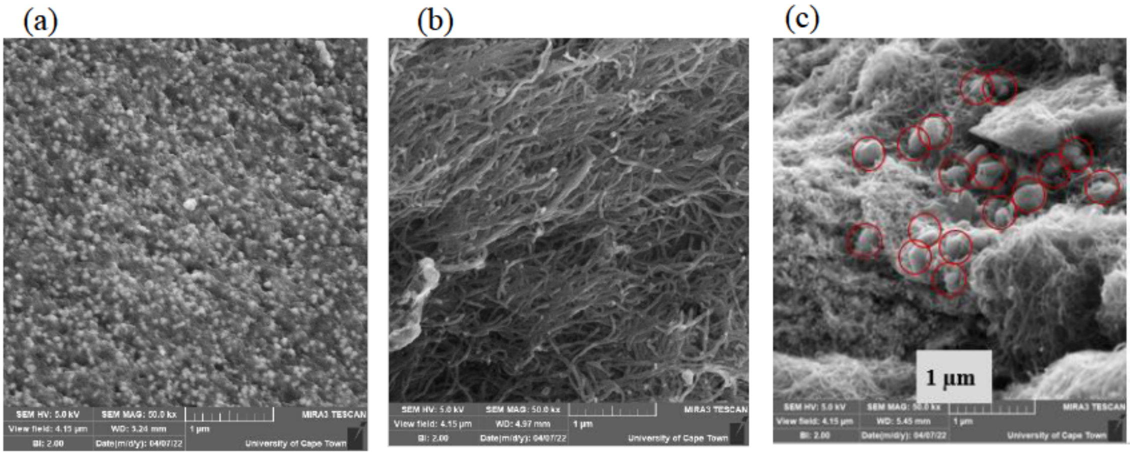

Figure 5-3: SEM images of (a) PVP AgNPs, (b) fMWCNTs, and (c) PVP-AgNPs/fMWCNTs.

(iv) Single particle Inductively Coupled Plasma Mass Spectrometry (sp-ICPMS) analysis.

The spICP-MS enables the determination of size of individual single particles. In this technique, the particle size is calculated as a sphere-equivalent diameter directly from the measured particle elemental mass (m) and specific density (ρ) using the equation 5-1:

$$V = \frac{m}{\rho} = \frac{4}{3}\pi r^3 \qquad \text{Equation 5-1}$$

where, V is the volume and r the radius of a particle. The spICP-MS mode for the average particle size distribution for the uncapped and capped PVP-AgNPs are represented in Figure 5-4a-b, respectively. The histograms of the uncapped AgNPs suggest that the maximum intensity signals were observed between 40 to 47 nm, resulting in the average particle size of 45 nm. For the capped PVP-AgNPs, the maximum intensity signals were observed between 25 to 30 nm, resulting in the average particle size of 27 nm as shown in Figure 5-4 (Liao, Li and Tjong 2019). The average higher diameter of the uncapped AgNPs is brought about the agglomeration of the semi spherical particles, whereas this is minimized by the introduction of the capping agent, which was polyvinylpyrrolidone in this study (Koczkur *et al.* 2015).

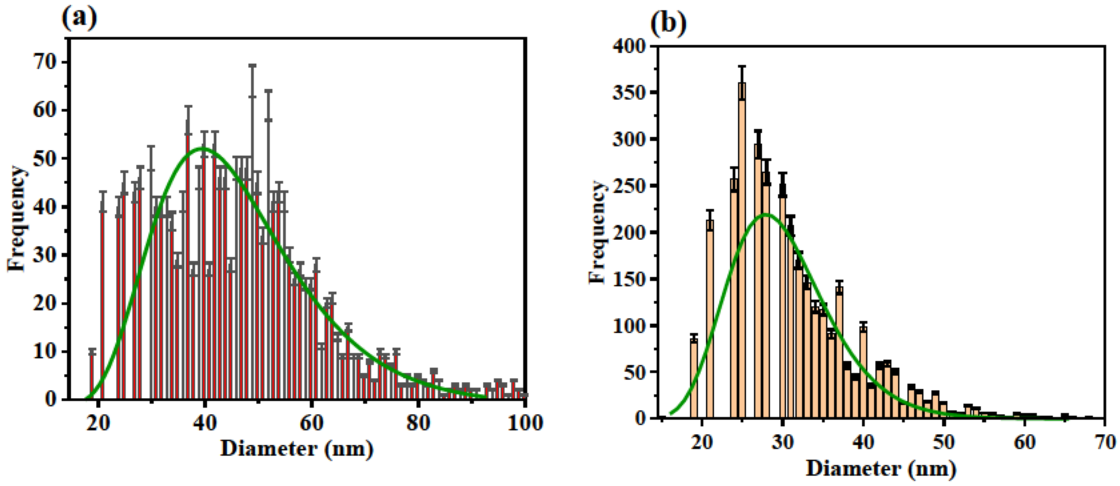

Figure 5-4: spICP-MS particle size distribution for (a) synthesized uncapped AgNPs and (b) PVP capped AgNPs suspensions.

(v) AF4 MALS analysis of AgNPs and PVP-AgNPs

Figure 5-5a-b shows the fractograms for the uncapped AgNPs and the capped PVP-AgNPs. There is a clear separation between the void peak signal (at 6 min) and the AgNPs sample peak eluting at 20 min, attributed to the sufficient sample relaxation in the focusing step (Naidoo *et al.* 2021). However, the uncapped AgNPs displayed a relatively broader and noisy signal due to possible agglomeration of the nanoparticles, in contrast to the signals for PVP capped AgNPs (17 min). The calculated radius of gyration (r_g) and the average hydrodynamic size (D_h) based on the sphere fit formalism using equation 5-2 were 18.2 nm and 46.9 nm for the uncapped AgNPs, and 9.2 nm and 23.7 nm for the capped PVP-AgNPs, respectively.

$$D_h = \frac{r_g}{0.775} \times 2 \qquad \text{Equation 5-2}$$

PVP capping resulted in a decreased retention time and radius of gyration, and the monodispersity and stabilization of AgNPs are well described as reported by (Malina *et al.* 2012) and summarized in Table 5-1. This was confirmed by the SEM images shown in Figure 5-3.

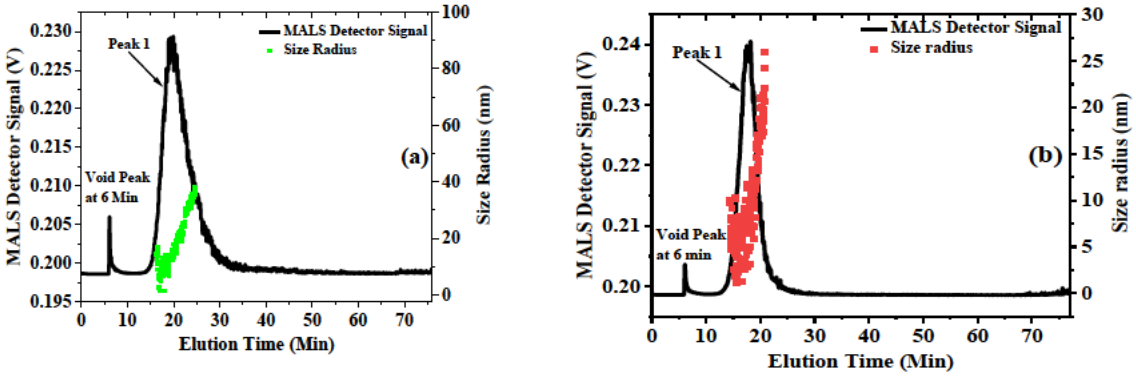

Figure 5-5: AF4-MALS fractograms of rg over MALS 90° for (a) uncapped AgNPs and (b) capped PVP-AgNPs suspension.

Table 5-1: Summary of uncapped and PVP-capped AgNPs information obtained from AF4-MALS and spICP-MS.

	AF4-MALS			spICP-MS
	Elution time (min)	**r_g mean (nm)**	**r_g range (nm)**	**mass-based mean diameter (nm)**
Uncapped AgNPs	20	18.2	5-38	40
PVP-capped AgNPs	17	9.2	1-28	27

5.1.1.2 Functionalization of MWCNTs

The electrochemical properties of f-MWCNTs and raw MWCNTs modified with GCE were investigated using CV in a 5 mM $[Fe(CN)_6]^{-3/-4}$ redox probe solution. Figure 5-6 shows the CV responses on GCE/fMWCNTs and GCE/MWCNTs electrodes. The anodic currents for bare GCE, GCE/MWCNTs, and GCE/fMWCNTs were 21.225 µA, 70.068 µA, and 128.54 µA, respectively, proving that the electrochemical properties and surface area of GCE/fMWCNTs are enhanced with acid functionalization. Hence fMWCNTs were used throughout the study.

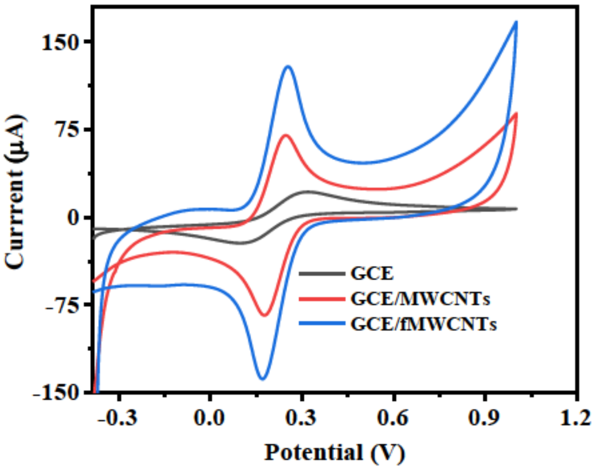

Figure 5-6: Cyclic voltammograms of bare GCE, GCE/MWCNTs and GCE/f-MWCNTs electrodes in 5mM $[Fe(CN)_6]^{-3/-4}$ solution topped up to the mark with pH 7 0,1 M PBS

5.1.1.3 Electrochemical performance of GCE/PVP-AgNPs/fMWCNTs/T1R2

(i) Cyclic voltametric characterization of electrodes

A CV measurement was performed on bare GCE, GCE/PVP-AgNPs, GCE/fMWCNTs, and GCE/PVP-AgNPs/fMWCNTs in a 5 mM $[Fe(CN)_6]^{-3/-4}$ solution prepared in 0.1 M PBS at pH 7 in order to investigate their electrochemical performance. Figure 5-7a shows comparative CVs obtained at a scan rate of 0.025 V/s. The nanocomposite-modified electrode (GCE/PVP-AgNPs/fMWCNTs) showed a greater current response than other electrodes tested. The anodic peak observed at 0.74 V and the reverse cathodic peak noticed at 0.6 V are because of the oxidation and reduction of AgNPs in the nanocomposite. The anodic current responses are as follows, in descending order: GCE/PVP-AgNPs/fMWCNTs (161.2 µA) > GCE/fMWCNTs (128.9 µA) > GCE/MWCNTs (70.1 µA) > GCE (21.5 µA) > GCE/PVP-AgNPs (14.3 µA).

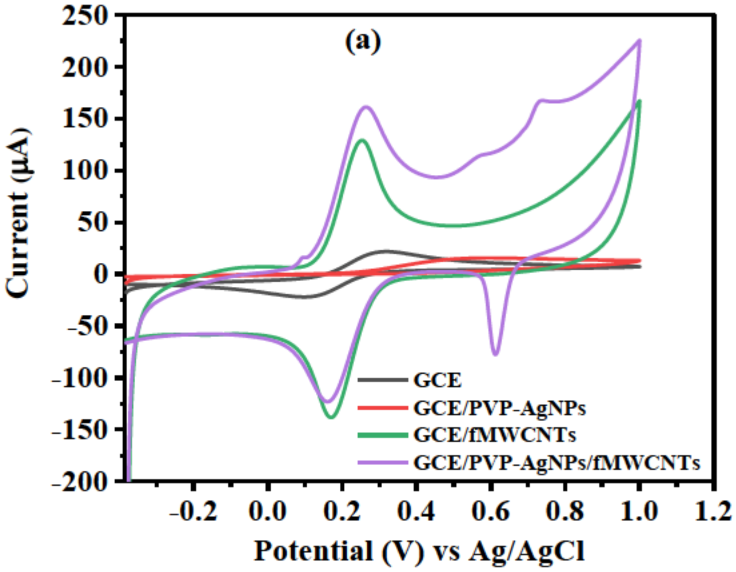

Figure 5-7: (a) Cyclic voltammograms for bare and modified electrodes in 5 mM $[Fe(CN)_6]^{-3/-4}$ solution prepared in 0.1 M PBS vs Ag/AgCl.

(ii) Electrochemical impedance spectroscopic study of electrodes

In order to understand the mechanism of electron transfer occurring at the electrode-electrolyte interface in a 5 mM [Fe (CN)$_6$]$^{-3/-4}$ solution at a fixed potential of 0.2 V between the 100 kHz and 0.1 Hz frequency range, EIS was applied. Figure 5-8b shows the Nyquist plots for bare and modified electrodes. Randle's circuit [R(Q[RW]) was used in fitting EIS data for GCE and [R(Q[RC])] for GCE/PVP-AgNPs, GCE/fMWCNTs and GCE/PVP-AgNPs/fMWCNTs (Figures 5-8c-d). In Table 5-2, the EIS data is summarized and the percent error indicates that the Randles-Sevcik requirements have been met, as confirmed by a low chi-square value (< 1) and a low percentage error (Jesila *et al.* 2021). The charge transfer resistance (R_{ct}) values tend to decrease from the highest R_{ct} value for bare GCE, to the lowest R_{ct} value for GCE/PVP-AgNPs/fMWCNTs. This R_{ct} value's trend is inversely proportional to the current values trend which increases with each electrode modification.

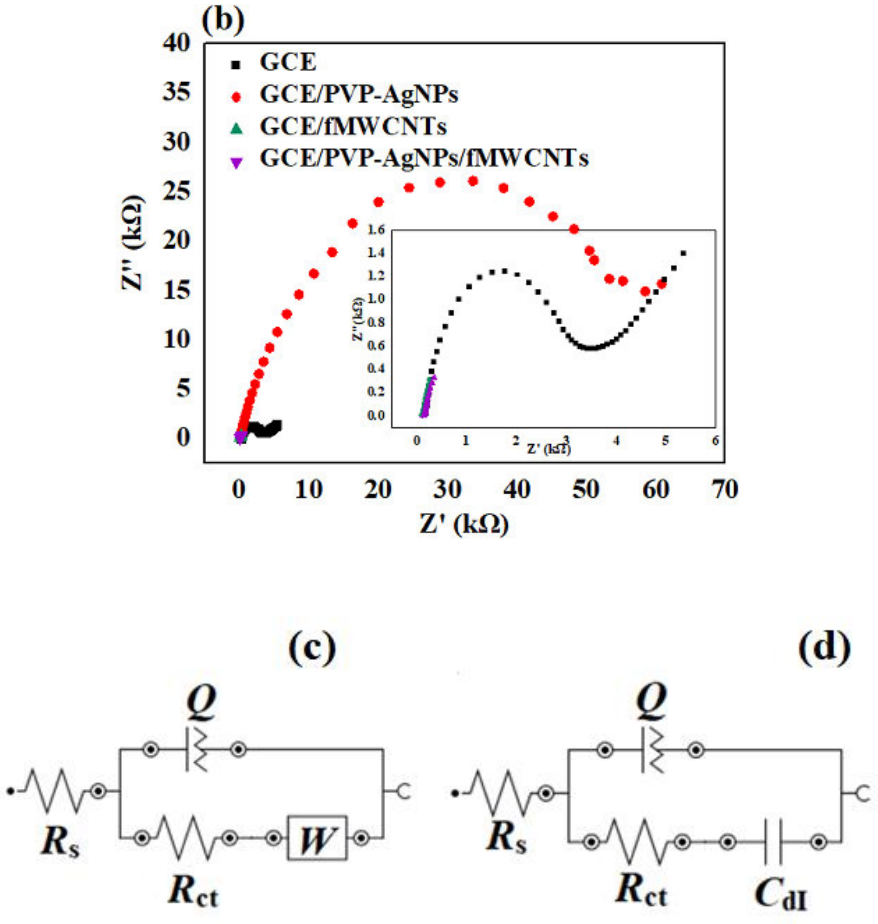

Figure 5-8: (b) Nyquist plots obtained for bare and modified electrodes in 5 mM [Fe (CN)6]$^{-3/-4}$ solution prepared in 0.1 M PBS. (c-d) Equivalent circuits used in fitting EIS data for GCE ([R(Q[RW]) and [R(Q[RC])] for GCE/PVP-AgNPs, GCE/fMWCNTs, and GCE/PVP-AgNPs/fMWCNTs.

Table 5-2: Summary of equivalent circuit parameters from impedance spectra in 5 mM [Fe (CN)$_6$]$^{3-/-4}$

Electrode	R_s(kΩ) (%Error)	R_{ct} (kΩ) (%Error)	Q **(F) (%Error)**
GCE	0.169 (1.68)	3.160 (1.67)	1.25E-06 (7.82)
GCE/PVP-AgNPs	0.155 (2.09)	62.409 (1.85)	1.43E-06 (3.58)
GCE/fMWCNTs	0.106 (0.6)	0.1581 (2.68)	0.0034 (4.61)
GCE/PVP-AgNPs/fMWCNTs	0.133 (1.45)	0.056 (4.52)	0.0027 (3.56)

(iii) Scan rate variation on GCE/PVP-AgNPs/fMWCNTs

CV was used to determine the effect of scan rates (0.01-0.3 V/s) on the peak potentials and currents of a 5 mM [Fe(CN)$_6$]$^{-3/-4}$ solution at the GCE/PVP-AgNPs/fMWCNTs electrode (Figure 5-9a). An increase in both anodic and cathodic peak currents with increased scan rates was observed, with the anodic and cathodic peak potentials shifting to more positive and more negative values, respectively, suggesting effective mass transport between the electrodes (Bojang and Wu 2020). Figure 5-9b-c shows the linear dependence of the redox peak currents (oxidation; I_{pa} and reduction; I_{pc}) on the scan rates and the square root of scan rate ($v^{1/2}$) with a regression coefficient (R^2) of 0.99, suggesting that the electrode reaction is diffusion-controlled (Uwaya, Wen and Bisetty 2022). The relationship between the logarithm of peak current (log I_p) versus the logarithm of scan rate (log v) is evident in Figure 5-9d, which produced a linear regression coefficient of 0.9952 and a slope < 1, further supporting a diffusion-controlled reaction. The slopes obtained from the plots of peak potentials (oxidation; E_{pa} and reduction; E_{pc}) versus the logarithm of scan rate Figure 5-9e were used to calculate the charge transfer coefficient (α) and the number of electrons transferred (n) simultaneously on applying equation 5-3. The number of electrons (n) was calculated as 0.56 ≈ 1 using equation 5-3, and the electron transfer coefficient (α) was calculated as 0.54, which is closer to 0.5 in equation 5-3, for a perfectly diffusion-controlled reaction.

$$-\frac{2.303RT}{\propto nF} \; and \; \frac{2.303RT}{(1-\propto)nF} \qquad \text{Equation 5-3}$$

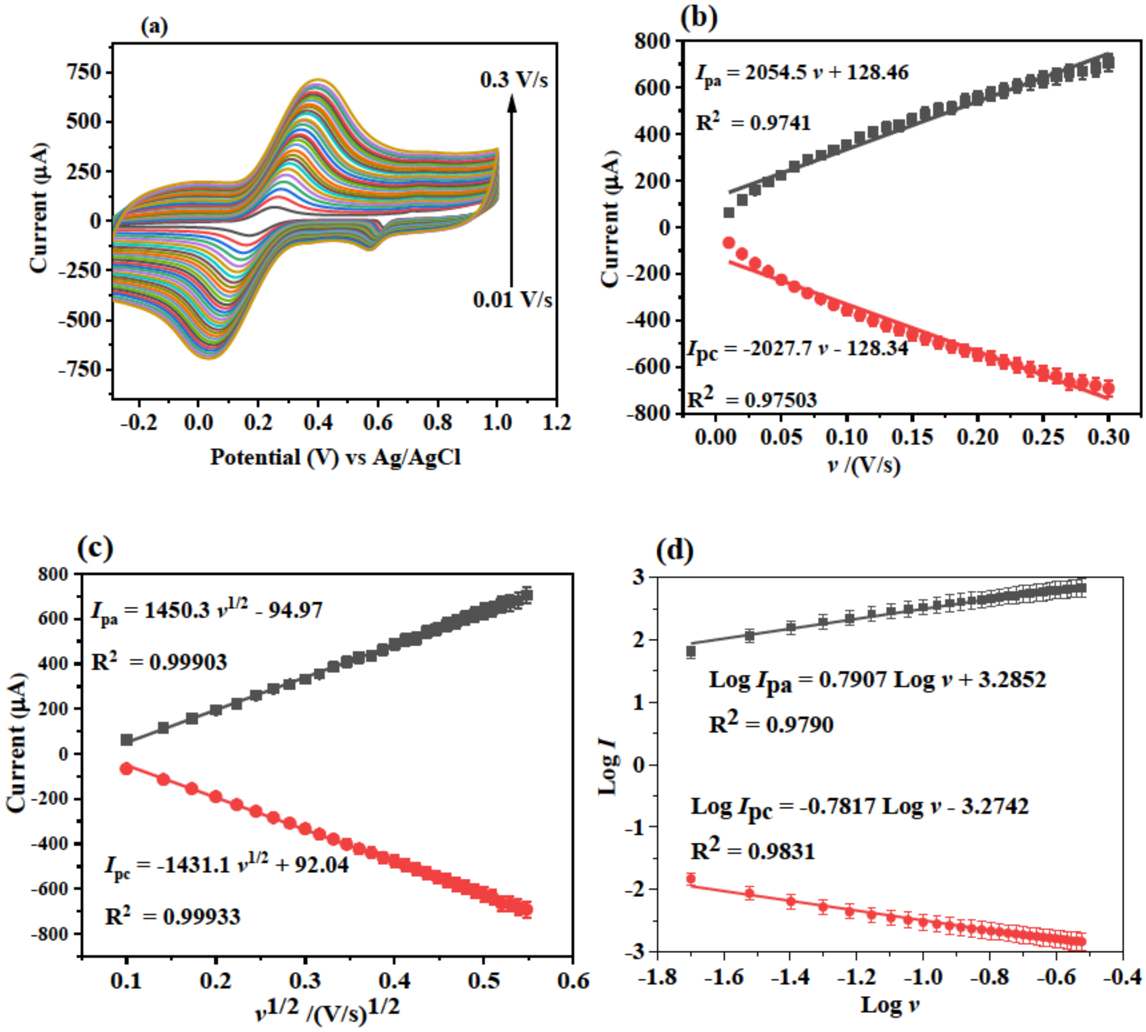

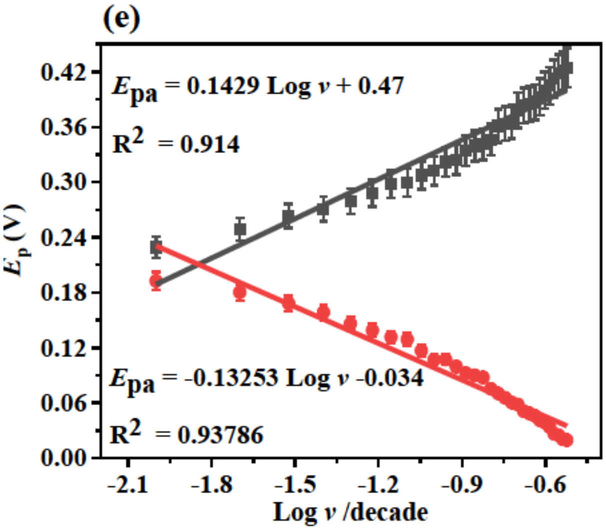

Figure 5-9: (a) Cyclic voltammograms in 5 mM [Fe (CN)6]$^{3-/-4}$ solution at various scan rate ranging from (0.01 – 0.3 V/s) on GCE/PVP-AgNPs/fMWCNTs electrode vs Ag/AgCl. Linear plots of (b) I_p versus scan rate- v (c) I_p versus $v^{1/2}$ (d) log Ip versus log v (e) E_p versus log of v.

5.1.1.4 Optimization of analytical parameters of the GCE/PVP-AgNPs/fMWCNTs/T1R2

(i) Optimization of solution pH and deposition time

Electrodes are affected by the pH of the supporting electrolyte. In Figure 5-10a, the effect of pHs of PBS in a range of 4-9 on the sensitivity of nanocomposite/TIR2 modified electrodes (GCE/PVP-AgNPs/fMWCNTs/TIR2) towards 240 µM ASP was studied using CV at a scan rate of 0.025 V/s. It was found that the oxidation current reached its maximum at pH 7, but the peak cannot be accurately resolved, so pH 8 was used throughout the experiments to detect ASP. A slight shift in anodic current and potential (Figure 5-10b) is noticed, suggesting the occurrence of the transfer of protons and electrons on the proposed sensor (GCE/PVP-AgNPs/fMWCNTs/T1R2). The effect of deposition time (10-160 s) on the peak current of ASP (240 µM) was also investigated using DPV Figure 5-10c on the same electrode. The results indicate a rise and fall of oxidation current with increasing deposition time, with the optimum peak current at 30 s. The deposition time of 30 s was therefore chosen for further measurements.

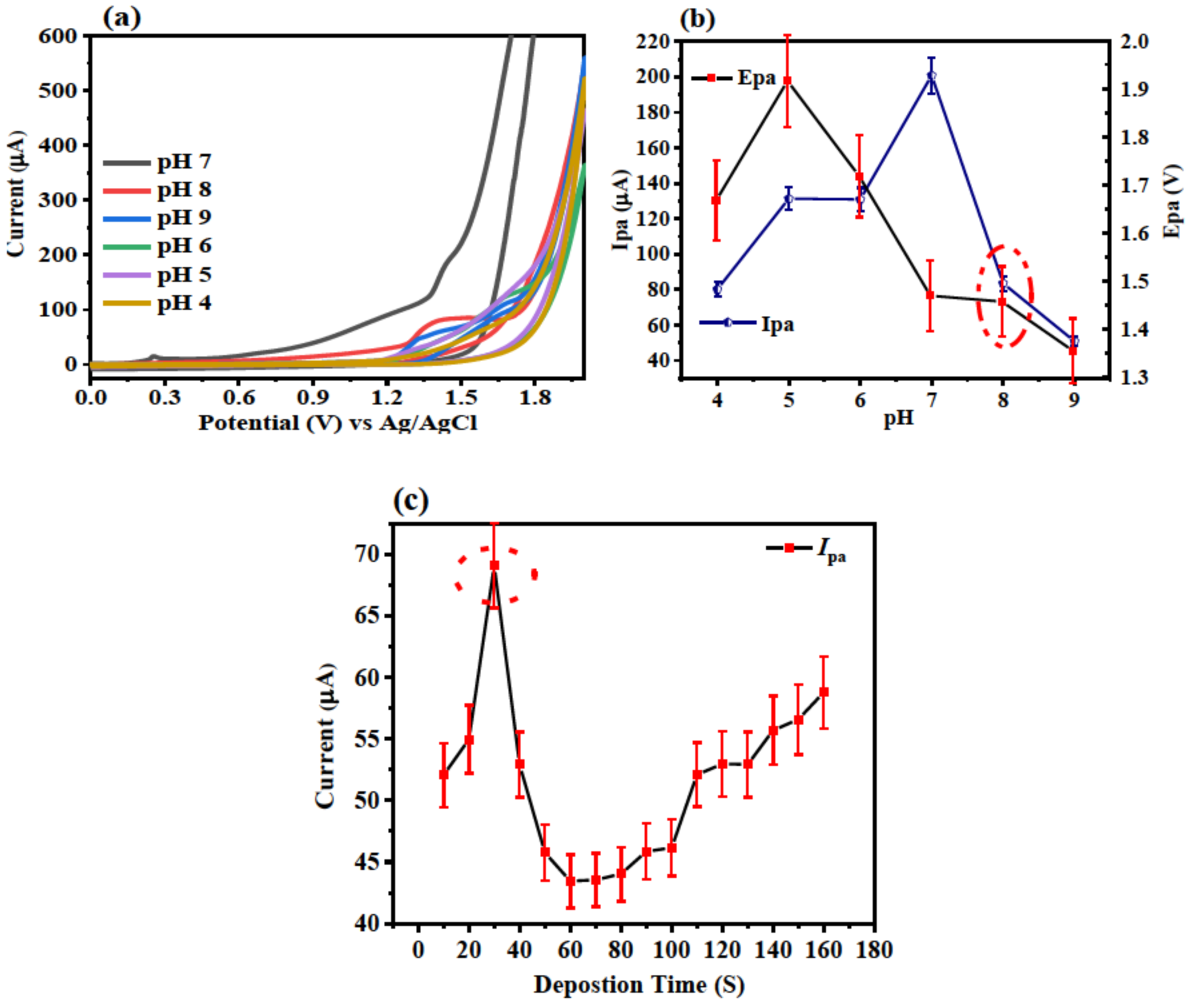

Figure 5-10: (a) Effect of pH on the oxidation (I_{pa}) of 240 µM ASP vs Ag/AgCl (b) The relationship between peak current and potential on ASP(c) The effect of deposition time on oxidation current (I_{pa})of ASP on GCE/PVP-AgNPs/fMWCNTs/T1R2 sensor.

5.1.1.5 Electrochemical behaviour of ASP on GCE/PVP-AgNPs/fMWCNTs/T1R2

(i) Cyclic voltammetry characterization

The electrochemical behaviour of 240 µM ASP on bare and modified electrodes in the presence and absence of TIR2 was studied using CV (Figure 5-11). An irreversible oxidation process was observed on the modified electrodes, with the exception of bare GCE. ASP potential was observed at 1.4 V on GCE/PVP-AgNPs/fMWCNTs/T1R2, with a similar result obtained in the literature (Balgobind *et al.* 2016a). Consequently, the oxidation current increased with the respective electrodes, GCE (13.84 µA), GCE/fMWCNTs (27.69 µA), GCE/PVP-AgNPs (147.58 µA), GCE/PVP-AgNPs/fMWCNTs (163.85 µA), and GCE/PVP-

AgNPs/fMWCNTs/T1R2 (191.52 µA). The amplified peak current at GCE/PVP-AgNPs/fMWCNTs/T1R2 indicates strong electrocatalytic activity of the nanocomposite towards ASP oxidation enhanced with the presence of TIR2.

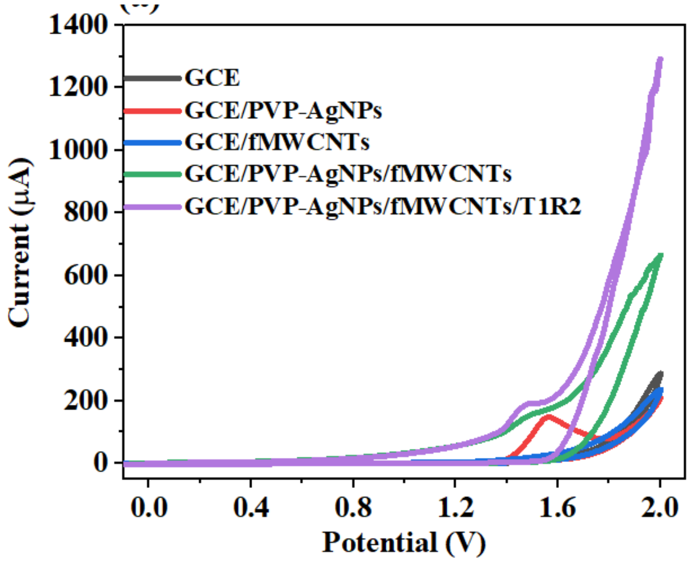

Figure 5-11: Cyclic voltammograms at 0.025 V/s obtained for bare and modified electrodes vs Ag/AgCl in pH 8 0.1 M PBS containing 240 µM ASP.

(ii) Electrochemical impedance spectroscopic study of ASP

EIS was further employed to understand the interfacial characteristics of the electrodes in response to electro-oxidation of 240 µM ASP. Figure 5-12a depicts the Nyquist plots derived from the EIS-fitted data. Figure 5-12b is Randle's circuit ([R(RQ)]) applied in the fitting of EIS data for all the electrodes (GCE, GCE/PVP-AgNPs, GCE/fMWCNTs, GCE/PVP-AgNPs/fMWCNTs, and GCE/PVP-AgNPs/fMWCNTs/T1R2). The lowest R_{ct} value was observed on the GCE/PVP-AgNPs/fMWCNTs/T1R2 electrode. The EIS data are summarized in Table 5-3.

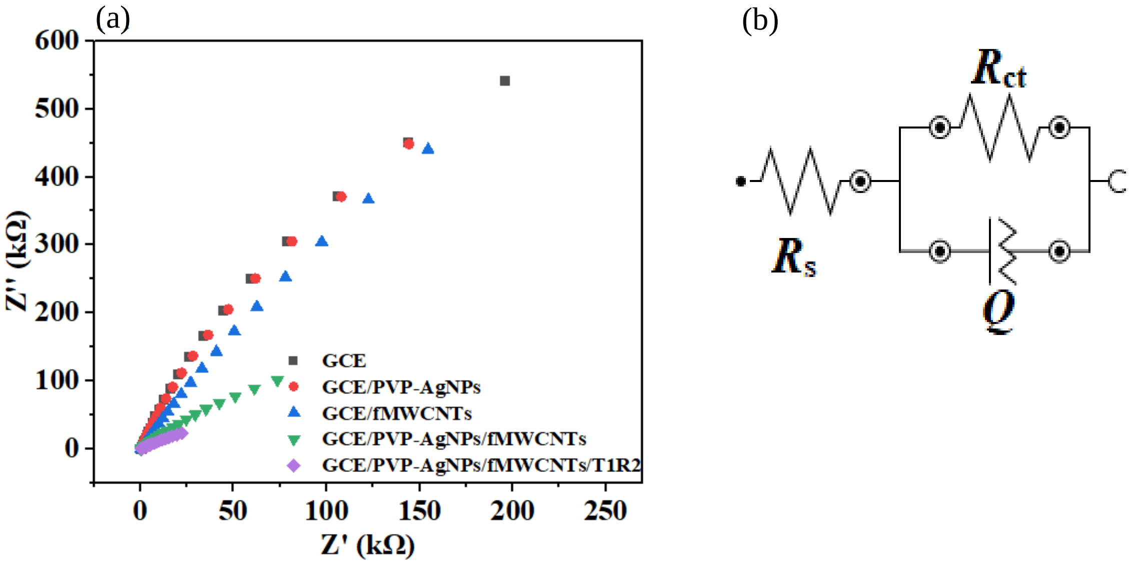

Figure 5-12: (a) Nyquist plots obtained for bare and modified electrodes vs Ag/AgCl in 0.1 M PBS containing 240 µM ASP, pH 8 at a fixed 1.4 V potential. (b) is the equivalent circuit ([R(RQ)]) applied in fitting EIS data for the electrodes.

Table 5-3: Summary of EIS data acquired from 240 µM of Aspartame in pH 8 0.1 M PBS.

Electrode	**R_s(kΩ) (%Error)**	**R_{ct} (kΩ) (%Error)**	χ^2
GCE	164.77 (1.02)	5084 (2.84)	0.11
GCE/PVP-AgNPs	223.7 (1.06)	2758.2 (3.32)	0.11
GCE/fMWCNTs	175.43 (1.00)	3028 (7.573)	0.11
GCE/PVP-AgNPs/fMWCNTs	213.76 (1.99)	606 (4.71)	0.25
GCE/PVP-AgNPs/fMWCNTs/T1R2	173.06 (3.42)	272.57 (3.11))	0.92

(iii)Scan rate variation on GCE/PVP-AgNPs/fMWCNTs/T1R2

Figure 5-13a shows the effect of scan rate in the range of 0.01-0.2 V/s on the voltammetric response of 240 µM ASP at the GCE/PVP-AgNPs/fMWCNTs/T1R2 electrode under optimum conditions. The oxidation peak current (I_{pa}) was proportional to the scan rate (v) as well as the square root of the scan rate (Figures 5-13b-c), with a linear regression coefficient of 0.9944, indicating the electrochemical process is diffusion controlled. A further confirmation was obtained from Figure 5-13d, showing the plot of the logarithm of I_{pa} versus the scan rate. A slope of 0.53, which is close to the theoretical value of 0.5, further confirms a diffusion-controlled reaction (Uwaya and Fayemi 2021b). Figure 5-13e shows a linear plot of anodic oxidation peak potential (E_{pa}) versus the log v with a regression coefficient of 0.9724. The transfer coefficient, α, was calculated as 0.46 using equation 5-4 (Gowda and Nandibewoor 2014a).

$$\mathrm{E_p - E_{\frac{p}{2}} = \frac{1.85RT}{\propto F} = \frac{47.7}{\alpha} mV} \qquad \text{Equation 5-4}$$

where $E_{p/2}$ is the potential at which the current is at half peak value. Subsequently, α was then applied to calculate the number of electrons as 1.28 (approximately 1), transferred in the electro-oxidation of ASP using equation 5-5.

$$\mathrm{E_p = \frac{2.3RT}{(1-\alpha)nF}} \qquad \text{Equation 5-5}$$

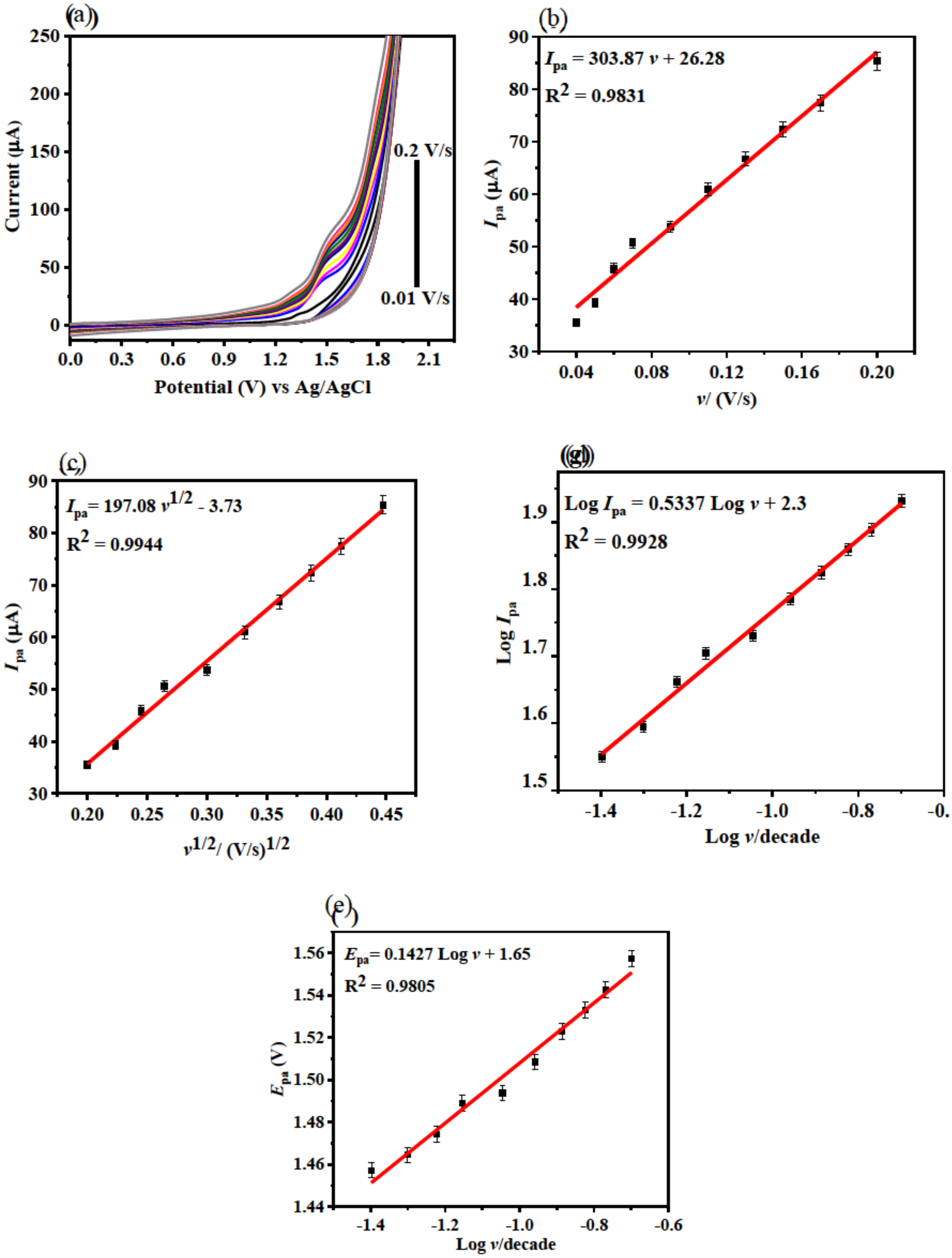

Figure 5-13: (a) Cyclic voltammograms in 240 µM ASP solution at various scan rate ranging from (0.01 – 0.2 V/s) on GCE/PVP-AgNPs/fMWCNTs electrode vs Ag/AgCl, linear plots of (b) I_p versus scan rate- v (c) I_p versus $v^{1/2}$, (d) Log I_p vs Log v, and (e) E_{pa} vs Log v.

5.1.1.6 Sensitivity of ASP on GCE/PVP-AgNPs/fMWCNTs/T1R2

(i) Analytical performance of GCE/PVP-AgNPs/fMWCNTs/T1R2 electrode

In order to determine the limit of detection (LOD) and the sensitivity of the electrochemical immunosensor (GCE/PVP-AgNPs/fMWCNTs/T1R2), different ASP concentrations were measured applying DPV within a potential window of 1 to 2 V. Figure 5-14a shows a decrease in ASP oxidation peak currents with increasing concentrations ranging from 2.89 to 27.61 µM, consistent with previous findings (Balgobind *et al.* 2016a). The results also show a gradual disappearance of the ASP oxidation peaks, which may be attributed to ASP saturation at the electrode. The limit of detection (LOD) and limit of quantification (LOQ) were computed as 0.40 and 1.34 µM, respectively, based on the calibration plots in Figure 5-14b, using equations 5-6 and 5-7.

$$\mathrm{LOD} = \frac{3\mathrm{Standard\ Deviation}}{\mathrm{Slope}} \qquad \text{Equation 5-6}$$

$$\mathrm{LOQ} = \frac{10\ \mathrm{Standard\ Deviation}}{\mathrm{Slope}} \qquad \text{Equation 5-7}$$

The obtained linear regression equation was I_{pa} (µA) = -10.87 [ASP] + 585.03, with a correlation coefficient of 0.9170. The calculated LODs of the developed sensor in comparison with the literature are presented in Table 5-4. Th limit of detection for this study is comparable to the previously designed methods which are sensitive for aspartame. The developed sensor showed improved LOD of 0.40 µM for aspartame than the previously designed method which employed electropolymerized molecular imprinted polymers with quartz crystal measurements, producing LOD of 31 µM (David *et al.* 2016). This study also shewed improved and comparable limits of detection of aspartame, with previous work by (Balgobind *et al.* 2016a), which is analogous in terms of materials used for modifying glassy carbon working electrode. The only sensitive electrochemical method for sensing aspartame in food beverages was developed by (Chen *et al.* 2021), which employed Palladium nanoparticles with single walled carbon nanotubes.

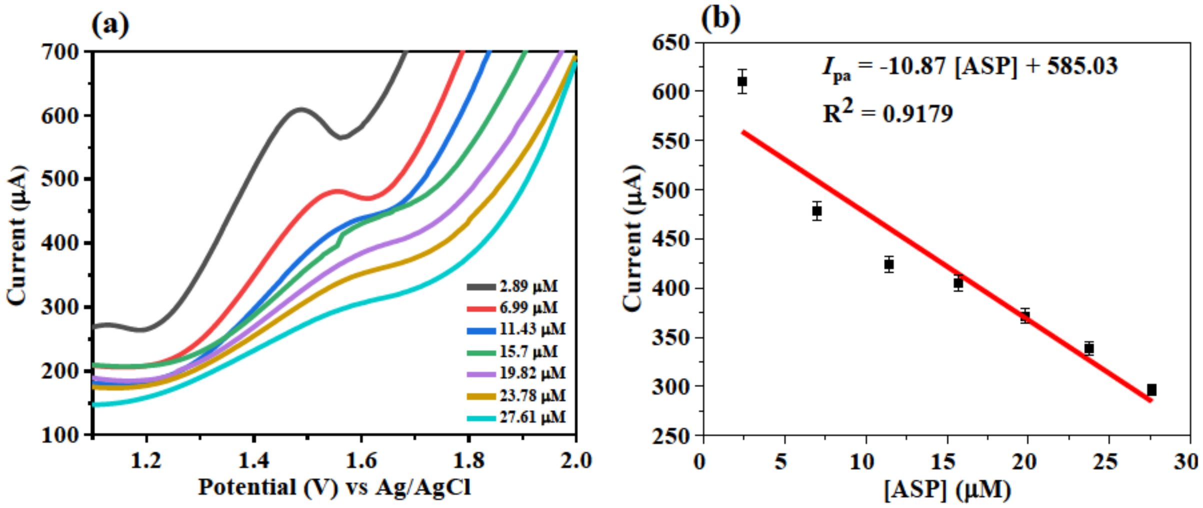

Figure 5-14: (a) GCE/PVP-AgNPs/fMWCNTs/T1R2 response to increasing ASP concentrations measured by DPV vs Ag/AgCl. (b) calibration plot of I_{pa} versus ASP concentrations (2.89 to 27.61 μM) in 0.1 M PBS pH 8.

Table 5-4: Comparison of the analytical performances of the designed immunosensor with the previously reported conventional techniques and sensors.

Electrode	Technique	Linear Ranges (μM)	LOD (μM)	LOQ (μM)	**Ref.**
Colloidal sphere-patterned polyterthiophene thin film	QCM[a]	12.5 - 200	31.75	105.84	(Tiu *et al.* 2016)
Post-column photochemical reactor	LC[b]	3.4 - 68	1.7	____	(Galletti and Bocchini 1996b)
BDDE	SWV[c]	5 - 40	0.467	5	(Medeiros *et al.* 2008b)
ZnONPs/MWCNTs/GCE	DPV[d]	12.00 - 24	3.68	12.25	(Balgobind *et al.* 2016a)
PdNPs/SWCNTs	CV[d]	1 - 120	0.001	____	(Chen *et al.* 2021)
GCE/PVP-AgNPs/fMWCNTs/T1R2	DPV[e]	2.89 - 27.61	0.401	1.34	This current work (Hloma, Uwaya and Bisetty 2022)

a: Quartz crystal microbalance (QCM), b: liquid chromatography (LC), c: Square-wave voltammetry (SWV), d: Cyclic voltammetry, e: Differential pulse voltammetry

(ii) Analytical Performance of the Designed Sensor of Aspartame Determination

The practicability of the designed immunosensor (GCE/PVP-AgNPs/fMWCNTs/T1R2) was examined in the prepared ASP containing sugar-free dietary samples (Coca-Cola, Lucozade Energy, and aQuelle sparkling-flavoured drinks) using DPV. A summary of the results obtained showing recoveries of ASP on each dietary sample is presented in Table 5-5 below. The developed sensor showed recoveries which ranged from 74% to 109.68% amongst the three food beverage samples analysed, with RSD values less than 2.38%, which is comparable with the recoveries shown in (Chen *et al.* 2021), ranging from 86.5% to 93.4% with acceptable RSD value lower 4.21%. The designed sensor maintains recoveries in the same approximation with GCE/ZnONPs/MWCNTs sensor designed by ranging from 83% to 98.0%.

Table 5-5: Analytical performance of GCE/PVP-AgNPs/fMWCNTs/T1R2 vs Ag/AgCl on sugar free

Sr.N	Added (µM)	Found (µM)	Recovery (%)	RSD (%)
Coca-Cola (No Sugar)				
1	19.82	19.49	98.34	1.02
2	31.72	26.83	84.59	1.67
Lucozade Energy drink				
1	2.38	1.78	74	2.01
2	6.99	7.11	101.69	1.56
aQuelle sparkling flavoured drink				
1	6.99	7.67	109.68	2.38
2	11.43	10.86	95	1.89

(iii) Repeatability, Reproducibility and Stability of GCE/PVP-AgNPs/fMWCNTs/T1R2

Figure 5-15a displays the results of six repetitive DPV scans in 240 µM ASP for the TIR2 nanocomposite modified electrode (GCE/PVP-AgNPs/fMWCNTs/T1R2). A relative standard deviation of 6.2% is acceptable for repeatability. In addition, reproducibility studies were also conducted on 5 different GCE/PVP-AgNPs/fMWCNTs/T1R2 electrodes (Figure 5-15b), using DPV in the same ASP concentration (240 µM). The RSD of 5.6% was estimated, indicating good reproducibility. The storage stability studies of GCE/PVP-AgNPs/fMWCNTs/T1R2 were carried out three times, for a total of 10 days. On the second measurement, a 11.76 % decrease in oxidation current was recorded, while a 38% decrease was recorded on the third measurement, the designed sensor is fairly stable concluding from the storage stability studies as presented in Figure 5-15c.

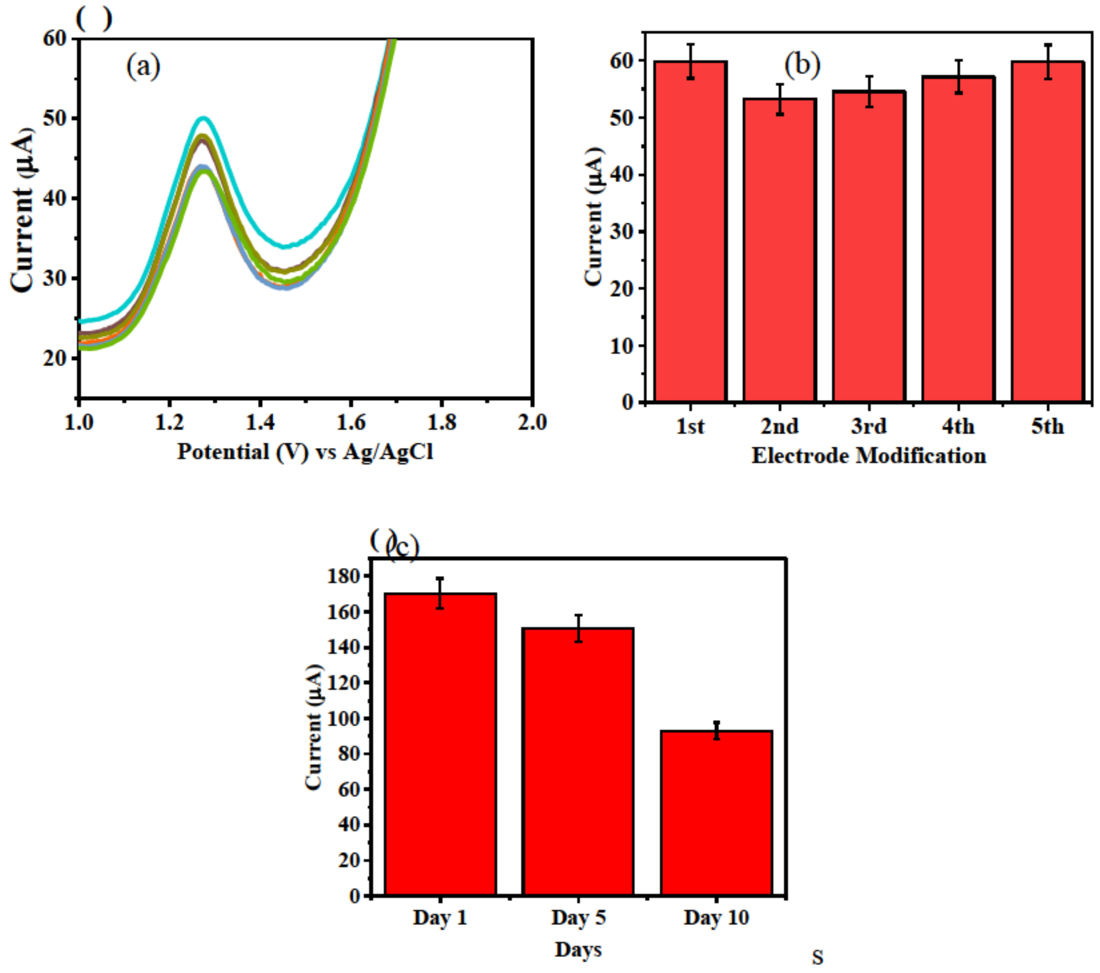

Figure 5-15: DPVs vs Ag/Ag/AgCl (a) repeatability, (b) reproducibility and (c) stability of GCE/PVP-AgNPs/fMWCNTs/T1R2 in pH 0.1 M PBS containing 240 µM aspartame.

(iv) Interferences Studies

The selectivity of the designed sensor to 240 µM ASP amidst possible interfering species (Acesulfame K, Ascorbic Acid, Rebaudioside A, and Saccharin) of the same concentration was examined. As shown in Table 5-6, possible interferents had no effect on the determination of ASP with RSD values of less than 5%, which indicates good precision of the method.

Table 5-6: Summary of the selectivity study of GCE/PVP-AgNPs/fMWCNTs/T1R2 vs Ag/AgCl towards 240 µM ASP 0.1M PBS, pH 8.

No.	Interference	Concentration (µM)	RSD[a] (%)	% Decrease in I_{pa} of aspartame
1	Acesulfame K	240 µM	2.88	8.22
2	Ascorbic acid	240 µM	2.36	2.21
3	Rebaudioside A	240 µM	2.56	6.26

5.1.2 Computational details

5.1.2.1 Molecular Docking

Molecular docking of ASP onto T1R2 was performed to investigate the ASP-T1R2 receptor interactions, as shown in Figures 5-16a-b. The best docked structure that characterizes the binding pocket of ASP and the amino acid residues involved with the T1R2 interaction is shown in Figures 5-16a. The stability of the ASP-T1R2 complex is established on closer inspection of the 2D interaction maps (Figure 5-16b). The major forces contributing to the stability of the complex are van der Waals interactions, where the amino acid residues surrounding ASP are Ala-166, Ser-144, Trp-304, Ala-305, Ile-327, Val-384, Glu-302, Thr-326, Arg-383, and Val-64. Also, the strong hydrogen bonding with Asp-142, together with the alkyl and pi-alkyl bonding (Ile-167 and Tyr-215), contributes to the stabilization of the T1R2-ASP complex. However, the amino acids indicated in red are classified as having unfavourable interactions, in accordance with those reported by (Patel and Narechania 2018).

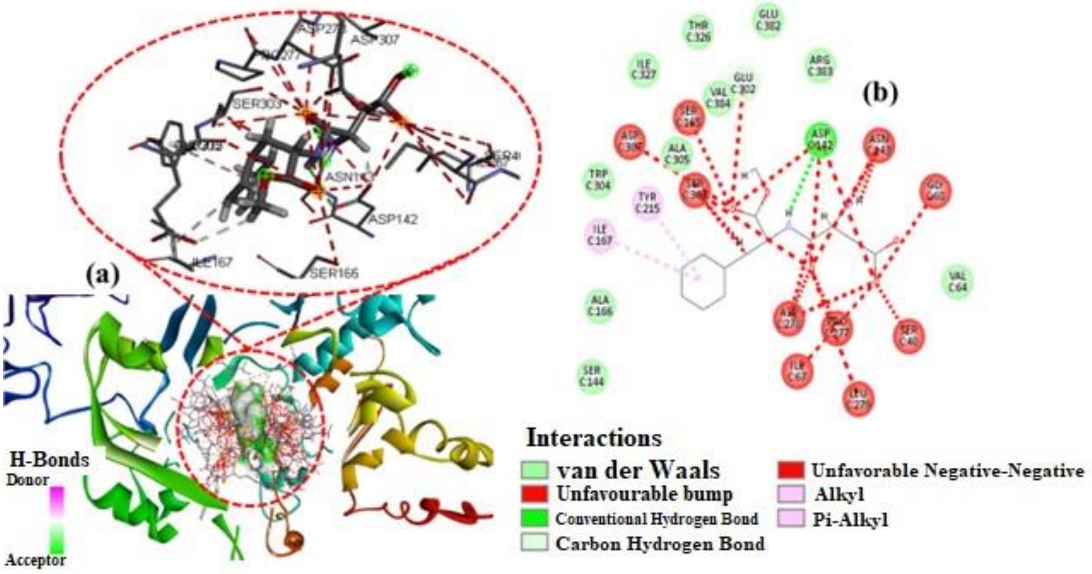

Figure 5-16: (a) Close-up view of the docked T1R2-ASP complex. (b) 2D plot showing amino acid residues involved in the bond formation with ASP molecule.

5.1.2.2 Density functional theory (DFT) Calculations

The frontier molecular orbital (FMO) approach provides insight into how the analyte of interest interacts with other species. Figure 5-17 shows the HOMO-LUMO of the free aspartame molecule. As can be seen in these maps, the HOMO level is delocalized over the CO-N-C and at the NH_2 positions with an unsymmetrical distribution of the orbitals. In contrast, the LUMO is uniformly distributed over the methyl-amino and phenyl propanoate positions in a symmetrical manner. Also, the calculated HOMO-LUMO energy gap (6.1 eV) is used to explain the charge transfer within the ASP molecule, affecting the chemical reactivity of the molecule (Sheikhi *et al.* 2018), summarized in Table 5-7. This finding indicates that the ASP molecule has active sites through which it can react with the electrode surface.

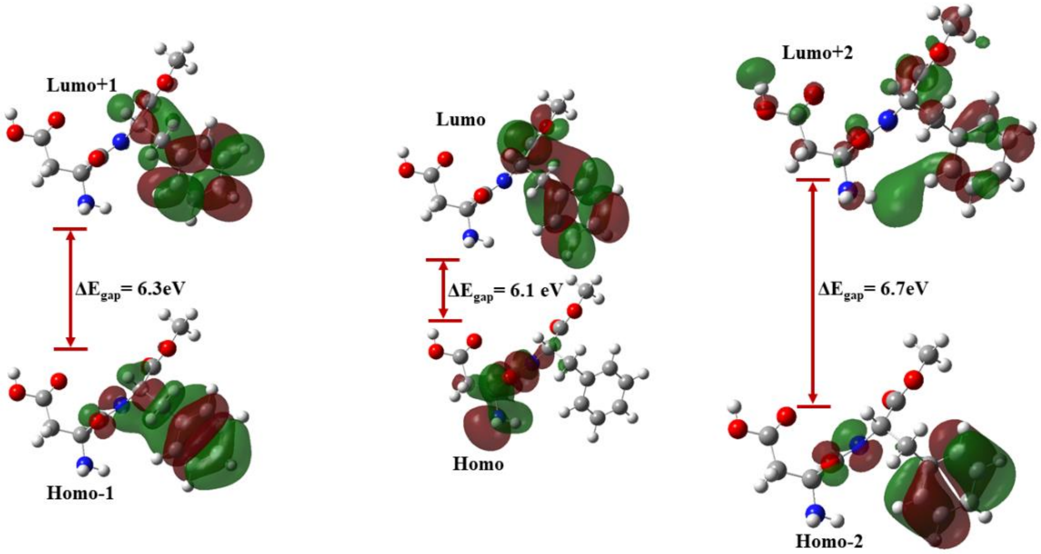

Figure 5-17: HOMO - LUMO, HOMO-1 - LUMO+1, and HOMO-2 – LUMO+2 plots for aspartame at B3LYP/6-31G** level.

Table 5-7: Summary of energy values for the lowest unoccupied molecular orbitals and the highest occupied molecular orbitals of aspartame.

Aspartame	E/ha	E/eV	ΔE_{gap}/eV
Lumo+2	-0.01628	-0.4430	-6.6962
Lumo+1	-0.02319	-0.6310	-6.3291
Lumo	-0.02741	-0.7459	-6.0455
Homo	-0.24958	-6.7914	-6.0455
Homo-1	-0.25578	-6.9601	-6.3291
Homo-2	-0.26236	-7.1392	-6.6962

5.1.2.3 Monte Carlo simulations and molecular dynamics

The MC adsorption energies presented in Figure 5-18 depict the relationship between the adsorption energy of the adsorbate-substrate system that mimics the experimental electrode layer-by-layer strategy implemented in this study. The more highly negative adsorption energy (-63722 kcal/mol) corresponds to greater interaction energies that characterize the stability of the adsorbate-substrate interactions, in accordance with our previous studies (Uwaya, Gumede and Bisetty 2021). Accordingly, the following trend in computed adsorption energies is observed: GCE/PVP-AgNPs > GCE/PVP-AgNPs/fMWCNTs > GCE/PVP-AgNPs/fMWCNTs/T1R2, demonstrating the increasing stability of the nanocomposite compared to individual nanomaterials used for the electrode modification steps. The stronger interaction is brought about by the presence of the carboxylic acid (-COOH) functionalized on the MWCNTs, providing a greater surface area for maximum interaction.

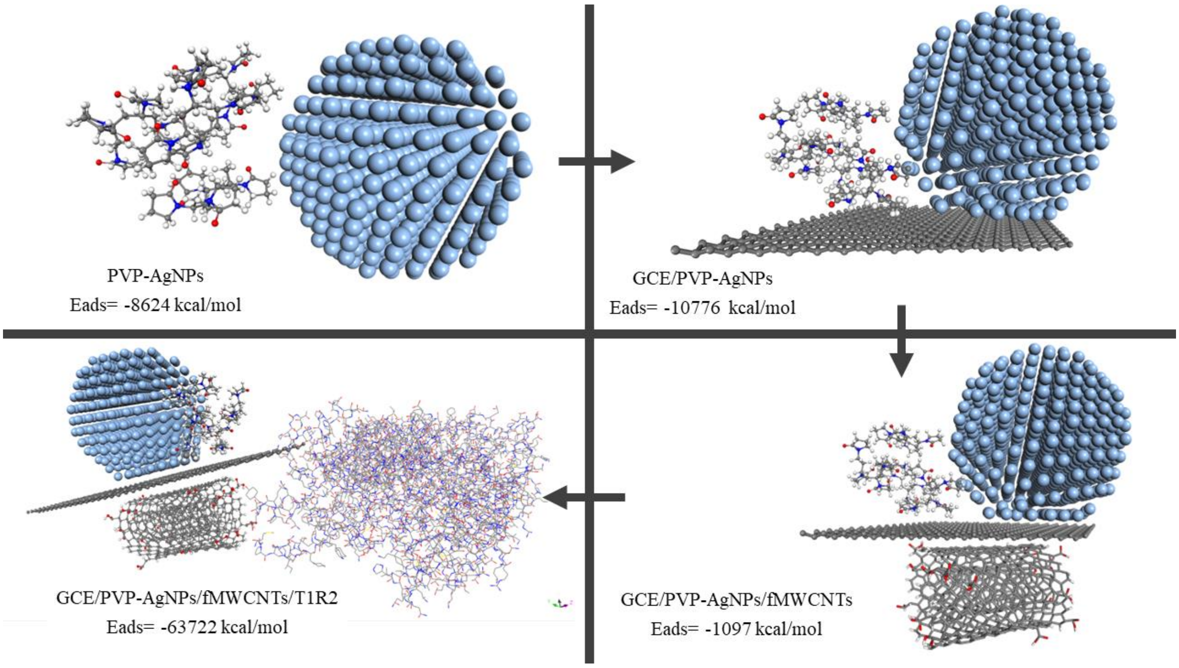

Figure 5-18: Monte Carlo simulations of the different electrodes for sensing aspartame.

5.1.2.4 MD Simulations

We then proceeded with MD simulations to compute the binding energies to assess how well the adsorbate-substrate interactions are in relation to the total energy of the system. The total energy (E_{tot}) is carefully taken into account while calculating the binding energy (E_b) of a layer-by-layer system, or within the substrate-adsorbate complex. The energy of all individual systems combined with the energy of interactions between substrates (E_s) and adsorbates (E_a) is known as E_{tot}. As a result, E_b is determined using the equation 5-8 given below.

$$\mathrm{Eb} = \mathrm{Etot} - \mathrm{Es} - \mathrm{Ea} \qquad \text{Equation 5-8}$$

The binding energies (E_b) were calculated and summarized in Table 5-8.

The following trend in E_b is observed: GCE/PVP-AgNPs/fMWCNTs/T1R2/Aspartame < GCE/PVP-AgNPs/fMWCNTs/T1R2 < GCE/PVP-AgNPs/fMWCNTs < GCE/PVP-AgNPs.

The negative binding energies confirm a greater stability of GCE/PVP-AgNPs/fMWCNTs/T1R2/Aspartame than the GCE/PVP-AgNPs/fMWCNTs/T1R2 electrode fabrication in each simulation. This is attributed to van der Waals energy as a major contributor to the complex formation, suggesting physisorption as evidence of the presence of aspartame on the electrode surface. Additionally, electrostatics and valence electrons were also considered to support the high negative binding energies.

Table 5-8: Calculated adsorption (Eads) and Binding energies (Eb) of the electrode modifications.

Electrode	E_{ads} energy (kcal/mol)	Eb energy (kcal/mol)
GCE/PVP-AgNPs/fMWCNTs/T1R2/ASP	-	-91753.395
GCE/PVP-AgNPs/fMWCNTs/T1R2	-63722	-24875.395
GCE/PVP-AgNPs/fMWCNTs	-1097	60485.335
GCE/PVP-AgNPs	-10776	84762.763

5.1.3 Significance of the Computational work

According to the computational results derived from DFT calculations, this study provides a better understanding of the oxidation of aspartame at pH 8 in phosphate buffer on GCE-PVP-AgNPs-fMWCNTs-T1R2. ASP has an energy band gap of -6.1 eV, which is a relatively low amount of energy required to transfer electrons from the highest occupied molecular orbital to the lowest unoccupied molecular orbital, rendering ASP to be an electroactive molecule associated with high chemical reactivity (Lephalala *et al.* 2020). A computational model was developed to effectively replicate the experimental layer-by-layer electrode for the detection of aspartame. In this section, we relate experimental analysis to Monte Carlo adsorption energies (Eads), considering the charge transfer resistance (R_{ct}) and the oxidation peak currents. In addition, the lowest adsorption energy value with the highest adsorbate-substrate interaction results in higher oxidation currents and less charge transfer resistance (Murti *et al.* 2018). The higher R_{ct} value (994380 kΩ) at the GCE/PVP-AgNPs electrode displayed a low oxidation current and a lower Eads (-10776 kcal/mol). The opposite was observed for the nanocomposite electrode, which was used throughout the study to detect ASP. The nanocomposite (GCE/PVP-AgNPs/fMWCNTs/T1R2) had the lowest R_{ct} value (2067.2 kΩ), because of the presence of carboxylic acid functionalized MWCNTs fused with PVP-AgNPs with high surface area and catalytic activity, which facilitated higher electron transfer, resulting in high oxidation currents. This result is further supported by the lower Eads (-10975 kcal/mol) in contrast to the higher Eads (-10776 kcal/mol) for the GCE/PVP-AgNPs nanocomposite. This finding was further corroborated by the lower binding energies computed using MD simulations.

5.1.4 Conclusion

In the first case study, a novel detection of ASP using GCE/PVP-AgNPs/fMWCNTs/T1R2 was described. A variety of complementary analytical measurement techniques, such as SEM, spICPMS, UV-Vis, TGA, etc were employed for the separation and characterization of PVP-AgNPs capped with PVP. The electro-oxidation of ASP was noticed by a well-defined oxidation peak potential at 1.4 V vs Ag/AgCl. The immunosensor sensor showed a linear dynamic range of 2.89–27.61 µM ($R^2 = 0.9170$) based on differential pulse voltammetry, with limits of detection and quantification (S/N = 3) of 0.40 and 1.34 µM, respectively. Supplementary studies carried out in silico included molecular docking of ASP into the T1R2 antibody, Monte Carlo simulations on the nanomaterials used for electrode modifications, and molecular dynamics simulations.

The results of these case studies may contribute to the development of an immunosensor that can potentially be used to quantify ASP in the food and beverage industry.

5.2 Case Study 2

Design of an immunosensor for the detection of Reb A in food beverages using nanocomposite modified glassy carbon electrodes:

The second case study deals with Rebaudioside A (Reb A), a non-nutritive sweetener often used in the food and beverage sectors. It was detected and quantified using an electrochemical immunosensor. Here, the results for the immunosensor developed by fabricating GCE with zeolitic imidazolate framework-67 (ZIF-67) in combination with fMWCNTs and the immobilization of the T1R2 receptor are presented. The qualitative and quantitative analysis of rebaudioside A was done using CV, EIS, and DPV utilizing a 5 mM [Fe $(CN)_6]^{3-/-4}$ redox probe. Computational analyses helped to support the experimental findings. Specifically, adsorption experiments were performed to better comprehend the mechanistic relationships between Reb A, the nanocomposite, and T1R2, employed in the modification of the GCE electrode.

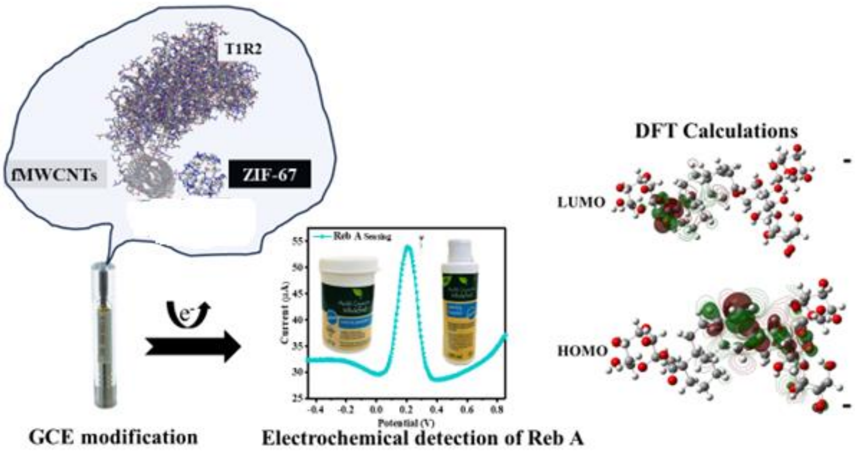

Scheme 5-3: Schematic diagram for the oxidation reaction mechanism of Reb A at GCE/ZIF-67/fMWCNTs/T1R2 electrode in 5 mM $[Fe(CN)_6]^{-3/-4}$.

5.2.1 Experimental

5.2.1.1 Characterization of ZIF-67 and fMWCNTs

(i) FTIR Studies

The FTIR spectra of ZIF-67, fMWCNTs and ZIF-67/fMWCNTs are represented by Figures 5-19a, b, and c, respectively. The FITR spectrum for ZIF-67 presented in Figure 5-19a shows a weak broad band at 3257 cm^{-1} assigned to N-H vibrations resulting from the 2-mthyl imidazole. The C=N bonds resulted in the stretching observed at 1714 cm^{-1} and 1505 cm^{-1}. The bond formed between the metal precursor and N (Co-N) produced the weak absorption band at 905 cm^{-1} (Rafiei *et al.* 2018; Archana *et al.* 2019). FTIR spectrum for fMWCNTs is presented in Figure 5-19b. The peaks observed at 3649 cm^{-1} and 1715 cm^{-1} are attributed to the stretching vibrations of the hydroxyl and carbonyl functional groups (-OH and C=O), respectively (Li *et al.* 2021a). The FTIR spectra for the MOF composite (fMWCNTs/ZIF-67) shown in Figure 5-19c consist of characteristic peaks observed in individual ZIF-67 and fMWCNTs. The decrease in intensity of the peaks, an appearance of 2914 cm^{-1} vibration, and a shift in the carbonyl peak to a higher wave number noticed in the MOF composite suggest a possible occurrence of interaction between ZIF-67 and fMWCNTs/ZIF-67.

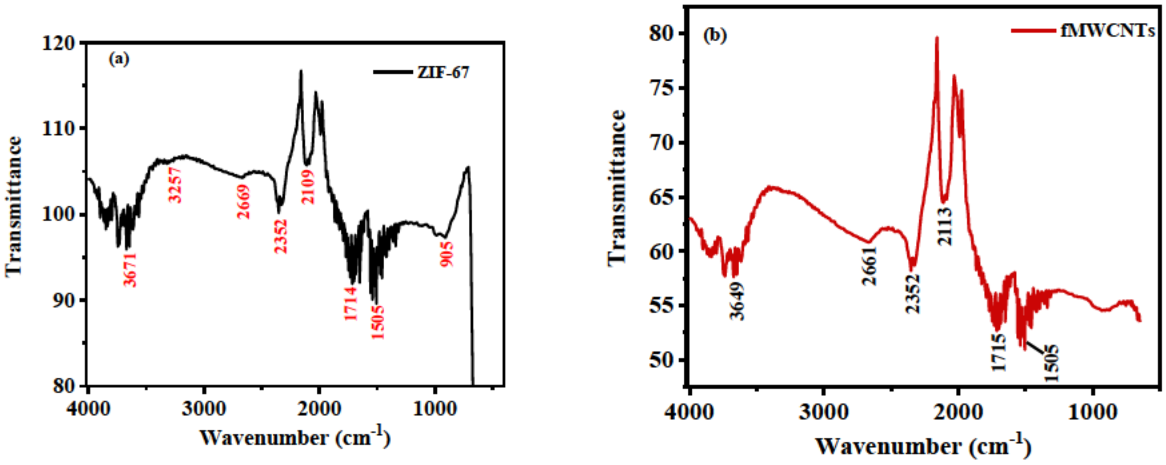

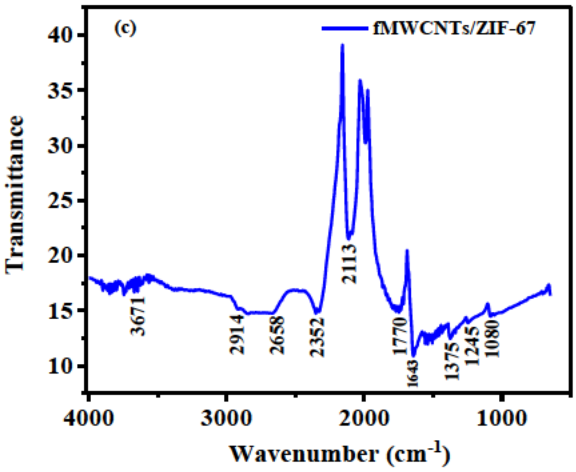

Figure 5-19: (a) FTIR spectra of the synthesized ZIF-67, (b) fMWCNTs, and (c) the nanocomposite ZIF-67/fMWCNTs.

(ii) EDS analysis

The EDS elemental analysis performed on the synthesized ZIF-67fMWCNTs, the ZIF-67/fMWCNTs (MOF composite), is displayed in Figure 5-20a-c. As revealed in Figure 5-20a, there is a high elemental abundance of Cobalt (65.33%), which was the precursor metal; evidently, the other elements present are carbon (3.53%) and oxygen (31.15%), respectively. The traces of Sulphur (<1%) present in both the (b) fMWCNTs and (c) ZIF-67/fMWCNTs could possibly be due to the use of oxidizing acids (HNO_3:H_2SO_4) for acid functionalization of MWCNTs (Hloma, Uwaya and Bisetty 2022). According to the literature, the sample holder and some components of the aqueous sample may have contributed to the aluminium (Al) emission present in fMWCNTs and ZIF-67/fMWCNTs spectrum (Hernández-Morales *et al.* 2019). There is a notable non-detection of nitrogen from the 2-methylimidazole organic linker used during the synthesis of ZIF-67; this happens when the sample has a high decomposition temperature, resulting in elemental analysis deducing low results for the element (Gazulla *et al.* 2013) (Figure 20a). Also, a decrease in the intensity of Co and an increased intensity of C are noticed in ZIF-67/fMWCNTs (Figure 5-20c). The results confirm the existence of interaction between ZIF-67 and fMWCNTs, suggesting successful synthesis of the ZIF-67/fMWCNTs composite (Figure 5-20c).

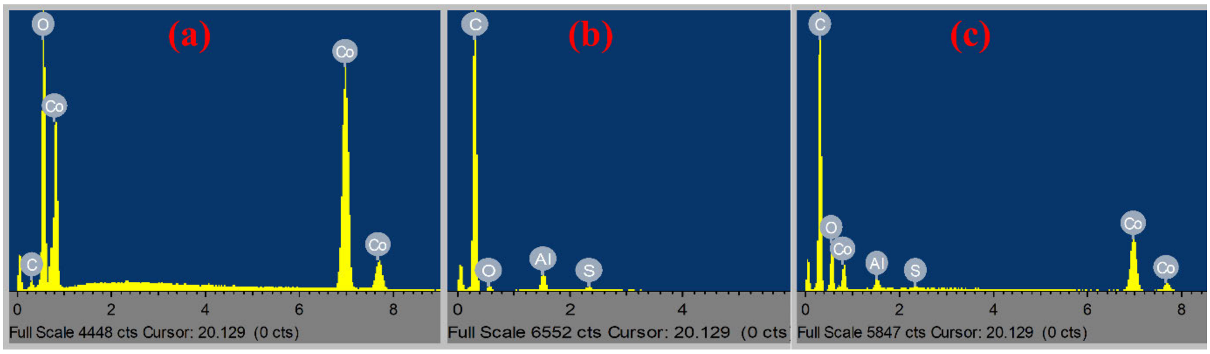

Figure 5-20: EDS elemental analysis of (a) ZIF-67, (b) fMWCNTs, and (c) ZIF-67/fMWCNTs nanocomposite

(iii) SEM studies

The SEM images at Figures 5-21a-c below represent morphology studies of the cobalt-based metal organic framework, with the SEM image showing the polyhedral and granular shape of ZIF-67 (Qian, Sun and Qin 2012; Guo *et al.* 2016) in Figure 5-21c, anchored on the surfaces of the conductive acid-functionalized multi-walled carbon nanotubes. The interaction between the fMWCNTs and ZIF-67 is confirmed in Figure 5-21c, as it is revealed that polyhedral ZIF-67 particles hosted (attached).

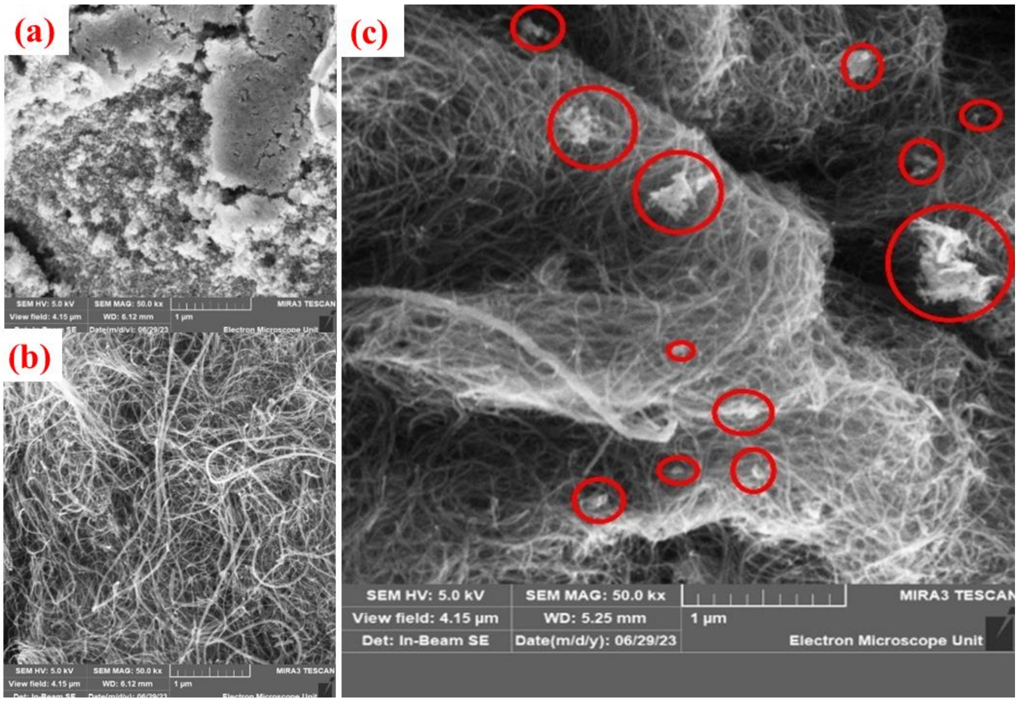

Figure 5-21: a) SEM image of the synthesized ZIF-67, (b) SEM image of fMWCNTs, and (c) SEM image of the nanocomposite ZIF-67/fMWCNTs.

(iv) TGA Studies

The thermal stability of ZIF-67, fMWCNTs, and fMWCNTs/ZIF-67 was studied via TGA in the presented thermograms below (Figures 5-22a, b, and c, respectively). In Figure 5-22a, the thermographic curve showed that the ZIF-67 is relatively thermally stable, exhibiting only 6% weight loss from 25 to 800 ℃. There is less than 1% of the physically adsorbed water as the remaining weight of the sample is 99% at 100 ℃. The ZIF-67 is reported to be thermally stable up to 350 ℃, as there is 3% weight loss observed from 350 to 600 ℃, which is attributed to the decomposition of organic constituents (Qian, Sun and Qin 2012; Shahsavari *et al.* 2022). The fMWCNTs in Figure 5-22b also showed thermal stability, exhibiting only one weight loss at elevated temperatures, with literature revealing that the combustion of MWCNTs is expected at 530 ℃ (Rather 2016). Figure 5-22c represents the thermal analysis of ZIF-67/fMWCNTs, with 80% weight loss at 100 ℃ due to the physically adsorbed water on the nanocomposite. The ZIF-67/fMWCNTs nanocomposite showed thermal stability from 100 to 600 ℃, where the sample underwent further % weight loss, with a fraction of 5% of the total sample left at 800 ℃.

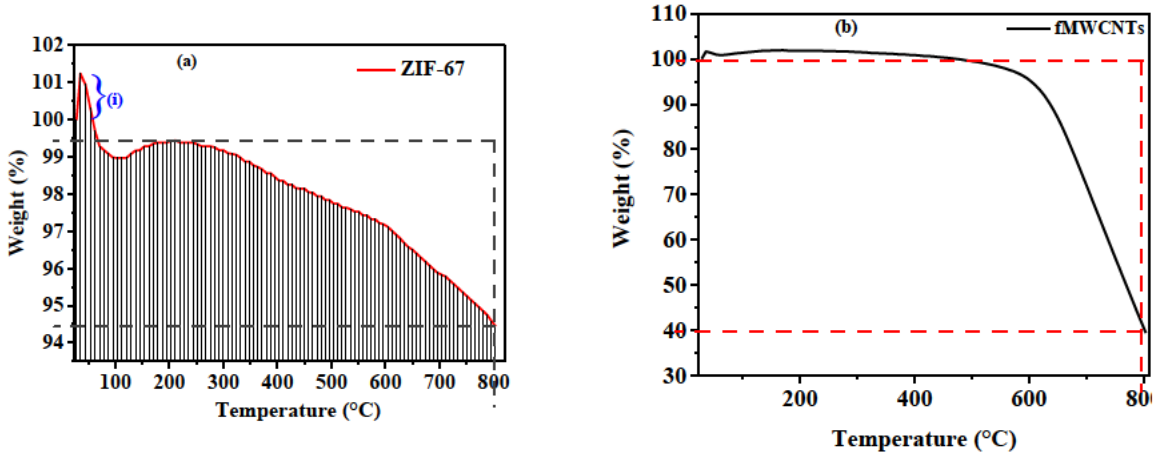

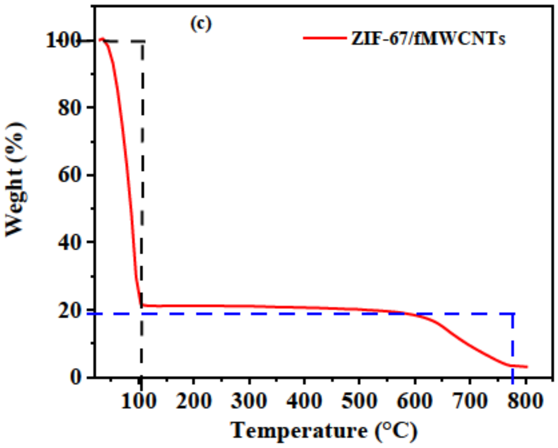

Figure 5-22: (a) TGA spectra of the synthesized ZIF-67, (b) fMWCNTs, and (c) the nanocomposite ZIF-67/fMWCNTs.

5.2.1.2 Electrochemical Characterization of electrodes

(i) Cyclic voltametric characterization of electrodes

A CV measurement was performed on a bare GCE, GCE/ZIF-67, GCE/fMWCNTs, GCE/ZIF-67/fMWCNTs, and GCE/ZIF-67/fMWCNTs/T1R2 in a 5 mM $[Fe(CN)_6]^{-3/-4}$ solution in order to investigate the electrochemical performance of the different electrodes. Figure 5-23a displays comparative CVs obtained at a scan rate of 0.025 V/s for the layer-by-layer electrodes. A well-defined redox peak is noticed at all the electrodes, with a greater current response at the T1R2 immobilized MOF composite modified electrode (GCE/ZIF-67/fMWCNTs/T1R2) compared to the rest of the electrodes studied. The observed amplified current could be attributed to increased active surface area and active transfer of electrons resulting from the presence of fMWCNTs and TIR2. The anodic current responses are as follows in descending order: GCE/ZIF-67/fMWCNTs/T1R2 (120 µA) > GCE/ZIF-67/fMWCNTs (96 µA) > GCE/fMWCNTs (74 µA) > GCE/ZIF-67 (28 µA) > GCE (23 µA).

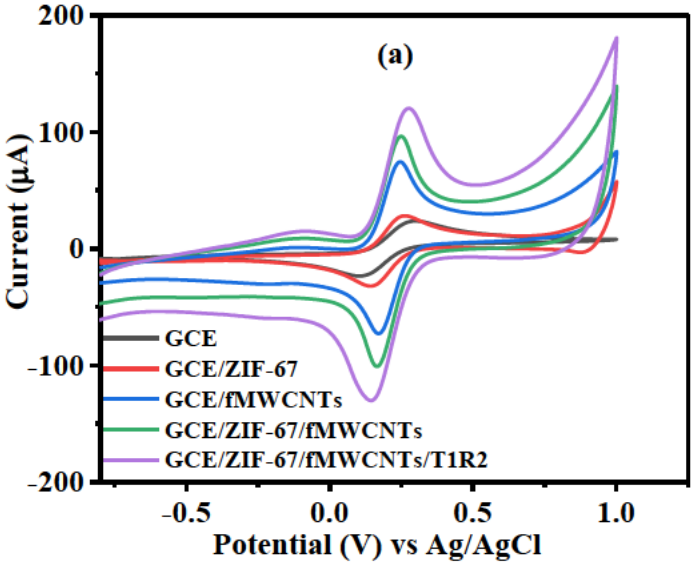

Figure 5-23: (a)Layer by layer electrochemical characterization of GCE/f-MWCNTs/ZIF-67/T1R2 vs Ag/AgCl in the presence of the redox probe.

(ii) Electrochemical impedance spectroscopic study of electrodes

In order to understand the mechanism of electron transfers occurring at the electrode-electrolyte interface in a 5 mM $[Fe (CN)_6]^{-3/-4}$ solution at a fixed potential of 0.2 V between frequencies of 100 kHz and 0.1 Hz, EIS was applied. Figure 5-24a displays the Nyquist plots for bare and modified electrodes. The kinetic region of charge transfer resistance is reflected on the semi-circle and the arc of the Nyquist plot, while the straight region of the semicircle corresponds to Warburg (the electrode diffusion pathway).

The Randle's circuit [R(Q[RW]) was used in fitting EIS data for GCE (Figure 5-24b) and [R(Q[RC])] for GCE/PVP-AgNPs, GCE/fMWCNTs and GCE/PVP-AgNPs/fMWCNTs, Figure 5-24c. The low charge transfer resistance (R_{ct}) in this study is related to the more conductive electrode with high oxidation and reduction current, which is the GCE/ZIF-67/fMWCNTs/T1R2 value. The introduction of fMWCNTs and TIR2 improved the electrocatalytic properties of ZIF-67 by lowering resistance to charge transfer. The high R_{ct} value in unmodified electrode is due to low current, the R_{ct} values are inversly proportional to the current response of the CV measurements, as summarized in Table 5-9.

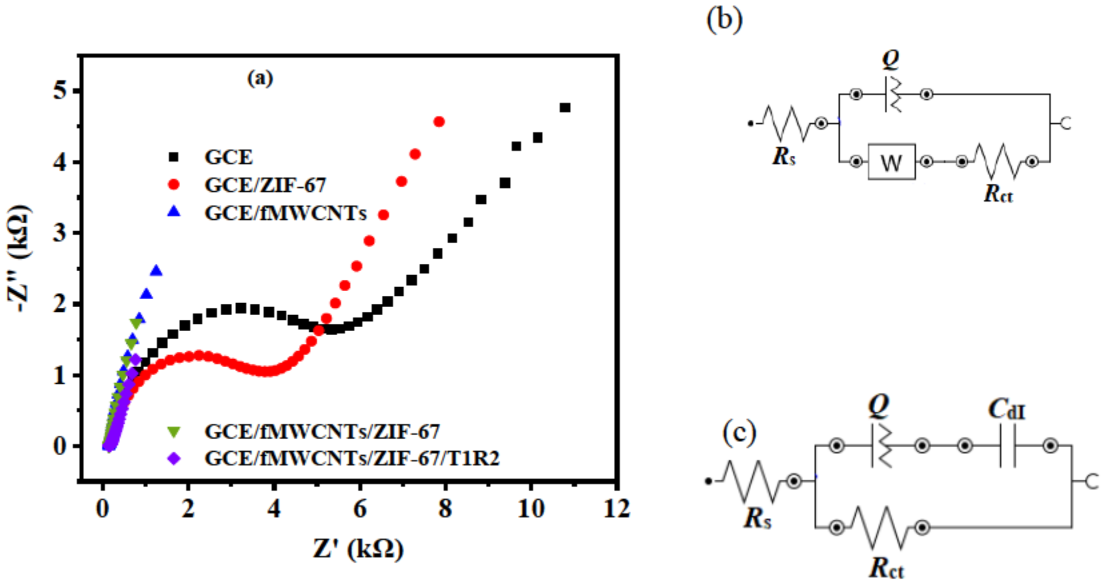

Figure 5-24: (a) Nyquist plots obtained for bare GCE and modified electrodes vs Ag/AgCl at a fixed 0.2 V potential. Equivalent circuits employed in fitting of EIS data (b) GCE and (c) GCE/ZIF-67, GCE/fMWCNTs, GCE/ZIF-67/fMWCNTs, and GCE/ZIF-67/fMWCNTs/T1R2.

Table 5-9: Summary of EIS data acquired from unmodified and modified electrodes vs Ag/AgCl in 5 mM $[Fe(CN)_6]^{-3/-4}$

Electrode	R_s(kΩ)	R_{ct} (kΩ)	X^2
GCE	110.56 (2.26)	18280 (1.358)	0.1182
GCE/ZIF-67	104.64(1.90)	14412.6 (2.648)	0.0255
GCE/fMWCNTs	102.9 (1.564)	13863 (8.560)	0.2657
GCE/fMWCNTs/ZIF-67	90.86 (1.875)	11852 .68(3.522)	0.0975
GCE/fMWCNTs/ZIF-67/T1R2	119.39 (1.635)	11251.2 (7.596)	0.09910

(iii) Scan rate variation

The effect of scan rates (0.04-0.2 Vs^{-1}) on the peak potentials and currents of $[Fe(CN)_6]^{-3/-4}$ solution at the GCE/ZIF-67/fMWCNTs/T1R2 electrode and the type of electrode reaction were investigated using CV (Figure 5-25a). A steady increase in both anodic and cathodic peak currents with increased scan rates was observed. Also, the anodic and cathodic peak potentials were observed to have shifted to more positive and negative, respectively, with the gradual increase in scan rates, indicating efficient mass transport between the electrodes, as shown in Figure 5-25b (Bojang and Wu 2020). Figure 5-25c shows that redox peak currents (oxidation; I_{pa} and reduction; I_{pc}) linearly depend on the square root of scan rate ($v^{1/2}$) with a regression coefficient (R^2) of 0.9998 for I_{pa} and 0.9999 for I_{pc}, designating that the electrode reaction is diffusion controlled (Uwaya, Wen and Bisetty 2022). The active surface area (0.9147 cm^2) was calculated using the Randle Sevcik equation (3.4).

The relationship between the logarithms of peak currents (log I_p) versus the logarithm of scan rate (log v), as evident in Figure 5-25d, yielded a linear regression coefficient of 0.9986 and 0.993 with a slope value < 1, confirming further a diffusion-controlled reaction.

The slopes obtained from the plots of peak potentials (oxidation; E_{pa} and reduction; E_{pa}) versus the logarithm of scan rate (Figure 5-25e) were used to calculate the coefficient of the electron transfer (α) and the number of electrons transferred (n) on the nanocomposite modified electrode. The number of electrons (n) and the coefficient of electron transfer (α) were calculated to be 0.63 ≈ 1 and 0.53, respectively. The value of α is closer to 0.5 for a perfectly diffusion-controlled reaction.

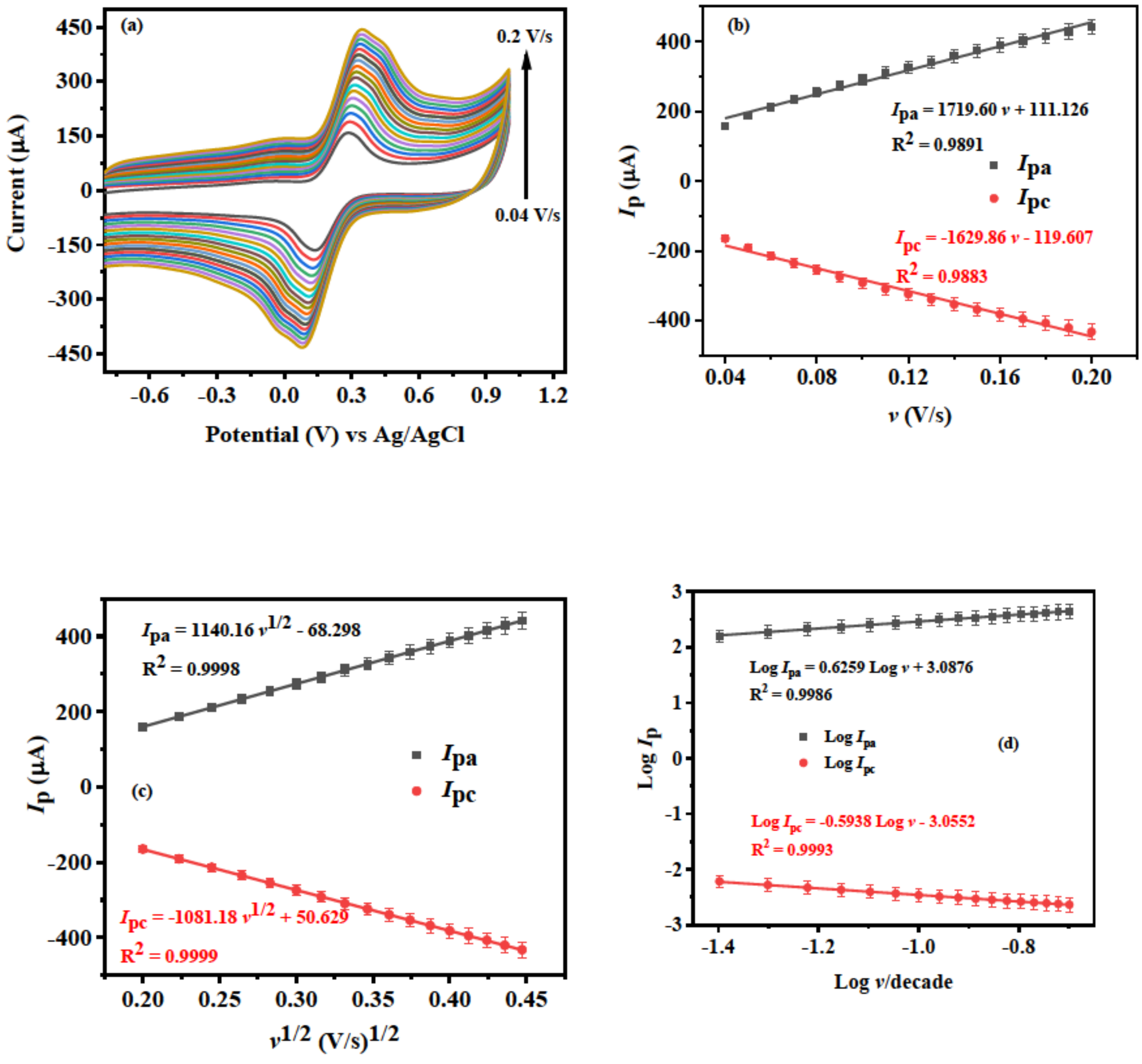

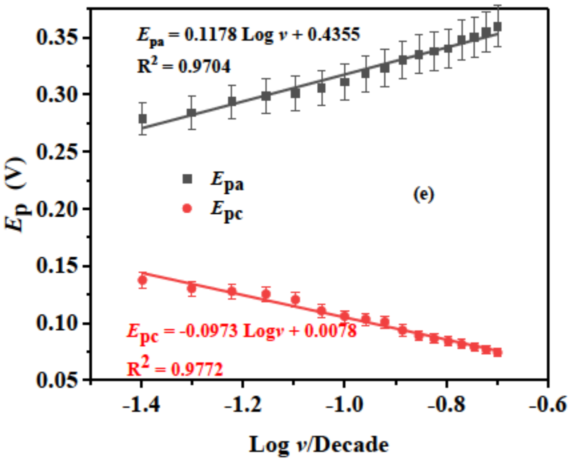

Figure 5-25: (a) GCE/ZIF-67/fMWCNTs vs Ag/AgCl in 5 mM $[Fe(CN)_6]^{-3/-4}$ solution prepared in pH 7 0.1 M Phosphate buffer (scan rate: 0.04-0.0.2V/s, inner to outer), (b) Anodic and cathodic peak currents as scan rate is varied, (c) linear plots of (c) anodic and cathodic peak currents versus square root of scan rates, (d) logarithms of currents, and (e) Peak potentials versus logarithms of scan rates.

5.2.1.3 Electrochemical behaviour of Reb A

(i) Cyclic voltammetric study of Reb A

The electrochemical behaviour of Reb A was determined via indirect sensing in a redox probe ($[Fe(CN)_6]^{-3/-4}$) prepared in pH 7 0.1 PBS buffer. Figure 5-26 shows the cyclic voltammetric responses of Reb A on the bare and modified (GCE, GCE/f-MWCNTs, GCE/ZIF-67, GCE/ZIF-67/fMWCNTs, and GCE/f-MWCNTs/ZIF-67/T1R2) electrodes in 5 mM $[Fe(CN)_6]^{-3/-4}$ at a 0.025 V/s scan rate. The observed well-defined redox peaks for all the electrodes could be due to the high electron transfer efficiency between the electrode surface and the $[Fe(CN)_6]^{-3/-4}$ in solution. The nanocomposite modified electrode displayed an optimal current response compared to the rest of the electrodes, indicating better electrocatalytic activity towards Reb A resulting from the increased active surface area and electrical conductivity of the nanocomposite. However, a decrease in anodic and cathodic peak currents was observed at the antibody-immobilized nanocomposite electrode, suggesting poor electron transport due to the blocking of the electrode surface (Kunene *et al.* 2021). The anodic current responses are as follows, in descending order: GCE/ZIF-67/fMWCNTs/T1R2(77.58 µA) > GCE/ZIF-67/fMWCNTs (71.38 µA) > GCE/fMWCNTs/ (47.61 µA) > GCE/ZIF-67/ (27.39 µA) > GCE/ (21.46 µA). results in the decrease of anodic peak current (I_{pa} =14.43 µA).

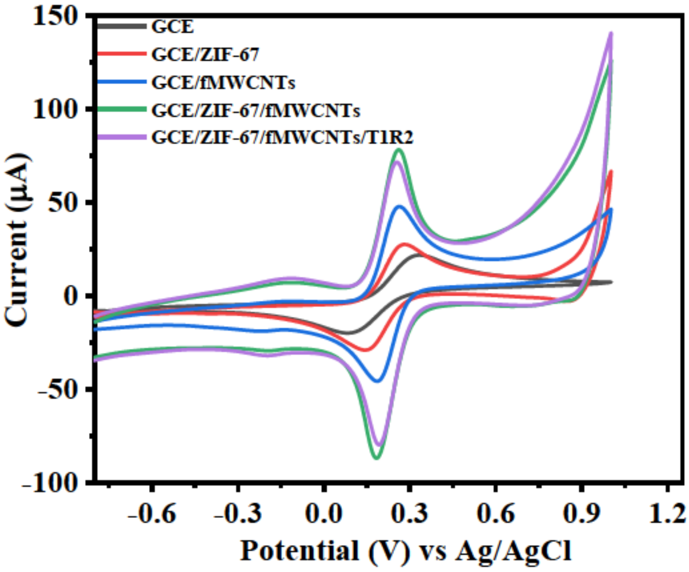

Figure 5-26 : (a) Unmodified and modified GCE electrochemical sensing of 0.3 mM Reb A in $[Fe(CN)_6]^{-3/-4}$) prepared in pH 7 0.1 PBS buffer in the presence of T1R2 antibody vs Ag/AgCl.

(ii) Electrochemical impedance spectroscopic study of Reb A

Information about the degree of charge transfer kinetics of Reb A at the surfaces of the electrodes (GCE, GCE/ZIF-67, GCE/fMWCNTs, GCE/ZIF-67/fMWCNTs, and GCE/ZIF-67/fMWCNTs/T1R2) was obtained using EIS. Figure 5-27a displays overlayed Nyquist plots from the EIS-fitted data obtained at the bare and modified electrodes in 5 mM $[Fe(CN)_6]^{-3/-4}$ in the presence of Reb A.

Figure 5-27b illustrates the Randles circuit used in fitting EIS data for GCE, GCE/ZIF-67, GCE/ZIF-67/fMWCNTs and GCE/ZIF-67/fMWCNTs/T1R2 with circuit descriptions of [R(Q[WR])]. The Numerical values of the circuit parameters are summarized in Table 5-10.

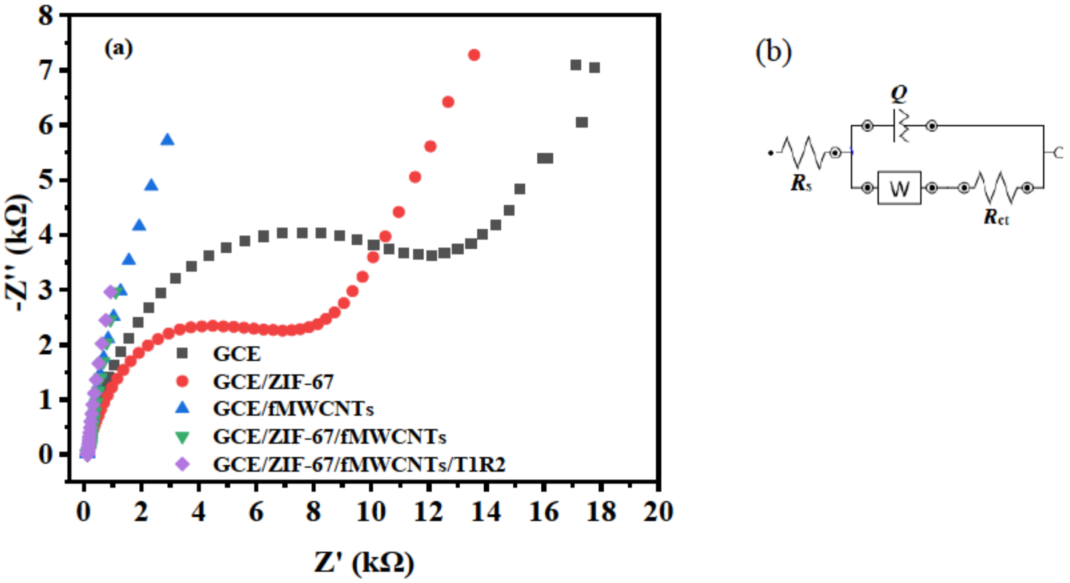

Figure 5-27: (a) Nyquist plots obtained for bare GCE, GCE/ZIF-67, GCE/f-MWCNTs, and GCE/f-MWCNTs/ZIF-67 electrodes vs Ag/AgCl at a fixed 0.2 V potential in 5mM [Fe(CN)6]$^{-3/-4}$, and (c) Illustrates circuits used in fitting EIS data for GCE, GCE/ZIF-67, GCE/ZIF-67/fMWCNTs/T1R2

Table 5-10: Summary of EIS data acquired from 0.3 mM of Reb A in 5mM [Fe(CN)$_6$]$^{-3/-4}$ vs Ag/AgCl.

Electrode	R_s**(kΩ)**	R_{ct} **(kΩ)**	X^2
GCE	107.18 (1.89)	11140 (2.002)	0.12553
GCE/ZIF-67	104.73 (1.768)	6257.9 (4.027)	0.084385
GCE/fMWCNTs	118.5 (1.490)	17407 (14783)	0.30586
GCE/fMWCNTs/ZIF-67	117.72 (1.411)	13816 (11.703)	0.089725
GCE/fMWCNTs/ZIF-67/T1R2	119.39 (1.229)	12867 (11.124)	0.099953

(iii) Scan rate variation

The type of electrochemical reaction at the electrode and the kinetics of electro-oxidation of 0.3 mM Reb A on the GCE/ZIF-67/fMWCNTs/T1R2 sensor was investigated using CV with scan rate variations ranging from 0.03-0.20 V/s, as shown in Figure 5-28a. A direct proportionality between the anodic and cathodic peak currents (I_{pa} and I_{pc}) and scan rate (v) was noticed as presented in Figure 5-28b. The plot inferred a diffusion-controlled electrode reaction due to the linear increase in I_{pa} and I_{pc} versus the square root of scan rate ($v^{1/2}$), with the regression coefficient (R^2) of 0.9974 and 0.9988 for I_{pa} and $I_{pc,}$ respectively, as in Figure 5-28c (Uwaya and Fayemi 2021b). The diffusion-controlled electrode process was further proved by the slopes of 0.7751 and -0.7755 for the linear relation between log I_p and log v (Figure 5-28d). The slope values were < 1, with a regression coefficient of 0.9893 and 0.9980 for log I_{pa} and I_{pc}.

The plot of anodic and cathodic peak potentials (E_{pa} and E_{pc}) versus the natural logarithm of scan rate (v) was a straight line with a regression coefficient of 0.9545 and 0.9689 and a slope of 0.0903 as shown in Figure 5-28e. The number of electrons (n) and the coefficient of electron transfer (α) were calculated to be $0.51 \approx 1$ and 0.39, respectively. The value of α is closer to 0.5 for a perfectly diffusion-controlled reaction.

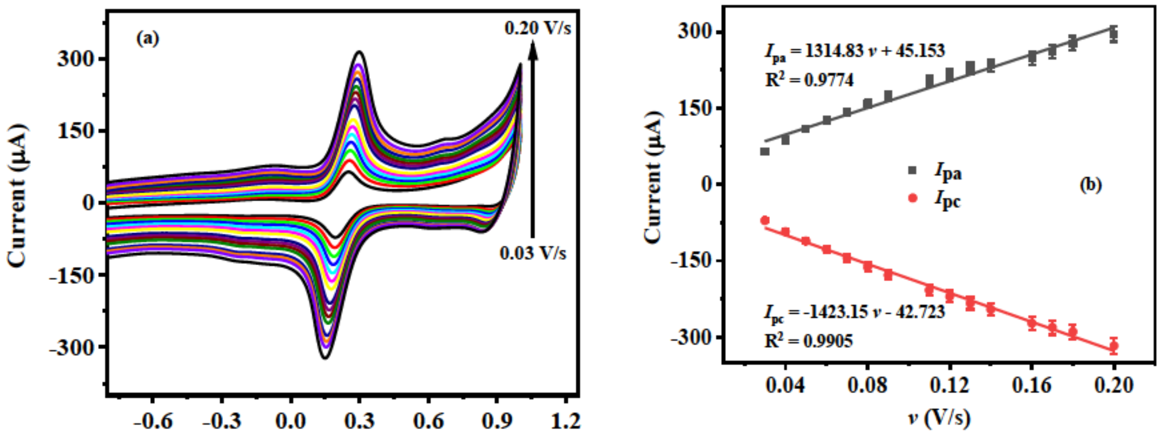

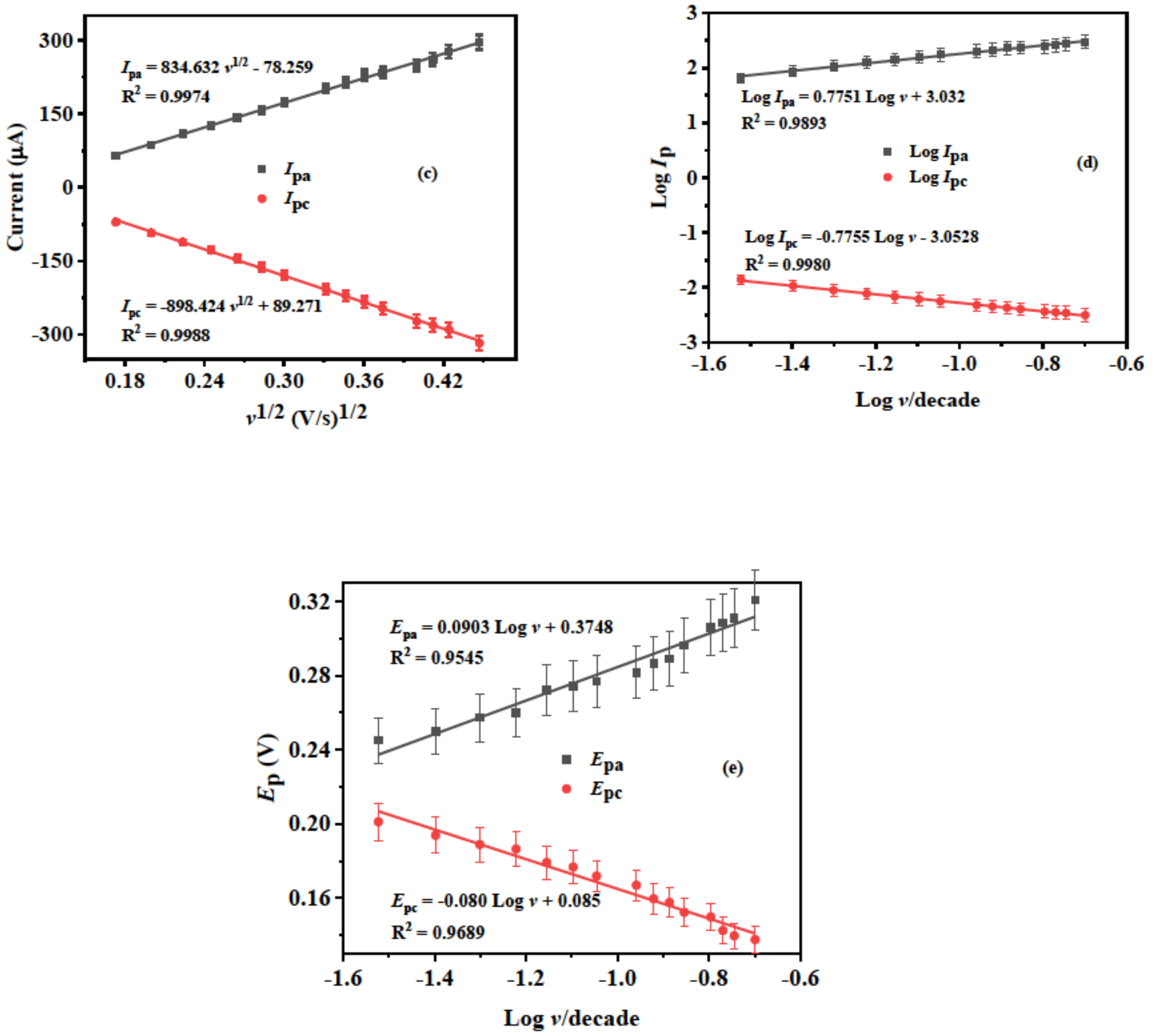

Figure 5-28: (a) GCE/ZIF-67/f-MWCNTs in 5 mM $K_3[Fe(CN)_6]$ solution prepared in pH 7 0.1 M PBS containing 0.3 mM Reb A (scan rate: 0.03-0.20 V/s, inner to outer),linear plots of (b) anodic and cathodic currents vs scan rates, (c) anodic and cathodic peak currents versus square root scan rate, (d) log of current vs log of scan rate, and (e) anodic and cathodic potentials versus logarithms of scan rates

5.2.1.4 Electrochemical behaviour of Reb A on GCE/ZIF-67/fMWCNTs/T1R2

(i) Linear Dynamic Range

DPV was used to determine the linear concentration range, detection limit, and sensitivity of Reb A on GCE/ZIF-67/fMWCNTs/T1R2 within a potential window of -0.35 V to 0.75 V. Figure 5-29a demonstrates an increase in oxidation peak currents as Reb A concentrations were increased from 0.9901 µM to 8.2569 µM, which is consistent with previous findings reported by (Bathinapatla *et al.* 2016). The result also shows a gradual appearance of the Reb A effect on the oxidation peaks at 0.2 V, which could be ascribed to the accumulation of Reb A at the surface of the working electrode, GCE/ZIF-67/fMWCNTs/T1R2, in the presence of the redox probe. The limit of detection (LOD) and quantification (LOQ) were computed to be 1.10 µM and 3.33 µM, respectively, by applying the formula; LOD = $\frac{3.3S}{m}$ and LOQ = $\frac{10S}{m}$ where s represents the standard deviation of the intercept of the y-coordinates from the line of the best fit of the calibration plot. Figure 5-29b and *m* represent the gradient of the same line. The obtained quadratic regression equation was I_{pa} = -0.944 [Reb A]^2 + 13.689 [Reb A] + 14.066, with a correlation coefficient value of 0.9753 (Naidoo *et al.* 2023). The method we relied on this study consisted of Pt/AuNPs-GO/MWCNTs/Cyt c, which is more sensitive than the current study, reporting an LOD of 0.264 µM (Bathinapatla *et al.* 2016), whereas the second report for detecting Reb A did not specify the limits of detection (Woelwer-Rieck *et al.* 2010a).

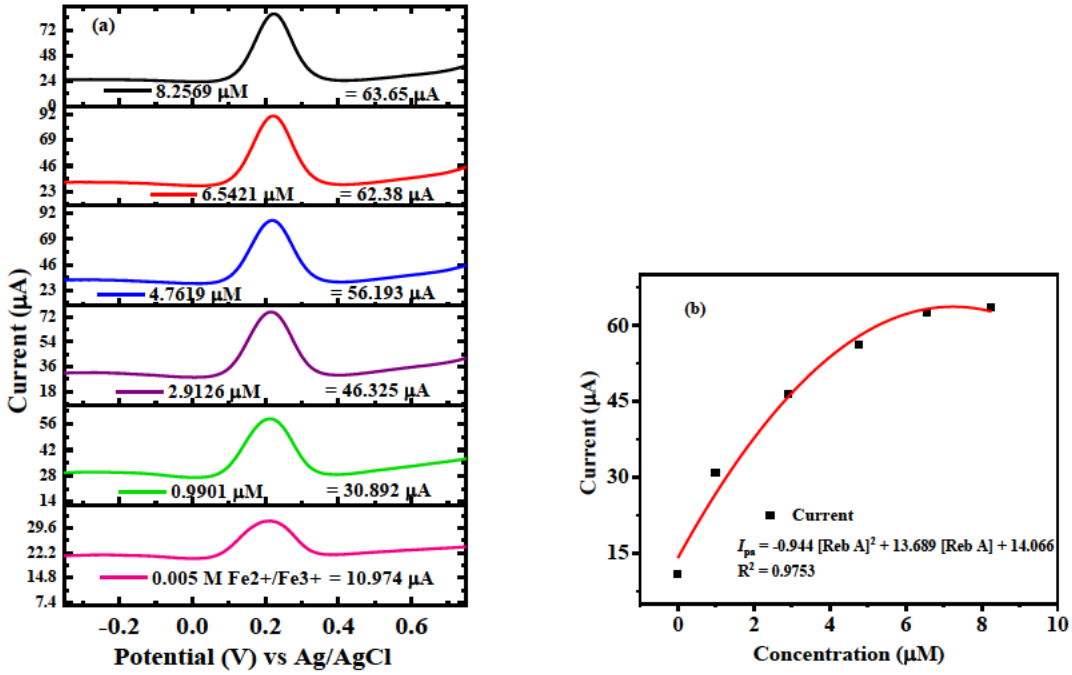

Figure 5-29: (a) Electrochemical DPV responses of Reb A with the quadratic calibration plot of GCE/ZIF-67/fMWCNTs/T1R2 vs Ag/AgCl at various concentrations (0.9901 µM to 8.2569 µM) in 5 mM $[Fe(CN)_6]^{-3/-4}$.

Table 5-11: Comparison of the analytical performances of the previously reported conventional techniques and modified nanostructured for Reb A detection.

Electrode/Column	Technique	Linear Ranges	LOD & LOQ	Ref.
Develosil 250 mm x 4.6 m and Luna HILIC 150 mm x 4.6 mm.	HPLC	25 mg/L to 500 mg/L	1.07 mg/L and 3.56 mg/L	(Lorenzo *et al.* 2014)
Luna HILIC analytical column with a mobile phase consisting of acetonitrile/ water (85:15 v/v)	SPE HPLC	Not reported	LOD and LOQ not reported-	(Woelwer-Rieck *et al.* 2010b)
Pt/AuNPs-GO/MWCNTs/Cyt c	DPV	0.075 µ–1.25 µM	0.264 µM and 0.752 µM	(Bathinapatla *et al.* 2016)
GCE/ZIF-67/fMWCNTs/T1R2	DPV^{e}	0.9901 µM to 8.2569 µM	1.10 µM and 3.33 µM	This current work

HPLC: High-performance liquid chromatography, SPE HPLC: Solid-phase extraction HPLC SWV Square-wave voltammetry, CV: Cyclic voltammetry, DPV: Differential pulse voltammetry.

(ii) Repeatability, Reproducibility, Stability and Storage stability of GCE/ZIF-67/fMWCNTs/T1R2/Reb A

The repeatability of the TIR2 MOF composite modified electrode was determined by 8 repetitive DPV scans in 5 mM $[Fe(CN)_6]^{-3/-4}$ containing 0.3 mM REB A, as displayed in Figure 5-30a. The electrode (GCE/ZIF-67/fMWCNTs/T1R2) measurements are relatively repeatable as there was 3% RSD. Reproducibility studies of GCE/ZIF-67/fMWCNTs/T1R2 were conducted using 5 different electrodes for the 5 repetitive measurements, and the RSD for repetitive measurements was calculated to be 4.26%, indicating acceptable reproducibility as shown in Figure 5-30b. Figure 5-30c demonstrates the stability of GCE/ZIF-67/fMWCNTs/T1R2 through 25 runs of cyclic voltammograms. The relatively small decrease in anodic and cathodic current indicates how stable the electrode is. Figure 5-30d reveals the storage stability of GCE/ZIF-67/fMWCNTs/T1R2. After a 10-day period, there was a 20.34% reduction in peak height measured on the second measurement (day 5), while a 36.66% reduction was recorded on the third measurement (day 10). The decrease in current observed with each successive measurement is due to the degradation of ZIF-67/fMWCNTs nanocomposite, leading to less conductivity (Gvozdenović *et al.* 2014).

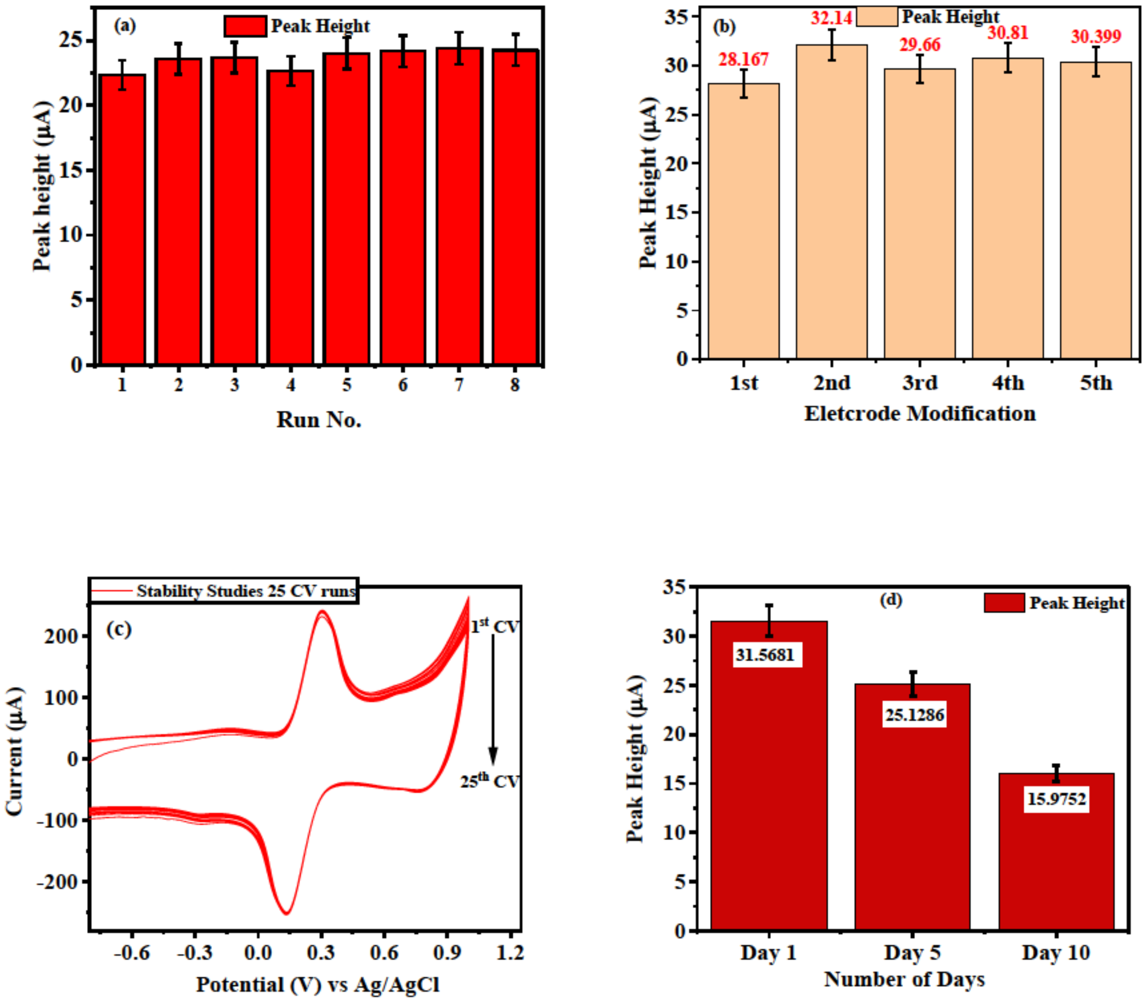

Figure 5-30: DPVs (a) repeatability and (b) reproducibility, and (c) stability of GCE/ZIF-67/fMWCNTs/T1R2 vs Ag/AgCl in 5 mM $[Fe(CN)_6]^{-3/-4}$ containing 5.88 mM Reb A (d) Storage stability of

(iii) Interferences Studies

Reb A is often not used individually as a sweetener; the sweetness is intensified by combining or coupling it with other sweeteners such acesulfame K, saccharin, Rebaudioside A etc. Selectivity of the electrode was determined in the presence of possible interfering species, including acesulfame K, ascorbic Acid, Rebaudioside A and saccharin, using DPV.

The selectivity studies of the developed sensor (GCE/ZIF-67/fMWCNTs/T1R2) were carried out by simultaneous analysis of the 0.3 mM standard of the possible interfering species (acesulfame K, aspartame, rebaudioside A, xylitol, and saccharin) in the presence of 0.3 mM Reb A in a 5 mM $[Fe(CN)_6]^{-3/-4}$ solution. The results are summarized in Table 5-12 below, showing the % decrease or increase in anodic peak current in the presence of other sweeteners. The same trend about interfering species on Reb A determination is observed in (Bathinapatla *et al.* 2016), which result in increase or decrease in oxidation current in the presence of interference species, the only limitation in comparing the two studies is that the interference species used are not identical. The increase/decrease in *I*pa in the indirect peak of the redox probe is brought about by different factors, one being that with each interference species studied, a different modified electrode is used. The method is deemed sensitive in the presence of these interference species due to low RSD values, less than 3.60%.

Table 5-12: shows the effects of the interfering species (Xylitol, acesulfame K, aspartame, and saccharin) on the determination of Reb A in the presence of the redox probe solution.

No.	Interference	Concentration (mM)	RSD^a (%)	% ↑ or ↓ in I_{pa} of Reb A
1	Acesulfame K	0.3 mM	1,36	4.68↓
2	Aspartame	0.3 mM	1,48	8.66↓
3	Rebaudioside A	0.3 mM	2,21	
4	Xylitol	0.3 mM	1,53	4.47↑
5	Saccharin	0.3 mM	3,60	1.40↓
6	Acesulfame K, Aspartame, Reb A, Xylitol, and Saccharin	0.3mM	2.33	9.84↑

(iv) Analytical Performance of the Designed Sensor of Reb A Determination

The analytical feasibility and performance of the designed sensor (GCE/ZIF-67/fMWCNTs/T1R2) for the accurate detection of Reb A in the prepared sugar-free Coca-Cola sample were investigated by DPV following the standard addition method. 200 µL of the diluted sample was transferred into an electrolytic cell, containing 10 mL of 5 mM $[Fe(CN)_6]^-$

$^{3/-4}$, spiked with known concentrations of Reb A, and analysed in triplicate as shown in Table 5-13.

Table 5-13: Analytical performance of GCE/ZIF-67/fMWCNTs/T1R2 vs Ag/AgCl on real sample (liquid and solid) supplements at pH 8 0.1 M PBS buffer

Sr.N	Added (µM)	Found (µM)	Recovery (%)	RSD (%)
Real sample liquid supplement (Reb A)				
1	2.9126	3.0663	105.28	6.53
2	4.7619	5.4275	113.98	3.65
3	6.4521	6.9013	105.49	2.02
Real sample solid supplement (Reb A)				
1	2.9126	3.1049	106.60	7.82
2	4.7619	4.4357	93.15	3.64
3	6.4521	6.8328	105.90	2.71

5.2.2 Computational chemistry results and discussion

5.2.2.1 Molecular docking with PatchDock

As seen in Figures 5-31a-c, molecular docking was used to study the interactions between the Reb A and T1R2 receptors. Figure 5-31a provides a close-up image of the best docked structure, which describes Reb A's binding pocket and the amino acid residues implicated in the T1R2 interaction. A deeper look at the 2D interaction maps in Figure 5-31c reveals that the Reb A-T1R2 complex is stable. Van der Waals interactions are one of the main factors in the stability of the complex, and the amino acid residues around Reb A that participate in these interactions are valine (VAL), proline (PRO), cysteine (CYS), leucine (LEU), arginine (ARG), threonine (THR), serine (SER), lysine (LYS), and histidine (HIS). The types of interactions deduced from the docked structure between the receptor and the ligand are unfavourable donor-donor interactions, conventional hydrogen bonds, carbon hydrogen bonds, pi-lone pair interactions, and alkyl interactions (Patel and Narechania 2018).

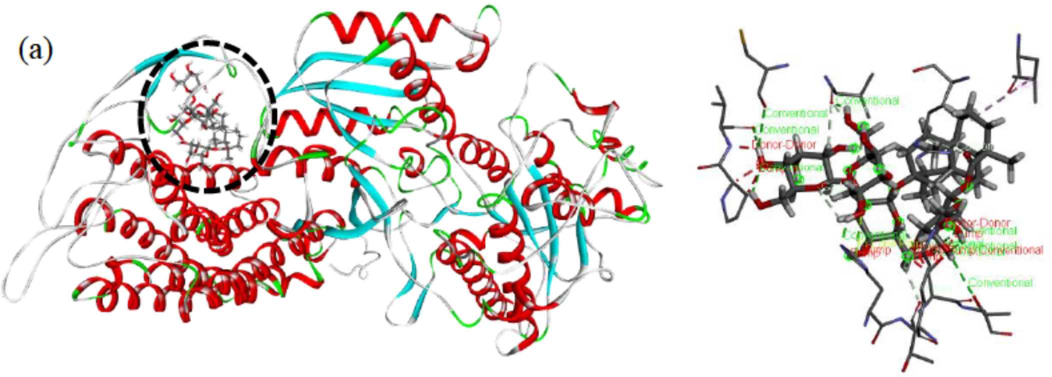

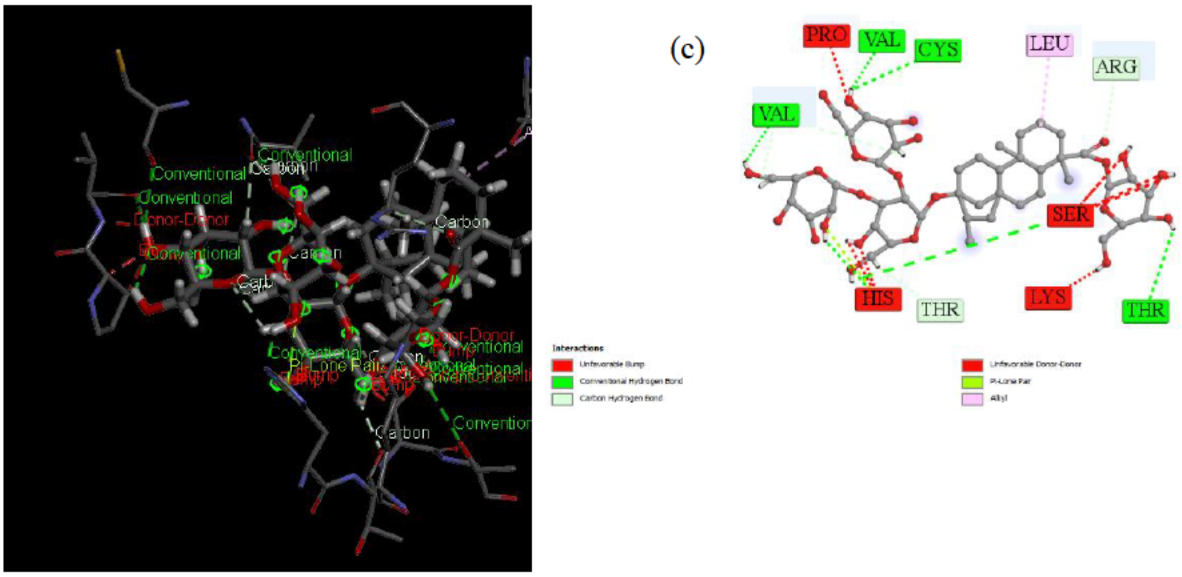

Figure 5-31: (a)A close-up view of molecular docking of T1R2 and Reb A complex, (b) Ligand (Reb A) with possible interactions with receptor (T1R2), and (c) shows 2D types of unfavourable and favourable interactions between Reb A and the amino acids of the receptor

5.2.2.2 Molecular docking with PyRx

The additional molecular docking information was obtained using the PyRx application between the receptor-ligand (T1R2-Reb A) complex. Figure 5-32a-d below shows 4 favourable docked configurations with binding affinities between T1R2 in the CPK model while the ligand is represented in the ball and stick model, with Figure 5-32a being the most favourable docked configuration with a binding affinity of -10.9 kcal/mol, followed by Figure 5-32b as the second favourable configuration with a binding affinity of -10.6 kcal/mol, followed by Figure 5-32c, at -.9.3 kcal/mol binding affinity, and Figure 5-32d at -8 kcal/mol binding affinity. The PyRx application was employed in this study to predict the interactions between T1R2 and Reb A in terms of binding affinities and RMSD values, as summarized in Table 5-13 (Mohamed Nageib *et al.* 2023). Root-mean-square-distance (RMSD) is a quantitative tool utilized to compare the similarities between two structures by calculating the distances between n pairs of atoms in two structures, in this case between the receptor T1R2 and ligand Reb A. As evident in Table 5-14, for the most favourable docked configuration, the RMSD value is zero, and the RMSD value increases as the docking configuration is unfavourable (Yadav and Chowdhury 2022).

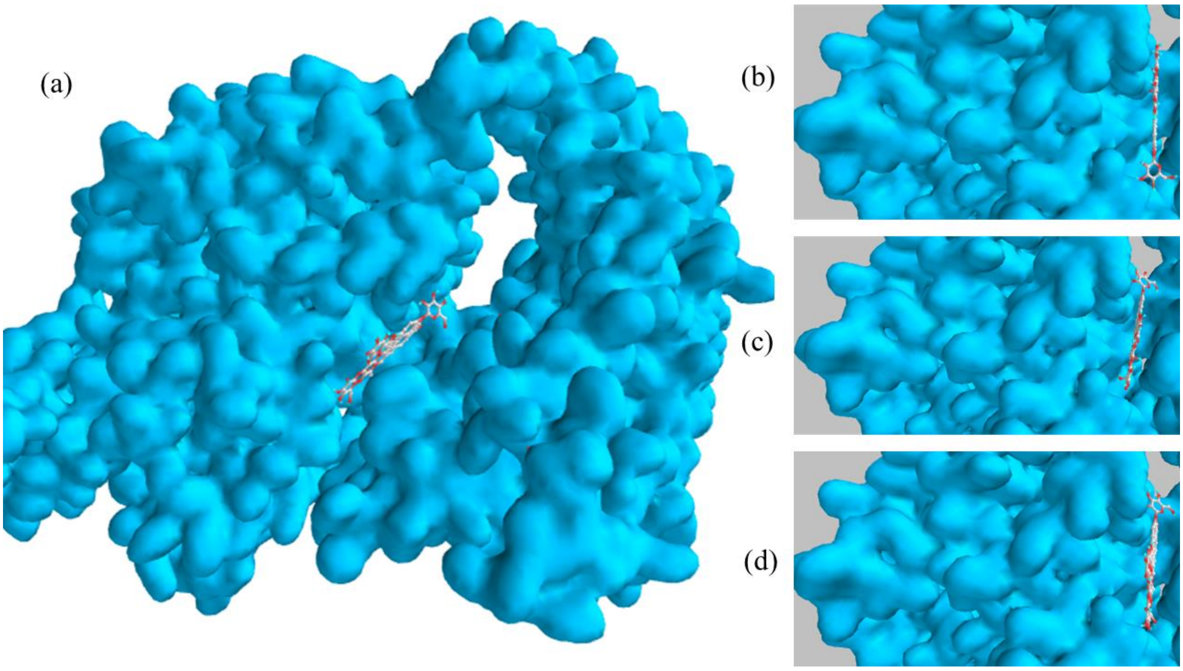

Figure 5-32: (a) Docked macromolecule-ligand complex of T1R2-Rebaudioside A, (b) Highly favoured docked configurations with binding affinities of -10.9 kcal/mol, (b) -10.6 kcal/mol, (c) -9.3 kcal/mol, and (d) -8 kcal/mol.

Table 5-14: Docking information of the macromolecule/ligand complex derived from PyRx.

Macromolecule/ligand	Binding affinity (kcal/mol)	Mode	RMSD lower bound	RMSD upper bound
T1R2-Rebaudioside A	-10.9	0	0	0
T1R2-Rebaudioside A	-10.6	2	1.098	1.595
T1R2-Rebaudisode A	-9.3	1	1.568	5.357
T1R2-Rebaudioside A	-8	1	1.5	10.176

5.2.2.3 Density functional theory (DFT) calculations

Figure 5-33 shows the HOMO-LUMO plot for the free molecule of Reb A. The most suitable functional groups or atoms to undertake oxidation or reduction reactions can be easily identified by the frontier molecular orbitals of a molecule based on these configurations and DFT diagrams. The highest occupied molecular orbitals (HOMO), which are located at the oxygen atoms in three glucose rings, contain the less securely bound electrons. Whereas the ester carbonyl groups are surrounded by the lowest unoccupied molecular orbitals (LUMO). The outcomes demonstrated that the ester carbonyl groups will provide the simplest path for the molecule to accept electrons. A quasi-reversible reduction process involving a single electron transfer between the ester carbonyl group and the electrode surface was the suggested mechanism for Reb A (Bathinapatla *et al.* 2016). To describe redox reactions more accurately, the molecule's HOMO-LUMO band gaps were estimated, with this study calculating the band gap energy of free Reb A to be ΔE = -0.59472 eV. The low value of the structure’s energy band gap is associated with its electrochemical reactivity, with the molecule being highly reactive when possessing a low energy band gap. The contour lines on the free molecule Reb A were observed around the electron densities, with the lines becoming more distant as one moves away from the high electron density within the structure.

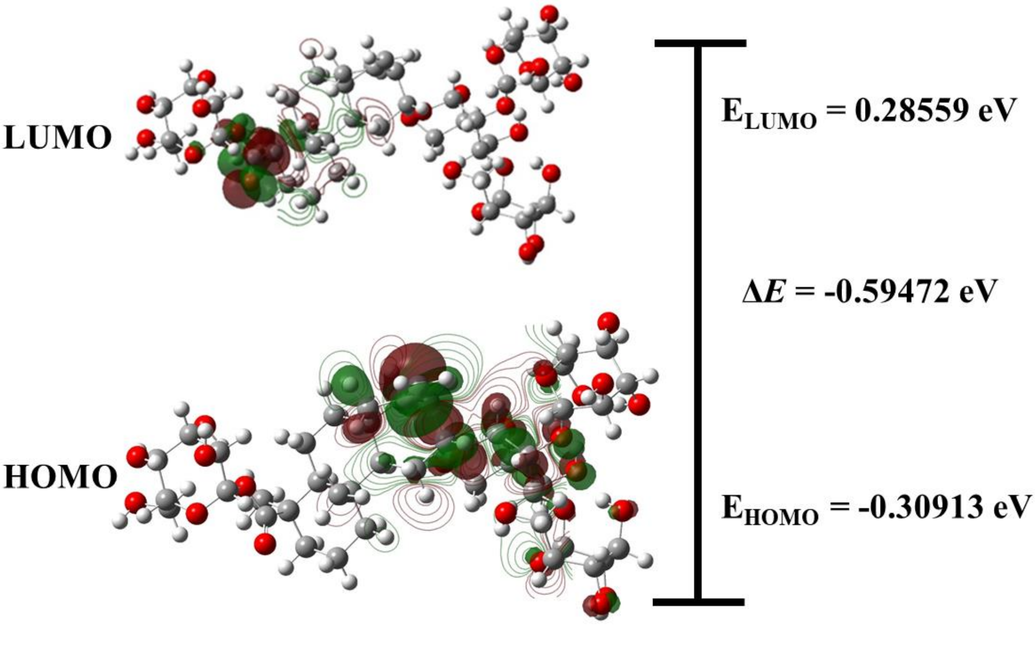

Figure 5-33: HOMO-LUMO plots for Reb A at B3LYP/6-31G** level

5.2.2.4 Monte Carlo simulations

The link between the adsorption energy of the adsorbate-substrate system (the electrode and the modifying nanomaterials) is illustrated in Figure 5-34 through MC adsorption energies. This figure replicates the layer-by-layer experimental electrode technique used in this investigation to detect Reb A. According to our earlier research (Uwaya, Gumede and Bisetty 2021), the more intensely negative adsorption energy (GCE/ZIF-67/fMWCNTs/T1R2: -63668.33 kcal/mol) relates to larger interaction energies that characterize the stability of the adsorbate-substrate interactions. As a result, the estimated adsorption energies show the following trend: GCE/ZIF-67 = -4173.78 kcal/mol > GCE/ZIF-67/fMWCNTs = -10937.66 kcal/mol > GCE/ZIF-67/fMWCNTs/T1R2 = -63668.33 kcal/mol. In comparison to the individual sensing materials (ZIF-67 and fMWCNTs) utilized for the electrode modification processes, the final electrode shows an increasing stability of the MOF composite due to the presence of the fMWCNTs, which increases surface area and conductivity.

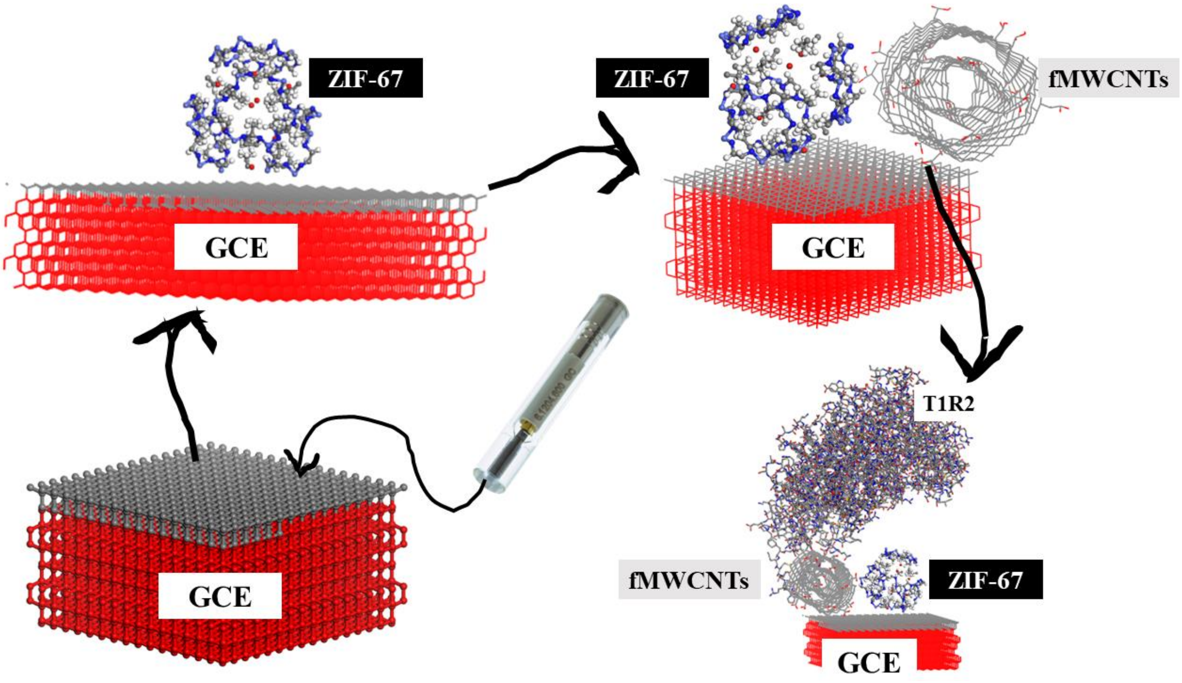

Figure 5-34: Monte Carlo simulations of the different electrodes for Reb A.

5.2.3 Conclusion

The second case study developed an indirect immunosensor for the detection of RebA in the presence of a redox probe. The developed electrode is comprised of GCE modified with ZIF-67/fMWCNTs nanocomposite and a drop casted T1R2 antibody. The stable electrode had a linear dynamic range of 0.9901 µM to 8.2569 µM ($R^2 = 0.8850$). The limit of detection (LOD) and quantification (LOQ) were computed to be 1.10 µM and 3.33 µM, respectively. This case study also used Patch Dock and PyRx to better understand the interactions between Reb A and T1R2, closing in with Monte Carlo calculations that were highly negative for the final electrode (GCE/ZIF-67/fMWCNTs/T1R2), indicating the stability of the electrode.

The results of this study may contribute to the development of an onsite immunosensor that can potentially be used to quantify Reb A in the food and beverage industry.

5.3 Case Study 3:

Development of an PVP-AgNPs/rGO immunosensor for the detection of aspartame in food samples using nanocomposite modified Pt electrode.

The third and last case study for this study utilized a platinum electrode (PtE) as the working electrode (WE) for the electrochemical immunosensing of aspartame. The nanocomposite of PVP-AgNPs and reduced graphene oxide (rGO) with immobilized T1R2 were used to modify PtE. The electrochemical detection of aspartame was achieved under optimum conditions at pH 8 in a 0.1 M phosphate buffer solution, utilizing the CV, EIS, and DPV electrochemical tools.

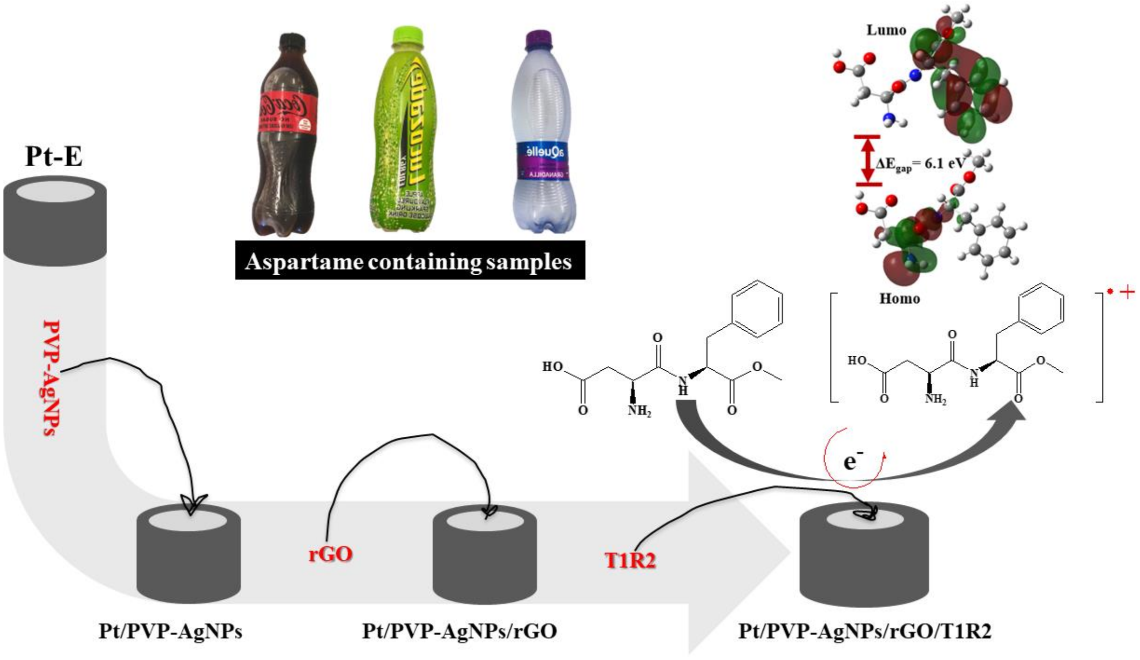

Scheme 5-4: Schematic diagram for the oxidation reaction mechanism of Aspartame at GCE/PVP/rGO/T1R2 in PBS supporting electrolyte.

5.3.1 Experimental

5.3.1.1 Characterization

(i) EDS analysis

Figure 5-35a-c shows the EDS spectra of PVP-AgNPs, rGO, and PVP-AgNPs/rGO nanocomposite, reflecting the presence of silver (Ag), carbon (C), oxygen (O), chlorine (Cl), sodium (Na), and sulphur (s). The presence of chlorine in the PVP-AgNPs spectrum is suspected to be caused by the biomolecules used for capping AgNPs (Moond *et al.* 2023). While the traces of S detected in both the (b) rGO and (c) PVP-AgNPs/rGO spectrum are due to the use of oxidizing acids (HNO_3:H_2SO_4) for acid functionalization of rGO (Hloma, Uwaya and Bisetty 2022; Mafamadi, Etale and Daramola 2023). Even though the rGO used in this study was commercially obtained, the carboxylation of graphene oxide involves a reaction step with concentrated NaOH, hence the presence of Na in both 5-35b and c (Guo *et al.* 2020). Table 5-15 summarizes the percentage weight of each element present in electrode materials (PVP-AgNPs, rGO, and PVP-AgNPs/rGO). The EDS also confirms the presence of Ag, C and O in both the bare PVP-AgNPs and the PVP-AGNPs/rGO in Figures 5-35a and c.

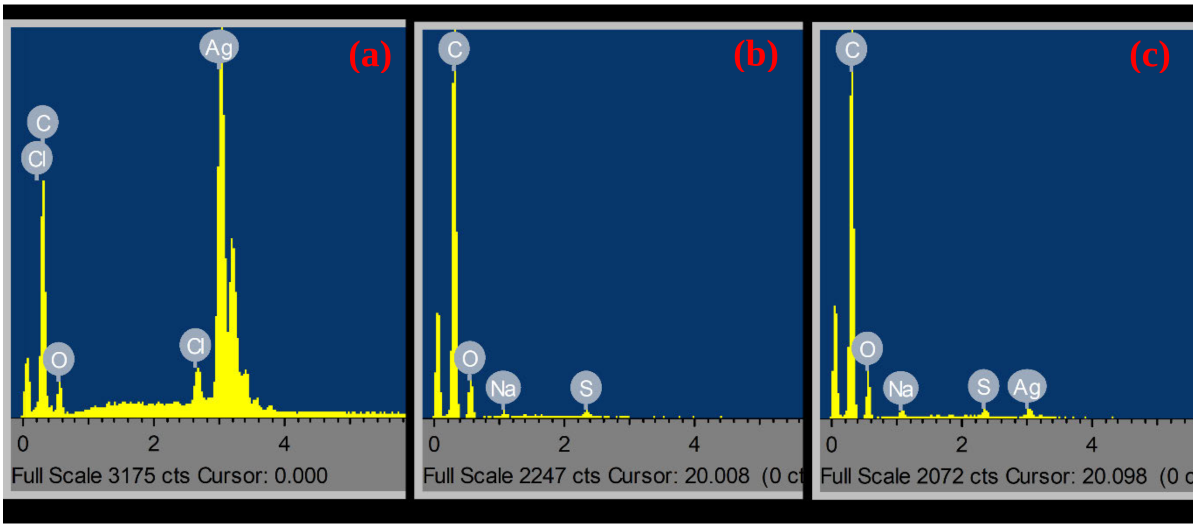

Figure 5-35: EDS elemental analysis of (a) PVP-AgNPs, (b) rGO, and (c) PVP-AgNPs/rGO nanocomposite

Table 5-15: Summarized elemental weight (%) composition of PVP-AgNPs, rGO and PVP-AgNPs/rGO.

Sample	%C	%O	%Na	%S	%Ag	%Cl	Total
PVP-AgNPs	28.83	14.06	0	0	56	1.11	100
rGO	73.55	25.14	0.74	0.56	0	0	100
PVP-AgNPs/rGO	78.44	17.05	0.57	0.59	3.36	0	100

(ii) SEM studies

Figure 5-36a-c represents PVP-AgNPs, rGO and PVP-AgNPs/rGO SEM micrographs, respectively. Figure 5-36a shows monodispersed and semi-spherical-shaped PVP-AgNPs, which correlates with the literature (Liao, Li and Tjong 2019). The SEM image of rGO shows a sheath like crumpled silk veil wave (Figure 5-36b), while an attachment of spherically-shaped PVP-AgNPs on the rGO sheet, circled in red, is noticed in the PVP-AgNPs/rGO image, suggesting an interaction between the semi-spherical-capped AgNPs and rGO (Figure 5-36c) (Saleem, Haneef and Abbasi 2018) (PVP-AgNPs circled red in Figure 5-36c).

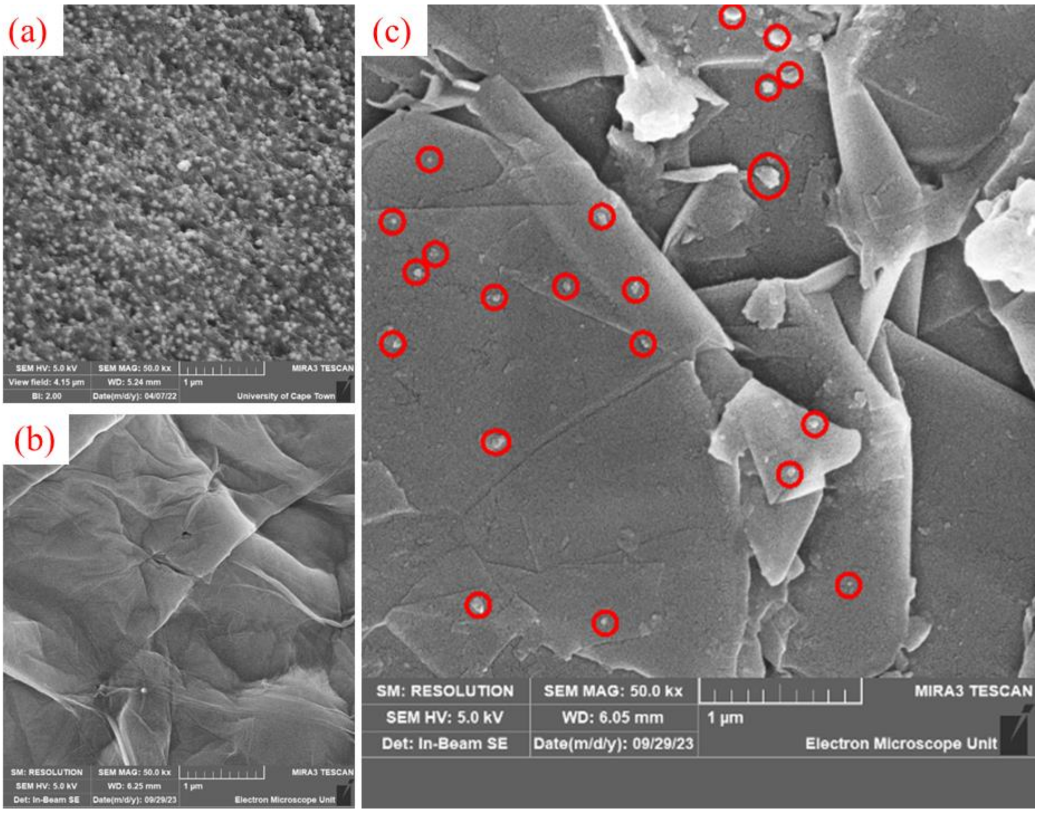

Figure 5-36: SEM image of the synthesized PVP-AgNPs, (b) SEM image of rGO, and (c) SEM image of the nanocomposite PVP-AgNPs/rGO.

5.3.1.2 Electrochemical Characterization of electrodes

(i) Cyclic voltametric characterization of electrodes

Cyclic voltammetry measurements were conducted to explore the electrochemical properties and performances of bare PtE, PtE/PVP-AgNPs, PtE/rGO, PtE/PVP-AgNPs/rGO, and PtE/PVP-AgNPs/rGO/T1R2 in a 5 mM $[Fe(CN)_6]^{-3/-4}$ solution prepared in 0.1 M PBS at pH 8. In electrochemistry, the ferro/ferricyanide redox pair is one of the most researched and is distinguished by a heterogeneous electron transport with n = 1 (Bathinapatla *et al.* 2016; Pajkossy, Ceblin and Meszaros 2021). Comparative cyclic voltammograms for the various electrodes acquired at a scan rate of 0.025 V/s are displayed in Figure 5-37. In comparison to the other electrodes evaluated, the nanocomposite modified electrode (PtE/PVP-AgNPs/rGO/T1R2) exhibited a higher current response, suggesting improved electrocatalytic activity owing to the synergy of the sensing leading to increased active surface area. The anodic peak at 0.1 V is due to the redox probe oxidation whilst the second peak is attributed to the oxidation of AgNPs in the PVP-AgNPs/rGO nanocomposite.

The anodic current responses are as follows, in descending order: PtE/PVP-AgNPs/rGO/T1R2 (91.03 μA) > PtE/PVP-AgNPs/rGO (40.71 μA) > PtE/rGO (25.50 μA) > PtE (22.19 μA) > PtE/PVP-AgNPs (17.01 μA).

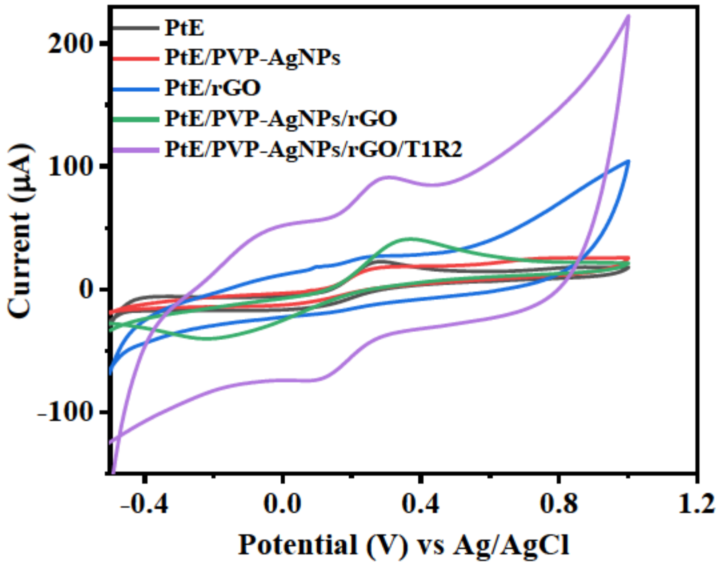

Figure 5-37: CVs of PtE and modified electrode vs Ag/AgCl in the redox probe (5 mM $[Fe(CN)_6]^{-3/-4}$).

(ii) Electrochemical impedance spectroscopic study of electrodes

EIS was performed in a 5 mM $[Fe(CN)_6]^{-3/-4}$ solution at a fixed potential of 0.2 V in order to comprehend the mechanism of electron transfers occurring at the electrode-electrolyte interface between the 100 kHz and 0.1 Hz frequency ranges. The Nyquist spectra for bare and modified electrodes (PtE to PtE/PVP-AgNPs/rGO/T1R2) are shown in Figure 5-38a.

Fitting the EIS data for PtE, PtE/PVP-AgNPs, PtE/rGO, PtE/PVP-AgNPs/rGO, and PtE/PVP-AgNPs/rGO/T1R2 with the circuit description of [R([RW]Q)] in Figure 5-38b was done using Randle's circuit. A low chi-square value (< 1) and a low percentage error suggest that the Randles-Sevcik conditions have been met in Table 5-16, which summarizes the EIS data.

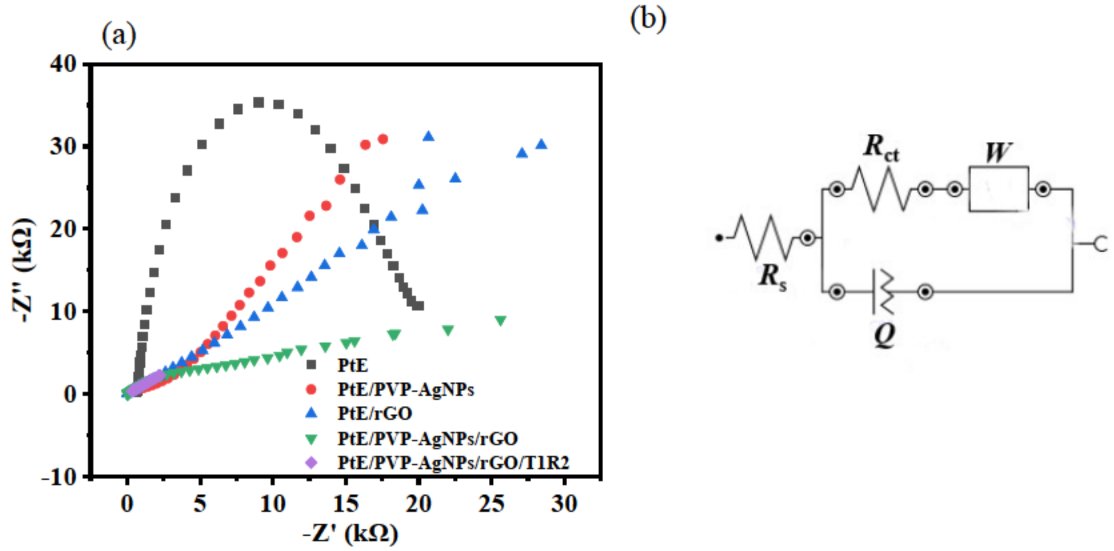

Figure 5-38: (a) Nyquist plots obtained for bare PtE, PtE/PVP-AgNPs, PtE/rGO, PtE/PVP-AgNPs/rGO and PtE/PVP-AgNPs/rGO/T1R2 electrodes vs Ag/AgCl at a fixed 0.2 V potential. (b) shows Randles circuit used in fitting the EIS data for the used electrodes.

Table 5-16: Summary of EIS data acquired from 5 mM $[Fe(CN)_6]^{-3/-4}$ redox probe in layer-by-layer electrodes vs Ag/AgCl.

Electrode	**R_s(kΩ)(%Error)**	**R_{ct}(kΩ)(% Error)**	**X^2**
PtE	375.22 (0.945)	18672.8 (1.955)	0.1119
PtE/PVP-AgNPs	356.95 (1.068)	28118 (7.072)	0.1377
PtE/rGO	343.53 (1.585)	9963.36 (16.427)	0.1012
PtE/PVP-AgNPs/rGO	352.8 (1.276)	6597.9 (5.453)	0.1762
PtE/PVP-AgNPs/rGO/T1R2	342.95 (1.1159)	2393 (6.971)	0.1642

(iii) Scan rate Variation

Cyclic voltammograms presented in Figure 5-39a, are recorded at varied scan rates from 0.02-0.21 Vs^{-1} in $[Fe (CN)_6]^{-3/-4}$ solution at the PtE/PVP-AgNPs/rGO/T1R2 electrode. The results were employed to investigate the impact of scan rate variations on the peak potentials and currents, as well as the kinetics of the electrode. On the other hand, the anodic and cathodic peak potentials were observed to shift to more positive and negative values, respectively, with the gradual increase in scan rates, indicating an efficient mass transport between the electrodes. as shown in Figure 5-39b (Bojang and Wu 2020). A steady increase in both the anodic and cathodic peak currents was also observed with increased scan rates (Bojang and Wu 2020). The oxidation peak current (I_{pa}) and reduction peak current (I_{pc}) in Figure 5-39c are linearly dependent on the square root of the scan rate ($v^{1/2}$). The regression coefficient (R^2) for I_{pa} is 0.9909, and for I_{pc} it is 0.9968. These results indicate that the electrode reaction is diffusion-regulated (Uwaya, Wen and Bisetty 2022). The active surface area (cm^2) calculated using the I_{pa} slope value of Figure 5-39c on applying the Randle Sevcik equation (3.4) was found to be 0.3579 cm^2.

The relationship between the logarithms of peak currents (Log I_{pa}) and the logarithm of scan rate (Log v) presented in Figure 5-39e gave regression coefficients of 0.9350 and 0.9983 for anodic and cathodic reactions with slope values <1, further supporting a diffusion-controlled reaction.

The slopes obtained from the plots of oxidation and reduction peak potentials (E_{pa} and E_{pc}) versus the logarithm of scan rate (Figure 5-39e) were used to calculate the coefficient of the electron transfer (α) and the number of electrons transferred (n) on the nanocomposite modified electrode. The number of electrons (n) was calculated to be $0.75 \approx 1$, and the coefficient of electron transfer (α) was calculated to be 0.45, which is closer to 0.5 for a perfectly diffusion-controlled reaction.

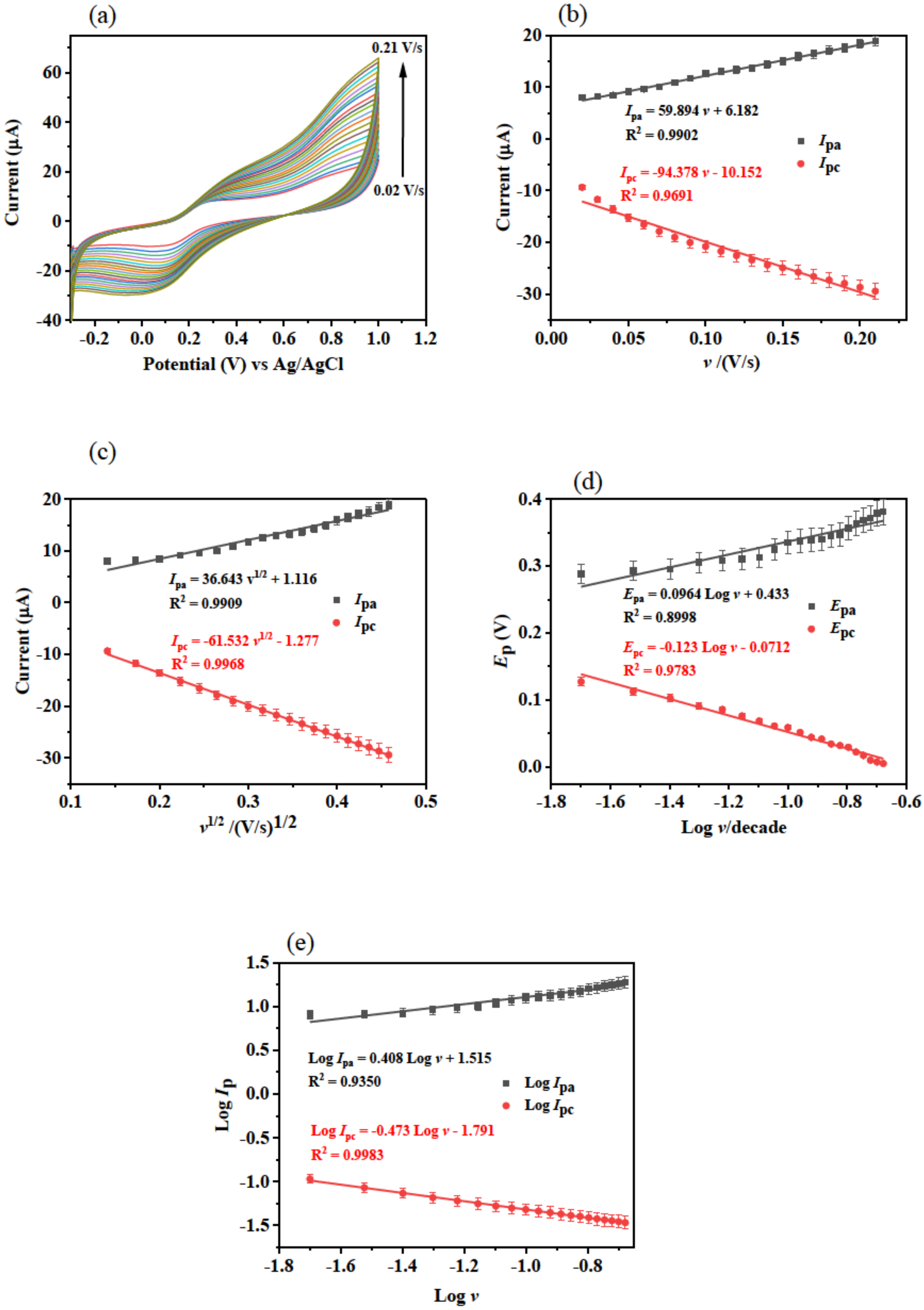

Figure 5-39: (a) PtE/PVP-AgNPs/rGO/T1R2 vs Ag/AgCl cyclic voltammograms in 5mM $[Fe(CN)_6]^{-3/-4}$ solution prepared in pH 8 0.1M Phosphate buffer (v: 0.02-0.0.21V/s, inner to outer), (b) Anodic and

cathodic peak currents as scan rate is varied, (c) Linear plots of anodic and cathodic peak currents vs square root scan rates, (d) Anodic and cathodic peak potentials versus log *v*, and (e) Log I_p versus Log *v*.

(iv) Electrochemical behaviour of Aspartame

The electrochemical characteristics and performances of bare Pt-E, PtE/PVP-AgNPs, PtE/rGO, PtE/PVP-AgNPs/rGO, and PtE/PVP-AgNPs/rGO/T1R2 in pH 8 0.1 M PBS at pH 8 solution were investigated using cyclic voltammetry experiments. Figure 5-40 shows comparative cyclic voltammograms obtained at a scan rate of 0.025 V/s for the different electrodes. The nanocomposite-modified electrode (PtE/PVP-AgNPs/rGO/T1R2) showed the second greatest current response with a more resolved peak of ASP when compared to the other electrodes studied. The unmodified Pt electrode performed poorly, whereas the nanocomposite (PVP-AgNPs/rGO) electrode with T1R2 had the maximum conductivity.

The anodic current responses are as follows in descending order: PtE/PVP-AgNPs/rGO (352.4780 µA) > PtE/PVP-AgNPs/rGO/T1R2 (301.3000 µA) > PtE/rGO (268.3105 µA) > PtE/PVP-AgNPs (264.804 µA) > PtE (234.1918 µA).

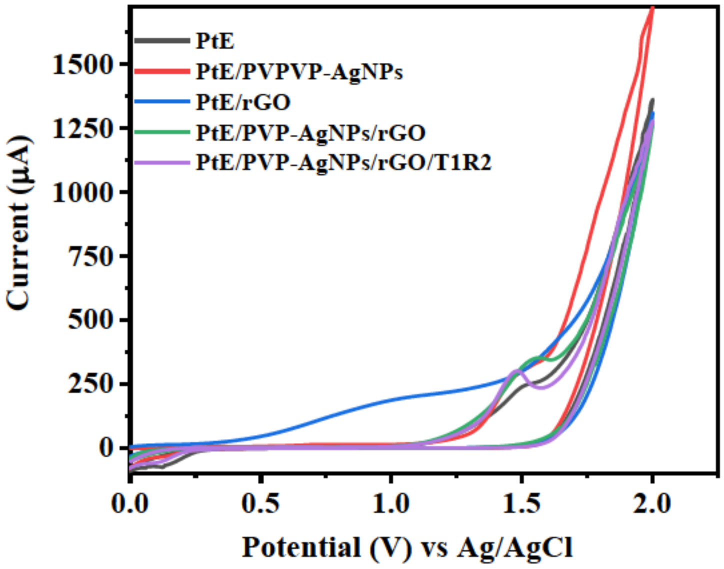

Figure 5-40: Layer by layer electrochemical (PtE, PtE/PVP-AgNPs, PtE/rGO, and PtE/PVP-AgNPs/rGO, PtE/PVP-AgNPs/rGO/T1R2 vs Ag/AgCl) sensing of 0.9901 µM Aspartame in pH 8 0,1 M PBS in the presence of T1R2 antibody

(v) Electrochemical impedance spectroscopic study of electrodes

Fitting the EIS data for PtE and PtE/PVP-AgNPs, PtE/rGO, PtE/PVP-AgNPs/rGO, and PtE/PVP-AgNPs/rGO/T1R2 with the description of [R(RQ)] in Figure 5-41a was done using Randle's circuit (Figure 5-41b). A low chi-square value (< 1) and a low percentage error suggest that the Randles-Sevcik conditions have been met in Table 5-17, which summarizes the EIS data. The semicircle seems to decrease from the electrode with high charge transfer resistance (R_{ct}) to the smallest semi-circle of the electrode with the least R_{ct} value.

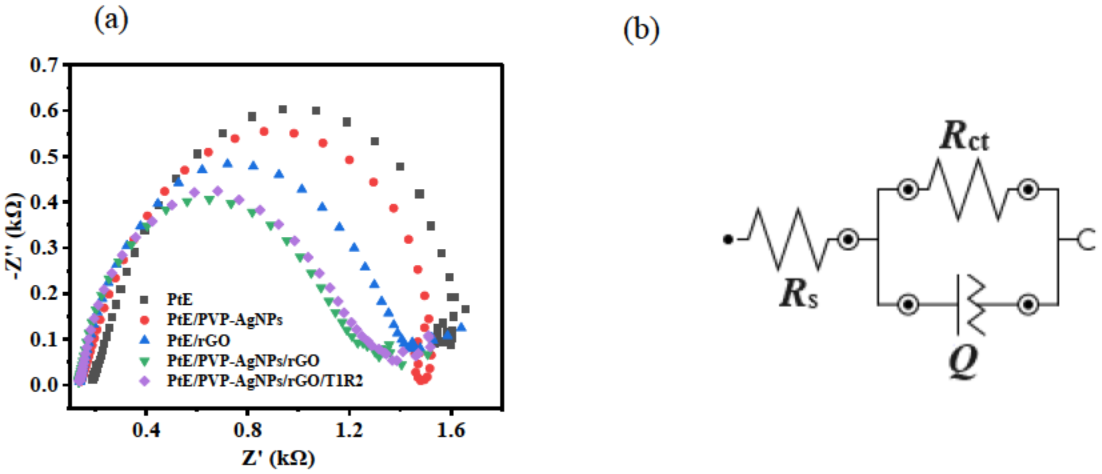

Figure 5-41: (a) Nyquist plots obtained for bare PtE, PtE/PVP-AgNPs, PtE/rGO/, PtE/PVP-AgNPs/rGO and PtE/PVP-AgNPs/rGO/T1R2 electrodes vs Ag/AgCl at a fixed 0.2 V potential in 0.1 M pH PBS and (b) Illustrates circuit ([R(RQ)]) used in fitting EIS data for all the unmodified and modified electrodes

Table 5-17: Summary of EIS data acquired from 240 µM of Aspartame in pH 8 0.1M PBS vs Ag/AgCl.

Electrode	**R_s(kΩ)(%Error)**	**R_{ct} (kΩ)(Error)**	**X^2**
PtE	168.62(1.545)	1408.3(1.923)	0.23783
PtE/PVP-AgNPs	135.3(1.362)	1267.9(1.876)	0.26428
PtE/rGO	146.67(1.359)	1199.8(1.768)	0.28131
PtE/PVP-AgNPs/rGO	128.2(1.630)	1079.4(1.585)	0.20686

PtE/PVP-AgNPs/rGO/T1R2	136.58(1.515)	1092.9(1.678)	0.19672

5.3.1.3 Optimization of analytical parameters of the PtE/PVP-AgNPs/rGO/T1R2

(i) Optimization of pH and Deposition time

The supporting electrolyte's pH has an impact on the performance of the electrodes. The sensitivity of the nanocomposite/TIR2 modified electrode (PtE/PVP-AgNPs/rGO/TIR2 electrode) to 0.9901 µM ASP was investigated using CV at a scan rate of 0.025 V/s. The influence of PBS pHs in a range of 4–9 is shown in Figures 5-42a and b. Since the oxidation current was determined to be at its greatest at pH 8, this pH was used throughout the experiments to determine the optimal concentration of ASP. The anodic peak was clearly resolved as pH 8. Through the use of DPV, Figure 5-42c on the same electrode (PtE/PVP-AgNPs/rGO/T1R2) shows the impact of deposition time (5-60 s) on the peak current of ASP. The findings show an increase and a decrease in anodic current as the deposition times increased, with 30 s deposition as optimum.

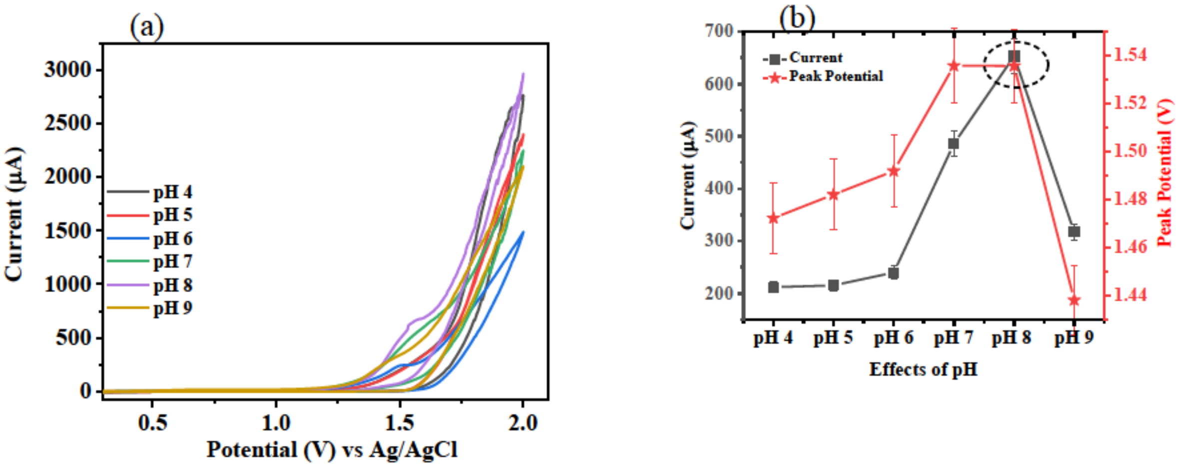

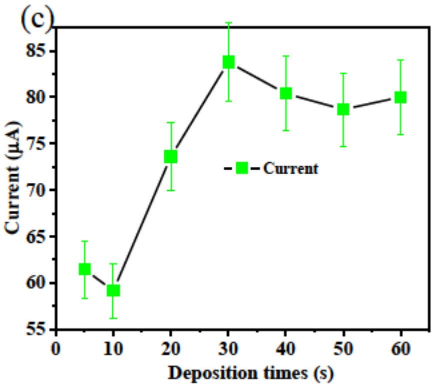

Figure 5-42: (a) The role of pH on the oxidation current vs Ag/AgCl (I_{pa}) of 0.9901 μM ASP (b) The relationship between anodic peak current ASP and the changing pHs, and (c) the effect of deposition time on the anodic current.

(iii) Scan rate variation

The impact of varying scan rates between 0.02 and 0.20 V/s on cyclic voltammetric responses of 240 μM ASP at the PtE/PVP-AgNPs/rGO/T1R2 electrode when using optimal pH 8 PBS conditions is depicted in Figure 5-43a. As shown in Figure 5-43b, the oxidation peak current (I_{pa}) had a regression coefficient of 0.9889 and was proportional to the scan rate (v). The electrochemical process is diffusion-controlled, as shown by the anodic peak current increasing linearly against the square root of the scan rate ($v^{1/2}$) (Figure 5-43c) and a linear regression coefficient of 0.9727.

Figure 5-43e shows the logarithm of the I_{pa} vs. scan rate (v) plot, providing additional confirmation that this is a diffusion-controlled reaction with a slope that is the first derivative of the equation, which is near the predicted value of 0.5 (Uwaya and Fayemi 2021a). Anodic oxidation peak potential (E_{pa}) vs. log v is plotted linearly in Figure 5-43d, with a regression coefficient of 0.9540. Equation 6-2 was utilized to get the transfer coefficient, α, which came out to be 0.437 (Gowda and Nandibewoor 2014b). Subsequently, α was then applied to calculate the number of electrons as 0.5843 (approximately 1).

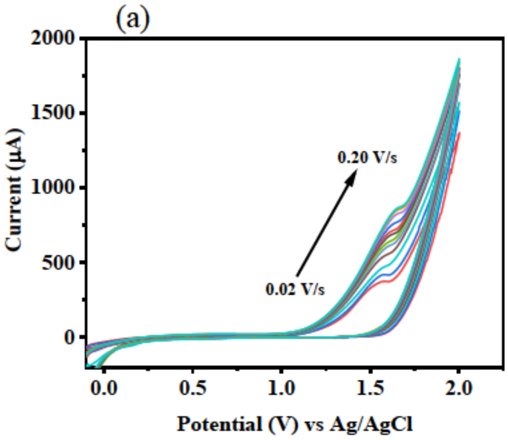
(a)
Current (μA)
2000
1500
1000
500
0
0.0
0.5
1.0
1.5
2.0
Potential (V) vs Ag/AgCl
0.20 V/s
0.02 V/s

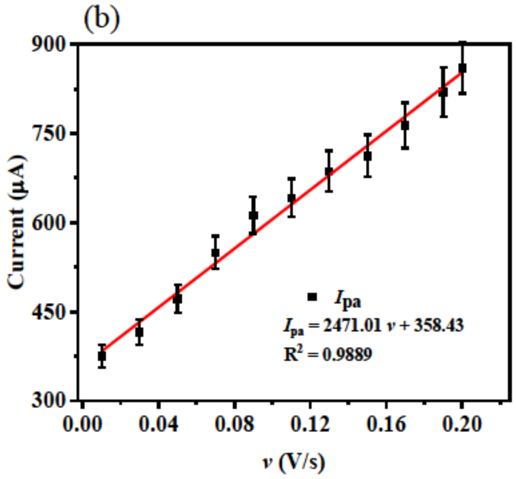
(b)
Current (μA)
900
750
600
450
300
0.00
0.04
0.08
0.12
0.16
0.20
v (V/s)
■ Ipa
Ipa = 2471.01 v + 358.43
R2 = 0.9889

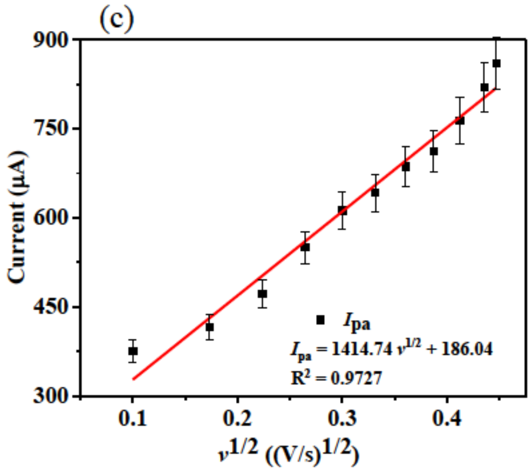
(c)
Current (μA)
900
750
600
450
300
0.1
0.2
0.3
0.4
v1/2 ((V/s)1/2)
■ Ipa
Ipa = 1414.74 v1/2 + 186.04
R2 = 0.9727

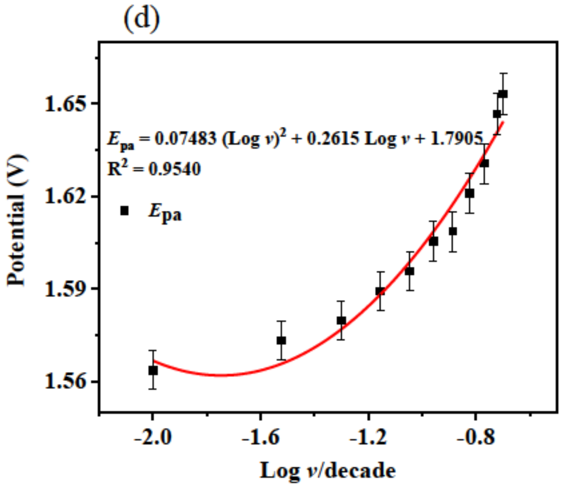
(d)
Potential (V)
1.65
1.62
1.59
1.56
-2.0
-1.6
-1.2
-0.8
Log v/decade
Epa = 0.07483 (Log v)2 + 0.2615 Log v + 1.7905
R2 = 0.9540
■ Epa

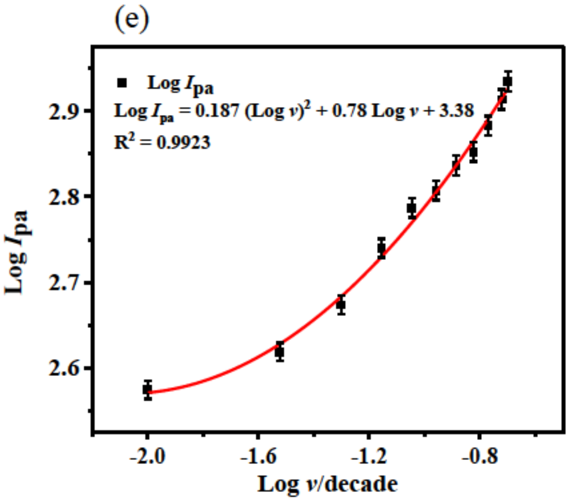
(e)
Log Ipa
2.9
2.8
2.7
2.6
-2.0
-1.6
-1.2
-0.8
Log v/decade
■ Log Ipa
Log Ipa = 0.187 (Log v)2 + 0.78 Log v + 3.38
R2 = 0.9923

Figure 5-43: (a) Pt/PVP-AgNPs/rGO/T1R2 vs Ag/AgCl cyclic voltammograms in pH 8 0.1 M Phosphate buffer in the presence of aspartame (*v*: 0.02-0.0.20 V/s, inner to outer), (b) Anodic peak currents as scan rate is varied, (c) Linear plots of anodic peak currents vs square root scan rates, (d) Anodic peak potentials versus log *v*, and (e) Log I_p versus Log *v*.

5.3.1.4 Electrochemical behaviour of ASP on Pt/PVP-AgNPs/rGO/T1R2

(i) Linear Dynamic Range

The linear concentration range, detection limit, and sensitivity of ASP on PtE/PVP-AgNPs/rGO/T1R2 were found using DPV within a 0.8 V to 1.8 V potential window. The results presented by (Balgobind *et al.* 2016b) are in line with Figure 5-44a, which shows a linear increase in oxidation peak currents as aspartame concentrations were increased from 2.3762 µM to 25.7838 µM. Additionally, as the aspartame concentration increases and accumulates at the surface of the working electrode, PtE/PVP-AgNPs/rGO/T1R2, the result demonstrates a gradual increase in anodic current on the oxidation peak at 1.45 V.

By using the formulas LOD = (3.3S/*m*) and LOQ = (10S/*m*), where s is the standard deviation of the intercept of the y-coordinates from the line of best fit of the calibration plot and *m* is the slope of the calibration curve, the limits of detection (LOD) and quantification (LOQ) were calculated to be 5.85 µM and 17.73 µM, respectively. The gradient of the same line is shown in Figures 5-44 b with the linear regression equation I_{pa} (µA) = 1.1240 [ASP] + 63.568, and it had a correlation coefficient value of 0.9529.

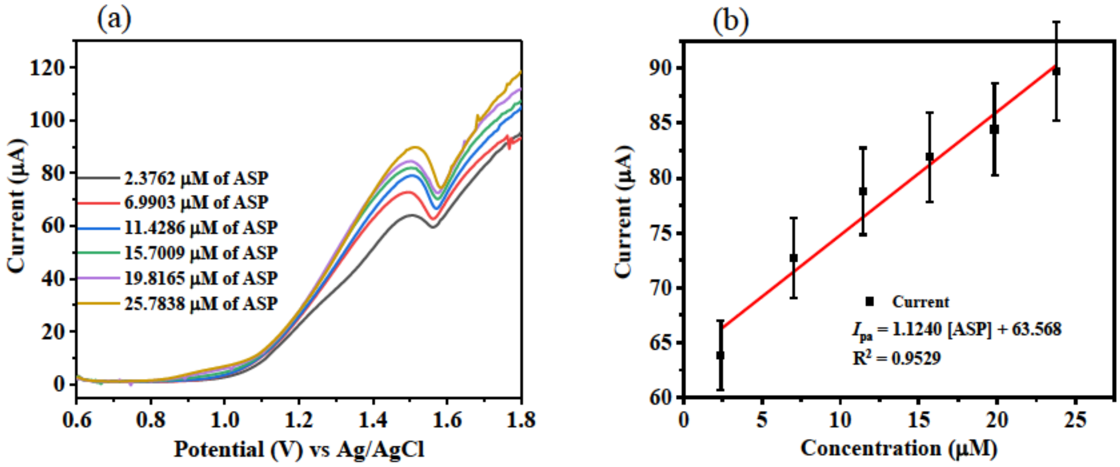

Figure 5-44: (a) PtE/PVP-AgNPs/rGO/T1R2 vs Ag/AgCl DPV responses as the concentration of ASP is increased. (b) Calibration graph of the anodic current (I_{pa}) versus ASP concentrations (0.9901–4.9180 µM) in 0.1 M PBS pH 8.

(ii) Repeatability, Reproducibility and Stability of PtE/PVP-AgNPs/rGO/T1R2/ASP

The designed immunosensor's repeatability was assessed by five repetitive DPV scans in 0.1 M PBS containing 240 µM ASP. As shown in Figure 5-45a (bar graph), the electrode (PtE/PVP-AgNPs/rGO/TIR2) readings are relatively repeatable, as there was 3.65% RSD. PtE/PVP-AgNPs/rGO/T1R2's reproducibility investigations were carried out with five distinct electrodes for the five repeated measurements. The computed RSD for repetitive measurements was 10.68%, suggesting a greater dispersion of the measured anodic currents, as seen in Figure 5-45b. PtE/PVP-AgNPs/rGO/T1R2's stability after 25 cycles of cyclic voltammograms was studied; the comparatively significant drop in anodic current suggests that the electrode nanocomposite becomes unstable and non-conductive with additional experiments. The storage stability of PtE/PVP-AgNPs/rGO/T1R2 is shown in Figure 5-45c. Within a 10-day period, the oxidation current decreased by 49.79% on day 5 of the second measurement, and by 20.84% on day 10 of the third measurement.

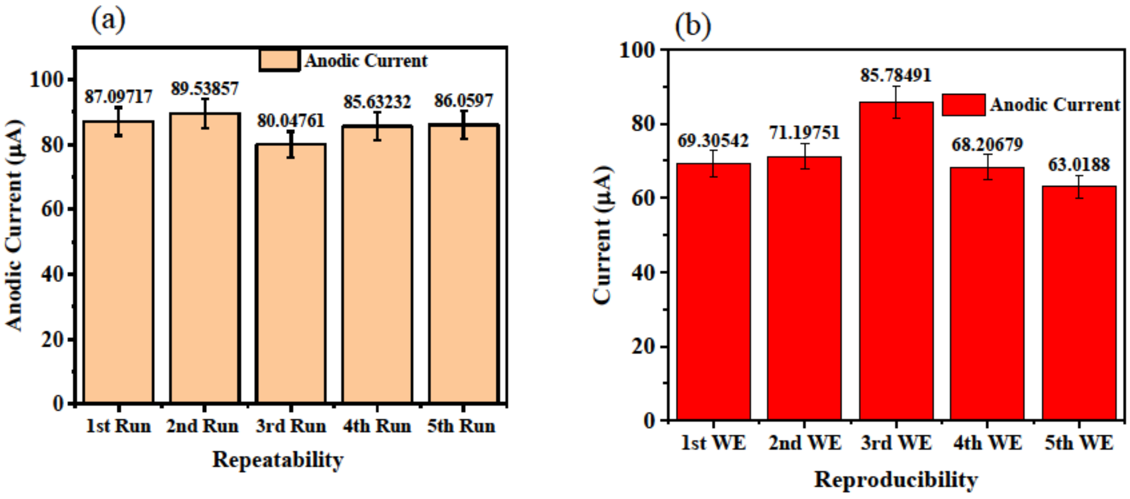

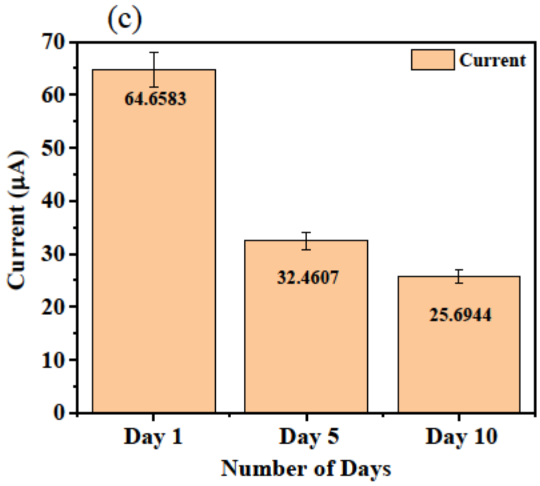

Figure 5-45: Bar graphs of (a) repeatability and (b) reproducibility, and (c) Storage stability studies of PtE/PVP-AgNPs/rGO/T1R2 in 0.1 M pH 8 phosphate buffer 240 µM of ASP

(iii) Interferences Studies

A simultaneous and individual analysis of the 240 µM standard of each potential interfering species (acesulfame K, aspartame, rebaudioside A, xylitol, and saccharin) in the presence of 240 µM ASP in pH 8 phosphate buffer solution was used to conduct the selectivity studies of the developed sensor (PtE/PVP-AgNPs/rGO/T1R2). Table 5-18 presents a summary of the findings, indicating the percentage change in anodic peak current when additional sweeteners are present.

Table 5-18: Summary of interference studies on the detection of ASP by PtE/PVP-AgNPs/rGO/T1R2 vs Ag/AgCl.

No.	Interference	Concentration (µM)	RSD^a (%)	% ↓ and ↑ in I_{pa} of aspartame
1	Acesulfame K	240 µM	2.76	5.33↓
2	Xylitol	240 µM	3.94	4.38↓
3	Rebaudioside A	240 µM	2.20	2.50↓
4	Aspartame	240 µM		

5	Saccharin	240 µM	2.21	1.88↑
6	Ace K, Xylitol, Reb A, ASP, Saccharin	240 µM	3.49	5.44↑

(iv) Analytical Performance of the Designed Sensor of ASP Determination

The analytical feasibility and performance of the designed sensor (Pt/PVP-AgNPs/rGO/T1R2) for the accurate detection of Aspartame in the prepared sugar-free Coca-Cola, Lucozade energy drink, and aQuelle sparkling flavoured drink sample were investigated by DPV following the standard addition method. 200 µL of the diluted sample was transferred into an electrolytic cell, containing 10 mL of pH 8 0.1 M PBS buffer, spiked with known concentrations of Reb A, and analysed in triplicate as shown in Table 5-19.s

Table 5-19: Analytical performance of PtE/PVP-AgNPs/rGO/T1R2 vs Ag/AgCl on real samples (Coca-Cola No Sugar, Lucozade, and AQuelle) at pH 8 0.1 M PBS buffer

Sr.N	Added (µM)	Found (µM)	Recovery (%)	RSD (%)
Coca-Cola (No Sugar)				
1	2.3762	2.3917	100.65	5.33
2	6.9903	7.0715	101.16	3.54
3	11.4286	11.2130	98.11	5.92
Lucozade Energy drink				
1	2.3762	2.4923	90.24	3.64
2	6.9903	6.6731	95.46	2.60
3	11.4286	11.7120	102.48	4.78
aQuelle sparkling flavoured drink				
1	2.3762	2.7760	116.82	2.29
2	6.9903	6.1018	87.29	4.85

3	11.4286	11.9920	104.93	5.63

5.3.2 Computational Chemistry results and discussion

5.3.2.1 Monte Carlo Simulations

The adsorption energy of the adsorbate-substrate system (the electrode and the modifying nanomaterials) mimicking the experimental electrodes is illustrated in Figure 5-46 through MC adsorption energies. This figure replicates the layer-by-layer experimental electrode technique used in this investigation to detect ASP in food and beverage samples. The trend noted by the literature on this study implies that (Bisetty, Kanchi and Hloma 2021; Uwaya, Gumede and Bisetty 2021), the more intensely negative adsorption energy (PtE/PVP-AgNPs/rGO/T1R2: -6.363389e+004 kcal/mol) relates to larger interaction energies that characterize the stability of the adsorbate-substrate interactions. As a result, the estimated adsorption energies show the following trend: PtE/PVP-AgNPs = -2.596625e+004 kcal/mol > PtE/PVP-AgNPs/rGO = -2.144516e+003 kcal/mol. In comparison to the individual nanomaterials utilized for the electrode modification processes, the final electrode shows the increasing stability of the nanocomposite.

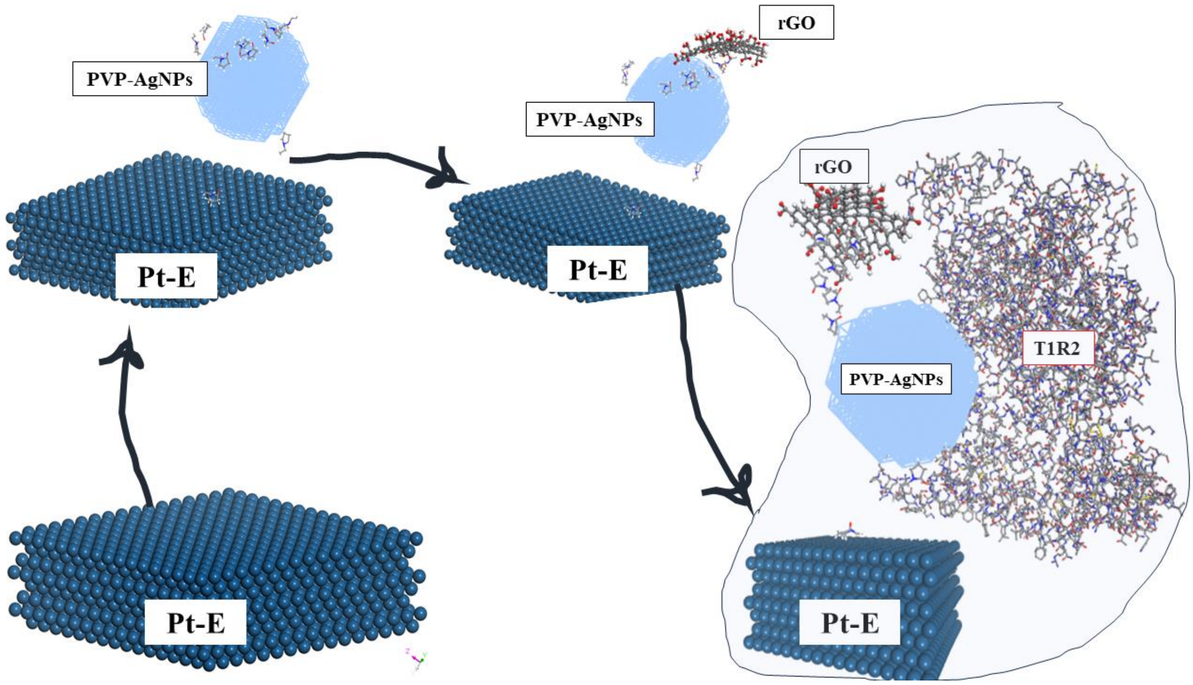

Figure 5-46: Monte Carlo simulations of the different electrodes for ASP

5.3.3 Conclusion

The third and final case study of this thesis was developed to detect aspartame; in this case, platinum was modified as the working electrode. The PVP-AgNPs/rGO/T1R2 was used to fabricate Pt, and the electrode performed well with a linear increase in oxidation peak currents as aspartame concentrations were increased from 2.3762 µM to 25.7838 µM. By using the formulas LOD = (3.3S/*m*) and LOQ = (10S/*m*), where s is the standard deviation of the intercept of the y-coordinates from the line of best fit of the calibration plot and *m* is the slope of the calibration curve, the limits of detection (LOD) and quantification (LOQ) were calculated to be 5.85 µM and 17.73 µM, respectively.

The results of this case study may contribute to the development of an immunosensor that can potentially be used to quantify ASP in the food and beverage industry.

CHAPTER 6: CONCLUSION AND RECOMMENDATIONS

6.1 Concluding Remarks

This study presents insights into the development of novel human sweet taste receptor nanocomposite-modified electrochemical immunosensors for the detection of Aspartame and Rebaudioside A. Computational methods were employed to explore biomolecular interactions at the nanostructure interface.

Nanomaterials were successfully synthesized using cost-effective green and chemical synthesis for silver nanoparticles and chemical synthesis for ZIF-67. The synthesis of nanomaterials was then followed by a series of characterization tools, including SEM, AF4, sp-ICPS, TGA, FTIR, UV-vis and EDS.

The first case study successfully developed an electrochemical immunosensor for detecting Aspartame, using a step-by-step electrode fabrication strategy (from bare GCE to fully fabricated GCE/PVP-AgNPs/fMWCNTs/T1R2 vs Ag/AgCl), under optimized conditions, the sensor demonstrated a linear range of 2.89 to 27.61 µM. The limit of detection and quantification were computed as 0.40 µM and 1.34 µM, respectively. In order to demonstrate the effectiveness of the developed ASP immunosensor, it was applied to Coca Cola Zero Sugar, aQuelle and Lucozade samples, with average recoveries of 91.47%, 102.34%, and 87.85%, respectively. The computational results were in agreement with the experimental results.

The second case study focused on an electrochemical immunosensor for the detection of Reb A by modifying GCE with ZIF-67/fMWCNTs/T1R2 vs Ag/AgCl. The immunosensor showed a substantial exponential increase in oxidation peak currents as Reb A concentrations ranged from 0.9901 µM to 8.2569 µM. The limits of detection and quantification were determined as 1.10 µM and 3.33 µM, respectively. The sensor demonstrated recoveries of 108.25% and 101.88%, for liquid and solid samples, respectively.

In the third and final case study, an ASP immunosensor was developed by modifying a platinum electrode (PtE) with PVP-AgNPs/rGO/T1R2 vs Ag/AgCl. Optimized conditions showed a linear dynamic range of 2.3762 µM to 25.7838 µM, with calculated limits of detection and quantification at 5.85 µM and 17.73 µM, respectively. The immunosensor was applied to detect ASP in samples of Coca Cola Zero Sugar, aQuelle and Lucozade, with average recoveries of 103.31%, 96.06%, and 103.01%, respectively.

Molecular docking was used for ligand-protein interactions, providing insights into chemical interactions between analytes and recognition elements. For this purpose, ASP and Reb A were docked against the rigid T1R2 human sweet taste receptor. The study demonstrated positive correlations between experimental and computational methods, validating the effectiveness of the nanocomposites. The immunosensors exhibited desirable properties—selectivity, high sensitivity, and cost-effectiveness throughout the thesis, from green nanoparticle synthesis to interference studies.

The synergy between experimental and computational methods evident in this study, can be attributed to a positive correlation between the results of electrochemical layer-by-layer electrode surface modification and the corresponding calculated layer-by-layer adsorption energies employed for the electrode modification steps. An increase in the oxidation current of the ASP/Reb A in the presence of nanocomposites (PVP-AgNPs/fMWCNTs/T1R2, ZIF-67/fMWCNTs/T1R2, and PVP-AgNPs/rGO/T1R2) indicates enhanced adsorption capabilities compared to the unmodified GCE and PtE.

Desirable immunosensor properties include selectivity, sensitivity, and cost-effectiveness, all of which are demonstrated throughout the thesis. Starting from the green synthesis of nanoparticles, the developed sensors showed acceptable selectivity during interference studies.

The results of these three case studies may contribute to the development of an immunosensor that can potentially be used to quantify ASP/RebA in the food and beverage industry.

6.2 Recommendations for Future work

The following suggestions for future artificial (ASP) and natural (Reb A) sweetener detection could be focused on for effective sweetener detection on the developed immunosensors:

(i) The use of different nanomaterials from different metals when synthesizing nanoparticles for further enhancement of the performance of the developed immunosensor.
(ii) The use of hybrid nanoparticles has proven to perform well in the sensor industry.

(iii) The future of sensors for the detection of sweeteners would be to commercialize the already designed immunosensors. This can be achieved in terms of developing portable disposable electrode devices to be used by food and safety agencies to ensure compliance.

REFERENCES

Abhilash, M., Paul, M. V. S., Varghese, M. V. and Nair, R. H. 2011. Effect of long term intake of aspartame on antioxidant defense status in liver. *Food and Chemical Toxicology,* 49 (6): 1203-1207.

Ahmed, D. S., Haider, A. J. and Mohammad, M. 2013. Comparesion of functionalization of multi-walled carbon nanotubes treated by oil olive and nitric acid and their characterization. *Energy Procedia,* 36: 1111.

Akkermans, R. L., Spenley, N. A. and Robertson, S. H. 2013. Monte Carlo methods in materials studio. *Molecular Simulation*, 39 (14-15): 1153-1164.

Alavi, M. and Moradi, M. 2022. Different antibacterial and photocatalyst functions for herbal and bacterial synthesized silver and copper/copper oxide nanoparticles/nanocomposites: A review. *Inorganic Chemistry Communications*, 142: 109590.

Alazwari, M. A., Abu-Hamdeh, N. H., Nusier, O. K. and Karimipour, A. 2021. Vacancy defect influence on nanofluid flow and absorbed thermal energy in a nanochannel affected by Universal Force Field via composed approach of embedded atom model/molecular dynamics method. *Journal of Molecular Liquids*, 333: 115927.

Alghoraibi, I., Soukkarieh, C., Zein, R., Alahmad, A., Walter, J.-G. and Daghestani, M. 2020. Aqueous extract of Eucalyptus camaldulensis leaves as reducing and capping agent in biosynthesis of silver nanoparticles. *Inorganic and Nano-Metal Chemistry*, 50 (10): 895-902.

References

Ali, K., Ahmed, B., Dwivedi, S., Saquib, Q., Al-Khedhairy, A. A. and Musarrat, J. 2015. Microwave accelerated green synthesis of stable silver nanoparticles with Eucalyptus globulus leaf extract and their antibacterial and antibiofilm activity on clinical isolates. *PloS one*, 10 (7): e0131178.

Altunayar-Unsalan, C. and Unsalan, O. 2021. Structural and anharmonic vibrational spectroscopic analysis of artificial sweetener alitame: A DFT study for molecular basis of sweet taste. *Journal of Molecular Structure*, 1246: 131157.

An, J. Y., Azizov, S., Kumar, A. P. and Lee, Y. I. 2018. Quantitative analysis of artificial sweeteners by capillary electrophoresis with a dual-capillary design of molecularly imprinted solid-phase extractor. *Bulletin of the Korean Chemical Society*, 39 (11): 1315-1319.

Archana, K., Pillai, N. G., Rhee, K. Y. and Asif, A. 2019. Super paramagnetic ZIF-67 metal organic framework nanocomposite. *Composites Part B: Engineering*, 158: 384-389.

Arya, S., Mahajan, P., Mahajan, S., Khosla, A., Datt, R., Gupta, V., Young, S.-J. and Oruganti, S. K. 2021. influence of processing parameters to control morphology and optical properties of Sol-Gel synthesized ZnO nanoparticles. *ECS Journal of Solid State Science and Technology*, 10 (2): 023002.

Assadi-Porter, F. M., Tonelli, M., Maillet, E. L., Markley, J. L. and Max, M. 2010. Interactions between the human sweet-sensing T1R2–

T1R3 receptor and sweeteners detected by saturation transfer difference NMR spectroscopy. *Biochimica et Biophysica Acta (BBA)-Biomembranes*, 1798 (2): 82-86.

Ayyappa, B., Kanchi, S., Singh, P., Sabela, M. I., Dovey, M. and Bisetty, K. 2015a. Analytical evaluation of steviol glycosides by capillary electrophoresis supported with molecular docking studies. *Journal of the Iranian Chemical Society*, 12: 127-136.

Ayyappa, B., Kanchi, S., Singh, P., Sabela, M. I., Dovey, M. and Bisetty, K. 2015b. Analytical evaluation of steviol glycosides by capillary electrophoresis supported with molecular docking studies. *Journal of the Iranian Chemical Society*, 12 (1): 127-136.

Balachandran, A., Sreenilayam, S. P., Madanan, K., Thomas, S. and Brabazon, D. 2022. Nanoparticle production via laser ablation synthesis in solution method and printed electronic application - A brief review. *Results in Engineering*, 16: 100646.

Balgobind, K., Kanchi, S., Sharma, D., Bisetty, K. and Sabela, M. I. 2016a. Hybrid of ZnONPs / MWCNTs for electrochemical detection of aspartame in food and beverage samples. *Journal of Electroanalytical Chemistry*, 774 (2016): 51-57.

Balgobind, K., Kanchi, S., Sharma, D., Bisetty, K. and Sabela, M. I. 2016b. Hybrid of ZnONPs/MWCNTs for electrochemical detection of aspartame in food and beverage samples. *Journal of Electroanalytical Chemistry*, 774: 51-57.

References

Bathinapatla, A., Kanchi, S., Singh, P., Sabela, M. I. and Bisetty, K. 2016. An ultrasensitive performance enhanced novel cytochrome c biosensor for the detection of rebaudioside A. *Biosensors and Bioelectronics*, 77: 116-123.

Belin, T. and Epron, F. 2005. Characterization methods of carbon nanotubes: a review. *Materials Science and Engineering: B*, 119 (2): 105-118.

Bergs, D., Burghoff, B., Joehnck, M., Martin, G. and Schembecker, G. 2012. Fast and isocratic HPLC-method for steviol glycosides analysis from Stevia rebaudiana leaves. *Journal für Verbraucherschutz und Lebensmittelsicherheit*, 7 (2): 147-154.

Berthomieu, C. and Hienerwadel, R. 2009. Fourier transform infrared (FTIR) spectroscopy. *Photosynthesis research*, 101: 157-170.

Bindhu, M., Umadevi, M., Esmail, G. A., Al-Dhabi, N. A. and Arasu, M. V. 2020. Green synthesis and characterization of silver nanoparticles from Moringa oleifera flower and assessment of antimicrobial and sensing properties. *Journal of Photochemistry and Photobiology B: Biology*, 205: 111836.

Biovia, D. S. 2016. Discovery Studio modelling. v. 16.10. 15350 ed. *San Diego: Dassault Systemes,*

Bisetty, K., Kanchi, S. and Hloma, P. 2021. Evaluation of the catalytic activity of graphene oxide and zinc oxide nanoparticles on the electrochemical sensing of T1R2-Rebaudioside A complex supported by in silico methods. *Pure and Applied Chemistry*, (000010151520201104)

Bojang, A. A. and Wu, H. S. 2020. Characterization of electrode performance in enzymatic biofuel cells using cyclic voltammetry and electrochemical impedance spectroscopy. *Catalysts*, 10 (7): 782.

Bollella, P. 2022. Enzyme-based amperometric biosensors: 60 years later … Quo Vadis? *Analytica Chimica Acta*, 1234: 340517.

Brandão, A., Rosoiu, S., Costa, R., Silva, A., Anicai, L., Pereira, C. and Enachescu, M. 2022. Dispersion Stability of MWCNTs Decorated with Ag Nanoparticles through Pulse Reversed Current Electrodeposition Using a Deep Eutectic Solvent. In: Proceedings of *Biol. Life Sci. Forum*. s Note: MDPI stays neutral with regard to jurisdictional claims in published …,

Brizuela, A. B., Raschi, A. B., Castillo, M. V., Leyton, P., Romano, E. and Brandán, S. A. 2013. Theoretical structural and vibrational properties of the artificial sweetener sucralose. *Computational and Theoretical Chemistry*, 1008: 52-60.

Brusick, D. J. 2008. A critical review of the genetic toxicity of steviol and steviol glycosides. *Food and Chemical Toxicology*, 46 (7, Supplement): S83-S91.

Bueno-Hernández, N., Vázquez-Frías, R., Abreu y Abreu, A. T., Almeda-Valdés, P., Barajas-Nava, L. A., Carmona-Sánchez, R. I., Chávez-Sáenz, J., Consuelo-Sánchez, A., Espinosa-Flores, A. J.,

References

Hernández-Rosiles, V., Hernández-Vez, G., Icaza-Chávez, M. E., Noble-Lugo, A., Romo-Romo, A., Ruiz-Margaín, A., Valdovinos-Díaz, M. A. and Zárate-Mondragón, F. E. 2019. Review of the scientific evidence and technical opinion on noncaloric sweetener consumption in gastrointestinal diseases. *Mexican Journal of Gastroenterology*, 84 (4): 492-510.

Caputo, F., Industry, S. and Sieg, C. WP2612: Meeting regulatory needs in the characterization of lipid nanoparticles (LNPs) for RNA delivery via FFF-MALS.

Carakostas, M. C., Curry, L., Boileau, A. and Brusick, D. 2008. Overview: the history, technical function and safety of rebaudioside A, a naturally occurring steviol glycoside, for use in food and beverages. *Food and Chemical Toxicology*, 46 (7): S1-S10.

Cecilia, C., Anca, F., Mihaela, T. and Robert, S. 2015. Immunosensors. In: Toonika, R. ed. *Biosensors*. Rijeka: IntechOpen, Ch. 6. Available: https://doi.org/10.5772/60524 (Accessed 2023-03-04).

Celiński, M., Borucka, M., Gloc, M., Gajek, A. and Sałasińska, K. 2020. Determination of explosion characteristics, fire behavior and thermal degradation products of aspartame. *Fire Safety Journal*, 117: 103208.

Chang, C.-S. and Yeh, T. S. 2014. Detection of 10 sweeteners in various foods by liquid chromatography/tandem mass spectrometry. *journal of food and drug analysis*, 22 (3): 318-328.

Chappell, G. A., Heintz, M. M., Borghoff, S. J., Doepker, C. L. and Wikoff, D. S. 2021. Lack of potential carcinogenicity for steviol glycosides - Systematic evaluation and integration of mechanistic data into the totality of evidence. *Food and Chemical Toxicology*, 150: 112045.

Chen, D., Zhao, J., Zhang, P. and Dai, S. 2019. Mechanochemical synthesis of metal–organic frameworks. *Polyhedron*, 162: 59-64.

Chen, J., Huang, H., Zeng, Y., Tang, H. and Li, L. 2015. A novel composite of molecularly imprinted polymer-coated PdNPs for electrochemical sensing norepinephrine. *Biosensors and Bioelectronics*, 65: 366-374.

Chen, L., Zhang, Y., Zhou, Y., Shi, D. and Feng, X.-s. 2023. Sweeteners in food samples: An update on pretreatment and analysis techniques since 2015. *Food Chemistry*, 408: 135248.

Chen, Y., Wei, D., He, K., Li, H. and Sun, F. 2021. Electrochemical method for detection of aspartame in beverage using Pd modified single walled carbon nanotubes sensor (PdNPs/SWCNTs). *INTERNATIONAL JOURNAL OF ELECTROCHEMICAL SCIENCE*, 16 (5)

Cheng, C. and Wu, S.-C. 2011. Simultaneous analysis of aspartame and its hydrolysis products of Coca-Cola Zero by on-line postcolumn derivation fluorescence detection and ultraviolet detection coupled two-dimensional high-performance liquid chromatography. *Journal of Chromatography A*, 1218 (20): 2976-2983.

Cheng, L., Li, R., Liu, G., Zhang, Y., Tang, X., Wang, J., Liu, H. and Qin, Y. 2018. Potential antibacterial mechanism of silver nanoparticles and the optimization of orthopedic implants by advanced modification technologies. *International journal of nanomedicine*, 13: 3311.

Choi, E. Y., Park, K., Yang, C. M., Kim, H., Son, J. H., Lee, S. W., Lee, Y. H., Min, D. and Kwon, Y. U. 2004. Benzene-templated hydrothermal synthesis of metal–organic frameworks with selective sorption properties. *Chemistry–A European Journal*, 10 (21): 5535-5540.

Choi, W., Shin, H.-C., Kim, J. M., Choi, J.-Y. and Yoon, W.-S. 2020. Modeling and applications of electrochemical impedance spectroscopy (EIS) for lithium-ion batteries. *Journal of Electrochemical Science and Technology*, 11 (1): 1-13.

Corrêa de Carvalho, R., Pereira Netto, A. D. and Marques, F. F. d. C. 2014. Simultaneous determination of strontium ranelate and aspartame in pharmaceutical formulation for the treatment of postmenopausal osteoporosis by capillary zone electrophoresis. *Microchemical Journal*, 117: 214-219.

Dąbrowska, S., Chudoba, T., Wojnarowicz, J. and Łojkowski, W. 2018. Current trends in the development of microwave reactors for the synthesis of nanomaterials in laboratories and industries: a review. *Crystals*, 8 (10): 379.

References

Dang, W., Sun, Y., Jiao, H., Xu, L. and Lin, M. 2020. AuNPs-NH2/Cu-MOF modified glassy carbon electrode as enzyme-free electrochemical sensor detecting H2O2. *Journal of Electroanalytical Chemistry*, 856: 113592.

David, B., Tiu, B., Pernites, R. B., Tiu, S. B. and Advincula, R. C. 2016. Colloids and Surfaces A : Physicochemical and Engineering Aspects Detection of aspartame via microsphere-patterned and molecularly imprinted polymer arrays. *Colloids and Surfaces A: Physicochemical and Engineering Aspects*, 495: 149-158.

Dhand, C., Dwivedi, N., Loh, X. J., Ying, A. N. J., Verma, N. K., Beuerman, R. W., Lakshminarayanan, R. and Ramakrishna, S. 2015. Methods and strategies for the synthesis of diverse nanoparticles and their applications: a comprehensive overview. *RSC Advances*, 5 (127): 105003-105037.

Ding, B., Zheng, P., Ma, P. a. and Lin, J. 2020. Manganese oxide nanomaterials: synthesis, properties, and theranostic applications. *Advanced Materials*, 32 (10): 1905823.

Dubascoux, S., Le Hecho, I., Hassellöv, M., Von Der Kammer, F., Gautier, M. P. and Lespes, G. 2010. Field-flow fractionation and inductively coupled plasma mass spectrometer coupling: History, development and applications. *Journal of Analytical Atomic Spectrometry*, 25 (5): 613-623.

El-Kady, M. M., Ansari, I., Arora, C., Rai, N., Soni, S., Verma, D. K., Singh, P. and Mahmoud, A. E. D. 2023. Nanomaterials: A comprehensive review of applications, toxicity, impact, and fate to environment. *Journal of Molecular Liquids*, 370: 121046.

Elgrishi, N., Rountree, K. J., McCarthy, B. D., Rountree, E. S., Eisenhart, T. T. and Dempsey, J. L. 2018. A practical beginner's guide to cyclic voltammetry. *Journal of chemical education*, 95 (2): 197-206.

Erkucuk, A., Akgun, I. and Yesil-Celiktas, O. 2009. Supercritical CO2 extraction of glycosides from Stevia rebaudiana leaves: Identification and optimization. *The Journal of Supercritical Fluids*, 51 (1): 29-35.

Fall, B., Sall, D. D., Hémadi, M., Diaw, A. K. D., Fall, M., Randriamahazaka, H. and Thomas, S. 2023. Highly efficient non-enzymatic electrochemical glucose sensor based on carbon nanotubes functionalized by molybdenum disulfide and decorated with nickel nanoparticles (GCE/CNT/MoS2/NiNPs). *Sensors and Actuators Reports*, 5: 100136.

Felix, F., Baccaro, A. and Angnes, L. 2018. Disposable Voltammetric Immunosensors Integrated with Microfluidic Platforms for Biomedical, Agricultural and Food Analyses: A Review. *Sensors,* 18 (12): 4124.

Feyziazar, M., Amini, M., Jahanban-Esfahlan, A., Baradaran, B., Oroojalian, F., Kamrani, A., Mokhtarzadeh, A., Soleymani, J. and de la Guardia, M. 2022. Recent advances on the piezoelectric, electrochemical, and optical biosensors for the detection of protozoan pathogens. *TrAC Trends in Analytical Chemistry*, 157: 116803.

Förster, H., Wolfrum, C. and Peukert, W. 2012. Experimental study of metal nanoparticle synthesis by an arc evaporation/condensation process. *Journal of Nanoparticle Research*, 14: 1-16.

Galletti, G. C. and Bocchini, P. 1996a. High-performance liquid chromatography with electrochemical detection of aspartame with a post-column photochemical reactor. *Journal of Chromatography A*, 729 (1): 393-398.

Galletti, G. C. and Bocchini, P. 1996b. High-performance liquid chromatography with electrochemical detection of aspartame with a post-column photochemical reactor. *Journal of Chromatography A*, 729 (1-2): 393-398.

Gandhi, H. and Khan, S. 2016. Biological Synthesis of Silver Nanoparticles and Its Antibacterial Activity. *Journal of Nanomedicine and Nanotechnology*, 7 (2): 1000366.

Gardana, C., Scaglianti, M. and Simonetti, P. 2010. Evaluation of steviol and its glycosides in Stevia rebaudiana leaves and commercial sweetener by ultra-high-performance liquid chromatography-mass spectrometry. *Journal of Chromatography A*, 1217 (9): 1463-1470.

Gardana, C., Simonetti, P., Canzi, E., Zanchi, R. and Pietta, P. 2003. Metabolism of stevioside and rebaudioside A from Stevia rebaudiana extracts by human microflora. *Journal of agricultural and food chemistry*, 51 (22): 6618-6622.

Gardea-Torresdey, J. L., Gomez, E., Peralta-Videa, J. R., Parsons, J. G., Troiani, H. and Jose-Yacaman, M. 2003. Alfalfa sprouts: a natural source for the synthesis of silver nanoparticles. *Langmuir*, 19 (4): 1357-1361.

Gazulla, M., Rodrigo, M., Blasco, E. and Orduña, M. 2013. Nitrogen determination by SEM-EDS and elemental analysis. *X-Ray Spectrometry*, 42 (5): 394-401.

Gezginci-Oktayoglu, S., Ercin, M., Sancar, S., Celik, E., Koyuturk, M., Bolkent, S. and Bolkent, S. 2021. Aspartame induces cancer stem cell enrichment through p21, NICD and GLI1 in human PANC-1 pancreas adenocarcinoma cells. *Food and Chemical Toxicology*, 153: 112264.

Gour, A. and Jain, N. K. 2019. Advances in green synthesis of nanoparticles. *Artificial cells, nanomedicine, and biotechnology*, 47 (1): 844-851.

Gowda, J. I. and Nandibewoor, S. T. 2014a. Electrochemical behavior of paclitaxel and its determination at glassy carbon electrode. *Asian Journal of Pharmaceutical Sciences*, 9 (1): 42-49.

Gowda, J. I. and Nandibewoor, S. T. 2014b. Electrochemical behavior of paclitaxel and its determination at glassy carbon electrode. *Asian J. Pharm. Sci.*, 9: 42.

Guo, S., Raya, J., Ji, D., Nishina, Y., Ménard-Moyon, C. and Bianco, A. 2020. Is carboxylation an efficient method for graphene oxide functionalization? *Nanoscale Advances*, 2 (9): 4085-4092.

Guo, X., Xing, T., Lou, Y. and Chen, J. 2016. Controlling ZIF-67 crystals formation through various cobalt sources in aqueous solution. *Journal of Solid State Chemistry*, 235: 107-112.

Gvozdenović, M. M., Popović, N., Stevanović, J. S., Grgur, B., Trišović, T. and Jugović, B. 2014. Electrochemical determination of ascorbic acid using electrochemically deposited polyaniline. In: Proceedings of *Proceedings of the 41st International Conference of Slovak Society of Chemical Engineering*. Tatranské Matliare: Slovak Society of Chemical Engineering, 654-657.

Haider, A. J., Jameel, Z. N. and Al-Hussaini, I. H. M. 2019. Review on: Titanium Dioxide Applications. *Energy Procedia*, 157: 17-29.

Harvey, D. 2000. *Modern analytical chemistry*. McGraw Hill.

Hasan, S. 2015. A review on nanoparticles: their synthesis and types. *Res. J. Recent Sci*, 2277: 2502.

He, K., Zeng, Z., Chen, A., Zeng, G., Xiao, R., Xu, P., Huang, Z., Shi, J., Hu, L. and Chen, G. 2018. Advancement of Ag–graphene based nanocomposites: an overview of synthesis and its applications. *Small*, 14 (32): 1800871.

He, X., Walker, B., Man, V. H., Ren, P. and Wang, J. 2022. Recent progress in general force fields of small molecules. *Current Opinion in Structural Biology*, 72: 187-193.

Hearn, L. and Subedi, P. 2009. Determining levels of steviol glycosides in the leaves of Stevia rebaudiana by near infrared reflectance spectroscopy. *Journal of Food Composition and Analysis*, 22 (2): 165-168.

Hernández-Morales, L., Espinoza-Gómez, H., Flores-López, L. Z., Sotelo-Barrera, E. L., Núñez-Rivera, A., Cadena-Nava, R. D., Alonso-Núñez, G. and Espinoza, K. A. 2019. Study of the green synthesis of silver nanoparticles using a natural extract of dark or white Salvia hispanica L. seeds and their antibacterial application. *Applied Surface Science*, 489: 952-961.

Hloma, P., Uwaya, G. E. and Bisetty, K. 2022. Smart electrochemical immunosensor for detection of aspartame in dietary products supported by in silico methods. *Biosensors and Bioelectronics: X*, 11: 100203.

Hoyos-Palacio, L. M., Castro, D. P. C., Ortiz-Trujillo, I. C., Palacio, L. E. B., Upegui, B. J. G., Mora, N. J. E. and Cornelio, J. A. C. 2019. Compounds of carbon nanotubes decorated with silver nanoparticles via in-situ by chemical vapor deposition (CVD). *Journal of materials research and technology*, 8 (6): 5893-5898.

Imran Din, M. and Rani, A. 2016. Recent advances in the synthesis and stabilization of nickel and nickel oxide nanoparticles: a green adeptness. *International journal of analytical chemistry*, 2016

Jaballah, M. B., Messaoud, N. B. and Dridi, C. 2022. Development of cost-effective and sustainable sensing nanoplatform based on green

AgNPs for the determination of BPA in water. *Journal of Materials Science: Materials in Electronics*, 33 (9): 6981-6998.

Jabbar, K. Q., Barzinjy, A. A. and Hamad, S. M. 2022. Iron oxide nanoparticles: Preparation methods, functions, adsorption and coagulation/flocculation in wastewater treatment. *Environmental Nanotechnology, Monitoring & Management*, 17: 100661.

Jackson, A. U., Tata, A., Wu, C., Perry, R. H., Haas, G., West, L. and Cooks, R. G. 2009. Direct analysis of Stevia leaves for diterpene glycosides by desorption electrospray ionization mass spectrometry. *Analyst*, 134 (5): 867-874.

Jadhao, D., Katekhaye, S. and Thorat, B. 2011. Improved RP-HPLC method for quantitative estimation of stevioside in Stevia rebaudiana Bertoni Burm. *Int. J. Phyto. Pharm*, 1: 27-34.

Jaitak, V. 2015. Interaction model of steviol glycosides from Stevia rebaudiana (Bertoni) with sweet taste receptors: A computational approach. *Phytochemistry*, 116: 12-20.

Jaitak, V., Bandna, B. S. and Kaul, V. K. 2009. An efficient microwave-assisted extraction process of stevioside and rebaudioside-A from Stevia rebaudiana (Bertoni). *Phytochemical Analysis*, 20 (3): 240-245.

Jamkhande, P. G., Ghule, N. W., Bamer, A. H. and Kalaskar, M. G. 2019. Metal nanoparticles synthesis: An overview on methods of preparation, advantages and disadvantages, and applications. *Journal of Drug Delivery Science and Technology*, 53: 101174.

Jesila, J. A., Umesh, N., Wang, S.-F., Mani, G., Alothman, A. A. and Alshgari, R. A. 2021. An electrochemical sensing of phenolic derivative 4-Cyanophenol in environmental water using a facile-constructed Aurivillius-structured Bi2MoO6. *Ecotoxicology and Environmental Safety*, 208: 111701.

Jiang, J., Pi, J. and Cai, J. 2018. The advancing of zinc oxide nanoparticles for biomedical applications. *Bioinorganic chemistry and applications*, 2018

Jun, L. Y., Mubarak, N., Yon, L. S., Bing, C. H., Khalid, M. and Abdullah, E. 2018. Comparative study of acid functionalization of carbon nanotube via ultrasonic and reflux mechanism. *Journal of environmental chemical engineering*, 6 (5): 5889-5896.

Jun, L. Y., Yon, L. S., Mubarak, N., Yeo, K. S., Khalid, M. and Bing, C. H. 2019. Comparison of drying method on acid-functionalized multi-walled carbon nanotube and their application for dye removal. In: Proceedings of *IOP Conference Series: Materials Science and Engineering*. IOP Publishing, 012057.

Kajal, N., Singh, V., Gupta, R. and Gautam, S. 2022. Metal organic frameworks for electrochemical sensor applications: A review. *Environmental Research*, 204: 112320.

References

Kakigi, Y., Suzuki, T., Icho, T., Uyama, A. and Mochizuki, N. 2013. Classification of stevia sweeteners in soft drinks using liquid chromatography and time-of-flight mass spectrometry. *Food Additives & Contaminants: Part A*, 30 (12): 2043-2049.

Karimi, F., Demir, E., Aydogdu, N., Shojaei, M., Taher, M. A., Asrami, P. N., Alizadeh, M., Ghasemi, Y. and Cheraghi, S. 2022. Advancement in electrochemical strategies for quantification of Brown HT and Carmoisine (Acid Red 14) From Azo Dyestuff class. *Food and Chemical Toxicology*, 165: 113075.

Karunakaran, R. and Keskin, M. 2022. Chapter 11 - Biosensors: components, mechanisms, and applications. In: Egbuna, C., Patrick-Iwuanyanwu, K. C., Shah, M. A., Ifemeje, J. C. and Rasul, A. eds. *Analytical Techniques in Biosciences*. Academic Press, 179-190. Available: https://www.sciencedirect.com/science/article/pii/B9780128226544000117 (Accessed

Kavita, V. 2017. DNA biosensors-a review. *J. Bioeng. Biomed. Sci*, 7 (2): 222.

Kedik, S., Fedorov, S., Yanul', N., Prokhorova, L., Smirnova, E. and Panov, A. 2003. Chromatographic determination of stevioside in raw plant material. *Pharmaceutical Chemistry Journal*, 37 (10): 529-532.

Khalil, A. M., Hassan, M. L. and Ward, A. A. 2017. Novel nanofibrillated cellulose/polyvinylpyrrolidone/silver nanoparticles films with electrical conductivity properties. *Carbohydrate Polymers*, 157: 503-511.

Kimmel, D. W., LeBlanc, G., Meschievitz, M. E. and Cliffel, D. E. 2012. Electrochemical sensors and biosensors. *Analytical chemistry*, 84 (2): 685-707.

Kirgöz, Ü. A., Odaci, D., Timur, S., Merkoçi, A., Alegret, S., Beşün, N. and Telefoncu, A. 2006. A biosensor based on graphite epoxy composite electrode for aspartame and ethanol detection. *Analytica Chimica Acta*, 570 (2): 165-169.

Koczkur, K. M., Mourdikoudis, S., Polavarapu, L. and Skrabalak, S. E. 2015. Polyvinylpyrrolidone (PVP) in nanoparticle synthesis. *Dalton transactions*, 44 (41): 17883-17905.

Kolb, N., Herrera, J., Ferreyra, D. and Uliana, R. 2001. Analysis of sweet diterpene glycosides from Stevia rebaudiana: improved HPLC method. *Journal of Agricultural and Food Chemistry*, 49 (10): 4538-4541.

Kounaves, S. P. 1997. Voltammetric techniques. *Handbook of instrumental techniques for analytical chemistry*: 709-726.

Kroese, D. P., Brereton, T., Taimre, T. and Botev, Z. I. 2014. Why the Monte Carlo method is so important today. *Wiley Interdisciplinary Reviews: Computational Statistics*, 6 (6): 386-392.

Kumar, H., Kaul, K., Bajpai-Gupta, S., Kaul, V. K. and Kumar, S. 2012. A comprehensive analysis of fifteen genes of steviol glycosides biosynthesis pathway in Stevia rebaudiana (Bertoni). *Gene*, 492 (1): 276-284.

Kumar, R., Al-Dossary, O., Kumar, G. and Umar, A. 2015. Zinc oxide nanostructures for NO 2 gas–sensor applications: a review. *Nano-Micro Letters*, 7 (2): 97-120.

Kunene, K., Sabela, M., Kanchi, S., Bechelany, M. and Bisetty, K. 2021. Functionalized Electrochemical Aptasensor for Sensing of Ochratoxin A in Cereals Supported by in Silico Adsorption Studies. *ACS Food Science & Technology*, 1 (10): 1849-1860.

Laborda, F., Bolea, E. and Jimenez-Lamana, J. 2014. *Single particle inductively coupled plasma mass spectrometry: a powerful tool for nanoanalysis*: ACS Publications.

Laschuk, N. O., Easton, E. B. and Zenkina, O. V. 2021. Reducing the resistance for the use of electrochemical impedance spectroscopy analysis in materials chemistry. *RSC Advances*, 11 (45): 27925-27936.

Le, A. V., Su, Y.-L. and Cheng, S.-H. 2019. A novel electrochemical assay for aspartame determination via nucleophilic reactions with caffeic acid ortho-quinone. *Electrochimica Acta*, 300: 67-76.

Lee, J. 2014. Electrochemical sensing of oxygen gas in ionic liquids on screen printed electrodes. Curtin University.

Lee, S. H., Salunke, B. K. and Kim, B. S. 2014. Sucrose density gradient centrifugation separation of gold and silver nanoparticles synthesized using Magnolia kobus plant leaf extracts. *Biotechnology and Bioprocess Engineering: BBE*, 19 (1): 169.

Lee, Y.-R., Kim, J. and Ahn, W.-S. 2013. Synthesis of metal-organic frameworks: A mini review. *Korean Journal of Chemical Engineering*, 30: 1667-1680.

Lei, Z. L. and Guo, B. 2022. 2D Material-Based Optical Biosensor: Status and Prospect. *Advanced Science*, 9 (4): 2102924.

Lephalala, M., Kanchi, S., Sabela, M. I. and Bisetty, K. 2020. Electrochemical Enzymatic Biosensing of Neotame Supported by Computational Methods. *Electroanalysis*: 1-13.

Leung, S. S. and Grant, D. J. W. 1997. Solid State Stability Studies of Model Dipeptides: Aspartame and Aspartylphenylalanine. *Journal of Pharmaceutical Sciences*, 86 (1): 64-71.

Li, J., Chen, Z. and Di, D. 2012. Preparative separation and purification of Rebaudioside A from Stevia rebaudiana Bertoni crude extracts by mixed bed of macroporous adsorption resins. *Food chemistry*, 132 (1): 268-276.

Li, J., Cheng, S., Zhao, Q., Long, P. and Dong, J. 2009. Synthesis and hydrogen-storage behavior of metal–organic framework MOF-5. *international journal of hydrogen energy*, 34 (3): 1377-1382.

Li, W., Diao, K., Qiu, D., Zeng, Y., Tang, K., Zhu, Y., Sheng, Y., Wen, Y. and Li, M. 2021a. A highly-sensitive and selective antibody-like sensor based on molecularly imprinted poly (L-arginine) on COOH-MWCNTs for electrochemical recognition and detection of deoxynivalenol. *Food Chemistry*, 350: 129229.

Li, W., Qi, W., Cai, L., Li, C., Sun, Y., Sun, M., Yang, X., Xiang, L., Xie, D. and Ren, T. 2020. Enhanced room-temperature NO2-sensing performance of AgNPs/rGO nanocomposites. *Chemical Physics Letters*, 738: 136873.

Li, X., Li, S., Li, H., Wang, J., Luo, Q. and Yin, X. 2021b. Quantification of artificial sweeteners in alcoholic drinks using direct analysis in real-time QTRAP mass spectrometry. *Food Chemistry*, 342: 128331.

Liang, T., Fu, Q., Shen, A., Wang, H., Jin, Y., Xin, H., Ke, Y., Guo, Z. and Liang, X. 2015. Preparation and chromatographic evaluation of a newly designed steviol glycoside modified-silica stationary phase in hydrophilic interaction liquid chromatography and reversed phase liquid chromatography. *Journal of Chromatography A*, 1388: 110-118.

Liao, C., Li, Y. and Tjong, S. C. 2019. Bactericidal and cytotoxic properties of silver nanoparticles. *International journal of molecular sciences*, 20 (2): 449.

Ling, W., Liew, G., Li, Y., Hao, Y., Pan, H., Wang, H., Ning, B., Xu, H. and Huang, X. 2018. Materials and techniques for implantable nutrient sensing using flexible sensors integrated with metal–organic frameworks. *Advanced Materials*, 30 (23): 1800917.

Liu, C.-C., Ko, C.-H., Wang, Y.-N., Fu, L.-M. and Lee, S.-Z. 2021. Rapid detection of artificial sweeteners in food using microfluidic chromatography detection system. *Chemical Engineering Journal*, 425: 131528.

Liu, Y., Grimm, M., Dai, W.-t., Hou, M.-c., Xiao, Z.-X. and Cao, Y. 2020. CB-Dock: a web server for cavity detection-guided protein–ligand blind docking. *Acta Pharmacologica Sinica*, 41 (1): 138-144.

Lorenzo, C., Serrano-Díaz, J., Plaza, M., Quintanilla, C. and Alonso, G. L. 2014. Fast methodology of analysing major steviol glycosides from Stevia rebaudiana leaves. *Food Chemistry*, 157: 518-523.

Luo, C., Liu, X., Liu, F., He, N., Yu, R. and Liu, X. 2022. AgNPs doping the fold carbon nanoflower composite for highly sensitive electrochemical detection of hydrogen peroxide. *Journal of Electroanalytical Chemistry*, 904: 115930.

Mafamadi, M., Etale, A. and Daramola, M. O. 2023. Synthesis and characterization of graphene oxide functionalized with dicarboxylic acids. *Materials Today: Proceedings*,

Magar, H. S., Hassan, R. Y. and Mulchandani, A. 2021. Electrochemical impedance spectroscopy (EIS): Principles, construction, and biosensing applications. *Sensors*, 21 (19): 6578.

Maki, K. C., Curry, L. L., Carakostas, M. C., Tarka, S. M., Reeves, M. S., Farmer, M. V., McKenney, J. M., Toth, P. D., Schwartz, S. L., Lubin, B. C., Dicklin, M. R., Boileau, A. C. and Bisognano, J. D. 2008. The hemodynamic effects of rebaudioside A in healthy adults with normal and low-normal blood pressure. *Food and Chemical Toxicology*, 46 (7, Supplement): S40-S46.

Malina, D., Sobczak-Kupiec, A., Wzorek, Z. and Kowalski, Z. 2012. SILVER NANOPARTICLES SYNTHESIS WITH DIFFERENT CONCENTRATIONS OF POLYVINYLPYRROLIDONE. *Digest Journal of Nanomaterials & Biostructures (DJNB)*, 7 (4)

Mäntele, W. and Deniz, E. 2017. *UV–VIS absorption spectroscopy: Lambert-Beer reloaded*: Elsevier.

Marinovich, M., Galli, C. L., Bosetti, C., Gallus, S. and La Vecchia, C. 2013. Aspartame, low-calorie sweeteners and disease: regulatory safety and epidemiological issues. *Food and Chemical Toxicology*, 60: 109-115.

Mauri, P., Catalano, G., Gardana, C. and Pietta, P. 1996. Analysis of stevia glycosides by capillary electrophoresis. *Electrophoresis*, 17 (2): 367-371.

Medeiros, R. A., Carvalho, A. E. d., Rocha-Filho, R. C. and Fatibello-Filho, O. 2008a. Simultaneous square-wave voltammetric determination of aspartame and cyclamate using a boron-doped diamond electrode. *Talanta*, 76 (3): 685-689.

Medeiros, R. A., de Carvalho, A. E., Rocha-Filho, R. C. and Fatibello-Filho, O. 2008b. Simultaneous square-wave voltammetric determination of aspartame and cyclamate using a boron-doped diamond electrode. *Talanta*, 76 (3): 685-689.

Medrano, L. C., Flores-Aguilar, J. F., Islas, G., Rodríguez, J. A. and Ibarra, I. S. 2019. Solid-phase extraction and large-volume sample stacking-capillary electrophoresis for determination of artificial sweeteners in water samples. *Food Analytical Methods*, 12 (2): 526-533.

Mehrotra, P. 2016. Biosensors and their applications–A review. *Journal of Oral Biology and Craniofacial Research*, 6 (2): 153-159.

Modan, E. M. and PLĂIAȘU, A. G. 2020. Advantages and disadvantages of chemical methods in the elaboration of nanomaterials. *The Annals of "Dunarea de Jos" University of Galati. Fascicle IX, Metallurgy and Materials Science*, 43 (1): 53-60.

Mohamed Nageib, A., Abdul Halim, A., Nurashikin Nordin, A. and Ali, F. 2023. Computational modelling analysis and synthesis of molecularly imprinted polymers (MIPs) with two functional monomers using bulk polymerization. *Materials Today: Proceedings*,

Mohammed, A. and Abdullah, A. 2018. Scanning electron microscopy (SEM): A review. In: Proceedings of *Proceedings of the 2018 International Conference on Hydraulics and Pneumatics—HERVEX, Băile Govora, Romania*. 7-9.

Mollazadeh, S., Sahebkar, A., Shahlaei, M. and Moradi, S. 2021. Nano drug delivery systems: Molecular dynamic simulation. *Journal of Molecular Liquids*, 332: 115823.

Moond, M., Singh, S., Sangwan, S., Rani, S., Beniwal, A., Rani, J., Kumari, A., Rani, I. and Devi, P. 2023. Phytofabrication of Silver Nanoparticles Using Trigonella foenum-graceum L. Leaf and Evaluation of Its Antimicrobial and Antioxidant Activities. *International journal of molecular sciences*, 24 (4): 3480.

Murali, A., Giri, V., Cameron, H. J., Sperber, S., Zickgraf, F. M., Haake, V., Driemert, P., Walk, T., Kamp, H., Rietjens, I. M. C. M. and van Ravenzwaay, B. 2022. Investigating the gut microbiome and metabolome following treatment with artificial sweeteners acesulfame potassium and saccharin in young adult Wistar rats. *Food and Chemical Toxicology*, 165: 113123.

Murti, B. T., Putri, A. D., Kanchi, S., Sabela, M. I., Bisetty, K. and Asiri, A. M. 2018. Light induced DNA-functionalized TiO2 nanocrystalline interface: Theoretical and experimental insights towards DNA damage detection. *Journal of Photochemistry and Photobiology B: Biology*, 188: 159-176.

Nabaei, V., Chandrawati, R. and Heidari, H. 2018. Magnetic biosensors: Modelling and simulation. *Biosensors and Bioelectronics*, 103: 69-86.

References

Naidoo, L., Kanchi, S., Drexel, R., Meier, F. and Bisetty, K. 2021. Measurement of TiO2 Nanoscale Ingredients in Sunscreens by Multidetector AF4, TEM, and spICP-MS Supported by Computational Modeling. *ACS Applied Nano Materials*,

Naidoo, L., Suvardhan, K., Sabela, M. I. and Bisetty, K. 2020. Multivariate optimization of field-flow fractionation of nanoscale synthetic amorphous silica in processed foods supported by computational modelling. *New Journal of Chemistry*, 44 (40): 17542-17551.

Naidoo, L., Uwaya, G. E., Meier, F. and Bisetty, K. 2023. A novel electrochemical sensor for the detection of zearalenone in food matrices using PEGylated Fe3O4 nanoparticles supported by in-silico and multidetector AF4. *Journal of Electroanalytical Chemistry*, 935: 117363.

Nakano, M., Fujiwara, T. and Koga, N. 2016. Thermal decomposition of silver acetate: physico-geometrical kinetic features and formation of silver nanoparticles. *The Journal of Physical Chemistry C*, 120 (16): 8841-8854.

Natsuki, J. and Natsuki, T. 2023. Silver Nanoparticle/Carbon Nanotube Hybrid Nanocomposites: One-Step Green Synthesis, Properties, and Applications. *Nanomaterials*, 13 (8): 1297.

Natsuki, J., Natsuki, T. and Hashimoto, Y. 2015. A review of silver nanoparticles: synthesis methods, properties and applications. *Int. J. Mater. Sci. Appl*, 4 (5): 325-332.

Nie, P., Zhao, Y. and Xu, H. 2023. Synthesis, applications, toxicity and toxicity mechanisms of silver nanoparticles: A review. *Ecotoxicology and Environmental Safety*, 253: 114636.

Ojha, A. 2020. Chapter 19 - Nanomaterials for removal of waterborne pathogens: opportunities and challenges. In: Vara Prasad, M. N. and Grobelak, A. eds. *Waterborne Pathogens*. Butterworth-Heinemann, 385-432. Available: https://www.sciencedirect.com/science/article/pii/B9780128187838000190 (Accessed

Okasha, E. F. 2016. Effect of long term-administration of aspartame on the ultrastructure of sciatic nerve. *Journal of Microscopy and Ultrastructure*, 4 (4): 175-183.

Oliveira, T. M. and Morais, S. 2018. New generation of electrochemical sensors based on multi-walled carbon nanotubes. *Applied Sciences*, 8 (10): 1925.

Orio, M., Pantazis, D. A. and Neese, F. 2009. Density functional theory. *Photosynthesis research*, 102: 443-453.

Pajkossy, T., Ceblin, M. U. and Meszaros, G. 2021. Dynamic electrochemical impedance spectroscopy for the charge transfer rate measurement of the ferro/ferricyanide redox couple on gold. *Journal of Electroanalytical Chemistry*, 899: 115655.

Patel, C. N. and Narechania, M. B. 2018. Targeting epidermal growth factor receptors inhibition in non-small-cell lung cancer: a computational approach. *Molecular Simulation*, 44 (17): 1478-1488.

Perrier, J. D., Mihalov, J. J. and Carlson, S. J. 2018. FDA regulatory approach to steviol glycosides. *Food and Chemical Toxicology*, 122: 132-142.

Petrikaitė, V., Skapas, M. and Stankevičius, E. 2023. Generation of gold and silver nanoparticles using laser ablation of thin bimetallic films and bulk targets in water. *Optical Materials*, 137: 113535.

Popova, A. D., Velcheva, E. A. and Stamboliyska, B. A. 2012. DFT and experimental study on the IR spectra and structure of acesulfame sweetener. *Journal of Molecular Structure*, 1009: 23-29.

Praveena, S. M., Cheema, M. S. and Guo, H. R. 2019. Non-nutritive artificial sweeteners as an emerging contaminant in environment: A global review and risks perspectives. *Ecotoxicology and Environmental Safety*, 170 (December 2018): 699-707.

Pundir, C. and Malik, A. 2019. Bio-sensing of organophosphorus pesticides: A review. *Biosensors and Bioelectronics*: 111348.

Qian, J., Sun, F. and Qin, L. 2012. Hydrothermal synthesis of zeolitic imidazolate framework-67 (ZIF-67) nanocrystals. *Materials Letters*, 82: 220-223.

Qu, F., Qi, Z.-H., Liu, K.-N. and Mou, S.-F. 1999. Determination of aspartame by ion chromatography with electrochemical integrated amperometric detection. *Journal of Chromatography A*, 850 (1): 277-281.

Rafiei, S., Tangestaninejad, S., Horcajada, P., Moghadam, M., Mirkhani, V., Mohammadpoor-Baltork, I., Kardanpour, R. and Zadehahmadi, F. 2018. Efficient biodiesel production using a lipase@ ZIF-67 nanobioreactor. *Chemical Engineering Journal*, 334: 1233-1241.

Rafique, M., Sadaf, I., Rafique, M. S. and Tahir, M. B. 2017. A review on green synthesis of silver nanoparticles and their applications. *Artificial cells, nanomedicine, and biotechnology*, 45 (7): 1272-1291.

Rajasekaran, T., Ramakrishna, A., Udaya Sankar, K., Giridhar, P. and Ravishankar, G. 2008. Analysis of predominant steviosides in Stevia rebaudiana Bertoni by liquid chromatography/electrospray ionization-mass spectrometry. *Food Biotechnology*, 22 (2): 179-188.

Rajeshkumar, S. and Naik, P. 2018. Synthesis and biomedical applications of cerium oxide nanoparticles–a review. *Biotechnology Reports*, 17: 1-5.

Rane, A. V., Kanny, K., Abitha, V. and Thomas, S. 2018. Methods for synthesis of nanoparticles and fabrication of nanocomposites. In: *Synthesis of inorganic nanomaterials*. Elsevier, 121-139.

Rappe, A., Colwell, K. and Casewit, C. 1993. Application of a universal force field to metal complexes. *Inorganic Chemistry*, 32 (16): 3438-3450.

Rather, S. U. 2016. Trimetallic catalyst synthesized multi-walled carbon nanotubes and their application for hydrogen storage. *Korean Journal of Chemical Engineering*, 33: 1551-1556.

Reverté, L., Prieto-Simón, B. and Campàs, M. 2016. New advances in electrochemical biosensors for the detection of toxins: Nanomaterials, magnetic beads and microfluidics systems. A review. *Analytica Chimica Acta*, 908: 8-21.

Roberts, A. 2016. The safety and regulatory process for low calorie sweeteners in the United States. *Physiology & Behavior*, 164: 439-444.

Roberts, A. and Renwick, A. G. 2008. Comparative toxicokinetics and metabolism of rebaudioside A, stevioside, and steviol in rats. *Food and Chemical Toxicology*, 46 (7, Supplement): S31-S39.

Saadatkhah, N., Carillo Garcia, A., Ackermann, S., Leclerc, P., Latifi, M., Samih, S., Patience, G. S. and Chaouki, J. 2020. Experimental methods in chemical engineering: Thermogravimetric analysis—TGA. *The Canadian Journal of Chemical Engineering*, 98 (1): 34-43.

Sadiq, M. U., Shah, A., Haleem, A., Shah, S. M. and Shah, I. 2023. Eucalyptus globulus Mediated Green Synthesis of Environmentally Benign Metal Based Nanostructures: A Review. *Nanomaterials*, 13 (13): 2019.

Sajid, M., Asif, M., Baig, N., Kabeer, M., Ihsanullah, I. and Mohammad, A. W. 2022. Carbon nanotubes-based adsorbents: Properties, functionalization, interaction mechanisms, and applications in water purification. *Journal of Water Process Engineering*, 47: 102815.

Saleem, H., Haneef, M. and Abbasi, H. Y. 2018. Synthesis route of reduced graphene oxide via thermal reduction of chemically exfoliated graphene oxide. *Materials Chemistry and Physics*, 204: 1-7.

Samah, N., Hisham, A. and Rahim, S. 2013. Determination of stevioside and rebaudioside A in Stevia rebaudiana leaves via preparative high performance liquid chromatography (prep-HPLC). *International Journal*, 4 (2)

Savin, A. V. and Mazo, M. A. 2020. The COMPASS force field: Validation for carbon nanoribbons. *Physica E: Low-dimensional Systems and Nanostructures*, 118: 113937.

Schick, C. 2009. Differential scanning calorimetry (DSC) of semicrystalline polymers. *Analytical and bioanalytical chemistry*, 395: 1589-1611.

Schneidman-Duhovny, D., Inbar, Y., Nussinov, R. and Wolfson, H. J. 2005. PatchDock and SymmDock: servers for rigid and symmetric docking. *Nucleic acids research*, 33 (suppl_2): W363-W367.

Shafii, B., Vismeh, R., Beaudry, R., Warner, R. and Jones, A. D. 2012. Large-scale profiling of diterpenoid glycosides from Stevia rebaudiana using ultrahigh performance liquid chromatography/tandem mass spectrometry. *Analytical and bioanalytical chemistry,* 403 (9): 2683-2690.

Shah, R., De Jager, L. S. and Begley, T. H. 2012. Simultaneous determination of steviol and steviol glycosides by liquid chromatography-mass spectrometry. *Food Additives & Contaminants: Part A*, 29 (12): 1861-1871.

Shahsavari, M., Mohammadzadeh Jahani, P., Sheikhshoaie, I., Tajik, S., Aghaei Afshar, A., Askari, M. B., Salarizadeh, P., Di Bartolomeo, A. and Beitollahi, H. 2022. Green synthesis of zeolitic imidazolate frameworks: A review of their characterization and industrial and medical applications. *Materials*, 15 (2): 447.

Shamkhalichenar, H. and Choi, J.-W. 2020. Non-enzymatic hydrogen peroxide electrochemical sensors based on reduced graphene oxide. *Journal of The Electrochemical Society*, 167 (3): 037531.

Sharma, D., Sabela, M. I., Kanchi, S., Bisetty, K., Skelton, A. A. and Honarparvar, B. 2018. Green synthesis, characterization and electrochemical sensing of silymarin by ZnO nanoparticles: experimental and DFT studies. *Journal of Electroanalytical Chemistry*, 808: 160-172.

Sharma, R. and Tripathi, A. 2022. Green synthesis of nanoparticles and its key applications in various sectors. *Materials Today: Proceedings*, 48: 1626-1632.

Shawky, A. M. and El-Tohamy, M. 2021. Signal amplification strategy of label-free ultrasenstive electrochemical immunosensor based ternary Ag/TiO2/rGO nanocomposites for detecting breast cancer biomarker CA 15-3. *Materials Chemistry and Physics*, 272: 124983.

Sheikhi, M., Shahab, S., Khaleghian, M. and Kumar, R. 2018. Interaction between new anti-cancer drug syndros and CNT (6, 6-6) nanotube for medical applications: geometry optimization, molecular structure, spectroscopic (NMR, UV/Vis, excited state), FMO, MEP and HOMO-LUMO investigation. *Applied Surface Science*, 434: 504-513.

Singh, R. and Singh, M. 2023. Molecularly imprinted electrochemical sensor for highly selective and sensitive determination of artificial sweetener Acesulfame-K. *Talanta Open*, 7: 100194.

Skládal, P. 2016. Piezoelectric biosensors. *TrAC Trends in Analytical Chemistry*, 79: 127-133.

Skoog, D. A., Holler, F. J. and Crouch, S. R. 2017. *Principles of instrumental analysis*. Cengage learning.

Sogne, V., Meier, F., Klein, T. and Contado, C. 2017. Investigation of zinc oxide particles in cosmetic products by means of centrifugal and asymmetrical flow field-flow fractionation. *Journal of Chromatography A*, 1515: 196-208.

Song, J. Y. and Kim, B. S. 2009. Rapid biological synthesis of silver nanoparticles using plant leaf extracts. *Bioprocess and biosystems engineering,* 32: 79-84.

Stegink, F. 2020. *Aspartame: physiology and biochemistry*. CRC Press.

Stojkovic, M., Mai, T. D. and Hauser, P. C. 2013. Determination of artificial sweeteners by capillary electrophoresis with contactless conductivity detection optimized by hydrodynamic pumping. *Analytica Chimica Acta,* 787: 254-259.

Sun, H., Ren, P. and Fried, J. 1998a. The COMPASS force field: parameterization and validation for phosphazenes. *Computational and Theoretical Polymer Science,* 8 (1-2): 229-246.

Sun, H., Ren, P. and Fried, J. R. 1998b. The COMPASS force field: parameterization and validation for phosphazenes. *Computational and Theoretical Polymer Science,* 8 (1): 229-246.

Sun, Y., Liu, D., Liu, W., Liu, H., Zhao, J., Chen, P., Wang, X. and Cheng, Y. 2022. Combination of ZIF-67 derived hollow porous Co9S8 nanocages and MWCNTs for electrochemical hydrogen storage applications. *International Journal of Hydrogen Energy*, 47 (89): 37870-37881.

Syafiuddin, A., Salim, M. R., Beng Hong Kueh, A., Hadibarata, T. and Nur, H. 2017. A review of silver nanoparticles: research trends, global consumption, synthesis, properties, and future challenges. *Journal of the Chinese Chemical Society*, 64 (7): 732-756.

Tighrine, A., Amir, Y., Alfaro, P., Mamou, M. and Nerín, C. 2019. Simultaneous extraction and analysis of preservatives and artificial sweeteners in juices by salting out liquid-liquid extraction method prior to ultra-high performance liquid chromatography. *Food Chemistry*, 277: 586-594.

Tiu, B. D. B., Pernites, R. B., Tiu, S. B. and Advincula, R. C. 2016. Detection of aspartame via microsphere-patterned and molecularly imprinted polymer arrays. *Colloids and Surfaces A: Physicochemical and Engineering Aspects*, 495: 149-158.

Tsuji, T., Thang, D.-H., Okazaki, Y., Nakanishi, M., Tsuboi, Y. and Tsuji, M. 2008. Preparation of silver nanoparticles by laser ablation in polyvinylpyrrolidone solutions. *Applied Surface Science*, 254 (16): 5224-5230.

Ulicny, J. and Kozar, T. 2018. Roadmap for Computer-Aided Modeling of Theranostics and Related Nanosystems. In: Proceedings of *EPJ Web of Conferences*. EDP Sciences, 05017.

Üstün Özgür, M. and Kasapoğlu, M. 2019. Development and Validation of a Simple Ultra Fast Liquid Chromatographic Method for the Simultaneous Determination of Aspartame, Acesulfame-K, Caffeine and Sodium Benzoate in Dietic Soft Drinks. *Journal of Analytical Chemistry*, 74 (6): 555-564.

References

Uwaya, G. 2021. Electrochemical detection of choline at green mediated nanocomposites modified electrode. North-West University (South Africa).

Uwaya, G., Gumede, N. J. and Bisetty, K. 2021. Electrocatalysis of Endosulfan Based on Fe3O4: An Experimental and Computational Approach. *ACS omega*,

Uwaya, G. E. and Bisetty, K. 2023. Integration of multiwalled carbon nanotubes with cobalt oxide for smart electrochemical sensing of epicatechin in foods. *Carbon Trends*, 10: 100240.

Uwaya, G. E. and Fayemi, O. E. 2021a. Electrochemical detection of choline at f-MWCNT/Fe3O4 nanocomposite modified glassy carbon electrode. *Materials Research Express*, 8 (5): 055403.

Uwaya, G. E. and Fayemi, O. E. 2021b. Electrochemical detection of choline at f-MWCNT/Fe3O4 nanocomposite modified glassy carbon electrode. *Mater. Res. Express.*, 8: 055403.

Uwaya, G. E., Sagrado, S. and Bisetty, K. 2022. Smart electrochemical sensing of xylitol using a combined machine learning and simulation approach. *Talanta Open*, 6: 100144.

Uwaya, G. E., Wen, Y. and Bisetty, K. 2022. A combined experimental-computational approach for electrocatalytic detection of epinephrine using nanocomposite sensor based on polyaniline/nickel oxide. *Journal of Electroanalytical Chemistry*: 116204.

Van der Bruggen, B., Mänttäri, M. and Nyström, M. 2008. Drawbacks of applying nanofiltration and how to avoid them: A review. *Separation and Purification Technology*, 63 (2): 251-263.

Verma, D., Chauhan, D., Das Mukherjee, M., Ranjan, K. R., Yadav, A. K. and Solanki, P. R. 2021. Development of MWCNT decorated with green synthesized AgNps-based electrochemical sensor for highly sensitive detection of BPA. *Journal of Applied Electrochemistry*, 51: 447-462.

Verma, G. and Mishra, M. 2018. Development and optimization of UV-Vis spectroscopy-a review. *World J. Pharm. Res*, 7 (11): 1170-1180.

Wikoff, D. S., Chappell, G. A., Fitch, S., Doepker, C. L. and Borghoff, S. J. 2020. Lack of potential carcinogenicity for aspartame – Systematic evaluation and integration of mechanistic data into the totality of the evidence. *Food and Chemical Toxicology*, 135: 110866.

Woelwer-Rieck, U., Lankes, C., Wawrzun, A. and Wüst, M. 2010a. Improved HPLC method for the evaluation of the major steviol glycosides in leaves of Stevia rebaudiana. *European Food Research and Technology*, 231 (4): 581-588.

Woelwer-Rieck, U., Lankes, C., Wawrzun, A. and Wüst, M. 2010b. Improved HPLC method for the evaluation of the major steviol glycosides in leaves of Stevia rebaudiana. *European Food Research and Technology*, 231: 581-588.

Wróbel, K. and Wróbel, K. 1997. Determination of aspartame and phenylalanine in diet soft drinks by high-performance liquid chromatography with direct spectrofluorimetric detection. *Journal of Chromatography A*, 773 (1): 163-168.

Xia, Y., Hu, X., Liu, Y., Zhao, F. and Zeng, B. 2022. Molecularly imprinted ratiometric electrochemical sensor based on carbon nanotubes/cuprous oxide nanoparticles/titanium carbide MXene composite for diethylstilbestrol detection. *Microchimica Acta*, 189 (4): 137.

Xie, A., Yuan, B., Lin, J., Pan, J., Li, M., Wang, J., Jiang, S., Zhu, S. and Luo, S. 2023. Highly sensitive and selective electrochemical sensor based on ZIF-67-derived Co3O4-LaMn0. 5Ni0. 5O3/MWCNTs for simultaneous detection of protocatechuic acid and ascorbic acid. *Surfaces and Interfaces*, 36: 102550.

Yadav, P. and Chowdhury, P. 2022. Effectivity of repurposed drugs against SARS-CoV-2 infections, A hope for COVID 19: inhibitor modelling studies by docking and molecular dynamics. *Heliyon*, 8 (12): e12327.

Yang, D.-j. and Chen, B. 2009. Simultaneous determination of nonnutritive sweeteners in foods by HPLC/ESI-MS. *Journal of agricultural and food chemistry*, 57 (8): 3022-3027.

Yang, J. C. and Park, J. Y. 2018. Surface imprinted conducting polymer patterns electrochemically grown from gold pinhole arrays on 2D inverse silica opals and their effective use in aspartame detection. *Sensors and Actuators B: Chemical*, 255: 463-470.

Yang, Y., Li, W. and Liu, J. 2021. Review of recent progress on DNA-based biosensors for Pb2+ detection. *Analytica Chimica Acta*, 1147: 124-143.

Yılmaz, S. and Uçar, A. 2014. A review of the genotoxic and carcinogenic effects of aspartame: does it safe or not? *Cytotechnology*, 66 (6): 875-881.

Yrjönen, T. 2004. Extraction and planar chromatographic separation techniques in the analysis of natural products.

Yu, C., Gou, L., Zhou, X., Bao, N. and Gu, H. 2011. Chitosan–Fe3O4 nanocomposite based electrochemical sensors for the determination of bisphenol A. *Electrochimica Acta*, 56 (25): 9056-9063.

Yu, W., Sisi, L., Haiyan, Y. and Jie, L. 2020. Progress in the functional modification of graphene/graphene oxide: A review. *RSC Advances*, 10 (26): 15328-15345.

Yuan, X., Zhang, X., Sun, L., Wei, Y. and Wei, X. 2019. Cellular toxicity and immunological effects of carbon-based nanomaterials. *Particle and Fibre Toxicology*, 16 (1): 1-27.

Zhang, L., Feng, L., Li, P., Chen, X., Jiang, J., Zhang, S., Zhang, C., Zhang, A., Chen, G. and Wang, H. 2020. Direct Z-scheme photocatalyst of hollow CoSx@ CdS polyhedron constructed by ZIF-67-templated one-pot solvothermal route: A signal-on photoelectrochemical sensor for mercury (II). *Chemical Engineering Journal*, 395: 125072.

Zhang, X., Sun, H., Tan, S., Gao, J., Fu, Y. and Liu, Z. 2019. Hydrothermal synthesis of Ag nanoparticles on the nanocellulose and their antibacterial study. *Inorganic Chemistry Communications*, 100: 44-50.

Zhang, Y. and Wei, Q. 2016. The role of nanomaterials in electroanalytical biosensors: A mini review. *Journal of Electroanalytical Chemistry*, 781: 401-409.

Zhao, Z., Li, H., Zhao, K., Wang, L. and Gao, X. 2022. Microwave-assisted synthesis of MOFs: Rational design via numerical simulation. *Chemical Engineering Journal*, 428: 131006.

Zhou, Z.-F., Feng, X.-Z., Zhan, T., Han, G.-C., Chen, Z. and Kraatz, H.-B. 2022. Facile bimetallic co-amplified electrochemical sensor for folic acid sensing based on CoNPs and CuNPs. *Analytical and bioanalytical chemistry*, 414 (23): 6791-6800.